Centre for Quantum and Optical Science
Faculty of Science, Engineering and Technology
Swinburne University of Technology

# Ultracold Atoms with Synthetic Gauge Field

A thesis submitted for the degree of
Doctor of Philosophy

CANDIDATE:
Xiao-Long Chen

SUPERVISORS:
A/Prof. Hui Hu
Prof. Xia-Ji Liu
Prof. Peter Drummond

Melbourne, Australia, 13 Decembber 2018

# Abstract

This thesis is devoted to the study of a three-dimensional weakly interacting Bose gas with one-dimensional Raman-type spin-orbit coupling. The spin-orbit coupling (SOC) arising from the interaction of a particle's spin with its motion plays a crucial role in various fields of physics. Plenty of studies are intrigued and give rise to many fascinating phenomena, such as quantum spin Hall effect, topological superfluidity and exotic bosonic phases of matter. Over the past few years, the SOC effects have been simulated and studied extensively in alkali-metal atomic quantum gases, owing to the high controllability of cold-atom platforms.

In this thesis, by employing a generalized Hartree-Fock-Bogoliubov theory with Popov approximation, we determine a finite-temperature phase diagram of three exotic condensation phases, i.e., the stripe (ST), plane-wave (PW) and zero-momentum (ZM) phases, against both quantum and thermal fluctuations. We find that the plane-wave phase is significantly broadened by thermal fluctuations. The phonon mode and sound velocity near the PW-ZM phase transition are thoughtfully analyzed. At zero temperature, we find that quantum fluctuations open an unexpected gap in sound velocity at the phase transition, in stark contrast to the previous theoretical prediction of a vanishing sound velocity. At finite temperature, thermal fluctuations continue to enlarge the gap and simultaneously shift the critical minimum of the sound velocity. For a Bose gas of $^{87}$Rb atoms at the typical experimental temperature, $T = 0.3T_0$, where $T_0$ is the critical temperature of an ideal Bose gas without spin-orbit coupling, our results of gap opening and critical minimum shifting in sound velocity, are qualitatively consistent with the recent experimental observation [Ji *et al.*, Phys. Rev. Lett. **114**, 105301 (2015)].

We also give an investigation of the exotic supersolid stripe phase at zero tem-

perature. By employing an improved ansatz, including high-order harmonics in the stripe phase, we show that the critical transition point from ST to PW phases is shifted to a relatively larger Rabi frequency compared to the prediction by the earlier work [Li *et al.*, Phys. Rev. Lett. **108**, 225301 (2012)] using a first-order stripe ansatz. We also determine the quantum depletion and superfluid density over a large range of Rabi frequency in different phases. The depletion exhibits an intriguing behaviour with a discontinuous jump at the ST-PW phase transition and a maximum at the PW-ZM phase transition. The superfluid density is derived through a phase-twist method. In the plane-wave and zero-momentum phases, it is remarkably suppressed along the SOC direction and vanishes at the transition, consistent with a recent work [Zhang *et al.*, Phys. Rev. A **94**, 033635 (2016)]. In the stripe phase, it decreases smoothly with increasing Rabi frequency. Our predictions would be useful for further theoretical and experimental studies of this intriguing supersolid stripe phase.

# Acknowledgement

All roads lead to Rome, but they make travellers diverse and beneficial. So does my fantastic journey in Melbourne, from impressive lives with many new friends to a richer harvest in science!

First of all, I am very grateful to my supervisors, A/Prof. Hui Hu and Prof. Xia-Ji Liu, and co-supervisor Prof. Peter Drummond, for their diligent scientific supervision, invaluable guidance and encouragements all the time. As a naive beginner, I was guided carefully by Hu and Liu who have taught me a lot to accomplish academic research with their rigorous attitude and breadth of knowledge in physics. I deeply appreciate every in-office discussions, group meetings and journal clubs they arranged for us, and all the financial support for conferences and workshops. It's a great privilege and an honour to learn aside them, and this will continuously profit and inspire me.

Tremendous thanks are present to all the past and current members in our group, Yun Li, Shi-Guo Peng, Peng Zou, Jia Wang, Brendan Mulkerin, Umberto Toniolo, Christiaan Hougaard, Sebastian Schiffer and many others, for their help and advice, and for the great times we spent together talking and discussing about physics and life. I am also indebted to Alberto Alberello, Bapin Kumar Rout, Filippo Nelli for the friendship in the office.

I want to thank all the members in the centre (CQOS), for the warm and friendly atmosphere they created for everyone. I will never forget the Christmas BBQ party when I first arrived, and the centre is like a big family from SOLL seminars to Footie &Pizza parties sharing joys together. I am indebted to Prof. Russell McLean for providing me with a spare bicycle although it was stolen, to Prof. Chris Vale for your kind explanations of all my questions related to cold-atom experiments, and

to Dr Brenton Hall for helping me join the tutorial group. My research is related to ultra-cold physics, but the memory of the centre is happy and of 'high temperature', which will be forever cherished.

It's very fortunate to have the opportunity to collaborate or meet with some great researchers. I'm greatly appreciated for the intriguing discussions and/or fruitful collaborations with Prof. Xi-Wen Guan, Prof. Kai-Jun Jiang, Prof. Shuai Chen, Dr Zeng-Qiang Yu, Prof. Ana Maria Rey, Prof. Thomas Gasenzer and many great others. Especially I want to thank Prof. Guan for his great hospitality during my visit to WIPM and many valuable pieces of advice in physics but also in future planning.

I would like to thank all the panel members of my PhD reviews, among them, are Dr Jesper Levinsen, A/Prof. Meera Parish, A/Prof. Andy Martin, Prof. Margaret Reid, Dr Tapio Simula, Prof. Andrei Sidorov, Dr Sascha Hoinka, and the others who have ever attend and help me.

Sincere thanks go to all the secretaries for their help in these years. Especially, I want to thank Tatiana Tchernova, for informing us important events and organizing various activities in the centre all the time and helping me with patience to deal with all the affairs such as scholarships and reimbursements. Special thanks to Jessica Hattersley for the enrollment at the beginning, to Olivia Doyle for organizing many fruitful activities and sorting 'Freetime newsletter' for postgraduates.

Very special thanks to the SUPRA scholarship granted by Swinburne University, supporting me to complete the PhD study with a comfortable living.

Last but not least, thank my parents for the priceless supports and encouragements. This thesis is dedicated to my wife, Dongbi Bai, for her precious love.

# Declaration

I, Xiao-Long Chen declare that this thesis entitled:

"*Ultracold Atoms with Synthetic Gauge Field*"

is my original work and contains no material which has been submitted previously, in whole or in part, in respect of any other academic award and to the best of my knowledge and belief contains no material previously published except where due reference is acknowledged in the text.

Xiao-Long Chen
Centre for Quantum and Optical Science
Faculty of Science, Engineering and Technology
Swinburne University of Technology
Melbourne, Australia
18 June 2018

# Contents

# List of Figures

# List of Tables

# Chapter 1

# Introduction

## 1.1 Historical overview

The heart of ultracold atomic physics lies in *low-temperature* regime, which was mainly developed in the context of liquid helium for many years. In 1908 H. K. Onnes first liquefied helium successfully reaching the Kelvin-scale temperature. After Onnes's seminal work, P. Kapitza [17], J. F. Allen and A. D. Misener [18] independently discovered in 1938 that below the $\lambda$-point ($T_\lambda = 2.17$ K at saturated vapour pressure) liquid $^4$He exhibits remarkable superfluid properties flowing without viscosity, which opened the door of understanding superfluidity and superconductivity in electron gas in a metal.

Meanwhile, in 1924, S. N. Bose tried to clarify the statistical behaviours of light quanta (photons) [19]. Soon in 1925, A. Einstein applied the statistical approach to an ideal non-interacting bosonic gas of $N$ indistinguishable particles of mass $m$, and surprisingly found that below a critical temperature particles start to condense macroscopically into the lowest-energy, single-particle state at the order of $\mathcal{O}(N)$ [20]. This exotic phenomenon is the well-known Bose-Einstein condensation (BEC), which is a consequence of purely statistical effects[21, 22].

This unique phenomenon doesn't attract too much attention until 1938 when F. London found the close relation between the $\lambda$-point and the critical BEC transition temperature $T_0 = 3.1$K of an ideal Bose gas at the same density, and suggested to understand the superfluidity in liquid helium in terms of Bose-Einstein condensa-

tion [23]. Thereafter intense theoretical studies were developed by researchers based on the concept of Bose-Einstein condensation. In 1938, an important two-fluid model was developed by Tisza [24] and was used by Landau in 1941 to successfully describe many properties of the superfluid $^4$He [25, 26]. Later in 1947 Bogoliubov first studied microscopically the weakly interacting Bose gas [27], followed by related predictions made by Landau and Lifshitz [28], Penrose [29], Penrose and Onsager [30]. On the experimental side, the investigations are focused on liquid helium to better understand its relationship to BEC. In 1956 Hall and Vinen experimentally verify the existence of quantized vortices in liquid helium [31], predicted by Onsager (1949) [32] and Feynman (1955) [33]. The great breakthrough comes after scientists overcome the temperature-limit in quantum gases by developing ingenious trapping and cooling techniques during the 1980s and 1990s [34–36]. Soon in 1995 physicists from JILA group, MIT group and Rice group successfully reached the ultracold Nano-Kelvin temperature regime in trapped Bose gases, and immediately realized the unique Bose-Einstein condensation using ultracold dilute alkali metal vapors, i.e., rubidium [37], sodium [38] and lithium [39], respectively (see Fig. 1.1). The successful achievements in the laboratory intrigue extensive studies both theoretically and experimentally, and the research of ultracold dilute atoms experiences a flourishing era in the following decades [10, 40, 41].

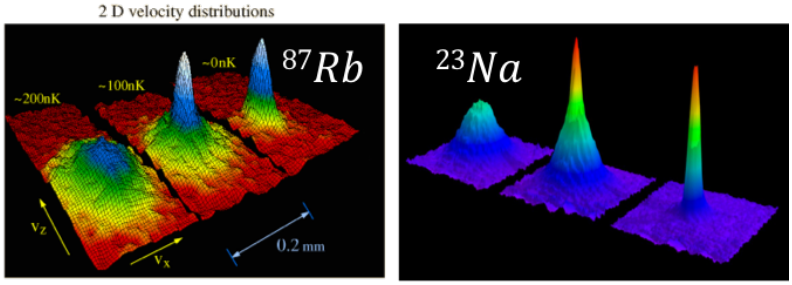


Figure 1.1: Figure of velocity-distribution of a gas of $^{87}$Rb (left) and $^{23}$Na (right) atoms in the experiment taken by means of the expansion method, 3 sets of temperature-data, leading to the first view of emergence of novel quantum phenomenon - Bose-Einstein condensation. Images from JILA and MIT webpages [1, 2].

### 1.1.1 Quantum statistics and ultracold atomic gases

#### Theoretical prediction

In nature, elementary particles can be classified into two categories, bosons and fermions, according to their quantum spin number. The first have integer spin and the latter have half-integer spin. They obey distinct quantum statistics in thermal equilibrium at low temperatures [10, 42].

In a system of identical ideal bosons, the corresponding wavefunction will be symmetric under the exchange of any pair of particles. The average number of particles in a single-particle state $i$ satisfies the Bose-Einstein statistics given by

$$f_{\mathrm{B}}(\epsilon_i) = \frac{1}{e^{(\epsilon_i - \mu_{\mathrm{B}})/k_{\mathrm{B}}T} - 1}, \tag{1.1}$$

with the energy $\epsilon_i$ of the single-particle state, the chemical potential $\mu_{\mathrm{B}} \leq 0$ and the equilibrium temperature $T$. Here $k_{\mathrm{B}}$ is the Boltzmann constant and we do not consider the degeneracy of energy levels. In the sufficiently low-temperature regime, there will be a large fraction of particles occupying the same lowest-energy quantum state. The fraction increases as the temperature continues to decrease (see the left in Fig. 1.2), until all particles populate the lowest level at zero temperature (see the left in Fig. 1.3).

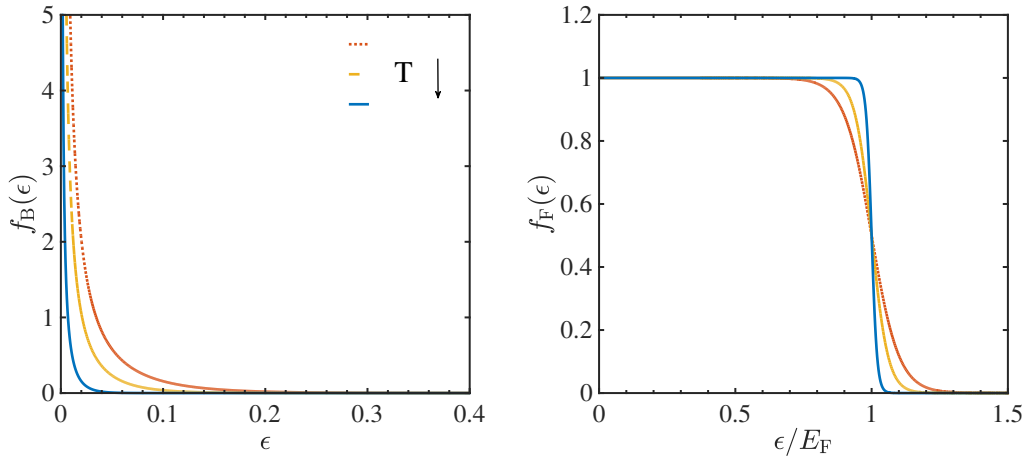


Figure 1.2: Quantum statistics in the energy level of (left) cold bosons; (right) cold fermions, when the temperature continues to decrease.

Fermions instead have the antisymmetric wavefunction under the interchange of a pair, and satisfy the so-called Fermi-Dirac statistics in thermodynamic equilibrium as

$$f_{\mathrm{F}}(\epsilon_i) = \frac{1}{e^{(\epsilon_i-\mu_{\mathrm{F}})/k_{\mathrm{B}}T}+1}, \tag{1.2}$$

where the chemical potential is $\mu_{\mathrm{F}} \leq E_{\mathrm{F}}$ with the Fermi energy $E_{\mathrm{F}} = (3\pi^2 n)^{2/3}/(2m)$ and the average density $n$. Due to the Pauli exclusion principle, two identical fermions can not occupy the same quantum state but instead need to be arranged in different low-energy quantum states until all fermions filling the Fermi level, see the right plots in Figs. 1.2 and 1.3.

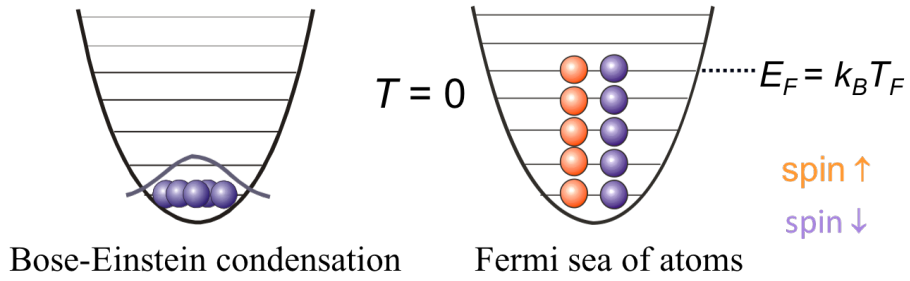


Figure 1.3: The populations at zero temperature in the energy level of (left) cold bosons: a Bose-Einstein condensate; (right) cold fermions: a Fermi sea.

It's obvious to find that, at sufficiently high temperature, the factor of quantum effect "$\pm 1$" is negligible and the statistics of bosons and fermions become the same classic Maxwell-Boltzmann statistics

$$f_{\mathrm{MB}}(\epsilon_i) = \frac{1}{e^{(\epsilon_i-\mu)/k_{\mathrm{B}}T}}. \tag{1.3}$$

Unless specifically stated, we will consider only the homogeneous Bose gases in three dimensions throughout the most of the thesis. For a free particle in three dimensional system with a volume $V$, there is one quantum state per volume $(2\pi\hbar)^3$ of phase space. The momentum space has the volume $4\pi p^3/3$ of a momentum less than $p$ with the corresponding energy of a particle $\epsilon_{\mathbf{p}} = p^2/(2m)$. Thus the total number of states $G(\epsilon)$ with energy less than $\epsilon$ is

$$G(\epsilon) = \frac{V}{(2\pi\hbar)^3}\frac{4\pi(2m\epsilon)^{3/2}}{3} = \frac{\sqrt{2}V}{3\pi^2}\frac{(m\epsilon)^{3/2}}{\hbar^3}, \tag{1.4}$$

and the density of states is given by

$$g(\epsilon) = \frac{dG(\epsilon)}{d\epsilon} = \frac{Vm^{3/2}}{\sqrt{2}\pi^2\hbar^3}\epsilon^{1/2}. \tag{1.5}$$

It's worth noting that, the density of states is $g(\epsilon) \propto \epsilon^{(d/2-1)}$ in $d$ dimensions, which becomes a constant in two dimensions ($d = 2$). The density of states plays an significant role when determining the existence of the condensate in low dimensions. This can be determined by calculating the excited particle number instead [42].

Integrating over the energy space, one can calculate the number of the excited particles given by

$$N_{\rm ex} = \int_0^\infty d\epsilon g(\epsilon) f_{\rm B}(\epsilon). \tag{1.6}$$

The BEC transition temperature $T_0$ can be determined by the condition that all the particles are populating the excited states as

$$N = N_{\rm ex}(T_0, \mu = 0) = \int_0^\infty d\epsilon g(\epsilon) \frac{1}{e^{\epsilon/k_{\rm B}T_0} - 1}, \tag{1.7}$$

with the chemical potential reaching zero $\mu = 0$. This equality can be rewritten in terms of a dimensionless variable $x \equiv \epsilon/(k_{\rm B}T_0)$ by

$$N = \frac{Vm^{3/2}}{\sqrt{2}\pi^2\hbar^3}(k_{\rm B}T_0)^{3/2}\int_0^\infty dx \frac{x^{1/2}}{e^x - 1} = \frac{Vm^{3/2}}{\sqrt{2}\pi^2\hbar^3}\Gamma(\frac{3}{2})\zeta(\frac{3}{2})(k_{\rm B}T_0)^{3/2}. \tag{1.8}$$

Here we evaluate the integral in Eq. (1.8) using the relation

$$\int_0^\infty dx \frac{x^{\alpha-1}}{e^x - 1} = \Gamma(\alpha)\zeta(\alpha), \tag{1.9}$$

with the gamma function $\Gamma(\alpha)$ and the Riemann zeta function $\zeta(\alpha) = \sum_{l=1}^\infty l^{-\alpha}$. Then the critical temperature of the BEC transition is written by

$$\begin{aligned} k_{\rm B}T_0 =& \left[\frac{\sqrt{2}\pi^2\hbar^3}{Vm^{3/2}}\frac{N}{\Gamma(3/2)\zeta(3/2)}\right]^{2/3} \\ =& \frac{2\pi}{[\zeta(3/2)]^{2/3}}\frac{\hbar^2 n^{2/3}}{m} \\ \approx& 3.31\frac{\hbar^2 n^{2/3}}{m}, \end{aligned} \tag{1.10}$$

where we have used the fact $\Gamma(3/2) \approx 0.886$ and $\zeta(3/2) \approx 2.612$ with the average density $n = N/V$ in the thermodynamic limit. In terms of the critical temperature $T_0$, we can calculate the number of excited particles at a temperature $T < T_0$ by

$$\begin{aligned} N_{\mathrm{ex}}(T, \mu = 0) =& \int_0^\infty d\epsilon g(\epsilon) \frac{1}{e^{\epsilon/k_{\mathrm{B}}T} - 1} \\ =& \frac{V m^{3/2}}{\sqrt{2}\pi^2\hbar^3} \Gamma(3/2)\zeta(3/2)(k_{\mathrm{B}}T)^{3/2} \\ =& N\left(\frac{T}{T_0}\right)^{3/2}. \end{aligned} \tag{1.11}$$

Therefore, the particle number of the condensate in a uniform Bose gas is given by the well-known form,

$$\begin{aligned} N_0(T) =& N - N_{\mathrm{ex}}(T) \\ =& N\left[1 - \left(\frac{T}{T_0}\right)^{3/2}\right]. \quad (T < T_0) \end{aligned} \tag{1.12}$$

In order to characterize the BEC transition, it's convenient to introduce the *phase-space density*, defined as

$$\mathcal{D}(T) \equiv n\lambda_{\mathrm{T}}^3, \tag{1.13}$$

with the thermal de Broglie wavelength $\lambda_{\mathrm{T}} = (2\pi\hbar^2/mk_{\mathrm{B}}T)^{3/2}$. At the transition temperature $T_0$, one may easily calculate the phase-space density using Eq. (1.10) as

$$\begin{aligned} \mathcal{D}_{\mathrm{BEC}}(T_0) =& n\left[\frac{2\pi\hbar^2}{mk_{\mathrm{B}}T_0}\right]^{3/2} \\ =& \zeta(3/2) \\ \approx& 2.612. \end{aligned} \tag{1.14}$$

In the classical temperature regime, the de Broglie wavelength $\lambda_{\mathrm{T}}$ is much smaller than the average distance between particles $d \equiv n^{-1/3}$, which means that the phase-space density is tiny and the behaviour of the system exhibits a classical behaviour. As the temperature decreases into the quantum regime, the de Broglie wavelength continues to increase and starts to be comparable with the average distance between particles. Meanwhile the phase-space density becomes at the order of unity and the

system consists of overlapped matter-waves characterized by typical quantum effects. This is significantly different from the classical one, see also in Fig. 1.4.

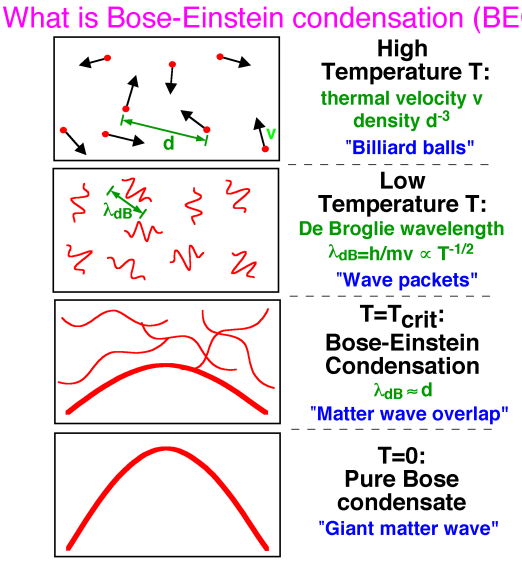


Figure 1.4: The de Broglie wavelength as temperature decreases. Image from MIT webpage [2].

### Experimental realization

In the last section, we know from the phase-space density that the occurrence of a Bose-Einstein condensation needs low temperatures and/or high particle densities. The typical particle density at the trap centre of a harmonically trapped atomic BEC cloud is about $10^{14}$ cm$^{-3}$ (see Tab. 1.1), and it needs an extremely low temperature of order $10^{-6}$K (i.e., $\mu$K) or less [see Eq. (1.14)] to achieve the condensation, which was one of the biggest challenges in the laboratory.

| | BEC | air (room $T$) | liquids &solids | nucleons in atomic nuclei |
|---|---|---|---|---|
| $n$ (cm$^{-3}$) | $10^{13}$-$10^{15}$ | $10^{19}$ | $10^{22}$ | $10^{38}$ |

Table 1.1: Typical density $n$ in various materials.

In order to reach the ultracold temperature scale and realize the Bose-Einstein condensation, one needs to employ step by step several advanced techniques, which

have been developed by experimental physicists in various fields of physics, such as magnetic trapping, laser cooling and trapping, evaporative cooling, etc. In the following, we will simply illustrate the important processes and their corresponding achieved temperature-scale, velocity and density (see Ref. [16] for a review). Initially the alkali metal atoms in the source chamber, i.e., Li, Na, K, Rb, Cs, are heated by oven to a temperature about 500K, and then the gaseous vapors escape into the ultrahigh vacuum chambers where they will be trapped by magnetic or optical fields. This process isolates the atoms from the classical material walls, and Ketterle *et al.* stated that such traps can store atoms for seconds or even minutes, which is long enough for cooling process [16]. The atomic beams can be then decelerated and cooled to a temperature about 1K by Zeeman slower using an inhomogeneous magnetic field. After that, the atoms is slow enough to be loaded into the so-called magneto-optical trap (MOT) where the atoms are confined and cooled using laser-cooling technique to reach $\mu$K temperature-scale. The next and very important procedure is evaporative cooling, which continuously removes the high-energy atoms from the trap and continuously decreases the temperature of the remaining atoms to nK-scale. The typical temperature, velocity, density and phase-space density after each cooling stage are approximately summarized in Tab. 1.2, respectively. With all the techniques and procedures described above, one can successfully achieve the temperature regime needed and immediately realize the Bose-Einstein condensation (see Fig. 1.1) in various alkali atoms, i.e., $^{87}$Rb [43], $^{23}$Na [38] and $^{7}$Li [44], and later in atomic hydrogen [45].

Instinctively, theoretical and experimental physicists started to think about similar quantum degeneracy in fermionic atoms as Bose-Einstein condensation in dilute Bose gases. Unlike bosonic atoms, fermionic atoms can not totally populate the same lowest state but form a Fermi sea in the energy level, see Fig. 1.3. Because of the Pauli exclusion principle, it has been a challenge to cool the temperature of fermions down in the laboratory. A few years after the observation of BEC, quantum degenerate Fermi gases were first achieved in a trapped atomic $^{40}$K gas by D. S. Jin's group in 1999 [46], and then the first strongly interacting Fermi gas was observed in 2002 by J. E. Thomas's group [47]. Later in 2004, D. S. Jin and cooperators continued to realize the Fermi condensate of fermionic pairs for the first time [48]. In the meantime, quantum fermionic degeneracy was also observed later by other

| | $T$ | $v$ (objects' average speed) | $n$ | $\mathcal{D}$ |
|---|---|---|---|---|
| Oven | 500 K | 300m/s (bullet) | $10^{14}$cm$^{-3}$ | $10^{-13}$ |
| Zeeman slower | 1 K | 50m/s (train) | $10^{14}$cm$^{-3}$ | $10^{-8}$ |
| Laser cooling | 50 $\mu$K | 1cm/s (ant) | $10^{11}$cm$^{-3}$ | $10^{-6}$ |
| Evaporative cooling | 500 nK | 1mm/s (snail) | $10^{14}$cm$^{-3}$ | 1 |
| BEC | $\sim$nK | | | $10^{7}$ |

Table 1.2: Typical cooling stages to BEC in the laboratory. Here $T$, $v$, $n$ are the average temperature, velocity and density of cold atoms, respectively. $\mathcal{D}$ is the phase-space density. The atomic velocity corresponds to the average speed of the objects in the parenthesis. Part of the data is from Ref. [16].

groups with $^{40}$K [49] and with $^{6}$Li [50–53], as well as the condensation of molecules of paired fermions [54–56]. In recent decades, the great achievements in the laboratory have intrigued comprehensive theoretical studies and provided an ideal platform to test and verify the predictions on ultracold Bose and Fermi gases.

### Advantages with ultracold atomic gases

At ultracold temperatures ($T < 1$mK), weakly interacting atomic gases can be well described by the so-called mean-field theories, which have been developed in 1950s and 1960s by Bogoliubov, Gross, Pitaevskii and others [10, 21, 22]. The gaseous condensates are usually described as *dilute* since they have an extremely low density even less than the one of air at room temperature, see Tab. 1.1. Thus when one moves to many-body picture, the range of interparticle interactions $r_0$ is much smaller than the average distance between particles $d = n^{-1/3}$. This implies that one can consider only two-body interactions and safely neglect three (or more)-particles interactions in these dilute systems. Besides, in ultralow-temperature regime, the relative kinetic energy and corresponding momenta of the atoms are strongly suppressed. At such small momenta, the scattering amplitude characterizing the two-body interaction is independent of energy or the scattering angle. And it depends only on a constant in the low-energy limit, which is called the $s$-wave scattering length "$a$" [21].

Therefore in ultracold dilute weakly interacting Bose gases, the effects of interaction can be characterized with a single parameter–scattering length $a$, satisfying

the diluteness condition $|a| \ll n^{-1/3}$ [21, 57]. One can introduce a relevant $s$-wave interaction strength

$$g = \frac{4\pi\hbar^2 a}{m}, \tag{1.15}$$

which plays a crucial role in the familiar Gross-Pitaevskii (GP) equation, or the nonlinear Schrödinger equation

$$i\hbar\frac{\partial}{\partial t}\hat{\Psi}(\mathbf{r},t) = \left(-\frac{\hbar^2\nabla^2}{2m} + V_{\text{ext}}(\mathbf{r},t) + g|\hat{\Psi}(\mathbf{r},t)|^2\right)\hat{\Psi}(\mathbf{r},t). \tag{1.16}$$

Here $\hat{\Psi}(\mathbf{r},t)$ is the time-dependent Bose field operator in real space with atomic mass $m$, satisfying the Bose commutation relations $[\hat{\Psi}(\mathbf{r}), \hat{\Psi}^\dagger(\mathbf{r}')] = \delta(\mathbf{r}-\mathbf{r}')$ and $[\hat{\Psi}(\mathbf{r}), \hat{\Psi}(\mathbf{r}')] = 0$. The relevant external trapping potentials are mostly harmonic traps $V_{\text{ext}}(\mathbf{r},t) = \sum_{i=x,y,z} m\omega_i^2 r_i^2/2$ with trapping frequency $\omega_i$ in realistic experiments. The GP theory in Eq. (1.16) is one of the most important approaches for physicists to study static and dynamic properties in dilute uniform or trapped Bose gases at low temperatures.

Over the last few years, many more techniques have been developed in the laboratory, such as Feshbach resonance [4, 58], optical lattices [41, 59, 60], absorption imaging [61, 62]. They bring obviously the systems of ultracold atoms remarkable advantages with high degrees of control and versatility, for instance, flexible tunability of interaction strength, easy access to the strongly correlated systems,

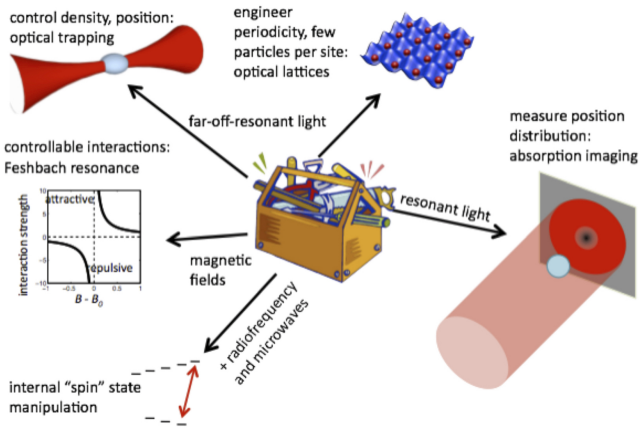


Figure 1.5: Tools and techniques applied in an ultracold atoms systems, such as optical lattices, Feshbach resonance, absorption imaging. Reproduced from Ref. [3].

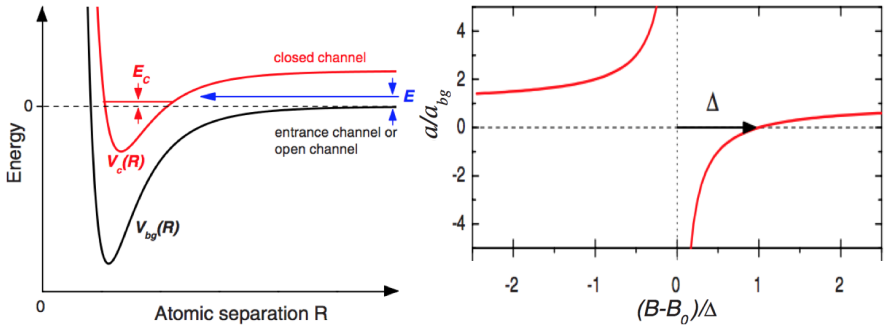


Figure 1.6: (left) Two-channel formalism for a magnetic Feshbach resonance. In ultracold gases, the colliding energy $E$ of two atoms approach near zero ($E \to 0$), and one can tune the bound state energy $E_c$ to around 0 via an external magnetic field $B$, to achieve the resonant coupling between the scattering state and molecular bound state if the magnetic moments of two channels are different. (right) $s$-wave scattering length $a(B)$ in unit of background scattering length $a_{bg}$ near a magnetically tuned Feshbach resonance. Particularly $a(B)$ can be very large, positive or negative near the magnetic field $B_0$ of resonance. Reproduced from Ref. [4].

ideal platform for quantum simulations of many model systems in condensed matter physics or in nuclear physics etc., see Fig. 1.5. All these developments lead to intense studies of intriguing topics in various fields to better understand many-body physics in nature.

Feshbach resonance has become a widely-used tool recently in the experiments and can be understood from a two-channel model as shown in Fig. 1.6, where $V_{bg}(R)$ is the background potential of two free atoms in the open channel and the potential $V_c(R)$ in the closed channel supports molecular bound states. The resonance occurs when the scattering state of two atoms with colliding energy $E$ in the open channel resonantly couples to a molecular bound state with energy $E_c$ in the closed channel, where the energy shift $\Delta E$ can be controlled via an external magnetic field $B$. By means of Feshbach resonance technique via varying the external magnetic field, experimentalists can successfully control the interatomic interactions. Hence the two-body $s$-wave scattering length can be tuned as a function of magnetic field

$$a_s(B) = a_{bg}\left(1 - \frac{\Delta}{B - B_0}\right). \tag{1.17}$$

Here $a_{bg}$ is the off-resonant background scattering length associated with $V_{bg}(R)$, while $\Delta$ is the resonance width and $B_0$ describes magnetic field position of the resonance where the scattering length diverges $[a_s(B_0) \to \pm\infty]$, see Fig. 1.6.

The great tunability of scattering length can help to achieve a wide range of interaction strength in dilute Bose gases, from ideal non-interacting, weak coupling regime to strongly interacting regime. It is powerful that one can achieve strong cor-

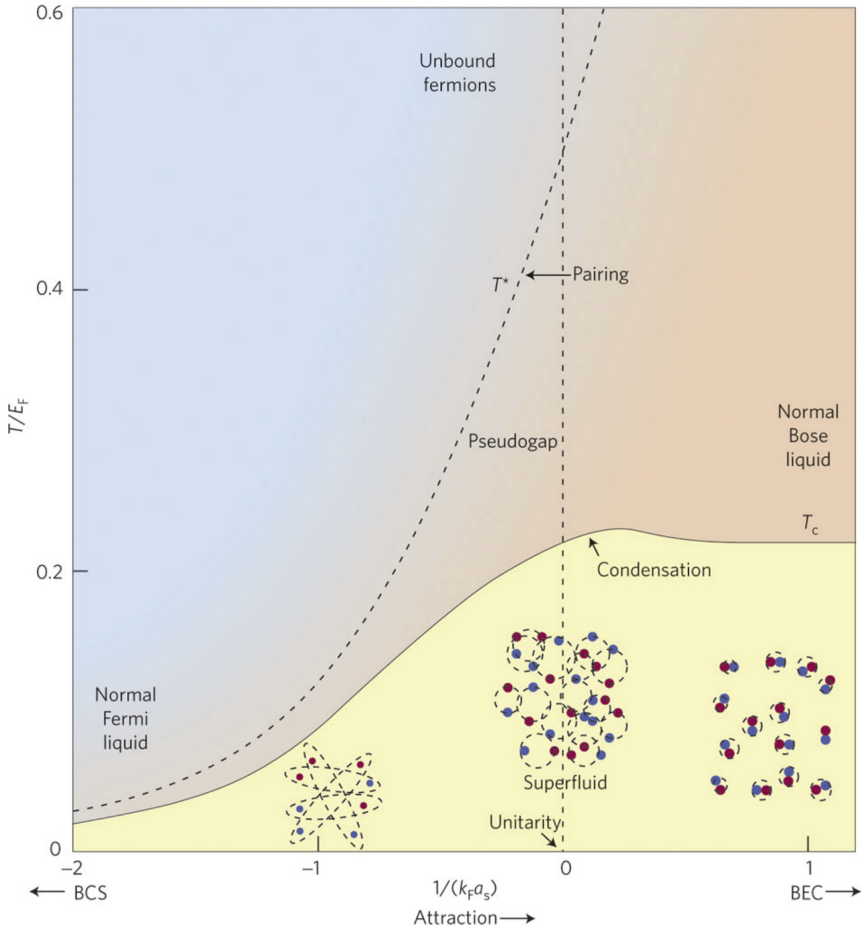


Figure 1.7: Pairs dissociation temperature $T^*$ and superfluidity critical temperature $T_c$ as a function of dimensionless parameter $1/(k_F a_s)$. The range of $1/(k_F a_s)$ successively describes from overlapped Cooper pairs in the BCS limit to tightly bound molecules in BEC limit. The unitary regime lies in the range $(-1, 1)$, where fermionic pairs correlate strongly. Reproduced from Ref. [5]

relations in experiments of dilute atomic gases. Particularly, one-dimensional (1D) ultracold Bose gases with strong repulsive interactions attract great interest theoretically and experimentally. In a 1D geometry, bosonic atoms can not pass each other or exchange places, and they are expected to exhibit a "fermionic" behaviour. Thus one-dimensional bosons and fermions share the identical energy spectra as well as probability distributions in real configurations, except that their momentum distributions are quite different. These one-dimensional bosons with strong repulsive interactions are often called impenetrable bosons or Tonks-Girardeau bosons [63], collective properties of which have been studied in this thesis and our recent works [64, 65].

Another interesting and fascinating subject under intense experimental studies via Feshbach resonance in the recent years is the so-called BCS-BEC crossover [66], which describes a smooth crossover from the BCS ground state of loosely bound Cooper pairs in the weak interaction limit to the BEC ground state of tightly bound molecules in the strong interaction limit, see Fig. 1.7. One of the exciting advantages of the crossover is the unitary regime, where the scattering length can be positive or negative infinitely large ($a_s \to \pm\infty$). The study of the unitary regime in ultracold atomic experiments can easily get access to the strongly correlated Fermi systems, while they are rather difficult to achieve in condensed matter and high-energy physics. Especially after experimental realization of unitary regime in ultracold Fermi gases [67], there are more and more motivations on theoretically and experimentally studying several novel quantum phenomena in the BCS-BEC crossover. For instance, the study of high transition temperature in the unitary regime may give valuable insights to the long-sought high-$T_c$ superconductivity [68]. Universal behaviours has attracted significant attention in the unitary limit [69], Feshbach resonance induced molecules [70], Efimov effects due to three-body physics [71–73], or the pseudogap state and critical pair-formation temperature [74, 75].

### 1.1.2 Synthetic gauge fields and spin-orbit coupling with ultracold atoms

Nowadays one of the greatest developments in dilute ultracold gases is the experimental realization of synthetic (artificial) gauge fields with neutral atoms [76, 77].

In gauge theories, gauge fields or gauge potentials play an important role in the understanding of fundamental interactions between elementary particles in nature. One of the typical examples is classical electromagnetism, where the electromagnetic (EM) fields are described by vector and scalar potentials, $\mathbf{A}$ and $\phi$. In detail, from Maxwells equations, the electric fields are induced by spatial gradient of the scalar potentials and/or the gradient of the vector potentials with respect to time, while the magnetic fields are generated by the curl of the vector potentials in space,

$$\begin{aligned} \mathbf{E} &= -\nabla\phi - \frac{\partial \mathbf{A}}{\partial t}, \\ \mathbf{B} &= -\nabla \times \mathbf{A}. \end{aligned} \tag{1.18}$$

In the relevant electromagnetic fields, the dynamic behaviour of a particle with electric charge $q$ and mass $m$ can be characterized by the Hamiltonian

$$\mathcal{H} = \frac{(\hat{\mathbf{p}} - q\mathbf{A})^2}{2m} + q\phi, \tag{1.19}$$

with the canonical momentum operator $\hat{\mathbf{p}} = -i\hbar\nabla$. By coupling with the vector potential $\mathbf{A}$, the physical momentum of the charged particle changes to $(\hat{\mathbf{p}} - q\mathbf{A})$ with a significantly modified dispersion relation $(\hat{\mathbf{p}} - q\mathbf{A})^2/(2m)$. This Hamiltonian can well describe the motion of a charged particle in a classical electromagnetic field and help us understand many underlying phenomena.

### Synthetic gauge fields

Owing to excellent control of degrees of freedom in experiments, ultracold atomic gases have become one of the ideal platforms for physicists to design a similar Hamiltonian with these gauge fields, and to explore relevant dynamics in the presence of gauge potentials. However, the utilized atoms are neutral and can not experience a Lorentz force as charged particles do in EM fields. This difficulty prevents the investigations in versatile cold atomic systems on many exotic phenomena, such as quantum Hall effect, topological insulator and superfluid [76]. One typical way to overcome the problem of neutrality is by rotating the Bose condensates [78–80], which can induce an effective Lorentz force, or Coriolis force, to further simulate the dynamics in gauge fields. However, the fragile stability of the Bose condensates

restricts rapid rotations in quantum gases. Another choice is by employing suitable laser fields via light-atom interaction [76, 77], which has been most widely used both theoretically and experimentally, and will be emphasized throughout this thesis.

In 2003 and 2004, P. Zoller *et al.* and G. Juzeliūnas *et al.* independently suggested to manipulate atomic internal states via two laser beams to create effective magnetism in optical lattices [81] and in degenerate Fermi gases [82], respectively. Following these influential proposals, two individual groups, X.-J. Liu *et al.* [83] and S. Zhu *et al.* [84], theoretically introduced the experimental scheme in 2006 to investigate the spin Hall effects in ultracold atomic systems. Meanwhile in 2005, experimental schemes to realize effective non-Abelian gauge fields were also proposed in optical lattices [85] and in continuous ultracold Bose or Fermi gases [86].

Nevertheless, the schemes proposed at the early stage were of many difficulties, and were too tough to achieve in the laboratory. In 2008, a more feasible scheme was developed by X.-J. Liu *et al.* [87]. They argued that, the effect of spin-orbit coupling can be observed in a simple Lambda-configuration, by coupling the internal electronic states (pseudospins) of atoms via two Raman laser beams. This accessible scheme was widely employed later and led to several breakthroughs in the laboratory [88]. Soon by means of laser beams in ultracold atomic gases, I. Spielman's group from NIST first realized synthetic Abelian gauge fields, i.e., magnetic fields in 2009 [6, 89] and electric fields in 2011 [90]. These achievements provided a new opportunity to reproduce and study classical electromagnetism between charged particles and electromagnetic fields in ultracold neutral atomic gases. For instance, one can mimic and investigate the dynamics of charged electrons in crystals (i.e., metals and semiconductors) as in condensed matter physics.

### Non-Abelian gauge field: Spin-orbit coupling

Soon after artificially realizing the Abelian gauge fields, the NIST group extended the developed scheme to generate versatile non-Abelian gauge potentials. In 2011, they successfully simulated the effect of spin-orbit coupling (SOC) using Raman lasers in ultracold alkali gases [7]. In detail, by coupling the internal degrees of freedom of neutral atomic $^{87}$Rb (spins) to the center-of-mass degrees of freedom (orbital motions) with two counterpropagating Raman laser beams via two-photon

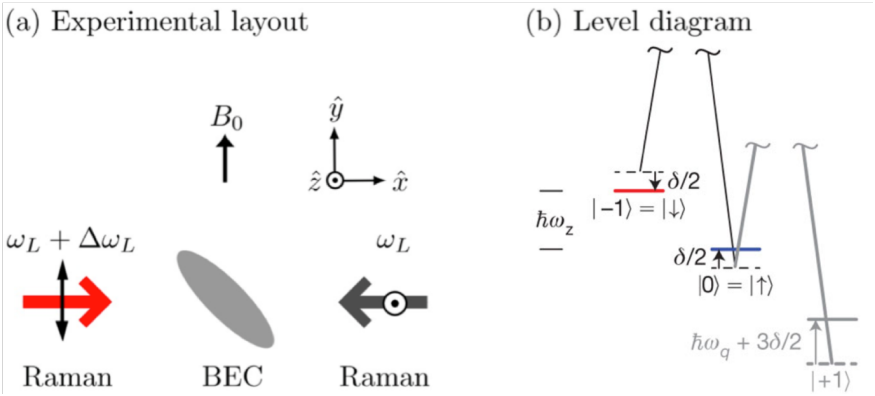


Figure 1.8: (a) The NIST experimental setup in Ref. [6] with $^{87}$Rb BEC in a dipole trap created by two laser beams in a bias field $B_0\hat{e}_y$. A pair of Raman laser beams are counterpropagating along $\hat{e}_x$ with frequencies $\omega_L$ and $(\omega_L + \Delta\omega_L)$, linearly polarized along $\hat{e}_z$ and $\hat{e}_y$, respectively. (b) Scheme of $^{87}$Rb BEC hyperfine states in $F = 1$ ground state in Ref. [7]. $\omega_Z$, $\omega_q$ and $\delta = (\Delta\omega_L - \omega_Z)$ are the linear, quadratic Zeeman shifts, and the detuning from Raman resonance, respectively.

process as shown in Fig. 1.8, I. Spielman and co-workers first realized the so-called Raman-induced spin-orbit coupling.

Here we revisit the NIST scheme using the $F = 1$ ground state manifold of $^{87}$Rb Bose-Einstein condensates and make a simple illustration of the synthetic SOC. In Fig. 1.8, adjusted Bias field $B_0$ gives rise to a large quadratic Zeeman shift $\omega_q$ much larger than the recoil energy $E_\mathrm{r} = \hbar^2 k_\mathrm{r}^2/(2m)$ of the lasers. Hence the third hyperfine state $|F = 1, m_F = 1\rangle$ is split far away from the other two states in the energy level, i.e, $|1, 0\rangle$ and $|1, -1\rangle$, and can be effectively decoupled. Thus the corresponding system can be described by an effective two-level Hamiltonian

$$\mathcal{H}^{\mathrm{SOC}} = \frac{\hbar^2(k_x - k_\mathrm{r}\sigma_z)^2}{2m} + \hbar\frac{\delta}{2}\sigma_z + \hbar\frac{\Omega}{2}\sigma_x. \tag{1.20}$$

on the basis of the other two hyperfine states $|\uparrow\rangle = |1, 0\rangle$ and $|\downarrow\rangle = |1, -1\rangle$. Here $\delta$ is the detuning from Raman resonance, $\Omega$ is the strength of Raman coupling. $\sigma_x$ and $\sigma_z$ are $2 \times 2$ Pauli matrices. In contrast to classical electromagnetic Hamiltonian in Eq. (1.19), the vector potential $k_\mathrm{r}\sigma_z$ here is of a matrix form. It's easy to find that after a spin rotation ($\sigma_z \to -\sigma_y$ and $\sigma_y \to \sigma_z$), the SOC term is of a one-dimensional (1D) form $\propto k_x\sigma_y$ which is the equal mixture of Rashba SOC form $(k_x\sigma_y - k_y\sigma_x)$

and Dresselhaus SOC form ($k_x\sigma_y + k_y\sigma_x$) in condensed matter physics. The seminal breakthroughs of realizing non-Abelian gauge fields in the laboratory, i.e., spin-orbit coupling, lead to fruitful theoretical research on SOC in quantum gases both theoretically [91–103] and experimentally [14, 104–106]. The effects of SOC give rise to exotic phase diagrams and many fascinating phenomena [91–95, 102], which will be discussed in detail in Chap. 2.

Meanwhile in 2012 by utilizing the same scheme, two independent groups from Shanxi university and MIT achieved the experimental realization of spin-orbit coupling in quantum degenerate Fermi gases ($^{40}$K and $^{6}$Li, respectively) [107, 108]. Furthermore, the group in Shanxi continued to create Feshbach molecules in spin-orbit coupled Fermi gases using Feshbach resonance technique [109]. To date, several groups have already realized this one-dimensional Raman-type SOC in atomic Bose [104, 106, 110, 111] and Fermi [112–114] gases.

On the theoretical side, several proposals are generated and developed to achieve high-dimensional spin-orbit couplings in atomic gases, such as the tripod scheme [115], ring-coupling scheme [116, 117], magnetic-field-gradient pulses scheme [118] and optical Raman lattices scheme [119, 120], etc. Very recently in 2016, two-dimensional (2D) spin-orbit coupling are successively achieved in Fermi gases by co-workers from Shanxi University and CUHK [121], and in Bose gases by co-workers from USTC and Peking University [122]. The USTC group and collaborators continued to realize a long-lived 2D SOC Bose gas with intriguing topological features [123], by employing an improved scheme [120].

Nowadays, the investigations of synthetic gauge fields and spin-orbit effects strongly appeal to both theoretical and experimental researchers, due to a splendid novel quantum world behind it. In condensed matter physics, the spin-orbit couplings can obviously affect electron transport and may give rise to new kinds of exotic quantum matters [41, 124–127]. Ultracold atomic gases have been proven to be a versatile platform to study these intriguing phenomena in the presence of SOC [77, 128, 129], such as spin Hall effects [83, 84, 130], integer (fractional) quantum Hall effect [131–133], quantum anomalous Hall effect in magnetic topological insulators [134, 135], topological superfluidity and Majorana fermions [119, 136–141]. With the help of optical lattices, synthetic gauge fields correspond to staggered or uniform magnetic fluxes, which provides a good testbed for quantum simulation of

model Hamiltonians in condensed matter physics and can help reveal the nature of the exotic supersolid using cold atoms [106, 142–144].

## 1.2 Thesis outline

Here we give briefly the outline of this thesis. In the current **chapter** 1, we have begun with a historical review of ultracold atomic gases from the theoretical prediction to the successful experimental realization. They exhibit an extremely high controllability of degrees of freedom in the laboratory with the help of several developed techniques, such as optical lattices and Feshbach resonance. After a quick review of classical electromagnetism, we provide a short introduction of gauge fields synthesized in quantum gases by employing light-matter interaction. In particular, we have explicitly reviewed the backgrounds and developments of simulating spin-orbit coupling using neutral ultracold atoms with many fascinating phenomena.

The specific system we concentrate on throughout this thesis is a weakly interacting Bose gas in three dimensions with a one-dimensional Raman-induced spin-orbit coupling (SOC) [7]. In **chapter** 2, we will revisit in detail the NIST scheme realizing this Raman-type SOC and derive the corresponding effective Hamiltonian. The single-particle dispersion is studied in the parameter spaces of the Rabi frequency and the laser detuning. By including many-body interactions, we characterize three generic phases over the range of the Rabi frequency, i.e., the stripe, plane-wave and zero-momentum phases, within a variational approach. We continue to study the phase diagram and the relevant properties of three phases, such as density profile, condensation momentum and spin polarization. The contents in Chaps. 1 and 2 are written to have a general review based on previous works.

In **chapter** 3, we introduce the theoretical method employed, Hartree-Fock-Bogoliubov theory within Popov approximation, which can well describe a weakly interacting Bose gas at zero and/or nonzero temperature. We first apply the method to investigate trivially single-component and two-component Bose gases, followed by an application of a generalized formalism to the system in the presence of the Raman-type SOC. We make an application of the approach to study carefully a one-dimensional weakly interacting Bose gas concentrating on the effect of finite particle number and finite temperature. We then map the system to a spin-polarized interacting Fermi gas using Bose-Fermi duality to explore the role of effective range. The last two applications are mainly from our recent publications in Refs. [64] and [65].

In the next **chapters** 4 &5, we thoroughly investigate this weakly interact-

ing Bose gas with the Raman-type SOC, by using the generalized Hartree-Fock-Bogoliubov method with Popov approximation described in the last chapter.

In **chapter** 4, emphasizing the quantum and thermal fluctuations at finite temperature, we determine a complete finite-temperature phase diagram of three exotic condensation phases. By minimizing the free energy of the system with a plane-wave ansatz for condensate wavefunction, we obtain the momentum in the partially condensed phase at finite temperature and compare it with the analytic one at zero temperature. The Bogoliubov excitation spectrum in the plane-wave and the zero-momentum phases are under intensive and careful studies, which straightforwardly help us determine the phase boundaries. Accordingly we explore thoughtfully phonon mode and calculate sound velocity, which shows an excellent agreement with the recent experiment [14]. The Landau critical velocity is further calculated and differs largely from the sound velocity in the plane-wave phase due to an intriguing roton-maxon structure in the elementary excitation spectrum. Besides, we also discuss the behaviour of other physical observables, such as the magnetization of the gas. This chapter is mostly from our recent publication in Ref. [103].

In **chapter** 5, we focus on the exotic stripe phase at zero temperature. By considering high-order harmonics in the trivial ansatz for ground-state wavefunction, we explore successively the density profile, the momentum of the condensate, the Bogoliubov excitation spectrum and the relevant sound velocity in the stripe phase. In particular, we show that the critical Rabi frequency between the stripe and plane-wave phases is revised after taking high-order harmonics into account at certain interaction strengths. The quantum depletion of total density is numerically calculated as a function of the Rabi frequency across all three phases. In the limit of zero Rabi frequency, it reproduces the analytic result of uniform Bose gases without SOC. We then derive an analytic expression of superfluid density for all three phases via a phase-twist method using a first-order ansatz. Meanwhile we compare the analytic prediction in the stripe phase with a more accurate numerical result using a high-order ansatz, and their difference is closely related to the interaction strengths. The results in this chapter are mainly from our recent publication in Ref. [145].

Finally, conclusions and outlooks are present in **chapter** 6. The appendix and bibliography are given at the end of the thesis, along with a list of publications co-authored during the PhD period.

# Chapter 2

# Three-dimensional Bose gases with Raman-type spin-orbit coupling

In this Chapter, we will review in detail the spin-orbit coupling in ultracold Bose gases first realized by I. Spielman's group from NIST in 2011, i.e., Raman-type spin-orbit coupling [7]. The NIST scheme will be illustrated thoroughly, and an effective Hamiltonian is derived. We will describe the single-particle behaviour in the presence of SOC, and introduce the generic phases when taking into account intra- and inter-species atomic interactions later. Various physical observables across distinct phases will be further studied.

## 2.1 Backgrounds and motivations

In Sec. 1.1.2, we have shown that spin-orbit interactions are ubiquitous in nature giving rise to many exotic phenomena. The successful realization of spin-orbit effect using ultracold atoms in 2011 has stimulated fruitful research. Considering the Raman-type spin-orbit coupling, several theoretical studies have been done on the low-energy properties [91–102, 146], including for instance fascinating ground states and phase diagram, BEC transition temperature, depletion of the Bose condensate, and collective modes and response functions. On the other hand, extensive experimental investigations have been carried out on spin-orbit coupled systems, including collective excitations [104], finite-temperature phase diagram [105], Bogoliubov exci-

tation spectrum [14] and the exotic bosonic supersolidity [106]. Therefore, aiming to study synthetic gauge fields in ultracold atoms and to reveal the underlying physics of novel states of matter and exotic phase diagrams, we focus on a weakly interacting Bose gas with the Raman-type spin-orbit coupling and study the relevant static and/or dynamic properties in the following chapters.

In the experiments of NIST [6, 7, 89, 90], a $^{87}$Rb Bose-Einstein condensates is prepared in $|F=1\rangle$ ground state manifold in an optical dipole trap. An extra uniform magnetic biased field $\mathbf{B}_0$ along the $y$-direction, i.e., $B_0\hat{\mathbf{e}}_y$, leads to three-sublevel hyperfine structure $|m_F=0,\pm1\rangle$ (pseudospins) with the linear and quadratic Zeeman shifts $\omega_Z$ and $\epsilon$ respectively. The Bose condensates are optically dressed by a pair of intersecting Raman laser beams in the $\hat{\mathbf{e}}_x$-$\hat{\mathbf{e}}_y$ plane at an angle $\theta$, and hence the internal states $|m_F\rangle$ are coupled with a strength $\Omega$ controlled by the intensity of the lasers. Thus the effective recoil momentum from a single photon is written as $k_{\mathrm{r}}=\frac{2\pi}{\lambda}\sin(\theta/2)$ with the laser wavelength $\lambda$, and the corresponding recoil energy acquired by rubidium atoms is $E_{\mathrm{r}}=\hbar^2k_{\mathrm{r}}^2/(2m)$. These two laser beams have different frequencies $\omega_L$ and $(\omega_L+\Delta\omega_L)$, and $\delta=(\Delta\omega_L-\omega_Z)$ is the laser detuning from Raman resonance. The detailed experimental setup can be seen in Fig. 2.1.

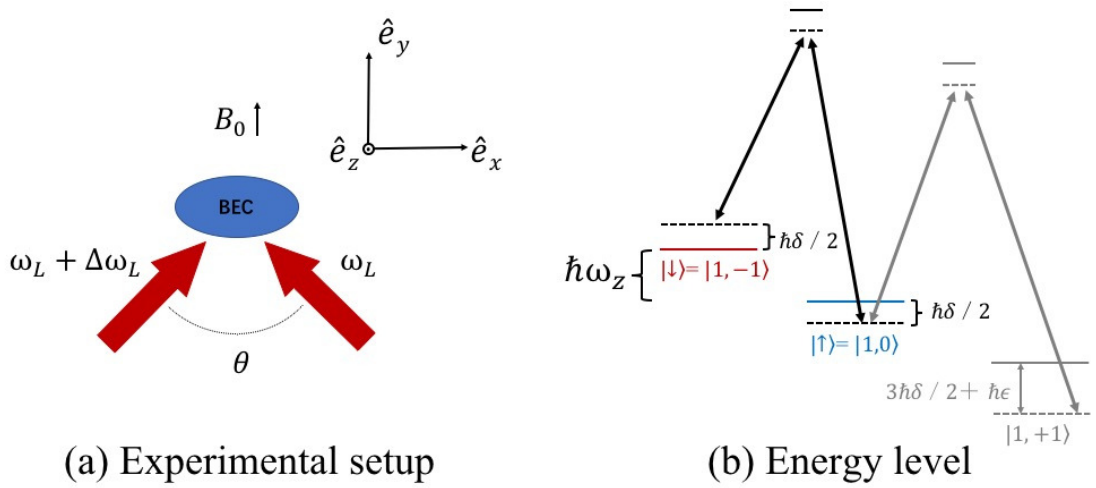


Figure 2.1: (a) The experimental setup of NIST scheme. (b) Energy level of $^{87}$Rb BEC hyperfine states in $F=1$ ground state.

In a frame rotating at the frequency $\Delta\omega_L$, within the rotating wave approximation, the corresponding system can be described in the basis of the pseudospin

states $\{|+1\rangle, |0\rangle, |-1\rangle\}$ in the figure by a three-level Hamiltonian

$$\mathcal{H}^{3-\text{level}} = \begin{pmatrix} \frac{\hbar^2\hat{\mathbf{k}}^2}{2m} + \frac{3\hbar\delta}{2} + \hbar\epsilon & \frac{\hbar\Omega}{2}e^{i2k_{\text{r}}x} & 0 \\ \frac{\hbar\Omega}{2}e^{-i2k_{\text{r}}x} & \frac{\hbar^2\hat{\mathbf{k}}^2}{2m} + \frac{\hbar\delta}{2} & \frac{\hbar\Omega}{2}e^{i2k_{\text{r}}x} \\ 0 & \frac{\hbar\Omega}{2}e^{-i2k_{\text{r}}x} & \frac{\hbar^2\hat{\mathbf{k}}^2}{2m} - \frac{\hbar\delta}{2} \end{pmatrix}. \tag{2.1}$$

In Ref. [6], the quadratic Zeeman shift $\epsilon$ is sufficiently large, i.e., $\epsilon > 4E_{\text{r}}$ in the experiment, and thus the contribution of state $|m_F = +1\rangle$ can be safely neglected. The lower-energy dispersion relation can be well described with the other two hyperfine states $|\uparrow\rangle = |F = 1, m_F = 0\rangle$ and $|\downarrow\rangle = |1, -1\rangle$ in Fig. 2.1 by an effective two-level Hamiltonian

$$\mathcal{H}^{2-\text{level}} = \begin{pmatrix} \frac{\hbar^2\hat{\mathbf{k}}^2}{2m} + \frac{\hbar\delta}{2} & \frac{\hbar\Omega}{2}e^{i2k_{\text{r}}x} \\ \frac{\hbar\Omega}{2}e^{-i2k_{\text{r}}x} & \frac{\hbar^2\hat{\mathbf{k}}^2}{2m} - \frac{\hbar\delta}{2} \end{pmatrix}. \tag{2.2}$$

The off-diagonal phase can be straightforwardly gauged away under a unitary transformation to the wave function $\Phi = U\Psi$ with

$$U = \begin{pmatrix} e^{ik_{\text{r}}x} & 0 \\ 0 & e^{-ik_{\text{r}}x} \end{pmatrix}, \tag{2.3}$$

and the effective Hamiltonian becomes

$$\mathcal{H}^{\text{SOC}} = U\mathcal{H}^{2-\text{level}}U^{\dagger} = \begin{pmatrix} \frac{\hbar^2(\hat{\mathbf{k}}-k_{\text{r}}\hat{\mathbf{e}}_x)^2}{2m} + \frac{\hbar\delta}{2} & \frac{\hbar\Omega}{2} \\ \frac{\hbar\Omega}{2} & \frac{\hbar^2(\hat{\mathbf{k}}+k_{\text{r}}\hat{\mathbf{e}}_x)^2}{2m} - \frac{\hbar\delta}{2} \end{pmatrix}, \tag{2.4}$$

or the familiar expression as

$$\mathcal{H}^{\text{SOC}} = \frac{\hbar^2(\hat{\mathbf{k}} - k_{\text{r}}\hat{\mathbf{e}}_x\sigma_z)^2}{2m} + \hbar\frac{\delta}{2}\sigma_z + \hbar\frac{\Omega}{2}\sigma_x, \tag{2.5}$$

with $2 \times 2$ Pauli matrices $\sigma_x$, $\sigma_z$ and the canonical momentum operator $\hat{\mathbf{k}} = -i\nabla$. Hence, the internal degrees of freedom of neutral atom (pseudospins) are coupled to the atomic orbital momentum $k_x$ along the SOC-direction, i.e., $\hat{\mathbf{e}}_x$, via Raman laser beams. This Raman-induced SOC is of one-dimensional nature as $\propto k_x\sigma_z$, which is an equal combination of the familiar two-dimensional Rashba SOC and Dresselhaus SOC in condensed matter physics.

Before we move to single-particle physics, it's easy to see that such a Bose condensate with the Raman-type SOC lacks Galilean invariance. By applying the unitary Galilean transformation along the SOC direction [57, 101, 147]

$$G = e^{-imvx/\hbar}, \tag{2.6}$$

the spin-orbit Hamiltonian in Eq. (2.5) reads

$$\begin{aligned}(\mathcal{H}^{\mathrm{SOC}})' =& G\mathcal{H}^{\mathrm{SOC}}G^{\dagger} \\ =& \frac{\hbar^2(k_y^2+k_z^2)}{2m} + \frac{\hbar^2(k_x+k_{\mathrm{r}}\sigma_z+mv/\hbar)^2}{2m} + \hbar\frac{\delta}{2}\sigma_z + \hbar\frac{\Omega}{2}\sigma_x \\ =& \mathcal{H}^{\mathrm{SOC}} + \frac{1}{2}mv^2 + \hbar v(k_x+k_{\mathrm{r}}\sigma_z).\end{aligned} \tag{2.7}$$

The transformed Hamiltonian has an extra velocity-dependent term $\hbar v k_{\mathrm{r}}\sigma_z$ which can not be gauged away and the physical momentum $k_x + k_{\mathrm{r}}\sigma_z$ does not commute with the Hamiltonian. Thus this system is proven to break Galilean invariance along the direction of the Raman-type SOC. We will see many interesting properties of this spin-orbit coupled Bose gas due to the lack of Galilean invariance in the following chapters.

## 2.2 Single-particle picture

Let's recall the usual form of the spin-orbit coupled Hamiltonian for the Raman-type SOC along $x$ axis as

$$\mathcal{H}^{\mathrm{SOC}} = \frac{\hbar^2(\hat{\mathbf{k}} - k_{\mathrm{r}}\hat{\mathbf{e}}_x\sigma_z)^2}{2m} + \hbar\frac{\delta}{2}\sigma_z + \hbar\frac{\Omega}{2}\sigma_x, \tag{2.8}$$

with the physical momentum being $\hat{\mathbf{k}} \mp k_{\mathrm{r}}\hat{\mathbf{e}}_x$ for spin-up and spin-down particles, respectively. $\Omega$ is the Raman coupling strength or the Rabi frequency, and $\delta$ is the detuning of the Raman lasers.

The momentum $\mathbf{k}$ is a good quantum number since the Hamiltonian is spatial translational invariant. Thus, by diagonalizing the matrix Hamiltonian, the eigenenergies of the system can be obtained analytically as [101]

$$\varepsilon_{\mathbf{k},\pm} = \frac{\hbar^2\mathbf{k}^2}{2m} + E_{\mathrm{r}} \pm \hbar\sqrt{\left(\frac{k_x k_{\mathrm{r}}}{m} - \frac{\delta}{2}\right)^2 + \left(\frac{\Omega}{2}\right)^2} \tag{2.9}$$

with the respective eigenstates of two branches as

$$\Phi_{\mathbf{k},+} = e^{i\mathbf{k}\cdot\mathbf{r}}\begin{pmatrix}\sin\theta\\ \cos\theta\end{pmatrix} \qquad \text{and} \qquad \Phi_{\mathbf{k},-} = e^{i\mathbf{k}\cdot\mathbf{r}}\begin{pmatrix}\cos\theta\\ -\sin\theta\end{pmatrix}. \tag{2.10}$$

Here, the variable $\theta$ is defined by

$$\theta(k_x) = \arcsin\left[\frac{1}{2}\left(1 - \frac{k_x k_{\mathrm{r}}/m - \delta/2}{\sqrt{(k_x k_{\mathrm{r}}/m - \delta/2)^2 + \Omega^2/4}}\right)\right]^2. \tag{2.11}$$

The helicity of the eigenenergies clearly reveals the spinor nature of the system. Without the dressing of two Raman laser beams, i.e., zero coupling strength $\Omega = 0E_{\mathrm{r}}$ and zero detuning $\delta = 0E_{\mathrm{r}}$, the single-particle dispersion relation in Eq. (2.9) are two parabolas intersecting at zero condensation momentum $k_x = 0$, see Fig. 2.2. In realistic condition of no dressing lasers, the coupling term $k_x k_{\mathrm{r}}$ disappears, and the dispersion relation recovers the conventional expression $\hbar^2\mathbf{k}^2/(2m)$ of free particles. Nevertheless, after switching on the Raman lasers and tuning the coupling strength $\Omega$ and the laser detuning $\delta$, the dispersion will experience dramatic changes.

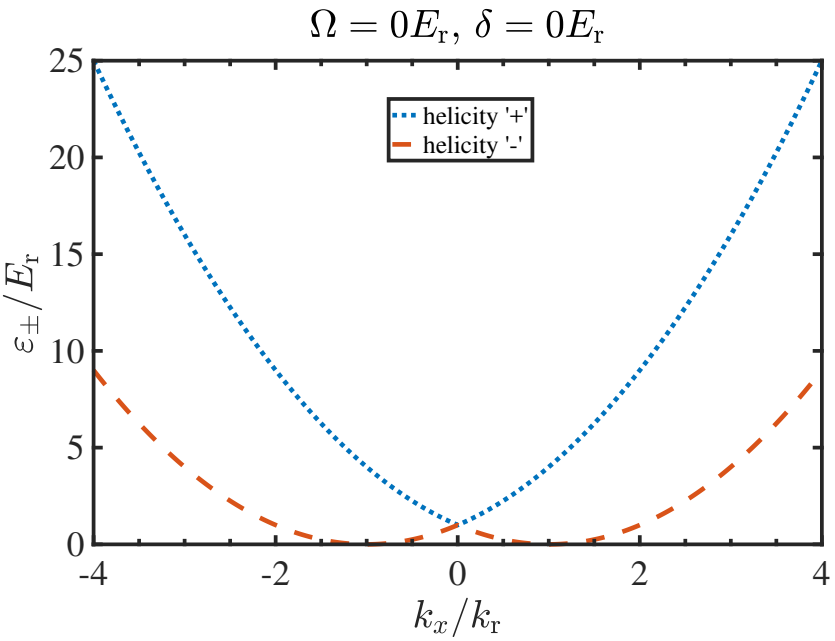


Figure 2.2: Single-particle dispersion in Eq. (2.9) when Raman lasers are turned off with $\Omega = 0E_r$ and $\delta = 0E_r$.

Under the condition of zero detuning $\delta = 0$, when we continue to increase the coupling strength $\Omega$ from $0.1E_r$, $0.5E_r$ to $0.9E_r$ as shown in Fig. 2.3, the two branches in the energy dispersion start to separate. The opening energy gap between them continues to enlarge as the coupling strength rises. The higher branches indicated by blue curves are approximately parabola, while the lower-energy branches exhibit a usual structure with an energy barrier at zero momentum and two degenerate minima at $\pm k_{x0}$. The condensation occurs at two minima, and the corresponding momentum is a function of the SOC coupling strength as

$$k_{x0} = k_r \sqrt{1 - \left(\frac{\Omega}{4E_r}\right)^2}, \tag{2.12}$$

calculated by minimizing the lower branch in Eq. (2.9).

Furthermore, when the coupling strength $\Omega$ continues to increase towards a critical value $\Omega_c = 4E_r$, the double-minimum structure will be softened with the central barrier being lowered and vanishing, as shown in Fig. 2.4. Meanwhile the positions of two minima $\pm k_{x0}$ will counter move, and eventually merge to be zero when the

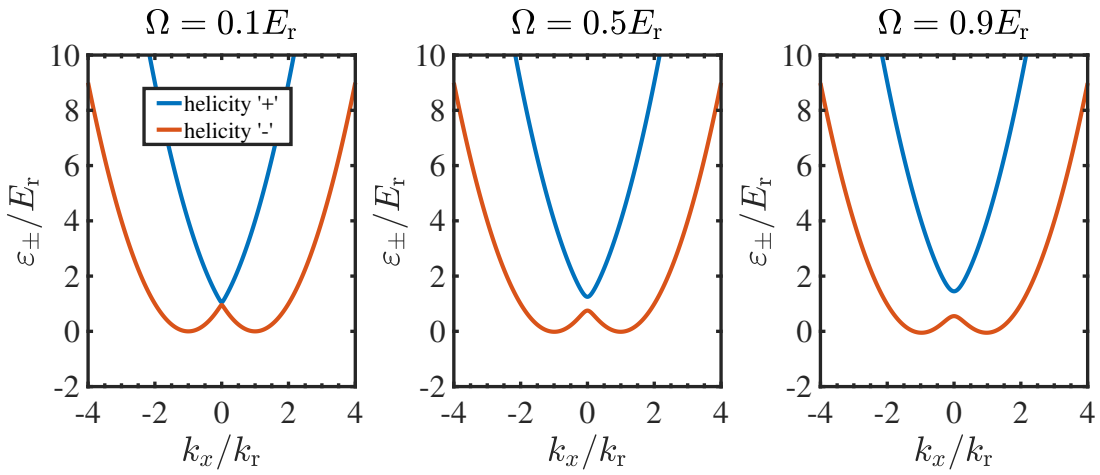


Figure 2.3: Single-particle dispersion for various values of $\Omega/E_r = 0.1$, 0.5 and 0.9 at $\delta = 0E_r$.

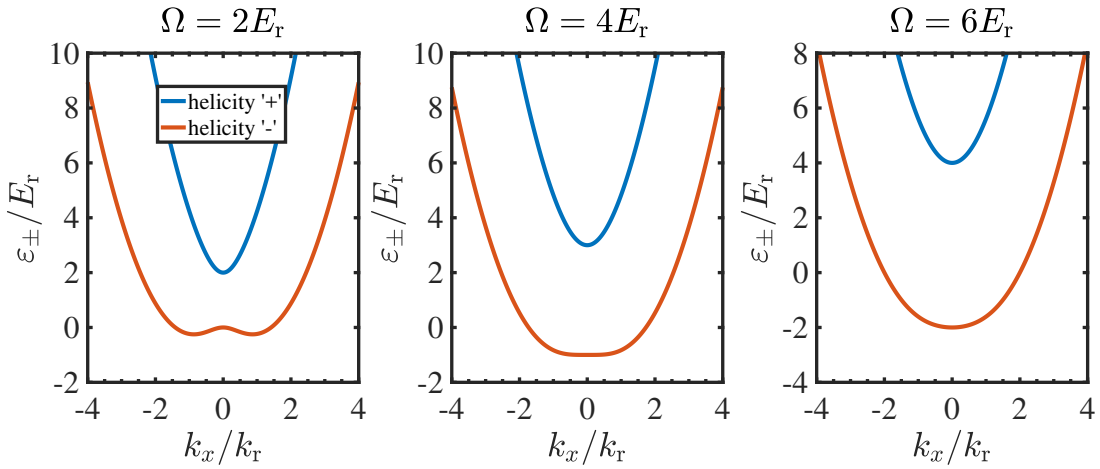


Figure 2.4: Single-particle dispersion for various values of $\Omega/E_r = 2$, 4 and 6 at $\delta = 0E_r$.

coupling strength reaches the critical point $\Omega_c$. At $\Omega = \Omega_c$, the lower branch of the dispersion behaves approximately as $\propto k_x^4$ with the central part very flat, and the condensation locates only at zero momentum $k_{x0} = 0$. When $\Omega$ exceeds the critical value $4E_r$, the lower branch becomes parabola-like and the condensates remain at zero momentum.

On the other hand, the variation of laser detuning $\delta$ at fixed coupling strength will also give rise to dramatic changes on single-particle dispersion. In Fig. 2.5, we have

presented the dependence of dispersion relation on various values of detuning $\delta = -1E_{\mathrm{r}}$ (left column), $0E_{\mathrm{r}}$ (middle column) and $1E_{\mathrm{r}}$ (right column). From upper panel to lower panel in the figure, the Raman coupling strength are subsequently fixed at $\Omega = 2E_{\mathrm{r}}$, $4E_{\mathrm{r}}$ and $6E_{\mathrm{r}}$. At zero detuning $\delta = 0$ as shown in Fig. 2.4, the dispersion relations are symmetric in momentum space, and the lower branch corresponds to a double-minimum structure with nonzero $k_{x0}$, center-flat-like and parabola-like with zero condensation momentum, respectively. However when the detuning $\delta$ becomes nonzero, all the dispersion at various $\Omega$ deform to be asymmetric. Meanwhile there is a global minimum in the lower branch locating at a finite momentum, whose sign is intimately related to the sign of $\delta$, see the left and right columns in Fig. 2.5.

In this thesis, aiming to explore the properties of exotic Bose superfluidity due to the degenerate double-minimum structure, and to carry out both qualitative and quantitative comparisons with recent experiments, we will focus on the case of zero detuning $\delta = 0$ in the rest of this manuscript.

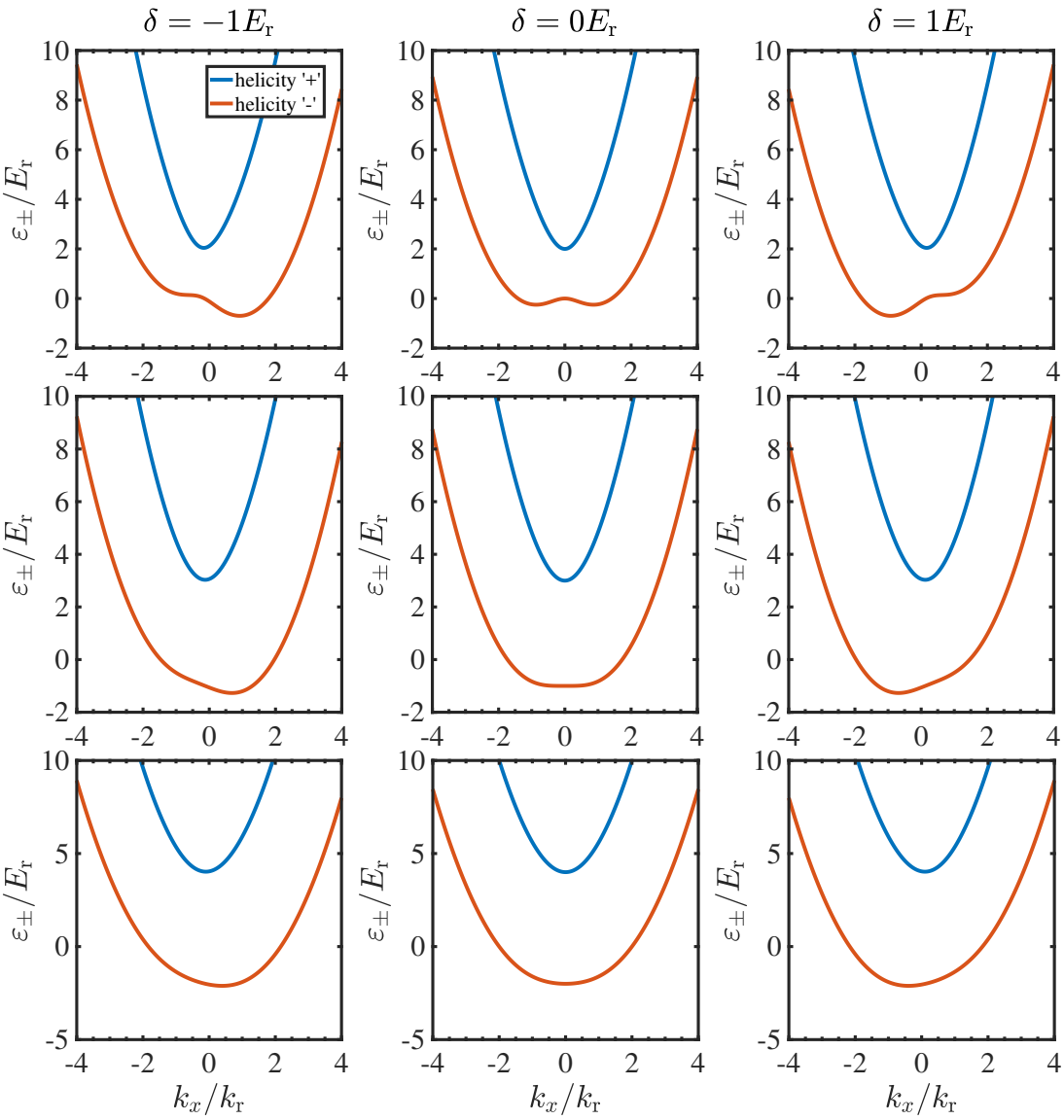


Figure 2.5: Single-particle dispersion for $\delta/E_r = -1$, 0 and $+1$ (from left to right) at various values of $\Omega/E_r = 2$, 4 and 6 (from upper to lower).

## 2.3 The generic phases of a SOC Bose gas

We have shown the single-particle dispersion as functions of the SOC coupling strength $\Omega$ and laser detuning $\delta$ in the last section. We will introduce interactions in this section and study their remarkable effects on the phases of matter, ground-state phase diagram and other thermodynamic properties. The following discussions are first given by Li *et al.* at the Gross-Pitaevskii level in Ref. [95].

The interaction Hamiltonian of a spinor Bose gas can be expressed by

$$\hat{H}_{\rm int} = \frac{1}{2}\int \mathrm{d}^3\mathbf{r} \sum_{\sigma,\sigma'=\uparrow,\downarrow} g_{\sigma\sigma'}\hat{\Phi}^\dagger_\sigma\hat{\Phi}^\dagger_{\sigma'}\hat{\Phi}_{\sigma'}\hat{\Phi}_\sigma(\mathbf{r}), \tag{2.13}$$

or explicitly by

$$\hat{H}_{\rm int} = \frac{1}{2}\int \mathrm{d}^3\mathbf{r} \left[g_{\uparrow\uparrow}\hat{\Phi}^\dagger_\uparrow\hat{\Phi}^\dagger_\uparrow\hat{\Phi}_\uparrow\hat{\Phi}_\uparrow + g_{\downarrow\downarrow}\hat{\Phi}^\dagger_\downarrow\hat{\Phi}^\dagger_\downarrow\hat{\Phi}_\downarrow\hat{\Phi}_\downarrow + 2g_{\uparrow\downarrow}\hat{\Phi}^\dagger_\uparrow\hat{\Phi}^\dagger_\downarrow\hat{\Phi}_\downarrow\hat{\Phi}_\uparrow\right]. \tag{2.14}$$

Here $\hat{\Phi}_\sigma(\mathbf{r})$ is the Bose field operator for spin-component $\sigma =\uparrow,\downarrow$. The interaction strengths are denoted by $g_{\sigma\sigma'} = 4\pi\hbar^2 a_{\sigma\sigma'}/m$ between the same components ($\sigma = \sigma'$) or different components ($\sigma \neq \sigma'$), with the corresponding $s$-wave scattering lengths $a_{\sigma\sigma'}$. In the following we consider the usual spin symmetric interaction strengths $g_{\uparrow\uparrow} = g_{\downarrow\downarrow} = g > g_{\uparrow\downarrow}$, which corresponds effectively to the experiment in Ref. [7].

In the single-particle picture in Sec. 2.2, the dispersion relation is of a double-minimum structure for $\Omega < 4E_{\rm r}$, and of a single-minimum structure for $\Omega \geq 4E_{\rm r}$. Due to the exotic degenerate double minima, the condensate can locate at either one of $\pm k_{x0}$ or their linear combinations. The corresponding wave function of the condensate with single momentum takes a form of

$$\Phi_{-k_{x0}} = e^{-ik_{x0}\cdot x}\begin{pmatrix}\sin\theta_0\\ -\cos\theta_0\end{pmatrix} \quad \text{or} \quad \Phi_{+k_{x0}} = e^{+ik_{x0}\cdot x}\begin{pmatrix}\cos\theta_0\\ -\sin\theta_0\end{pmatrix}, \tag{2.15}$$

with the angle variable $\theta_0 \equiv \theta(k_{x0})$ given in Eq. (2.11), while the condensation momentum is given in Eq. (2.12) as

$$k_{x0} = \begin{cases} k_{\rm r}\sqrt{1-\left(\frac{\Omega}{4E_{\rm r}}\right)^2}, & \Omega < 4E_{\rm r} \\ 0. & \Omega \geq 4E_{\rm r} \end{cases} \tag{2.16}$$

Therefore in the presence of interactions, without any loss of generality, one can start with a trial ansatz for the wave function of the condensate as

$$\Phi(\mathbf{r}) \equiv \begin{pmatrix} \Phi_\uparrow \\ \Phi_\downarrow \end{pmatrix} = \sqrt{\bar{n}} \left[ C_1 \begin{pmatrix} \sin\theta \\ -\cos\theta \end{pmatrix} e^{-ik_{x0}x} + C_2 \begin{pmatrix} \cos\theta \\ -\sin\theta \end{pmatrix} e^{ik_{x0}x} \right], \quad (2.17)$$

in terms of four variational parameters $k_{x0}$, $\theta$, $C_1$ and $C_2$. $\bar{n} = N/V$ is the average density with total particle number $N$ and volume $V$. The normalization condition is then written as

$$\int \mathrm{d}^3\mathbf{r} \left( |\Phi_\uparrow|^2 + |\Phi_\uparrow|^2 \right) = N, \qquad \text{or} \qquad |C_1|^2 + |C_2|^2 = 1. \quad (2.18)$$

The trial wave function in Eq. (2.17) will be substituted into the total Hamiltonian

$$\hat{H} = \int \mathrm{d}^3\mathbf{r} \left( \Phi_\uparrow^\dagger, \Phi_\downarrow^\dagger \right) \mathcal{H}^{\mathrm{SOC}} \begin{pmatrix} \Phi_\uparrow \\ \Phi_\downarrow \end{pmatrix} + \hat{H}_{\mathrm{int}}, \quad (2.19)$$

with the single-particle Hamiltonian $\mathcal{H}^{\mathrm{SOC}}$ in Eq. (2.8) and the interaction energy $\hat{H}_{\mathrm{int}}$ in Eq. (2.13). It's clear that the interaction energy is independent of $\theta$, and the minimization of the total energy with respect to $\theta$ gives straightforwardly to

$$k_{x0} = k_{\mathrm{r}} \cos(2\theta). \quad (2.20)$$

Thus we can replace terms with the variable $\theta$ and obtain the mean-field energy per particle $\varepsilon \equiv E/N$ in a new form as [95]

$$\varepsilon = E_{\mathrm{r}} - \frac{\Omega}{2} \frac{\sqrt{k_{\mathrm{r}}^2 - k_{x0}^2}}{k_{\mathrm{r}}} - F(\beta) \frac{k_{x0}^2}{2k_{\mathrm{r}}^2} + G_1(1 + 2\beta) \quad (2.21)$$

with only two variational parameters now, i.e., $k_{x0}$ and $\beta \equiv |C_1|^2|C_2|^2$. Here an extra term $\hbar^2 k_\perp^2/(2m)$ is absorbed in the equation, and the function $F(\beta)$ is defined as

$$F(\beta) = 2E_{\mathrm{r}} - 2G_2 + 4(G_1 + 2G_2)\beta \quad (2.22)$$

with two interaction energies

$$G_1 = \frac{(g + g_{\uparrow\downarrow})\bar{n}}{4} \qquad \text{and} \qquad G_2 = \frac{(g - g_{\uparrow\downarrow})\bar{n}}{4}. \quad (2.23)$$

We continue to minimize the mean-field energy functional with respect to the parameter $k_{x0}$, which gives the extremum in terms of $\beta$ as

$$k_{x0}(\beta) = \begin{cases} k_{\mathrm{r}}\sqrt{1-\frac{\Omega^2}{4F(\beta)^2}}, & \Omega < 2F(\beta) \\ 0, & \Omega \geq 2F(\beta) \end{cases} \tag{2.24}$$

which can be seen as the extension of the single-particle result in Eq. (2.16) to the many-body case with interactions. The last variational parameter $\beta$ is in the range of $[0, 1/4]$ obtained from the normalization condition in Eq. (2.18). We can replace $k_{x0} = k_{x0}(\beta)$ and the corresponding energy per particle is then a function of only one parameter $\beta$. In the case $G_2 < 0$, the energy is monotonically increasing with the energy minimum at the left end $\beta = 0$. When $G_2 > 0$, the energy is instead a non-monotonic function with the minima now at two ends of the range, i.e., $\beta = 0$ or $\beta = 1/4$.

According to the variational process described above, the ground-state wave functions or phases can be divided into three classifications:

1. The *stripe* phase (ST), with $\beta = 1/4$, i.e., finite $|C_1|$ and $|C_2|$. The wave function in Eq. (2.17) thus becomes the superposition of two plane waves with nonzero wave vectors $\pm k_{x0}$ respectively.

2. The *plane-wave* phase (PW), with $\beta = 0$, i.e., either $|C_1| = 0$ or $|C_2| = 0$. The wave function is a single plane wave located at a nonzero momentum $-k_{x0}$ or $+k_{x0}$.

3. The *zero-momentum* phase (ZM), with $k_{x0} = 0$. All of the atoms condense at zero momentum.

We focus on the case $G_2 > 0$, i.e., $g_{\uparrow\uparrow} = g_{\downarrow\downarrow} = g > g_{\uparrow\downarrow}$, where all the generic phases above are present in the parameter space of $\Omega$, and the positions of three phase transitions can be then determined in a variational method. In detail, there are two different cases:

- When the condition $E_{\mathrm{r}} > 2G_2 + \frac{2G_2^2}{G_1}$, i.e., $\bar{n} < \bar{n}^{(\mathrm{c})} \equiv \frac{g+g_{\uparrow\downarrow}}{g(g-g_{\uparrow\downarrow})}E_{\mathrm{r}}$, is satisfied, all the three phases are spanning one by one over the range of the coupling

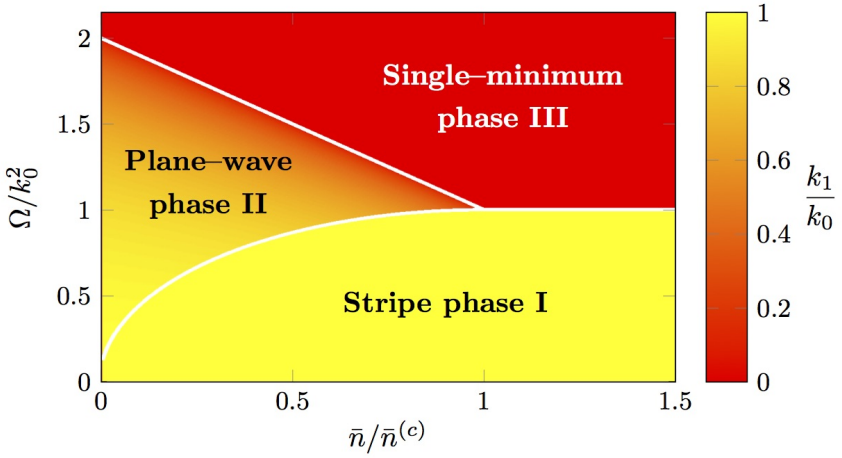


Figure 2.6: Phase diagram of three generic phases in a Raman-type spin-orbit-coupled BEC. Image from Ref. [8].

strength $\Omega$. The phase boundaries are

$$\Omega^{(\mathrm{ST-PW})} = 2\left[(2E_\mathrm{r}+G_1)(2E_\mathrm{r}-2G_2)\frac{2G_2}{G_1+2G_2}\right]^{1/2} \tag{2.25}$$

for the ST-PW phase transition, and

$$\Omega^{(\mathrm{PW-ZM})} = 4E_\mathrm{r} - 4G_2 \tag{2.26}$$

for the PW-ZM phase transition.

- In the opposite condition $E_\mathrm{r} < 2G_2 + \frac{2G_2^2}{G_1}$ or $\bar{n} > \frac{g+g_{\uparrow\downarrow}}{g(g-g_{\uparrow\downarrow})}E_\mathrm{r}$, only two phases, i.e., ST and ZM phases, exist. And the corresponding transition occurs at

$$\Omega^{(\mathrm{ST-ZM})} = 2(2E_\mathrm{r}+G_1) - 2\left[(2E_\mathrm{r}+G_1)G_1\right]^{1/2}. \tag{2.27}$$

The phase diagram in the parameter spaces of the average density $\bar{n}$ and the Raman coupling strength $\Omega$ is shown explicitly in Fig. 2.6. The details of the above derivations in the variational formalism can be seen in Appendix A.1. We will discuss thoroughly the general properties of three distinct phases in the following.

### 2.3.1 The plane-wave and zero-momentum phases

Let us start with the plane-wave and zero-momentum phases, which can be expressed with the same wave function as

$$\Phi(\mathbf{r}) = \sqrt{\bar{n}} \begin{pmatrix} \cos\theta \\ -\sin\theta \end{pmatrix} e^{ik_{x0}x}, \tag{2.28}$$

for either zero or finite wave vector $k_{x0}$. Hence, the wave function in the plane-wave phase is spatially dependent, while the one of the zero-momentum phase is homogeneous. However, the density distributions in both phases are uniform, possessing transnational-invariant symmetry.

We focus on all three phases in the region $\bar{n} < \bar{n}^{(\mathrm{c})}$, where the plane-wave and zero momentum phases are separated at $\Omega_{c2} \equiv \Omega^{(\mathrm{PW-ZM})}$ in Eq. (2.26). The Bose condensates occupy a single plane-wave state with the condensation momentum

$$k_{x0}/k_{\mathrm{r}} = \begin{cases} \sqrt{1-\Omega^2/\Omega_{c2}^2}, & (\Omega < \Omega_{c2} \text{ in PW}) \\ 0. & (\Omega \geq \Omega_{c2} \text{ in ZM}) \end{cases} \tag{2.29}$$

The spin polarization of the condensates along SOC-direction (i.e., $x$) and in the perpendicular plane can be calculated using Eq. (2.20) by

$$\begin{aligned} \langle\sigma_x\rangle &= -\sin(2\theta) = -\sqrt{1-\cos^2(2\theta)} = -\sqrt{1-k_{x0}^2/k_{\mathrm{r}}^2}, \\ \langle\sigma_z\rangle &= \cos(2\theta) = k_{x0}/k_{\mathrm{r}}. \end{aligned} \tag{2.30}$$

With the result in Eq. (2.29), the spin polarization in two respective phases can be straightforwardly rewritten as

$$\langle\sigma_x\rangle = \begin{cases} -\Omega/\Omega_{c2}, & (\Omega < \Omega_{c2} \text{ in PW}) \\ -1. & (\Omega \geq \Omega_{c2} \text{ in ZM}) \end{cases} \tag{2.31}$$

and

$$\langle\sigma_z\rangle = \begin{cases} \sqrt{1-\Omega^2/\Omega_{c2}^2}, & (\Omega < \Omega_{c2} \text{ in PW}) \\ 0. & (\Omega \geq \Omega_{c2} \text{ in ZM}) \end{cases} \tag{2.32}$$

It's obvious that the spin polarizations of both phases along the $z$-direction are the same with the expression of the condensation momentum in Eq. (2.29) as shown in Fig. 2.6. It depends on the Raman coupling strength in the PW phase, and is zero in

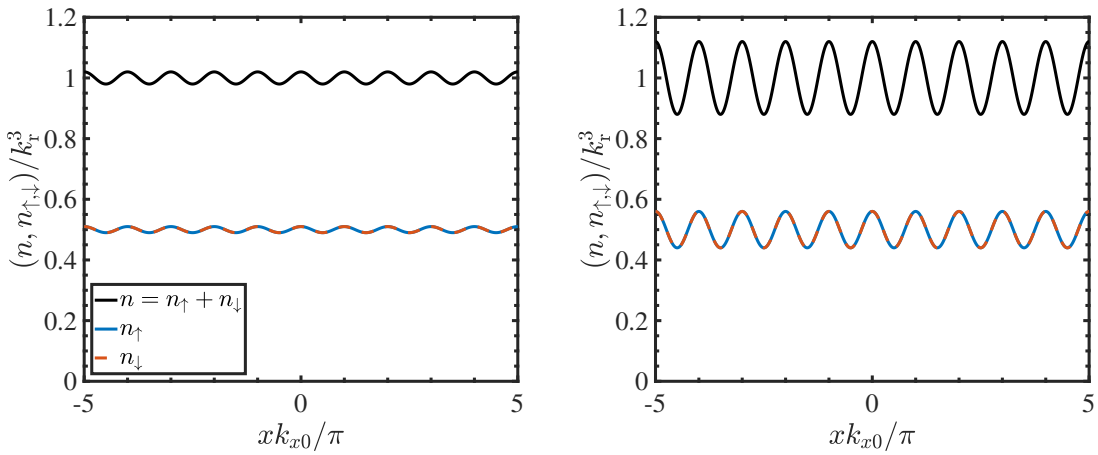


Figure 2.7: Typical density profile along the $x$-direction in the stripe phase at $\Omega = 0.1$ (left), and $0.6E_r$ (right). Parameters are the same as in Fig. 2.8.

the ZM phase, indicating an equal mixture of two spin components. Along the $x$ axis or SOC direction, the spin polarization in the PW phase depends linearly on $\Omega$, while in the ZM phase it is $-1$, indicating fully polarization along the direction of the SOC. In the following section, we will further study the exotic stripe phase, and illustrate the relevant properties, i.e., condensation momentum and spin polarizations, of all three phases together (see Fig. 2.8).

### 2.3.2 The supersolid stripe phase

The third generic ground-state phase in a Bose gas with the Raman-type spin-orbit coupling is called the stripe phase, because the density distribution is spatially modulated by the SOC strength, as shown in Fig. 2.7. In the stripe phase, $\beta = |C_1|^2|C_2|^2 = 1/4$, which means that $|C_1| = |C_2| = 1/\sqrt{2}$. Hence the corresponding wave function of a stripe phase can be simplified as

$$\Phi(\mathbf{r}) = \sqrt{\frac{\bar{n}}{2}}\left[\begin{pmatrix}\sin\theta\\ -\cos\theta\end{pmatrix}e^{-ik_{x0}x} + \begin{pmatrix}\cos\theta\\ -\sin\theta\end{pmatrix}e^{ik_{x0}x}\right], \tag{2.33}$$

with $\theta = \arccos(k_{x0}/k_r)/2$ and the condensation momentum $k_{x0}$ calculated from Eq. (2.24) as

$$\frac{k_{x0}^{(\mathrm{ST})}}{k_r} = \sqrt{1 - \frac{\Omega^2}{(4E_r + 2G_1)^2}}. \ (\Omega < \Omega_{c1}) \tag{2.34}$$

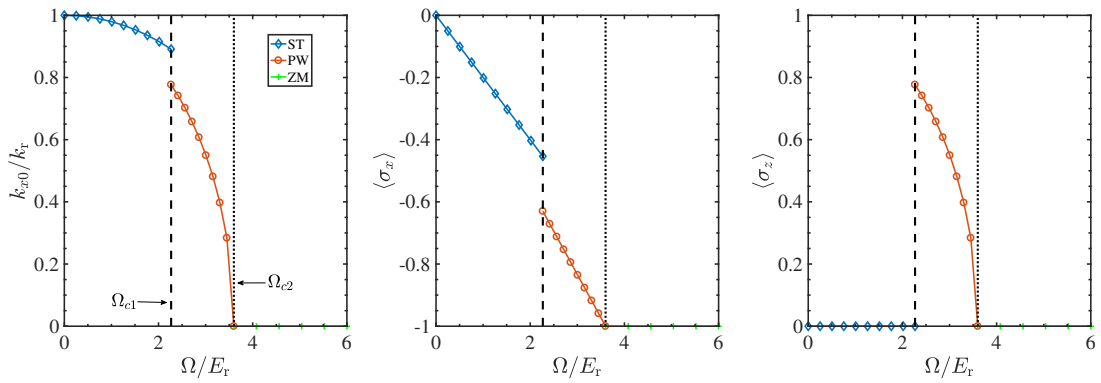


Figure 2.8: Condensation momentum, spin polarization along the $x$- and $z$-axis as a function of the coupling strength $\Omega$ across three generic phases. Here $g = 1.2E_r/k_r^3$, $g_{\uparrow\downarrow} = 0.8E_r/k_r^3$ and $\bar{n} = 1.0k_r^3$.

Here $\Omega_{c1} \equiv \Omega^{(\mathrm{ST-PW})}$ is the transition position between the stripe and the plane-wave phases given in Eq. (2.25). In the stripe phase $\Omega < \Omega_{c1}$, the condensation momentum is smoothly decreasing with the coupling strength $\Omega$, which is different from the one in Eq. (2.29) for the PW and ZM phases. Using Eqs. (2.34), the corresponding spin polarizations in the stripe phase are given by

$$\begin{aligned} \langle\sigma_x\rangle^{(\mathrm{ST})} &= -\frac{\Omega}{4E_r + 2G_1}, \\ \langle\sigma_z\rangle^{(\mathrm{ST})} &= \cos(2\theta)\left(|C_2|^2 - |C_1|^2\right) = 0. \end{aligned} \tag{2.35}$$

In Fig. 2.8, we take a typical set of parameters with intra-species interaction strength $g = 1.2E_r/k_r^3$, inter-species interaction strength $g_{\uparrow\downarrow} = 0.8E_r/k_r^3$ and the average density $\bar{n} = 1.0k_r^3$. This gives rise to two phase transitions in Eqs. (2.25) and (2.26) as

$$\Omega_{c1} = 2.27E_r, \text{ and } \Omega_{c2} = 3.60E_r. \tag{2.36}$$

In these parameters, the condensation momentum $k_{x0}$, the spin polarizations along the SOC direction and $z$-direction derived above are illustrated as a function of the coupling strength $\Omega$ across all three exotic phases. Two critical Rabi frequencies $\Omega_{c1}$ and $\Omega_{c2}$ are denoted by the dashed and dotted lines in the figure respectively.

In general, the findings reveal the first-order nature of the transition at $\Omega_{c1}$ between the stripe and the plane-wave phases, and the second-order nature of the transition at $\Omega_{c2}$ between the plane-wave and zero-momentum phases. Specifically,

the momentum and two spin polarizations exhibit a discontinuous jump at the ST-PW transition $\Omega_{c1}$, while at the PW-ZM transition position $\Omega_{c2}$ they are instead continuous. When we increase the coupling strength in the stripe phase (i.e., blue lines with diamonds), the momentum $k_{x0}/k_{\mathrm{r}}$ is smoothly decreasing from 1, and the spin polarization $\langle\sigma_x\rangle$ along the $x$-axis is linearly reducing while the polarization $\langle\sigma_z\rangle$ along the $z$-axis remains zero. In the plane-wave and zero-momentum phases denoted by the red and green lines respectively, the momentum $k_{x0}/k_{\mathrm{r}}$ and the polarization $\langle\sigma_z\rangle$ are the same, monotonically dropping towards zero at and beyond the transition $\Omega_{c2}$. Meanwhile the spin polarization $\langle\sigma_x\rangle$ decreases linearly with $\Omega$ and reaches zero at and beyond $\Omega_{c2}$, implying the non-magnetic character in the zero-momentum phase.

In summary, we have reviewed previous studies of a weakly-interacting Bose gas with the Raman-lasers-induced spin-orbit coupling. The single-particle physics are studied, and the typical grounds-state phases in the presence of interactions are well classified. In the next Chapter, we will thoroughly introduced a theoretical approach mostly used in the remaining of this thesis.

# Chapter 3

# Hartree-Fock-Bogoliubov theory with the Popov approximation

This chapter is mostly devoted to reviewing the Hartree-Fock-Bogoliubov theory within the Popov approximation, which can well describe a weakly interacting Bose gas at zero and/or nonzero temperature. In Secs. 3.1 and 3.2, we will briefly review the Hartree-Fock-Bogoliubov theory within the Popov approximation in ultracold Bose gases with single component or two components, and then generalize to the system in the presence of Raman-type spin-orbit coupling. In the last two sections, we make a trial application to discuss the effects of finite particle number and temperature in an interacting one-dimensional Bose gas (Sec. 3.3), and then map the system to a spin-polarized interacting Fermi gas using Bose-Fermi duality to explore the role of effective range (Sec. 3.4). The last two sections are mainly from our recent publications in Refs. [64] and [65].

## 3.1 Introduction

In quantum many-body systems, at zero temperature or extremely low temperature, the Gross-Pitaevskii (GP) formalism introduced in Sec. 1.1.1 and the famous Bogoliubov approximation can provide a good description of the ground-state wavefunction and energy at weak couplings [10]. Nevertheless, at finite temperature thermal atoms are non-negligible and the interactions between excited atoms start to play an important role in studying relevant thermodynamic properties, which makes the GP theory and Bogoliubov model invalid. The effect of thermal excited atoms was first taken into account by Popov in 1965 in the self-consistent Hartree-Fock-Bogoliubov approximation. This leads to the so-called Popov approximation, which is applicable to a weakly interacting Bose gas at much higher temperature regime. For a three-dimensional (3D) weakly interacting Bose gas, Shi and Griffin have shown that the Hartree-Fock-Bogoliubov-Popov theory is useful and valid in a large range of finite temperature except a small critical area near the transition temperature [148, 149].

## 3.2 Theoretical framework

### 3.2.1 Single-component Bose gases

In this section, we revisit Hartree-Fock-Bogoliubov method within Popov approximation (HFBP) in a three-dimensional homogeneous single-component Bose gas with weak interactions. We apply the theory to investigate the excitation spectrum in the zero-temperature limit, and compare it with the analytic result obtained from the Bogoliubov theory. Afterwards, we numerically study the behaviour of elementary excitation spectrum, condensate fraction and quantum depletion at finite temperature, particularly at the regime near the critical BEC transition. It's worth to mention that, we have recently studied collective modes and dynamical properties in a spherical Bose condensate [150], by means of the time-dependent HFBP formalism described in the following.

In a 3D weakly interacting Bose gas, the grand-canonical Hamiltonian takes the

form [151, 152]

$$\begin{aligned}\hat{\mathcal{H}}^{\mathrm{GC}} = &\int d^3\mathbf{r}\hat{\Phi}^\dagger(\mathbf{r},t)(\mathcal{H}_0-\mu)\hat{\Phi}(\mathbf{r},t)\\ &+\frac{1}{2}\iint d^3\mathbf{r}d^3\mathbf{r}'\hat{\Phi}^\dagger(\mathbf{r},t)\hat{\Phi}^\dagger(\mathbf{r}',t)U(\mathbf{r}-\mathbf{r}')\hat{\Phi}(\mathbf{r}',t)\hat{\Phi}(\mathbf{r},t),\end{aligned} \tag{3.1}$$

where $\hat{\Phi}(\mathbf{r},t)$ is the bosonic field operator, $\mu$ is the chemical potential and the single-particle Hamiltonian is

$$\mathcal{H}_0 = -\frac{\hbar^2}{2m}\nabla^2 + V_{\mathrm{ext}}(\mathbf{r}), \tag{3.2}$$

with an external trapping potential $V_{\mathrm{ext}}(\mathbf{r})$. By taking a $\delta$-function interaction $U(\mathbf{r}-\mathbf{r}') = g\delta(\mathbf{r}-\mathbf{r}')$ between bosons with the $s$-wave interaction strength $g$ given in Eq. (1.15), the Heisenberg equation of motion is written as

$$\begin{aligned}i\hbar\frac{\partial\hat{\Phi}(\mathbf{r},t)}{\partial t} &= \left[\hat{\Phi}(\mathbf{r},t),\hat{\mathcal{H}}^{\mathrm{GC}}\right]\\ &= (\mathcal{H}_0-\mu)\hat{\Phi}(\mathbf{r},t) + g\hat{\Phi}^\dagger\hat{\Phi}\hat{\Phi}(\mathbf{r},t).\end{aligned} \tag{3.3}$$

In the usual procedure, the field operator $\hat{\Phi}(\mathbf{r},t)$ can be separated into a classical field $\phi$ of the condensate and a non-condensate fluctuation operator $\hat{\eta}$ [153–156]:

$$\hat{\Phi}(\mathbf{r},t) \equiv \phi(\mathbf{r},t) + \hat{\eta}(\mathbf{r},t), \tag{3.4}$$

which leads to the expectation $\langle\hat{\Phi}\rangle = \phi$ and $\langle\hat{\eta}\rangle = 0$. Thus, we obtain straightforwardly $\langle\hat{\Phi}^\dagger\hat{\Phi}\rangle = |\phi|^2 + \langle\hat{\eta}^\dagger\hat{\eta}\rangle$ and $\langle\hat{\Phi}\hat{\Phi}\rangle = \phi^2 + \langle\hat{\eta}\hat{\eta}\rangle$.

Within the mean-field approximation, we can decouple the three-operator term $\hat{\Phi}^\dagger\hat{\Phi}\hat{\Phi}$ and its average as [157]

$$\begin{aligned}\hat{\Phi}^\dagger\hat{\Phi}\hat{\Phi} =&|\phi|^2\phi + 2(|\phi|^2+|\hat{\eta}|^2)\hat{\eta} + (\phi^2+\langle\hat{\eta}\hat{\eta}\rangle)\hat{\eta}^\dagger + 2\phi\hat{\eta}^\dagger\hat{\eta} + \phi^\dagger\hat{\eta}\hat{\eta},\\ \langle\hat{\Phi}^\dagger\hat{\Phi}\hat{\Phi}\rangle =&(|\phi|^2 + 2\langle\hat{\eta}^\dagger\hat{\eta}\rangle)\phi + \langle\hat{\eta}\hat{\eta}\rangle\phi^\dagger,\\ \hat{\Phi}^\dagger\hat{\Phi}\hat{\Phi} - \langle\hat{\Phi}^\dagger\hat{\Phi}\hat{\Phi}\rangle =&2(|\phi|^2+\langle\hat{\eta}^\dagger\hat{\eta}\rangle)\hat{\eta} + (\phi^2+\langle\hat{\eta}\hat{\eta}\rangle)\hat{\eta}^\dagger = 2\langle\hat{\Phi}^\dagger\hat{\Phi}\rangle\hat{\eta} + \langle\hat{\Phi}\hat{\Phi}\rangle\hat{\eta}^\dagger,\end{aligned} \tag{3.5}$$

with $\hat{\eta}^\dagger\hat{\eta}\hat{\eta} \simeq 2\langle\hat{\eta}^\dagger\hat{\eta}\rangle\hat{\eta} + \langle\hat{\eta}\hat{\eta}\rangle\hat{\eta}^\dagger$.

By taking an average on both sides of Eq. (3.3) and making use of Eq. (3.5), we then find that

$$i\hbar\frac{\partial\phi}{\partial t} = (\mathcal{H}_0-\mu)\phi + g\left[(n_c+2n_t)\phi + n_a\phi^*\right], \tag{3.6}$$

where $n_c \equiv |\phi(\mathbf{r},t)|^2$ is the time-dependent density of the condensate, $n_t \equiv \langle\hat{\eta}^\dagger\hat{\eta}\rangle$ is the non-condensate thermal density and $n_a \equiv \langle\hat{\eta}\hat{\eta}\rangle$ is the anomalous thermal density.

The equation of motion for the non-condensate operator $\hat{\eta}$ can be similarly obtained by $i\hbar\partial_t\hat{\eta} = i\hbar\partial_t(\hat{\Phi}-\phi)$ as

$$i\hbar\frac{\partial\hat{\eta}}{\partial t} = (\mathcal{H}_0-\mu)\hat{\eta} + g\left[2(n_c+n_t)\hat{\eta} + (\phi^2+n_a)\hat{\eta}^\dagger\right]. \tag{3.7}$$

To solve this equation, we then use the Bogoliubov transformation to expand the non-condensate operator $\hat{\eta}(\mathbf{r},t)$ and its conjugate as

$$\begin{aligned}\hat{\eta}(\mathbf{r},t) =& \sum_j\left[u_j(\mathbf{r})e^{-i\varepsilon_j t}\hat{\alpha}_j + v_j^*(\mathbf{r})e^{i\varepsilon_j t}\hat{\alpha}_j^\dagger\right],\\ \hat{\eta}^\dagger(\mathbf{r},t) =& \sum_j\left[v_j(\mathbf{r})e^{-i\varepsilon_j t}\hat{\alpha}_j + u_j^*(\mathbf{r})e^{i\varepsilon_j t}\hat{\alpha}_j^\dagger\right],\end{aligned} \tag{3.8}$$

i.e., the non-condensate operator $\hat{\eta}(\mathbf{r},t)$ is rewritten in a quasi-particle basis. The operators $\hat{\alpha}_j^\dagger$ and $\hat{\alpha}_j$ are the creation and annihilation operators for quasi-particles respectively. $u_j$ and $v_j$ are the corresponding amplitudes in the excited state $j$. Bogoliubov quasi-particles are assumed to be non-interacting, and their operators $\hat{\alpha}^\dagger$ and $\hat{\alpha}$ satisfy the bosonic commutation relations

$$\left[\hat{\alpha}_i,\hat{\alpha}_j^\dagger\right] = \delta_{ij},\ \ \left[\hat{\alpha}_i^\dagger,\hat{\alpha}_j^\dagger\right] = [\hat{\alpha}_i,\hat{\alpha}_j] = 0, \tag{3.9}$$

leading to the normalization condition $\int d^3\mathbf{r}(u_i^2(\mathbf{r}) - v_i^2(\mathbf{r})) = 1$ of the Bogoliubov wave-functions $u_i(\mathbf{r})$ and $v_i(\mathbf{r})$.

In the Popov approximation, the anomalous densities (i.e., $\langle\hat{\eta}^\dagger\hat{\eta}^\dagger\rangle$ and $\langle\hat{\eta}\hat{\eta}\rangle$) are omitted to ensure the theory is gapless [64, 157, 158]. We finally obtain the time-dependent Hartree-Fock-Bogoliubov equation (HFBP) [156, 157, 159], which consists of two parts:

(A) a modified Gross-Pitaevskii equation

$$i\hbar\frac{\partial\phi}{\partial t} = \left[\mathcal{H}_0 - \mu + g(n_c+2n_t)\right]\phi, \tag{3.10}$$

which, in the case of a static condensate wave function $\phi = \phi(\mathbf{r})$, takes the form,

$$\left[\mathcal{H}_0 - \mu + gn_0(\mathbf{r}) + 2gn_t(\mathbf{r})\right]\phi(\mathbf{r}) = 0. \tag{3.11}$$

The static density of the condensate is $n_0 \equiv |\phi(\mathbf{r})|^2$ and the thermal density is $n_t(\mathbf{r}) \equiv \langle \hat{\eta}^\dagger \hat{\eta} \rangle$.

(B) the coupled Bogoliubov equations

$$\begin{bmatrix} \mathcal{L} & \mathcal{M} \\ \mathcal{M}^* & \mathcal{L} \end{bmatrix} \begin{bmatrix} u_j(\mathbf{r}) \\ v_j(\mathbf{r}) \end{bmatrix} = \varepsilon_j \begin{bmatrix} +u_j(\mathbf{r}) \\ -v_j(\mathbf{r}) \end{bmatrix}, \tag{3.12}$$

which are obtained by substituting Eq. (3.8) back into the equation of motion for the non-condensate operator $\hat{\eta}$ in Eq. (3.7). In the coupled equations, we have defined

$$\mathcal{L} \equiv \mathcal{H}_0 - \mu + 2g\left(n_0(\mathbf{r}) + n_t(\mathbf{r})\right), \tag{3.13}$$

and

$$\mathcal{M} \equiv g\phi^2(\mathbf{r}). \tag{3.14}$$

In the modified Gross-Pitaevskii equation, there are condensate and non-condensate densities in the interaction energy term, both of which have to be solved self-consistently. For the quasi-particle occupation number $N_j$ of the $j$-th excited state, we have,

$$N_j \equiv \langle \hat{\alpha}_j^\dagger \hat{\alpha}_j \rangle = \frac{1}{e^{\beta \varepsilon_j} - 1}, \tag{3.15}$$

with the inverse temperature $\beta = 1/k_{\mathrm{B}}T$.

Therefore, using Eq. (3.8), the thermal density is given by

$$\begin{aligned} n_t(\mathbf{r}) &\equiv \langle \hat{\eta}^\dagger \hat{\eta} \rangle \\ &= \sum_j \left[u_j^2(\mathbf{r}) + v_j^2(\mathbf{r})\right] \langle \hat{\alpha}_j^\dagger \hat{\alpha}_j \rangle + \sum_j v_j^2(\mathbf{r}) \\ &= \sum_j \left[u_j^2(\mathbf{r}) + v_j^2(\mathbf{r})\right] N_j + \sum_j v_j^2(\mathbf{r}). \end{aligned} \tag{3.16}$$

It's worth noting that at zero temperature, the last term in the equation of $n_t$ is the so-called quantum depletion of the condensate as [21, 22]

$$n_{\mathrm{qd}}(\mathbf{r}) = \sum_j v_j^2(\mathbf{r}). \tag{3.17}$$

The chemical potential of the system, $\mu$, is to be determined by the number equation for the total number of atoms $N = N_0 + N_T$, where $N_0 = \int d^3\mathbf{r} n_0(\mathbf{r})$ and $N_T = \int d^3\mathbf{r} n_t(\mathbf{r})$.

In the uniform case ($V_{\text{ext}} = 0$), the Bogoliubov amplitudes of the quasiparticles in Eqs. (3.8) can be written as a plane-wave basis

$$u_j(\mathbf{r}) = u_{\mathbf{q}} \frac{e^{i\mathbf{q}\mathbf{r}}}{\sqrt{V}} \text{ and } v_j(\mathbf{r}) = v_{\mathbf{q}} \frac{e^{i\mathbf{q}\mathbf{r}}}{\sqrt{V}}, \tag{3.18}$$

with the quantum number $j$ becoming $\mathbf{q}$ here, and Eqs. (3.12) read in momentum space

$$\begin{bmatrix} \mathcal{L}(\mathbf{q}) & \mathcal{M} \\ \mathcal{M}^* & \mathcal{L}(\mathbf{q}) \end{bmatrix} \begin{bmatrix} u_{\mathbf{q}} \\ v_{\mathbf{q}} \end{bmatrix} = \varepsilon(\mathbf{q}) \begin{bmatrix} +u_{\mathbf{q}} \\ -v_{\mathbf{q}} \end{bmatrix}, \tag{3.19}$$

with

$$\mathcal{L}(\mathbf{q}) = \frac{\hbar^2 \mathbf{q}^2}{2m} - \mu + 2g\left(n_0 + n_t\right), \tag{3.20}$$

and

$$\mathcal{M} = g\phi^2. \tag{3.21}$$

We can numerically calculate the excitation spectrum at various values of temperatures using Eq. (3.19). It's worth noting that, there will two sets of solution for the excitation energies, i.e., positive $\varepsilon^+(\mathbf{q})$ and negative $\varepsilon^-(\mathbf{q})$, with respect to the quasiparticle momentum $\mathbf{q}$, since the Bogoliubov transformation doubles the size of Hilbert space for quasi-particles. The eigenstates with negative eigenvalues are also a group of mathematical solution but not physical. Hence in our calculations, we should physically take only the non-negative excitation energies. (see Fig. 3.1).

### At zero temperature

At zero temperature, the HFBP theory recovers the Bogoliubov theory. We start with the trivial uniform case, where the total atoms are condensate excluding quantum depletion ($n = n_0 = |\phi|^2$, $n_t = 0$), then Eq. (3.11) becomes

$$\mu\phi = gn\phi, \tag{3.22}$$

and the corresponding matrix on the left of Eqs. (3.19) becomes

$$\begin{bmatrix} \frac{\hbar^2\mathbf{q}^2}{2m} - \mu + 2gn & gn \\ gn & \frac{\hbar^2\mathbf{q}^2}{2m} - \mu + 2gn \end{bmatrix} = \begin{bmatrix} \frac{\hbar^2\mathbf{q}^2}{2m} + gn & gn \\ gn & \frac{\hbar^2\mathbf{q}^2}{2m} + gn \end{bmatrix}.$$

We can directly derive the analytic eigenvalue or excitation spectrum of the matrix, recovering the classic Bogoliubov form as

$$\varepsilon(\mathbf{q}) = \sqrt{\frac{\hbar^2\mathbf{q}^2}{2m}\left[\frac{\hbar^2\mathbf{q}^2}{2m} + 2gn\right]}, \tag{3.23}$$

with the squared Bogoliubov amplitudes

$$u_{\mathbf{q}}^2 = \frac{\hbar^2\mathbf{q}^2/(2m) + gn}{2\varepsilon(\mathbf{q})} + \frac{1}{2}, \; v_{\mathbf{q}}^2 = \frac{\hbar^2\mathbf{q}^2/(2m) + gn}{2\varepsilon(\mathbf{q})} - \frac{1}{2}. \tag{3.24}$$

Thus the quantum depletion in Eq. (3.17) can be calculated analytically as [21]

$$n_{\mathrm{qd}}^{(\mathrm{analytic})} = \frac{1}{V}\sum_{\mathbf{q}} v_{\mathbf{q}}^2 = n\frac{8}{3\sqrt{\pi}}(na^3)^{1/2}, \tag{3.25}$$

in terms of the $s$-wave scattering length $a$.

### At finite temperature

At finite temperature, in the uniform case, the Eq. (3.11) reads

$$\mu\phi = g\left(n_c + 2n_t\right)\phi, \tag{3.26}$$

and the corresponding matrix in Eqs. (3.19) becomes

$$\begin{bmatrix} \frac{\hbar^2\mathbf{q}^2}{2m} - \mu + 2g(n_c+n_t) & gn_c \\ gn_c & \frac{\hbar^2\mathbf{q}^2}{2m} - \mu + 2g(n_c+n_t) \end{bmatrix} = \begin{bmatrix} \frac{\hbar^2\mathbf{q}^2}{2m} + gn_c & gn_c \\ gn_c & \frac{\hbar^2\mathbf{q}^2}{2m} + gn_c \end{bmatrix}.$$

Here $n_c = |\phi|^2$ is the density of the condensate, and the non-condensate density $n_t \equiv \langle\hat{\eta}^\dagger\hat{\eta}\rangle$ can be calculated from Eq. (3.16) as $n_t = (1/V)\sum_{\mathbf{q}}\left[u_{\mathbf{q}}^2 + v_{\mathbf{q}}^2\right]\langle\hat{\alpha}_{\mathbf{q}}^\dagger\hat{\alpha}_{\mathbf{q}}\rangle + (1/V)\sum_{\mathbf{q}} v_{\mathbf{q}}^2$, where the occupation number of the quasiparticle at quasimomentum $\mathbf{q}$ takes the form $\langle\hat{\alpha}_{\mathbf{q}}^\dagger\hat{\alpha}_{\mathbf{q}}\rangle = 1/(e^{\beta\varepsilon_{\mathbf{q}}} - 1)$. Similar to the zero-temperature case, the analytic dispersion relation of excitation can be obtained as

$$\varepsilon(\mathbf{q}) = \sqrt{\frac{\hbar^2\mathbf{q}^2}{2m}\left[\frac{\hbar^2\mathbf{q}^2}{2m} + 2gn_c\right]}, \tag{3.27}$$

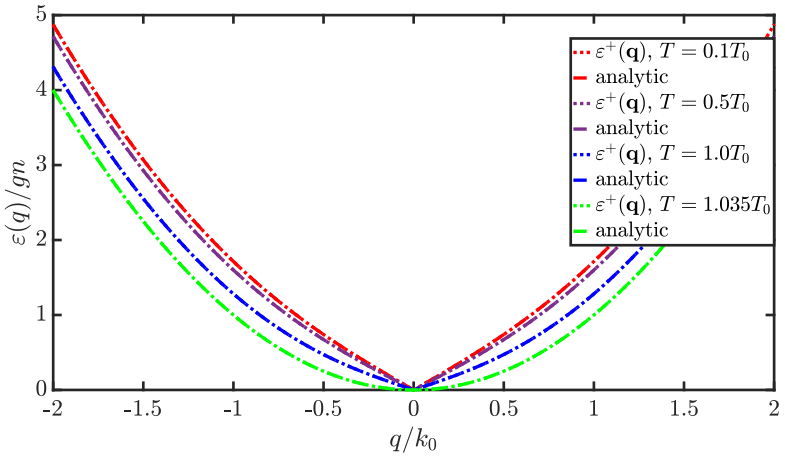


Figure 3.1: Excitation spectrum of a uniform single-component Bose gas at finite temperature. Energy and momentum are in units of the zero-temperature chemical potential $\mu = gn \equiv \frac{\hbar^2 k_0^2}{2m}$ and $k_0$, respectively. $T_0$ is the BEC temperature of an ideal Bose gas.

except that the density of the condensate $n_c$ and non-condensate density $n_t$ need to be calculated self-consistently using the coupled equations derived above. In Fig. 3.1, we show the excitation spectrum at finite temperatures calculated numerically using Eq. (3.19), denoted by $\varepsilon^+(\mathbf{q})$ in dotted curves. The analytic results, i.e., Eq. (3.27), are present in dashed lines, and coincide with the numerical ones.

By employing the above Hartree-Fock Bogoliubov method within Popov approximation for an ideal Bose gas, one recovers the BEC transition temperature $T_0$ in Eq. (1.10) derived in Sec. 1.1.1 as [10, 21]

$$k_{\mathrm{B}} T_0 = \frac{2\pi\hbar^2}{m} \left( \frac{n}{\zeta(3/2)} \right)^{2/3}, \tag{3.28}$$

as a function of the uniform density $n$ with $\zeta(3/2) \approx 2.612$. Nevertheless, in the presence of weak interactions, the transition temperature changes to

$$T_c^* = T_0 + \Delta T_c, \tag{3.29}$$

with a positive shift $\Delta T_c$ [10, 21, 160]. The leading-order shift in the limit $a \to 0$ is proportional to the gas parameter $n^{1/3}a$ as

$$\Delta T_c / T_0 \approx 1.3 \left( n^{1/3} a \right), \tag{3.30}$$

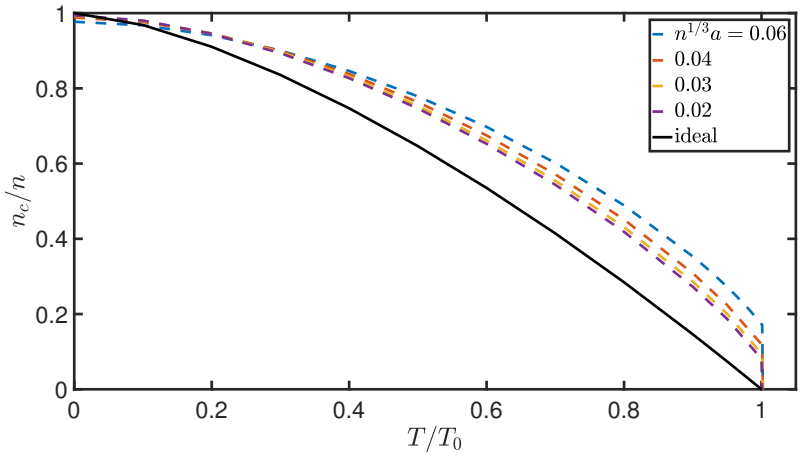


Figure 3.2: Condensate fraction $n_c/n$ at different values of the gas parameter $n^{1/3}a$. The solid line indicates $n_c/n = 1 - (T/T_0)^{3/2}$ in Eq. (1.12) for an ideal gas.

according to the most precise Monte Carlo calculations [161, 162].

The method we employed here, HFB theory with Popov approximation, is of first-order character. Hence it's not accurate enough to predict the second-order Bose-Einstein condensation for a weakly-interacting Bose gas [148, 149, 157]. Besides, the HFBP approximation gives rise to a discontinuity on the order parameter $\sqrt{n_c}$ and the density of the condensate at the transition position $T_0$, as shown in Fig. 3.2. The finite density fraction of the condensate at $T_0$ is given by [148]

$$\delta n_{\text{jump}}(T_0)/n = \frac{4\pi}{\zeta(3/2)^{4/3}} \cdot (n^{1/3}a) \tag{3.31}$$

as a function of the gas parameter $n^{1/3}a$. This finite gap or fraction in the density of the condensate indicates the break down of the first-order Popov approximation on the calculation of Bose-Einstein condensation temperature, due to the lack of non-negligible terms of the order $(gn_c)^{1/2}$ at sufficiently high temperature. The critical region is, or in another words the HFBP approximation is valid when,[148, 149]

$$T/T_0 \ll 1 - (n^{1/3}a). \tag{3.32}$$

In a dilute weakly-interacting Bose gas the typical density fraction $\delta n_{\text{jump}}(T_0)/n$ is very small due to the tiny $n^{1/3}a \ll 1$, implying a large applicable region for the HFBP approximation.

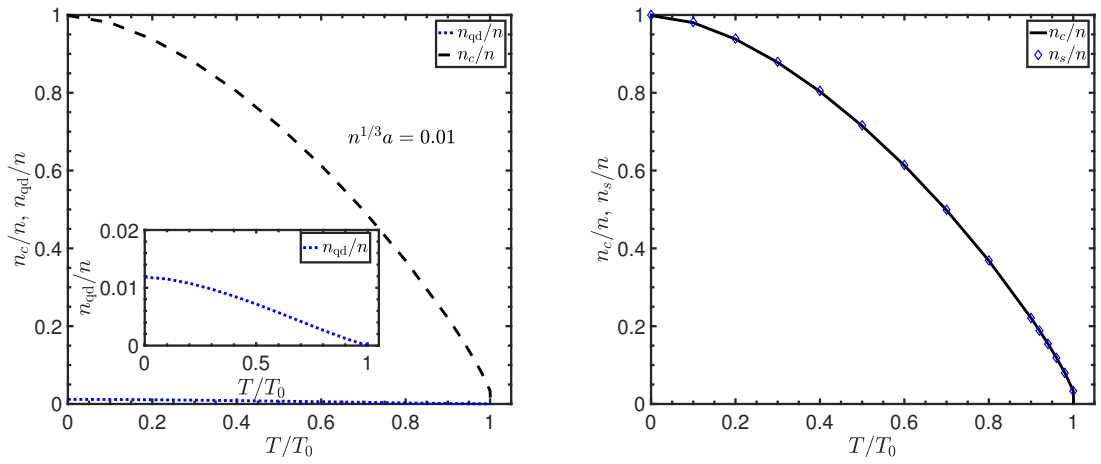


Figure 3.3: (left) condensate fraction $n_c/n$ (i.e., dashed black) and quantum depletion fraction $n_d/n$ (i.e., dotted blue). The inset zooms in on $n_d/n$. (right) the fraction of the condensate $n_c/n$, and of the superfluid $n_s/n$. Here the gas parameter is $n^{1/3}a = 0.01$.

In Fig. 3.2, by using HFBP approximation, we calculate the fraction $n_c(T)/n$ of the condensate as a function of finite temperature $T$ at various values of the gas parameter $n^{1/3}a$. As the gas parameter decreases, the finite gap at $T_0$ reduces towards zero and the condensate fraction approaches the curve of an ideal Bose gas. It's worth to mention here that, as the temperature decreases towards zero, the condensate fraction approaches to a value relatively lower than 1. This is because in the self-consistent calculations, we include the quantum depletion given in Eq. (3.25), which plays an important role at relatively low temperatures. To be explicit, for relatively smaller density $n/k_0^3$ or larger gas parameter $n^{1/3}a$, the quantum fluctuations deplete the condensate and the fraction becomes $n_c(T=0)/n = 1-8/(3\sqrt{\pi})(na^3)^{1/2}$ at zero temperature.

Furthermore, in Fig. 3.3, we take a sufficiently small $n^{1/3}a = 0.01$ of a typical dilute alkali gas, which implies a high validity of the HFBP method. Hence the quantum depletion denoted by dotted-blue line is tiny about $\sim 1\%$, leading to the negligible deviation between the condensate and superfluid fractions at finite temperature as shown in the right figure. Here the superfluid density is calculated using a phase-twist method described in Appendix C.

### 3.2.2 Two-component Bose gases

In order to generalize the HFBP approach to a two-pseudospin Raman-type spin-orbit coupled Bose gas, we can first extend the formalism described in the last section to a two-species Bose gas with a coherent coupling $h$.

The total Hamiltonian has a form of

$$\begin{aligned}\hat{\mathcal{H}}^{\mathrm{GC}} = &\int d^3\mathbf{r} \sum_{\sigma=\uparrow,\downarrow} \hat{\Phi}_\sigma^\dagger(\mathbf{r},t)(\mathcal{H}_0-\mu)\hat{\Phi}_\sigma(\mathbf{r},t) \\ &+\frac{1}{2}\int d^3\mathbf{r}\left(g\hat{\Phi}_\uparrow^\dagger\hat{\Phi}_\uparrow^\dagger\hat{\Phi}_\uparrow\hat{\Phi}_\uparrow + g\hat{\Phi}_\downarrow^\dagger\hat{\Phi}_\downarrow^\dagger\hat{\Phi}_\downarrow\hat{\Phi}_\downarrow + 2g_{\uparrow\downarrow}\hat{\Phi}_\uparrow^\dagger\hat{\Phi}_\downarrow^\dagger\hat{\Phi}_\downarrow\hat{\Phi}_\uparrow\right) \\ &+\int d^3\mathbf{r}\left(h\hat{\Phi}_\uparrow^\dagger\hat{\Phi}_\downarrow + h\hat{\Phi}_\downarrow^\dagger\hat{\Phi}_\uparrow\right),\end{aligned} \tag{3.33}$$

with the same intra-spin interaction strength $g_{\uparrow\uparrow} = g_{\downarrow\downarrow} = g$.

The Heisenberg equations of motion $i\hbar\frac{\partial\hat{\Phi}(\mathbf{r},t)}{\partial t} = \left[\hat{\Phi}(\mathbf{r},t), \hat{\mathcal{H}}^{\mathrm{GC}}\right]$ for the Bose operator fields thus give rise to

$$\begin{aligned}i\hbar\partial_t\hat{\Phi}_\uparrow &= (\mathcal{H}_0-\mu)\hat{\Phi}_\uparrow + g\hat{\Phi}_\uparrow^\dagger\hat{\Phi}_\uparrow\hat{\Phi}_\uparrow + g_{\uparrow\downarrow}\hat{\Phi}_\downarrow^\dagger\hat{\Phi}_\downarrow\hat{\Phi}_\uparrow + h\hat{\Phi}_\downarrow, \\ i\hbar\partial_t\hat{\Phi}_\downarrow &= (\mathcal{H}_0-\mu)\hat{\Phi}_\downarrow + g\hat{\Phi}_\downarrow^\dagger\hat{\Phi}_\downarrow\hat{\Phi}_\downarrow + g_{\uparrow\downarrow}\hat{\Phi}_\uparrow^\dagger\hat{\Phi}_\uparrow\hat{\Phi}_\downarrow + h\hat{\Phi}_\uparrow.\end{aligned} \tag{3.34}$$

Following the usual routine, we separate the field operator for spin-component $\sigma$ to a classic condensate field $\phi_\sigma$ and a fluctuation operator $\hat{\eta}_\sigma$ as

$$\hat{\Phi}_\sigma(\mathbf{r},t) = \phi_\sigma(\mathbf{r},t) + \hat{\eta}_\sigma(\mathbf{r},t). \tag{3.35}$$

The fluctuation operator and its conjugate can be then expanded in a quasiparticle basis ($\hat{\alpha}^\dagger$, $\hat{\alpha}$) via the Bogoliubov transformation given in Eqs. (3.8) as

$$\begin{aligned}\hat{\eta}_\sigma(\mathbf{r},t) =&\sum_j\left(u_{j\sigma}(\mathbf{r})e^{-i\varepsilon_j t}\hat{\alpha}_j + v_{j\sigma}^*(\mathbf{r})e^{i\varepsilon_j t}\hat{\alpha}_j^\dagger\right), \\ \hat{\eta}_\sigma^\dagger(\mathbf{r},t) =&\sum_j\left(v_{j\sigma}(\mathbf{r})e^{-i\varepsilon_j t}\hat{\alpha}_j + u_{j\sigma}^*(\mathbf{r})e^{i\varepsilon_j t}\hat{\alpha}_j^\dagger\right),\end{aligned} \tag{3.36}$$

for the spin-component $\sigma =\uparrow$ or $\downarrow$.

Similarly, we have the mean-field approximations of decoupling the three-operator

terms in Eq. (3.34) as

$$\begin{aligned}
\langle\hat{\Phi}^\dagger\hat{\Phi}\rangle =&|\phi|^2+\langle\hat{\eta}^\dagger\hat{\eta}\rangle,\quad \langle\hat{\Phi}\hat{\Phi}\rangle=\phi^2+\langle\hat{\eta}\hat{\eta}\rangle,\\
\hat{\Phi}^\dagger\hat{\Phi}\hat{\Phi}_\sigma =&|\phi|^2\phi+2(|\phi|^2+|\hat{\eta}|^2)\hat{\eta}+(\phi^2+\langle\hat{\eta}\hat{\eta}\rangle)\hat{\eta}^\dagger+2\phi\hat{\eta}^\dagger\hat{\eta}+\phi^\dagger\hat{\eta}\hat{\eta},\\
\langle\hat{\Phi}^\dagger\hat{\Phi}\hat{\Phi}\rangle_\sigma =&(|\phi|^2+2\langle\hat{\eta}^\dagger\hat{\eta}\rangle)\phi+\langle\hat{\eta}\hat{\eta}\rangle\phi^\dagger,\\
\hat{\Phi}^\dagger_\sigma\hat{\Phi}_\sigma\hat{\Phi}_{\sigma'} =&|\phi_\sigma|^2\phi_{\sigma'}+(|\phi_\sigma|^2+|\hat{\eta}_\sigma|^2)\hat{\eta}_{\sigma'}+(\phi^\dagger_\sigma\phi_{\sigma'}+\langle\hat{\eta}^\dagger_\sigma\hat{\eta}_{\sigma'}\rangle)\hat{\eta}_\sigma\\
&+(\phi_\sigma\phi_{\sigma'}+\langle\hat{\eta}_\sigma\hat{\eta}_{\sigma'}\rangle)\hat{\eta}^\dagger_\sigma+\phi_{\sigma'}\hat{\eta}^\dagger_\sigma\hat{\eta}_\sigma+\phi^\dagger_\sigma\hat{\eta}_\sigma\hat{\eta}_{\sigma'}+\phi_\sigma\hat{\eta}^\dagger_\sigma\hat{\eta}_{\sigma'},\\
\langle\hat{\Phi}^\dagger_\sigma\hat{\Phi}_\sigma\hat{\Phi}_{\sigma'}\rangle =&|\phi_\sigma|^2\phi_{\sigma'}+\phi_{\sigma'}|\hat{\eta}_\sigma|^2+\phi^\dagger_\sigma\langle\hat{\eta}_\sigma\hat{\eta}_{\sigma'}\rangle+\phi_\sigma\langle\hat{\eta}^\dagger_\sigma\hat{\eta}_{\sigma'}\rangle,\\
\hat{\Phi}^\dagger\hat{\Phi}\hat{\Phi}_\sigma-\langle\hat{\Phi}^\dagger\hat{\Phi}\hat{\Phi}\rangle_\sigma =&2(|\phi|^2+\langle\hat{\eta}^\dagger\hat{\eta}\rangle)\hat{\eta}+(\phi^2+\langle\hat{\eta}\hat{\eta}\rangle)\hat{\eta}^\dagger=2\langle\hat{\Phi}^\dagger\hat{\Phi}\rangle\hat{\eta}+\langle\hat{\Phi}\hat{\Phi}\rangle\hat{\eta}^\dagger,\\
\hat{\Phi}^\dagger_\sigma\hat{\Phi}_\sigma\hat{\Phi}_{\sigma'}-\langle\hat{\Phi}^\dagger_\sigma\hat{\Phi}_\sigma\hat{\Phi}_{\sigma'}\rangle =&(|\phi_\sigma|^2+\langle\hat{\eta}^\dagger_\sigma\hat{\eta}_\sigma\rangle)\hat{\eta}_{\sigma'}+(\phi^\dagger_\sigma\phi_{\sigma'}+\langle\hat{\eta}^\dagger_\sigma\hat{\eta}_{\sigma'}\rangle)\hat{\eta}_\sigma+(\phi_\sigma\phi_{\sigma'}+\langle\hat{\eta}_\sigma\hat{\eta}_{\sigma'}\rangle)\hat{\eta}^\dagger_\sigma\\
=&\langle\hat{\Phi}^\dagger_\sigma\hat{\Phi}_\sigma\rangle\hat{\eta}_{\sigma'}+\langle\hat{\Phi}^\dagger_\sigma\hat{\Phi}_{\sigma'}\rangle\hat{\eta}_\sigma+\langle\hat{\Phi}_\sigma\hat{\Phi}_{\sigma'}\rangle\hat{\eta}^\dagger_\sigma,
\end{aligned}\tag{3.37}$$

with the approximations $\hat{\eta}^\dagger_\sigma\hat{\eta}_\sigma\hat{\eta}_\sigma\simeq 2\langle\hat{\eta}^\dagger_\sigma\hat{\eta}_\sigma\rangle\hat{\eta}_\sigma+\langle\hat{\eta}_\sigma\hat{\eta}_\sigma\rangle\hat{\eta}^\dagger_\sigma$ and $\hat{\eta}^\dagger_\sigma\hat{\eta}_\sigma\hat{\eta}_{\sigma'}\simeq\langle\hat{\eta}^\dagger_\sigma\hat{\eta}_\sigma\rangle\hat{\eta}_{\sigma'}+\langle\hat{\eta}^\dagger_\sigma\hat{\eta}_{\sigma'}\rangle\hat{\eta}_\sigma+\langle\hat{\eta}_\sigma\hat{\eta}_{\sigma'}\rangle\hat{\eta}^\dagger_\sigma$.

We then sort out the equations of motion $i\hbar\partial_t\langle\hat{\Phi}_\sigma(\mathbf{r},t)\rangle=i\hbar\partial_t\phi_\sigma(\mathbf{r},t)$ for the condensate and $i\hbar\partial_t\hat{\eta}_\sigma(\mathbf{r},t)=i\hbar\partial_t(\hat{\Phi}_\sigma(\mathbf{r},t)-\phi_\sigma(\mathbf{r}))$ for the quasi-particle with the decoupling approximations given in Eqs. (3.37). By omitting the anomalous density terms $\langle\hat{\eta}_\sigma\hat{\eta}_{\sigma'}\rangle$ and $\langle\hat{\eta}^\dagger_\sigma\hat{\eta}^\dagger_{\sigma'}\rangle$, we obtain again two sets of coupled equations:

(A) a coupled Gross-Pitaevskii equation

$$\begin{aligned}
i\hbar\partial_t\phi_\uparrow(\mathbf{r},t)&=(\mathcal{H}_0-\mu)\phi_\uparrow+g(n_{c\uparrow}+2n_{t\uparrow})\phi_\uparrow+g_{\uparrow\downarrow}(n_{c\downarrow}+n_{t\downarrow})\phi_\uparrow+g_{\uparrow\downarrow}\langle\hat{\eta}^\dagger_\downarrow\hat{\eta}_\uparrow\rangle\phi_\downarrow+h\phi_\downarrow,\\
i\hbar\partial_t\phi_\downarrow(\mathbf{r},t)&=(\mathcal{H}_0-\mu)\phi_\downarrow+g(n_{c\downarrow}+2n_{t\downarrow})\phi_\downarrow+g_{\uparrow\downarrow}(n_{c\uparrow}+n_{t\uparrow})\phi_\downarrow+g_{\uparrow\downarrow}\langle\hat{\eta}^\dagger_\uparrow\hat{\eta}_\downarrow\rangle\phi_\uparrow+h\phi_\uparrow.
\end{aligned}\tag{3.38}$$

Here, the condensates occupy the zero-momentum state with real wave functions $\phi_\sigma=\phi^*_\sigma$. Thus the coupled equations can be rewritten as

$$\mu\begin{pmatrix}\phi_\uparrow\\ \phi_\downarrow\end{pmatrix}=\begin{bmatrix}\mathcal{H}_0+g(n_{c\uparrow}+2n_{t\uparrow})+g_{\uparrow\downarrow}n_\downarrow & h+g_{\uparrow\downarrow}n_{\rm sf}\\ h+g_{\uparrow\downarrow}n_{\rm sf} & \mathcal{H}_0+g(n_{c\downarrow}+2n_{t\downarrow})+g_{\uparrow\downarrow}n_\uparrow\end{bmatrix}\begin{pmatrix}\phi_\uparrow\\ \phi_\downarrow\end{pmatrix},\tag{3.39}$$

(B) a coupled Bogoliubov equations similar to Eq. (3.12)

$$\begin{bmatrix}\mathcal{L} & \mathcal{M}\\ \mathcal{M}^* & \mathcal{L}\end{bmatrix}\begin{bmatrix}U_j(\mathbf{r})\\ V_j(\mathbf{r})\end{bmatrix}=\varepsilon_j\begin{bmatrix}+U_j(\mathbf{r})\\ -V_j(\mathbf{r})\end{bmatrix},\tag{3.40}$$

but with different elements defined as

$$\mathcal{L} = \begin{pmatrix} \mathcal{H}_0 - \mu + 2gn_\uparrow + g_{\uparrow\downarrow}n_\downarrow & h + g_{\uparrow\downarrow}(\phi_\downarrow^*\phi_\uparrow + n_{\rm sf}) \\ h + g_{\uparrow\downarrow}(\phi_\uparrow^*\phi_\downarrow + n_{\rm sf}) & \mathcal{H}_0 - \mu + 2gn_\downarrow + g_{\uparrow\downarrow}n_\uparrow \end{pmatrix}, \tag{3.41}$$

$$\mathcal{M} = \begin{pmatrix} g\phi_\uparrow^2 & g_{\uparrow\downarrow}\phi_\downarrow\phi_\uparrow \\ g_{\uparrow\downarrow}\phi_\uparrow\phi_\downarrow & g\phi_\downarrow^2 \end{pmatrix}, \tag{3.42}$$

$$U_j(\mathbf{r}) = (u_{j\uparrow}(\mathbf{r}),\ u_{j\downarrow}(\mathbf{r}))^T \text{ and } V_j(\mathbf{r}) = (v_{j\uparrow}(\mathbf{r}),\ v_{j\downarrow}(\mathbf{r}))^T. \tag{3.43}$$

In the equations, we have introduced the relevant densities $n_{c\sigma} = \langle\phi_\sigma^\dagger\phi_\sigma\rangle$, $n_{t\sigma} = \langle\hat{\eta}_\sigma^\dagger\hat{\eta}_\sigma\rangle$ and $n_\sigma = n_{c\sigma} + n_{t\sigma}$ as the density of the condensate, non-condensate density and the total density for spin-component $\sigma$, respectively. Besides, $n_{\rm sf} = \langle\hat{\eta}_\uparrow^\dagger\hat{\eta}_\downarrow\rangle$ is the spin-flip density of the fluctuation operator, which becomes non-negligible and plays an important role at large enough temperatures.

The coupled equations described above are self-consistent and can be calculated numerically as shown in the single-component case. In a uniform gas ($V_{\rm ext} = 0$), the Bogoliubov amplitudes of the quasiparticles for spin $\sigma$ in Eq. (3.35) can be written again in a plane-wave basis as

$$u_{j\sigma}(\mathbf{r}) = u_{\sigma\mathbf{q}}\frac{e^{i\mathbf{qr}}}{\sqrt{V}} \text{ and } v_{j\sigma}(\mathbf{r}) = v_{\sigma\mathbf{q}}\frac{e^{i\mathbf{qr}}}{\sqrt{V}}. \tag{3.44}$$

We can define

$$U_\mathbf{q} = (u_{\uparrow\mathbf{q}},\ u_{\downarrow\mathbf{q}})^T \text{ and } V_\mathbf{q} = (v_{\uparrow\mathbf{q}},\ v_{\downarrow\mathbf{q}})^T, \tag{3.45}$$

and Eqs. (3.40) read in momentum space

$$\begin{bmatrix} \mathcal{L}(\mathbf{q}) & \mathcal{M} \\ \mathcal{M}^* & \mathcal{L}(\mathbf{q}) \end{bmatrix} \begin{bmatrix} U_\mathbf{q} \\ V_\mathbf{q} \end{bmatrix} = \varepsilon(\mathbf{q}) \begin{bmatrix} +U_\mathbf{q} \\ -V_\mathbf{q} \end{bmatrix}, \tag{3.46}$$

with the same $\mathcal{M}$ and

$$\mathcal{L}(\mathbf{q}) = \begin{pmatrix} \frac{\hbar^2\mathbf{q}^2}{2m} - \mu + 2gn_\uparrow + g_{\uparrow\downarrow}n_\downarrow & h + g_{\uparrow\downarrow}(\phi_\downarrow^*\phi_\uparrow + n_{\rm sf}) \\ h + g_{\uparrow\downarrow}(\phi_\uparrow^*\phi_\downarrow + n_{\rm sf}) & \frac{\hbar^2\mathbf{q}^2}{2m} - \mu + 2gn_\downarrow + g_{\uparrow\downarrow}n_\uparrow \end{pmatrix}. \tag{3.47}$$

We can numerically diagonalize the new matrix on the left of Eq. (3.46), and obtain two physical branches of excitation energy $\varepsilon_\pm(\mathbf{q})$ (see Fig. 3.4) with the corresponding Bogoliubov wave functions $u_{\sigma\mathbf{q}}$ and $v_{\sigma\mathbf{q}}$ at the quasiparticle momentum $\mathbf{q}$.

**At zero temperature**

At zero temperature, the excitation spectrum of the system with the Hamiltonian given in Eq. (3.33) can be obtained analytically, as shown in Ref. [163]. If the condition of the interaction strengths[1]

$$g_{\uparrow\downarrow} < g + 2h/n \tag{3.48}$$

is satisfied, the corresponding excitation spectrum exhibits the helicity in a form of

$$\begin{aligned}
\omega_1 &= \sqrt{\frac{\hbar^2\mathbf{q}^2}{2m}\left[\frac{\hbar^2\mathbf{q}^2}{2m} + (g + g_{\uparrow\downarrow})n\right]}, \\
\omega_2 &= \sqrt{\frac{\hbar^2\mathbf{q}^2}{2m}\left[\frac{\hbar^2\mathbf{q}^2}{2m} + (g - g_{\uparrow\downarrow})n + 4h\right] + 2h\left[(g - g_{\uparrow\downarrow})n + 2h\right]}.
\end{aligned} \tag{3.49}$$

It's straightforward to see that, in the limit of zero coherent coupling $h \to 0$, $\omega_2$ becomes the usual expression as

$$\omega_2^{(h\to 0)} = \sqrt{\frac{\hbar^2\mathbf{q}^2}{2m}\left[\frac{\hbar^2\mathbf{q}^2}{2m} + (g - g_{\uparrow\downarrow})n\right]}. \tag{3.50}$$

By employing the HFBP formalism in the limit of zero temperature $T \to 0$, we self-consistently calculate the excitation energy $\varepsilon_\pm$ using Eq. (3.46) at various values of the coherent coupling strength $h$. The energy spectra are shown in Fig. 3.4, where we set $T = 10^{-4}T_0$ in the realistic calculations. The numerical results are depicted in solid blue and red curves, and agree exactly with the corresponding analytic expressions $\omega_{1,2}$ at zero temperature given in Eqs. (3.49) denoted by the colorful symbols '+' and 'o' respectively.

In detail, the intra-species and inter-species interaction strength are set to be zero in the upper panel. The lower branch $\varepsilon_-$ of the spectra is independent of $h$ and exhibits the parabolic behaviour of a free particle, while the higher $\varepsilon_+$ has a finite energy gap increasing with the coupling strength $h$. In the lower panel, the interaction strengths are nonzero, i.e., $g/g_{\uparrow\downarrow} = 0.8/0.5$. In the presence of

[1]This is the regime we concentrate in the case with spin-orbit coupling where all three generic phases exist.

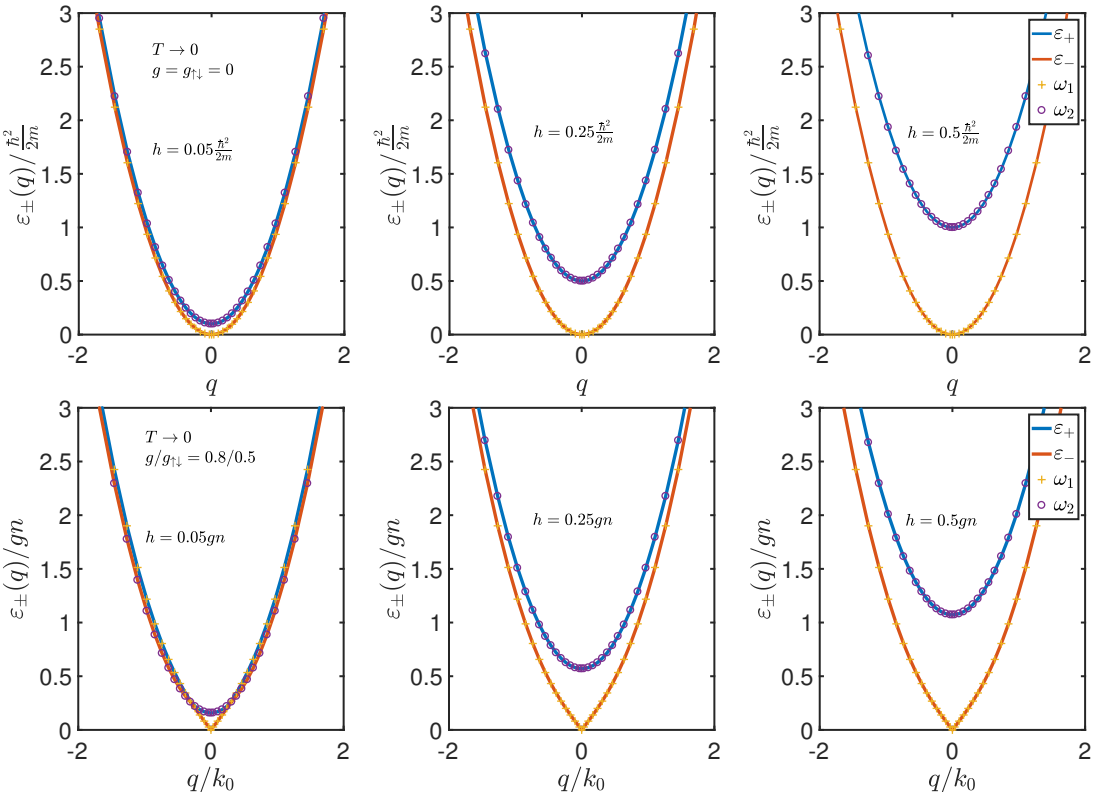


Figure 3.4: Excitation spectra at various values of the coherent strength $h$ in the limit $T \to 0$, obtained by the HFBP approximation in solid lines, and from Eqs. (3.49) denoted by the symbols. The interaction strengths are $g = g_{\uparrow\downarrow} = 0$ (upper) and $g/g_{\uparrow\downarrow} = 0.8/0.5$ (lower).

interactions, the lower branch $\varepsilon_-$ becomes distinct to the one without interactions, and it exhibits the linear phonon mode in the long-wavelength limit ($\mathbf{q} \to 0$) as in usual weakly interacting Bose gases. The higher branch $\varepsilon_+$ remains parabola-like with a increasing energy gap with $h$, similar to the one in the upper panel.

### 3.2.3 In the presence of spin-orbit coupling

It's straightforward to generalize the two-component case to the Bose gas with Raman-type spin-orbit coupling (SOC), except that the condensates can occupy a finite-momentum state due to the unique double-minimum single-particle dispersion, see in Sec. 2.2. We recall the Hamiltonian of a three-dimensional weakly interacting

Bose gas with the Raman-type SOC as

$$\hat{H} = \int d^3\mathbf{r}\hat{\Psi}^\dagger(\hat{\mathbf{r}})\mathcal{H}^{\mathrm{SOC}}\hat{\Psi}(\mathbf{r}) + \hat{H}_{\mathrm{int}}, \tag{3.51}$$

with the spinor function $\hat{\Psi}(\mathbf{r}) \equiv \left(\hat{\Phi}_\uparrow(\mathbf{r}),\ \hat{\Phi}_\downarrow(\mathbf{r})\right)^T$. The single-particle Hamiltonian $\mathcal{H}^{\mathrm{SOC}}$ in Eq. (2.8) and the interaction $\hat{H}_{\mathrm{int}}$ in Eq. (2.13) are written as

$$\begin{aligned}\mathcal{H}^{\mathrm{SOC}} =& \frac{\hbar^2(\hat{\mathbf{p}} - k_{\mathrm{r}}\hat{\mathbf{e}}_x\sigma_z)^2}{2m} + \hbar\frac{\delta}{2}\sigma_z + \hbar\frac{\Omega}{2}\sigma_x,\\ \hat{H}_{\mathrm{int}} =& \frac{1}{2}\int \mathrm{d}^3\mathbf{r} \sum_{\sigma,\sigma'=\uparrow,\downarrow} g_{\sigma\sigma'}\hat{\Phi}^\dagger_\sigma\hat{\Phi}^\dagger_{\sigma'}\hat{\Phi}_{\sigma'}\hat{\Phi}_\sigma(\mathbf{r}),\end{aligned} \tag{3.52}$$

with the canonical momentum operator $\hat{\mathbf{p}} = -i\nabla$ and Pauli matrices $\sigma_x$, $\sigma_z$. It's worth noting that, due to the SOC, the physical momentum are modulated to $\hat{\mathbf{p}} \mp k_{\mathrm{r}}\hat{\mathbf{e}}_x$ for pseudospin-up and pseudospin-down atoms, respectively. $g_{\sigma\sigma'} = 4\pi\hbar^2 a_{\sigma\sigma'}/m$ are interaction strengths for intra- ($\sigma = \sigma'$) and inter-species ($\sigma \neq \sigma'$), and $a_{\sigma\sigma'}$ are the corresponding $s$-wave scattering lengths. $k_{\mathrm{r}}\hat{\mathbf{e}}_x$ is the recoil momentum of the Raman lasers along the $x$-axis, with the corresponding recoil energy $E_{\mathrm{r}} = \hbar^2 k_{\mathrm{r}}^2/(2m)$. The detuning of the Raman lasers is assumed to be zero $\delta = 0$ and the Rabi frequency $\Omega$ can be flexibly tuned over a range, in accord with the recent experiments [14, 105]. We have shown in Sec. 2.3 that the inequality of intra-spin and inter-spin interactions $G_2 > 0$, is essential to the emergence of all three generic phases, particularly the spin-mixed stripe phase [95, 164]. Hence we will set $g_{\uparrow\uparrow} = g_{\downarrow\downarrow} = g > g_{\uparrow\downarrow}$ in the following investigations.

In the zero-temperature limit, the quasiparticle formalism in the Bogoliubov approximation level can be well applied to study the system with SOC, which can well describe the weakly-interacting dilute Bose gases at extremely low temperatures [10, 21]. To study the related physical properties of these systems at relatively high temperature, we generalize a Hartree-Fock-Bogoliubov theory [156, 157, 159] with Popov approximation [158] (HFBP) from the last section.

Following the conventional procedures described in the subsections 3.2.1 and 3.2.2, the Bose field operator $\hat{\Phi}_\sigma(\mathbf{r}, t)$ for spin component $\sigma = \uparrow, \downarrow$ can be rewritten as a combination of condensate wave function $\phi_\sigma$ and the non-condensate fluctuation

operator $\hat{\eta}_\sigma$ as

$$\begin{aligned}\hat{\Phi}_\sigma(\mathbf{r},t) =&\phi_\sigma(\mathbf{r},t)+\hat{\eta}_\sigma(\mathbf{r},t)\\ =&\phi_\sigma+\sum_j\left(u_{j\sigma}(\mathbf{r})e^{-i\varepsilon_j t}\hat{\alpha}_j+v^*_{j\sigma}(\mathbf{r})e^{i\varepsilon_j t}\hat{\alpha}^\dagger_j\right),\end{aligned} \tag{3.53}$$

where the fluctuation is expanded in a quasiparticle basis $(\hat{\alpha}^\dagger, \hat{\alpha})$ with the quasiparticle amplitudes $u(u^*)$, $v(v^*)$ and the quasiparticle frequency $\varepsilon_j$.

After substituting the new Bose field operators, Eqs. (3.53), into the equations of motion $i\partial_t\hat{\Phi}_\sigma(\mathbf{r},t) = \left[\hat{\Phi}_\sigma, \hat{H}\right]$, and then applying the mean-field decoupling of three operators [157], we recover two coupled equations similar to the usual two-component case in Sec. 3.2.2.

(A) The first is the modified Gross-Pitaevskii equation for the condensate

$$\left[\mathcal{H}^{\mathrm{SOC}}+g_{\uparrow\downarrow}n_{\mathrm{sf}}\sigma_x+\mathrm{diag}(\mathcal{L}_\uparrow,\mathcal{L}_\downarrow)\right]\phi=\mu\phi \tag{3.54}$$

with the spinor $\phi\equiv(\phi_\uparrow(\mathbf{r}),\phi_\downarrow(\mathbf{r}))^T$, the chemical potential $\mu$, the spin-flip terms $n_{\mathrm{sf}}$ and the diagonal element (here $\bar{\sigma}$ indicates a spin index different with $\sigma$.)

$$\mathcal{L}_\sigma\equiv g(n_{c\sigma}+2n_{t\sigma})+g_{\uparrow\downarrow}n_{\bar{\sigma}}. \tag{3.55}$$

(B) The other is the coupled Bogoliubov equation for the quasiparticles,

$$\left[\mathcal{H}^{\mathrm{SOC}}-\mu+\mathcal{A}_\uparrow\right]U_j+\mathcal{B}V_j = \varepsilon_jU_j, \tag{3.56a}$$

$$-\mathcal{B}U^*_j-\left[\mathcal{H}^{\mathrm{SOC}}-\mu+\mathcal{A}_\downarrow\right]V^*_j = \varepsilon_jV^*_j, \tag{3.56b}$$

where $U_j\equiv(u_{j\uparrow}(\mathbf{r}),u_{j\downarrow}(\mathbf{r}))^T$, $V_j\equiv(v_{j\uparrow}(\mathbf{r}),v_{j\downarrow}(\mathbf{r}))^T$, and

$$\mathcal{A}_\sigma\equiv\begin{bmatrix}2gn_\uparrow+g_{\uparrow\downarrow}n_\downarrow & g_{\uparrow\downarrow}\left(\phi_\sigma\phi^*_{\bar{\sigma}}+n_{\mathrm{sf}}\right)\\ g_{\uparrow\downarrow}\left(\phi_{\bar{\sigma}}\phi^*_\sigma+n_{\mathrm{sf}}\right) & 2gn_\downarrow+g_{\uparrow\downarrow}n_\uparrow\end{bmatrix}, \tag{3.57a}$$

$$\mathcal{B}\equiv\begin{bmatrix}g\phi^2_\uparrow & g_{\uparrow\downarrow}\phi_\uparrow\phi_\downarrow\\ g_{\uparrow\downarrow}\phi_\uparrow\phi_\downarrow & g\phi^2_\downarrow\end{bmatrix}. \tag{3.57b}$$

We have introduced again the corresponding density of the condensate $n_{c\sigma}\equiv\langle\phi^\dagger_\sigma\phi_\sigma\rangle$, fluctuation density $n_{t\sigma}\equiv\langle\hat{\eta}^\dagger_\sigma\hat{\eta}_\sigma\rangle$ and total density $n_\sigma=n_{c\sigma}+n_{t\sigma}$ for spin-component $\sigma$. In terms of the Bogoliubov wavefunctions $u(v)$, the non-condensate

density $n_{t\sigma}$ of spin $\sigma$ and the spin-flip term $n_{\rm sf}$ can be written explicitly as

$$\begin{aligned} n_{t\sigma} \equiv & \langle \hat{\eta}_\sigma^\dagger \hat{\eta}_\sigma \rangle = \sum_j \left[ (|u_{j\sigma}|^2 + |v_{j\sigma}|^2) \langle \hat{\alpha}_j^\dagger \hat{\alpha}_j \rangle + |v_{j\sigma}|^2 \right] \\ n_{\rm sf} \equiv & \langle \hat{\eta}_\sigma^\dagger \hat{\eta}_{\bar{\sigma}} \rangle = \sum_{j,\sigma\neq\bar{\sigma}} \left[ (u_{j\sigma}^* u_{j\bar{\sigma}} + v_{j\bar{\sigma}}^* v_{j\sigma}) \langle \hat{\alpha}_j^\dagger \hat{\alpha}_j \rangle + v_{j\bar{\sigma}}^* v_{j\sigma} \right], \end{aligned} \tag{3.58}$$

where $N_j \equiv \langle \hat{\alpha}_j^\dagger \hat{\alpha}_j \rangle$ is occupation number of the quasiparticles in $j$-th excited state, taking Bose-Einstein statistics as a function of the excitation energy $\varepsilon_j$ as $N_j = 1/(e^{\beta\varepsilon_j} - 1)$.

At zero temperature $T = 0$, after solving the relevant GP and Bogoliubov equations self-consistently, Eqs. (3.54) and (3.56), one can obtain straightforwardly the ground-state wave function $\phi(\mathbf{r})$ with respect to the Rabi frequency $\Omega$, as well as the corresponding Bogoliubov excitation spectrum $\varepsilon_j$. When we introduce thermal fluctuations at a nonzero temperature $T \neq 0$, the condensation phase and the corresponding excitation spectrum can be determined using the same approach. The properties of this system with the Raman-type SOC will be studied in detail at zero and nonzero temperatures in the next two chapters, Chaps. 4 and 5.

## 3.3 Application to one-dimensional Bose gases in harmonic traps

Many-particle systems in one dimension (1D) with a short-range interparticle interaction play an important role in understanding fascinating quantum many-body physics [165, 166]. For instance, a 1D interacting Bose gas is theoretically anticipated to experience different phases by changing interaction strength and temperature, and to exhibit a number of intriguing phenomena, such as effective fermionization and nontrivial quench dynamics [165, 166]. Since the realization of Bose-Einstein condensation in 1995, more and more experiments have dealt with 1D atomic bosons in a harmonic trap at ultra-cold temperature, which can help test theoretical predictions and understand all these unusual phenomena. At present, many experiments have been conducted and controlled by means of Feshbach resonances [12] or directly heating 1D quantum degenerate Bose gases [167], which measured and characterized various physical quantities, including momentum distribution [168], pair correlation [169] and quenching rate [170, 171]. Motivated by these rapid experimental advances, there are numerous theoretical studies based on sum-rule approach [172], variational method [173], local density approximation [11] and diffusion Monte Carlo simulations [174]. Experimental measured quantities, particularly momentum distribution [175] and pair correlation [176–178], have been predicted and compared with experimental data.

In the recent experiment [12], the Feshbach resonance technique is used to tune the interatomic interaction of a 1D Bose gas in a harmonic trap at extremely low temperature. The measured ratio of squared breathing mode frequency $\omega_{\mathrm{m}}^2/\omega_{\mathrm{ho}}^2$ exhibits a reentrant behaviour, from 4 in the non-interacting regime to 3 in the weakly interacting regime, and then back to 4 in the Tonks-Girardeau regime [63]. Most recently, this interesting reentrant behaviour was addressed by two theoretical works based on simulations at zero temperature [11, 174]. Choi and coworkers used a time-dependent modified nonlinear Schrödinger equation (m-NLSE) with a local chemical potential replacing the conventional nonlinear term [11]. Gudyma and collaborators combined a sum-rule approach in the mean-field regime and the local density approximation in the Tonks-Girardeau regime to describe the breathing mode [174].

Diffusion Monte Carlo simulations for few particle numbers were performed, in order to obtain density profiles as inputs to the sum-rule approach. Comparing all results together, we find that there are still deviations between experimental data and theoretical predictions, particularly in the deep weakly-interacting regime.

By considering *finite particle number* (i.e., varying in a range of $8 \sim 25$) and unavoidable *nonzero temperature* in the realistic experiment [12], we therefore would like to address in a more systematic way their effects on collective mode frequencies of a 1D trapped Bose gas. We note that, at large number of particles, the temperature dependence of mode frequencies has been recently investigated by using a hydrodynamic theory [173].

In this section, we investigate an interacting Bose gas confined in a 1D harmonic trap and study the low-lying collective-mode frequencies for a wide range of effective interaction parameter $\gamma_{\rm eff}$, covering all interaction regimes from the ideal noninteracting regime to the mean-field Thomas-Fermi regime and to the strongly interacting Tonks-Girardeau regime, by developing a generalized Bogoliubov theory at $T = 0$ and a Hartree-Fock-Bogoliubov theory with Popov approximation at finite temperature $T \neq 0$ depicted in Sec. 3.2.1.

The former theory concentrates on the zero-temperature case, where we follow the idea of the density-functional approach, use a generalized Gross-Pitaevskii equation, and take the local chemical potential for uniform density obtained from the Lieb-Liniger model as the exchange energy (i.e., the nonlinear term) [179, 180]. In the latter theory, the finite-temperature effect is taken into account through the self-consistent Hartree-Fock-Bogoliubov equations in the weakly interacting regime. By emphasizing the effects of finite particle number and nonzero temperature collective-mode frequencies, we compare our results with the experimental measurement [12] and the previous theoretical prediction [11].

### 3.3.1 Theoretical Framework: 1D atomic Bose gases

**$T = 0$ : A density functional method with Lieb-Liniger integrals**

We start with a 1D atomic Bose gas with a repulsive zero-range potential. The system of $N$ particles can be described with the Lieb-Liniger Hamiltonian [181, 182],

$$\mathcal{H} = -\frac{\hbar^2}{2m}\sum_{i=1}^{N}\frac{\partial^2}{\partial x_i^2} + g_{\text{1D}}\sum_{i<j}^{N}\delta(x_i - x_j), \tag{3.59}$$

where $m$ is the mass of atom and $g_{\text{1D}}$ is the 1D interaction strength of form

$$g_{\text{1D}} = \frac{2\hbar^2}{m a_{\text{1D}}}, \tag{3.60}$$

characterizing the interaction between bosons. $a_{\text{1D}}$ is the 1D scattering length calculated by [183]

$$a_{\text{1D}} = -\frac{a_\perp^2}{2a_{\text{3D}}}\left[1 - \mathcal{C}\frac{a_{\text{3D}}}{a_\perp}\right], \tag{3.61}$$

where $a_{\text{3D}}$ is the three-dimensional (3D) scattering length, $a_\perp = [\hbar/(m\omega_\perp)]^{1/2}$ is a two-dimensional (2D) harmonic oscillator characteristic length (see below) and the constant $\mathcal{C} \simeq 1.4603$. Experimentally, systems of 1D Bose gases are usually trapped in a cylindrically symmetric potential with strong transverse confinement and weak longitudinal confinement (i.e., with trapping frequencies $\omega_\perp \gg \omega_x$). Transverse excitations are not taken into account if the transverse vibrational energy $\hbar\omega_\perp$ is much greater than the chemical potential or the energy scale of the thermal cloud ($\hbar\omega_\perp \gg \mu, k_{\text{B}}T$) [12, 167–170]. However, the scattering of two atoms in the lowest transverse mode could strongly be affected by high transverse excitations, when the 3D scattering length $a_{\text{3D}}$ is close to the 2D harmonic oscillator length $a_\perp$. This leads to a confinement-induced Feshbach resonance, as can be seen in Eq. (3.61).

**Lieb-Liniger model** Lieb and Liniger investigated this 1D system at $T = 0$ and solved it exactly in 1960s. They dealt with the Hamiltonian (3.59) and the associated Schrödinger equation by means of Bethe ansatz [184], and obtained exactly the ground state as well as low-lying excited states in a uniform gas with a constant density $n = N/V$ [181, 182].

In the Lieb-Liniger model, they defined a dimensionless interaction parameter $\gamma(n)$ as a function of $g_{\text{1D}}$, which is

$$\gamma(n) \equiv \frac{mg_{\text{1D}}}{\hbar^2 n} = \frac{2}{na_{\text{1D}}}. \tag{3.62}$$

By solving exactly the Hamiltonian, they got a group of integral equations (i.e., Lieb-Liniger integrals), including the normalization condition and the equation of the ground state energy. The ground state energy has the form

$$E_0 = \frac{N\hbar^2 n^2}{2m} e(\gamma), \tag{3.63}$$

where $e(\gamma)$ is a dimensionless function of $\gamma$, which can be obtained by solving the following Lieb-Liniger integrals,

$$\begin{aligned} g(x) &= \frac{1}{2\pi} + \frac{1}{2\pi}\int_{-1}^{1} \frac{2\lambda}{(x-x')^2+\lambda^2} g(x')dx', \\ \lambda &= \gamma \int_{-1}^{1} g(x)dx, \\ e(\gamma) &= (\frac{\gamma}{\lambda})^3 \int_{-1}^{1} x^2 g(x)dx. \end{aligned} \tag{3.64}$$

In the integrals, $g(x)$ is the distribution function of the quasi-momentum, which is represented by the variable $x$ after a rescaling [181]. Thus, the variables $x, x'$ are all bounded in the range $[-1, 1]$, as shown in the upper and lower limits of the integrals. Variable $\lambda$ is proportional to $\gamma$ since the remaining integral part in $\lambda$ is fixed. Hence, $\lambda$ is also proportional to the interaction strength $g_{\text{1D}}$ for a fixed uniform density $n$.

By numerically solving the integrals, it can be shown that $e(\gamma)$ is a monotonically increasing function of $\gamma$ [181]. In the limit of $\gamma = 0$, $e(0) = 0$ and the ground state energy is $E_0 = 0$, corresponding to the case that all free bosons occupy the zero-momentum state. When $\gamma$ is sufficiently large, the asymptotic value of $e(\gamma)$ is $\pi^2/3$, which exactly coincides the predicted value for impenetrable bosons in 1D by Girardeau [63]. All the information of the ground state of 1D Bose gas can then be calculated from $e(\gamma)$. The energy per particle at the ground state is $\epsilon(n) = E_0/N = \hbar^2 n^2 e(\gamma)/(2m)$, and the corresponding chemical potential $\mu(n)$ is given by

$$\mu(n) = \frac{\partial(n\epsilon(n))}{\partial n} = \frac{\hbar^2 n^2}{2m}\mu(\gamma). \tag{3.65}$$

It is straightforward to see that the dimensionless chemical potential $\mu(\gamma)$ can be calculated by

$$\mu(\gamma) = 3e(\gamma) - \gamma e'(\gamma). \tag{3.66}$$

In Ref. [11], Choi and coworkers proposed the following analytic expression for the chemical potential at large $\gamma$,

$$\mu(n) \approx \frac{\pi^2}{2}\frac{\hbar^2 n^2}{m}\left[\frac{\gamma^2(n)(2+3\gamma(n))}{3(2+\gamma(n))^3}\right], \tag{3.67}$$

near the Tonks-Girardeau limit. Compared with the numerical results of Lieb-Liniger integrals, this expression turns out to be very accurate, as long as $\gamma$ is larger than 10.

**Generalized Gross-Pitaevskii theory** The Gross-Pitaevskii theory provides a good description of weakly-interacting atomic Bose-Einstein condensates at $T = 0$. However, it is known that the theory fails in low dimensions ($d \leq 2$) and therefore needs appropriate modifications. In Ref. [185], Kolomeisky and coworkers suggested an interesting modification in the Tonks-Girardeau limit for 1D trapped Bose gases. Here, we generalize their idea to all interaction strengths, following the procedure of using an improved exchange energy in the density-function approach.

Recall that the standard Gross-Pitaevskii equation with a condensate order parameter (wavefunction) $\Psi(x,t)$ is given by

$$i\hbar\frac{\partial\Psi(x,t)}{\partial t} = \left[\mathcal{H}_0 + g_{\text{1D}}n(x,t)\right]\Psi(x,t) \tag{3.68}$$

with the single particle Hamiltonian

$$\mathcal{H}_0 = -\frac{\hbar^2}{2m}\frac{\partial^2}{\partial x^2} + V_{\text{ext}}(x), \tag{3.69}$$

where $V_{\text{ext}}(x) = \frac{1}{2}m\omega_{\text{ho}}^2 x^2$ is the harmonic trapping potential and $n(x,t) = |\Psi(x,t)|^2$ is the particle density. The Hartree term $g_{\text{1D}}n(x,t)$ in Eq. (3.68) is only applicable in the weak coupling regime.

Away from the weak coupling regime ($na_{\text{1D}} \gg 1$ or $\gamma \ll 1$), we may use local density approximation (LDA) to determine the ground state of a trapped system. The LDA amounts to setting,

$$\mu = \mu_{\text{loc}}(n(x)) + V_{\text{ext}}(x), \tag{3.70}$$

with $\mu$ being the global chemical potential. Once we know the local chemical $\mu_{\rm loc}(n)$ for a uniform Bose gas from the Lieb-Liniger model, we can then determine the density profile $n(x)$ by inversely solving Eq. (3.70). The important observation made by Kolomeisky and coworkers is that in the Tonks-Girardeau limit, one may simply obtain a modified Gross-Pitaevskii equation by using $\mu_{\rm loc}(n) = \pi^2\hbar^2n^2/2m$ to replace the Hartree term $g_{\rm 1D}n$ [185]. Motivated by this work, one can use $\mu_{\rm loc}(n)$ calculated numerically in the Lieb-Liniger model, to obtain the corresponding result in the intermediate regime between the mean-field limit and the Tonks-Girardeau limit.

Modifying the interaction term $g_{\rm 1D}n$ to the local chemical potential $\mu_{\rm loc}(n)$, the generalized Gross-Pitaevskii equation reads,

$$i\hbar\frac{\partial\Psi(x,t)}{\partial t} = \left[\mathcal{H}_0 + \mu_{\rm loc}\left(n(x,t)\right)\right]\Psi(x,t), \tag{3.71}$$

which has the same form as the m-NLSE equation adopted by Choi and coworkers [11].

The idea of directly modifying the exchange-energy-like term at zero temperature is supported by the following derivation of the hydrodynamic equation. That is, we rewrite the order parameter as

$$\Psi(x,t) = n^{\frac{1}{2}}(x,t)e^{i\theta(x,t)}, \tag{3.72}$$

where $n(x,t)$ is now interpreted as the time-dependent *superfluid density* of the system and $\theta(x,t)$ is the associated phase. We therefore introduce a superfluid velocity field $\mathbf{v}(x,t) = \frac{\hbar}{m}\frac{\partial\theta(x,t)}{\partial x}\mathbf{e}_x$ and rewrite the generalized Gross-Pitaevskii equation in terms of the superfluid density $n(x,t)$ and superfluid velocity $\mathbf{v}(x,t)$:

$$\begin{aligned} m\frac{\partial\mathbf{v}}{\partial t} + \frac{\partial}{\partial x}(\mu_{\rm loc}(n) + V_{\rm ext}(x) + \frac{1}{2}m\mathbf{v}^2) = 0, \\ \frac{\partial n}{\partial t} + \frac{\partial}{\partial x}(n\mathbf{v}) = 0. \end{aligned} \tag{3.73}$$

Here we have neglected a quantum pressure term, which is small in the long wave-length limit. Thus, it is clear that our generalized Gross-Pitaevskii equation is identical to the standard 1D time-dependent hydrodynamic equations in the long wave-length limit. For a finite particle number system, it is preferable to use the

generalized Gross-Pitaevskii equation to understand the dynamics of interacting 1D Bose gases. The effect of finite particle number is taken into account by the quantum pressure term that is neglected in the hydrodynamic equations.

**Generalized Bogoliubov theory** We now consider excited states of 1D Bose gases, which can be treated as small oscillations around the superfluid density at the ground state (i.e., $\phi_0(x)$) with frequencies $\omega_j$. Their wavefunctions, $u_j$ and $v_j$, are given by [10],

$$\Psi(x,t) = e^{-i\mu t/\hbar}\left[\phi_0(x) + u_j(x)e^{-i\omega_j t/\hbar} + v_j^*(x)e^{i\omega_j t/\hbar}\right]. \tag{3.74}$$

The corresponding density $n = |\Psi(x,t)|^2$ is

$$n = |\phi_0|^2 + \left[\phi_0^*(u_j e^{-i\omega_j t/\hbar} + v_j^* e^{i\omega_j t/\hbar}) + \text{H.c.}\right], \tag{3.75}$$

where we keep only the linear terms in the complex functions $u_j$ and $v_j$. Accordingly, the local chemical potential $\mu_{\text{loc}}(n)$ can be written as

$$\mu_{\text{loc}}(n) = \mu_{\text{loc}}(n_0) + \frac{\partial \mu_{\text{loc}}}{\partial n}\left[e^{-i\omega_j t/\hbar}(\phi_0^* u_j + \phi_0 v_j) + \text{H.c.}\right] \tag{3.76}$$

in the Taylor expansion with $n_0(x) = |\phi_0(x)|^2$, where higher orders are neglected. Taking Eqs. (3.74) and (3.76) back into Eq. (3.71) and sorting out the terms in $e^{-i\mu t/\hbar}$, $e^{-i(\mu+\hbar\omega_j)t/\hbar}$, $e^{-i(\mu-\hbar\omega_j)t/\hbar}$, one obtains respectively the static generalized Gross-Pitaevskii equation,

$$\mu\phi_0(x) = \left[\mathcal{H}_0 + \mu_{\text{loc}}(n_0)\right]\phi_0(x), \tag{3.77}$$

as well as the coupled Bogoliubov equations

$$\begin{aligned} \mathcal{L}u_j(x) + \mathcal{M}v_j(x) &= +\hbar\omega_j u_j(x), \\ \mathcal{L}v_j(x) + \mathcal{M}u_j(x) &= -\hbar\omega_j v_j(x), \end{aligned} \tag{3.78}$$

where we have defined the operators

$$\mathcal{L} = \mathcal{H}_0 - \mu + \mu_{\text{loc}}(n_0) + \left[\frac{\partial \mu_{\text{loc}}(n)}{\partial n}\right]_{n=n_0} n_0, \tag{3.79}$$

and

$$\mathcal{M} = \left[\frac{\partial \mu_{\rm loc}(n)}{\partial n}\right]_{n=n_0} n_0. \tag{3.80}$$

The Bogoliubov wave-functions $u_j(x)$ and $v_j(x)$ satisfy the normalization condition,

$$\int_{-\infty}^{\infty} dx (u_i^*(x)u_j(x) - v_i^*(x)v_j(x)) = \delta_{ij}. \tag{3.81}$$

The above formalism (with $\mu_{\rm loc}(n) = g_{\rm 1D}n$) was first introduced by Pitaevskii, in order to investigate excitations of a vortex line in a uniform Bose gas. One can get the same result if one diagonalizes the Hamiltonian with Bogoliubov transformation [10]. In 1996, Burnett and colleagues used the coupled equations (3.78) to study the properties of excited states in 3D weakly-interacting trapped Bose gases [154].

After numerically solving the static Gross-Pitaevskii equation (3.77) and the coupled equations (3.78), one can obtain directly the profile of the ground state, as well as excited states with energies $\epsilon_j = \hbar\omega_j$ and hence the frequency $\omega_{\rm m}$ of the breathing or compressional monopole mode.

### $T \geq 0$ : **Hartree-Fock-Bogoliubov method with Popov approximation**

In order to take into account the effects of finite temperature and particle number in the trapped one-dimensional Bose gas, we employ the HFBP approximation described in Sec. 3.2.1. The interaction strength now takes a one-dimensional form given in Eq. (3.60). Besides, we need to introduce a small chemical potential difference $\Delta\mu$ to allow a finite particle number of condensate (see Eq. (3.85) below), which leads to

$$\tilde{\mu}\phi(x) = \left[\mathcal{H}_0 + g_{\rm 1D}(n_0(x) + 2n_t(x))\right]\phi(x). \tag{3.82}$$

Here $\Phi(x,t) = e^{-i\Delta\mu t/\hbar}\phi(x)$ and $\tilde{\mu} = \Delta\mu + \mu$. The matrix elements in Eq. (3.12) become

$$\mathcal{L} = \mathcal{H}_0 - \tilde{\mu} + 2g_{\rm 1D}\left(n_0(x) + n_t(x)\right), \tag{3.83}$$

and

$$\mathcal{M} = g_{\rm 1D}n_0(x). \tag{3.84}$$

For the density of the condensate, because our bosonic system has a finite particle number, we calculate the finite condensate particle number as $N_0 = \int dx n_0(x)$, i.e.,

$$N_0 = \frac{1}{e^{\beta\Delta\mu} - 1}, \tag{3.85}$$

with the inverse temperature $\beta = 1/k_{\mathrm{B}}T$. The quasi-particle occupation number is affected by the finite condensate number as well. The $j$-th quasi-particle occupation number $N_j \equiv \langle \hat{\alpha}_j^\dagger \hat{\alpha}_j \rangle$ reads

$$N_j = \frac{1}{e^{\beta(\hbar\omega_j + \Delta\mu)} - 1} = \frac{1}{(1 + \frac{1}{N_0})e^{\beta\hbar\omega_j} - 1}, \tag{3.86}$$

and the thermal density is then given by

$$n_t(x) \equiv \langle \hat{\eta}^\dagger \hat{\eta} \rangle = \sum_j \left[ u_j^2(x) + v_j^2(x) \right] N_j + \sum_j v_j^2(x). \tag{3.87}$$

The chemical potential of the system $\mu$, is fixed by the number equation for the total number of atoms $N = N_0 + N_T$, where $N_T = \int dx n_t(x)$.

## Results and Discussions

We perform numerical calculations of the above mentioned approaches and compare our results with the experiment data [12] and the previous theoretical predictions [11]. In the experiment, a 2D optical lattice is used to trap about $(1 \sim 4) \times 10^4$ Cs atoms in $(3 \sim 6) \times 10^3$ 1D tubes with $8 \sim 25$ atoms in the center tube. Choi *et al.* dealt with the case of a particle number $N = 25$ and introduced an effective dimensionless interaction parameter $\gamma_{\mathrm{eff}}$, which is defined as

$$\gamma_{\mathrm{eff}} \equiv \frac{2}{n_{\mathrm{TG}}(0)|a_{\mathrm{1D}}|} = \frac{g_{\mathrm{1D}}\pi}{\sqrt{2N}}. \tag{3.88}$$

Here, $n_{\mathrm{TG}}(0) = \sqrt{2Nm\omega_{\mathrm{ho}}/\hbar}/\pi$ is the peak density in the Tonks-Girardeau regime at the tube center [186].

In our calculations, harmonic oscillator units are used with $\hbar = \omega_{\mathrm{ho}} = m = 1$ and $k_{\mathrm{B}} = 1$. Length and energy are written in the units of harmonic oscillator length $a_{\mathrm{ho}} = [\hbar/(m\omega_{\mathrm{ho}})]^{1/2}$ and harmonic oscillator energy $\hbar\omega_{\mathrm{ho}} = [\hbar^2/(ma_{\mathrm{ho}}^2)]$, respectively.

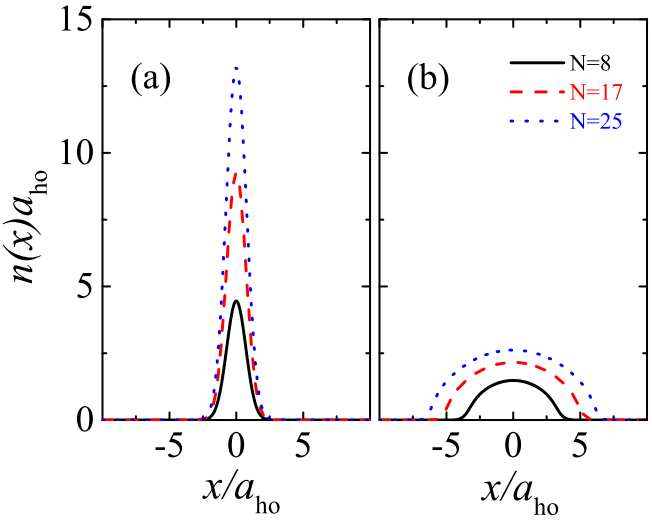


Figure 3.5: Density profiles in the mean-field regime (a) and in the Tonks-Girardeau regime (b), where the effective interaction parameter $\gamma_{\text{eff}} = 10^{-2}$ and 10 have been used, respectively. The results are calculated with $N = 8$ (black solid lines), $N = 17$ (red dashed lines) and $N = 25$ (blue dotted lines). The density $n(x)$ and position $x$ are taken in units of harmonic oscillator length $a_{\text{ho}} = \sqrt{\hbar/(m\omega_{\text{ho}})}$ and $a_{\text{ho}}^{-1}$, respectively.

We fix the particle number at $N = 8, 17, 25$, and vary the effective interaction parameter $\gamma_{\text{eff}}$. The ground state and collective modes of the 1D harmonically trapped Bose gas at $T = 0$ are obtained, by numerically solving the generalized Gross-Pitaevskii equation (3.77), and the generalized Bogoliubov equations (3.78), where the local chemical potential is obtained with Lieb-Liniger integrals [181, 182]. Then we introduce the non-condensate thermal density $n_t$ by means of the HFBP theory, and compare the ground states and collective behaviours at finite temperature with the result at $T = 0$.

### 3.3.2 Density profile

In this subsection, we study the density profile of the ground states. In particular, at zero temperature we compare the results obtained by the generalized Gross-Pitaevskii theory with those predicted by the HFBP theory.

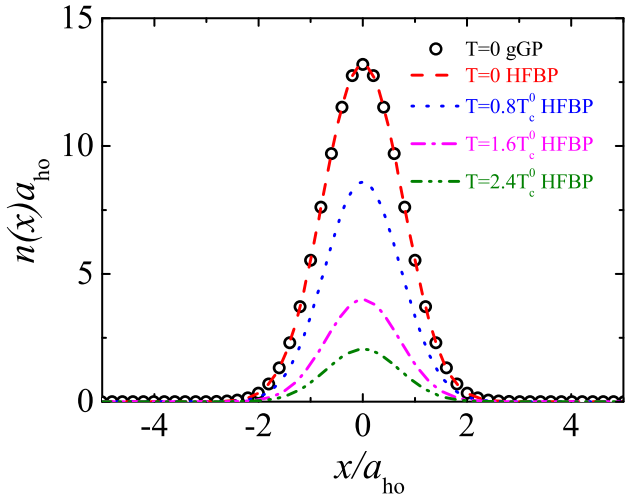


Figure 3.6: Density profile: at $T = 0$ predicted by the generalized Gross-Pitaevskii theory (black circles); at $T = 0$ (red dashed lines) and finite temperatures (other colorful lines) calculated by the HFBP theory. The results are shown at the effective interaction parameter $\gamma_{\text{eff}} = 10^{-2}$ in the mean-field regime. The particle number $N$ is fixed at 25. $T_c^0$ is the critical temperature for a 1D ideal Bose gas, which can be estimated as $k_B T_c^0 = \hbar\omega_{ho} N/\ln(2N)$ [9, 10].

### $T = 0$ case: the generalized Gross-Pitaevskii theory

The ground states for different particle number $N = 8, 17, 25$ at $T = 0$ are shown in Fig. 3.5, obtained by solving the generalized Gross-Pitaevskii theory. In the figure, we focus on the mean-field regime (with $\gamma_{\text{eff}} = 10^{-2}$, the left panel) and the Tonks-Girardeau regime (with $\gamma_{\text{eff}} = 10$, the right panel). At $\gamma_{\text{eff}} = 10^{-2}$, the density profile is roughly a Gaussian curve, while at $\gamma_{\text{eff}} = 10$ it tends to be a semicircle. In both regimes, for a given $\gamma_{\text{eff}}$, the height of density profiles is enhanced with increasing particle number.

### Finite $T$ at weak couplings: the HFBP theory

The 1D HFBP theory is valid only in the weak coupling regime. The corresponding density profiles at different temperatures are shown in Fig. 3.6. For $T = 0$, the density profile predicted by the generalized Gross-Pitaevskii theory (indicated as gGP in the figure) is also presented by black circle for comparison. It agrees well

with the prediction of the HFBP theory (i.e., the red dashed line). With increasing temperature, the condensate fraction decreases, as well as the condensate occupation number, leading to the decreasing of the height of density profiles.

### 3.3.3 Breathing mode

In this subsection, collective modes, especially the breathing mode, are investigated with the generalized Bogoliubov theory and the HFBP theory. The dipole mode frequency should precisely be the trapping frequency $\omega_{\rm ho}$, according to the Kohn theorem. We recover the result with a relative error about $0.1\% \sim 0.2\%$ with respect to $\omega_{\rm ho}$.

#### Particle number effect in two limits

The experiment on the breathing mode frequency was conducted for particle numbers in the range of $8 \sim 25$. There is a deviation between the experimental results [12] and one of previous numerical simulations at $N = 25$ in the weak coupling regime [11]. In order to check whether this is due to the effect of different particle number, we calculate the breathing mode frequency with different $N$.

In the deep weak coupling limit, it is convenient to define a Hartree parameter $\lambda = |a_{\rm 1D}|/(N a_{\rm ho}) \gg 1$. The sum-rule approach predicts that in the limit of $\lambda \gg 1$, the correction of a finite particle number on the squared breathing mode frequency is [187]

$$\begin{aligned} \frac{\omega_{\rm m}^2}{\omega_{\rm ho}^2} &\simeq 4(1 - c_{\rm N}\lambda^{-1}) \\ &= 4 - \frac{g_{\rm 1D}}{\sqrt{2\pi}} N, \lambda \to \infty \end{aligned} \tag{3.89}$$

where $c_{\rm N} = 1/\sqrt{8\pi}$ for all $N \geq 2$. This analytic prediction indicates that the squared breathing mode frequency ratio $\omega_{\rm m}^2/\omega_{\rm ho}^2$ is proportional to the particle number $N$ at a fixed $g_{\rm 1D}$.

In Fig. 3.7, we show our numerical results (solid line) at $\lambda = |a_{\rm 1D}|/(N a_{\rm ho}) \gg 1$, with the effective interaction parameter $\gamma_{\rm eff}$ varying from $4.4 \times 10^{-4}$ to $1.6 \times 10^{-3}$ at a constant $g_{\rm 1D} = 10^{-3}$. The analytic results Eq. (3.89) are also shown by the dashed line. There is a very good agreement, within a relative error 0.1%. Presumably, this

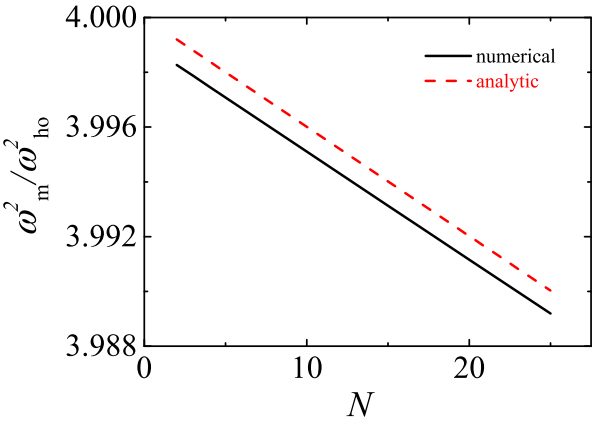


Figure 3.7: The ratio of the squared breathing mode frequency $\omega_m^2/\omega_{ho}^2$ as a function of the particle number $N$. Our numerical calculation is shown by the black solid line, and the analytic result Eq. (3.89) is shown by the red dashed line. All results are near the non-interacting limit with an interaction strength $g_{1D} = 10^{-3}$ in the trap units.

small discrepancy is due to the over-estimation of the mode frequency in the sum-rule approach, which predicts only an upper bound for the mode frequency [188].

In the opposite limit of strong couplings, which is characterized by the parameter $\Lambda = Na_{1D}^2/a_{ho}^2 \ll 1$, the correction on the breathing mode frequency due to a finite $N$ is also known [189]:

$$\begin{aligned}\frac{\omega_m^2}{\omega_{ho}^2} &\simeq 4(1 - C_N\sqrt{\Lambda}) \\ &= 4 - \frac{8}{g_{1D}} C_N\sqrt{N}, \Lambda \to 0\end{aligned} \tag{3.90}$$

where $C_N$ is given for all $N \geq 2$ by

$$\begin{aligned}C_N =& \frac{3\sqrt{2N}}{\pi\sqrt{\pi}} \frac{\Gamma(N-\frac{5}{2})\Gamma(N+\frac{1}{2})}{\Gamma(N)\Gamma(N+2)} \\ &\times_3 F_2\left(\frac{3}{2}, 1-N, -N; \frac{7}{2}-N, \frac{1}{2}-N; 1\right).\end{aligned} \tag{3.91}$$

The $N$-dependence of $C_N$ is very weak and its value varies from $C_2 \approx 0.282$ to $C_\infty \approx 0.306$, and to $C_{25} \approx 0.305$ in our case. It is clear from Eq. (3.90) that for a

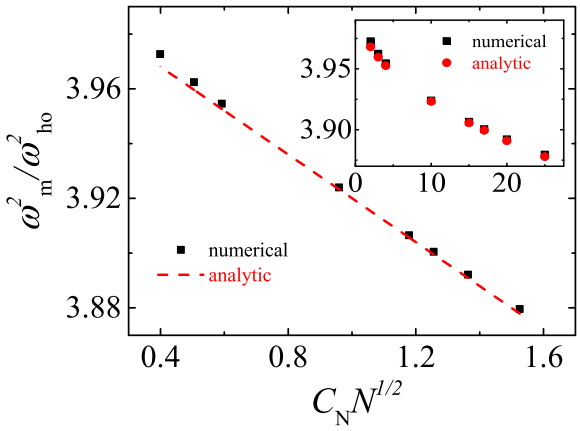


Figure 3.8: The ratio of the squared breathing mode frequency $\omega_m^2/\omega_{ho}^2$ as a function of $C_N\sqrt{N}$ (black squares), compared with the analytic prediction (Eq. (3.90)) that is shown by the red dashed line. The inset shows the same ratio as a function of the particle number $N$. Here, we take an interaction strength $g_{1D} = 10^2$.

fixed $g_{1D}$, the ratio of the squared breathing mode frequency $\omega_m^2/\omega_{ho}^2$ has a linear dependence on the combined variable $C_N\sqrt{N}$.

In Fig. 3.8, we verify this linear behaviour by taking a fixed $g_{1D} = 10^2$ in the Tonks-Girardeau regime, for which the effective interaction parameter $\gamma_{eff}$ varies from 44 to 157.

### Finite temperature effect in the weak coupling limit

Here we consider the finite temperature effect in the weakly interacting limit, by calculating collective mode frequencies using the weak-coupling HFBP theory. It is known that at sufficiently low temperature, this effect is small since the thermal fraction of the system is negligible. For example, Debbie Jin's group has shown that the measured collective oscillating frequencies of a 3D Bose gas at temperature $T < 0.48T_c^0$ have a good agreement with the theoretical predictions at $T = 0$ [190], where $T_c^0$ is the BEC transition temperature of an ideal Bose gas confined in a harmonic trap. To emphasize the effect of finite temperature on the collective mode, we consider here $T > 0.48T_c^0$.

In Fig. 3.9, we compare the ratios of the squared breathing mode frequency at $T = 0$ and $T = 0.8T_c^0$. The mode frequency becomes larger at finite temperature. At

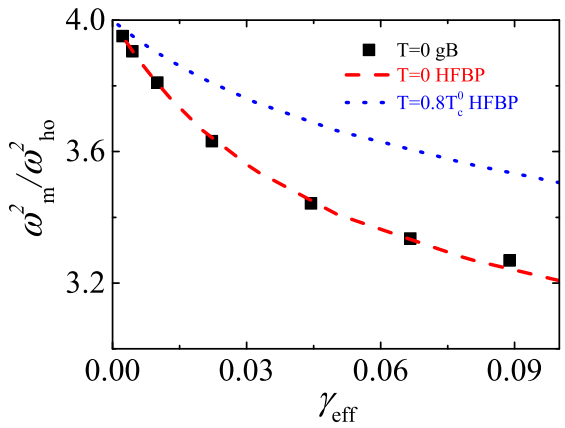


Figure 3.9: The ratio of the squared breathing mode frequency $\omega_{\rm m}^2/\omega_{\rm ho}^2$ at $N = 25$ in the weakly-interacting regime. We have shown the results at $T = 0$ predicted by the generalized Bogoliubov theory (black squares) and by the HFBP theory (red dashed line) and the results at $T = 0.8T_{\rm c}^0$ given by the HFBP theory (blue dotted line). Here $T_c^0$ is the BEC transition temperature for an ideal Bose gas confined in a harmonic trap.

sufficiently large temperature, actually we anticipate that the ratio approaches the ideal gas limit, i.e., $\omega_{\rm m}^2/\omega_{\rm ho}^2 = 4$. We also compare the zero temperature ratios, predicted by the generalized Bogoliubov theory (symbols, indicated as gB in the figure) and the HFBP theory (dashed line). There is a good agreement, as anticipated.

### Comparisons with the experiment and previous theory

We now address the breathing mode frequency in all interaction regimes, emphasizing its dependence on finite particle number and nonzero temperature. We vary the effective interaction parameter $\gamma_{\rm eff}$ from $2.2 \times 10^{-3}$ to $2.9 \times 10^{2}$, and thus cover all the regimes from the non-interacting limit, the mean-field regime to the Tonks-Girardeau limit. The results are presented as a function of the interaction parameter shown in the linear (Fig. 3.10) and logarithmic scales (Fig. 3.11), in comparison with the experimental data [12] and a previous theoretical prediction [11].

In general, in these figures the squared frequency ratio $\omega_{\rm m}^2/\omega_{\rm ho}^2$ of the breathing mode decreases from 4 in the non-interacting limit to 3 in the weakly-interacting mean-field regime, and then increase back to 4 again in the strongly-interacting

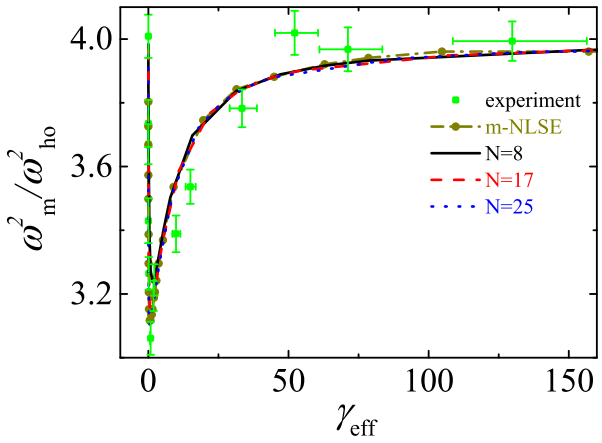


Figure 3.10: The ratio of the squared breathing mode frequency $\omega_m^2/\omega_{ho}^2$ as a function of the effective interaction parameter $\gamma_{eff}$. $\gamma_{eff}$ covers all interaction regimes and varies from $2.2 \times 10^{-3}$ to $2.9 \times 10^2$. We consider three particle numbers: $N = 8$ (black solid line), $N = 17$ (red dashed line) and $N = 25$ (blue dotted line). We have compared our result with a previous theoretical prediction obtained by using time-dependent modified nonlinear Schrödinger equation (m-NLSE) (yellow dot-dashed line) [11] and the experimental data (green squares with error bars) [12].

Tonks-Girardeau regime.

In greater detail, the previous theoretical work (see the results indicated as m-NLSE in the figures) considered a particle number $N = 25$ [11]. Here we have performed numerical calculations with the same number of particles. We have also considered two other particle numbers, $N = 8$ and $N = 17$, since in the experiment the range of the particle number $N$ is $8 \sim 25$ [12]. For the case with a particle number $N = 25$, our results agree very well with the m-NLSE predictions. The good agreement is easy to understand, as both theories start from the same generalized Gross-Pitaevskii equation. The different numerical treatments, i.e., the time-dependent simulations in Ref. [11] and our solution of the generalized Bogoliubov equations, only lead to a negligible difference. By further comparing both theoretical predictions at $N = 25$ with the experimental data, we find a good agreement in the mean-field and Tonks-Girardeau regimes, where the breathing mode frequency essentially does not depend on the particle number. However, near the non-interacting limit, the discrepancy between experiment and theory becomes evi-

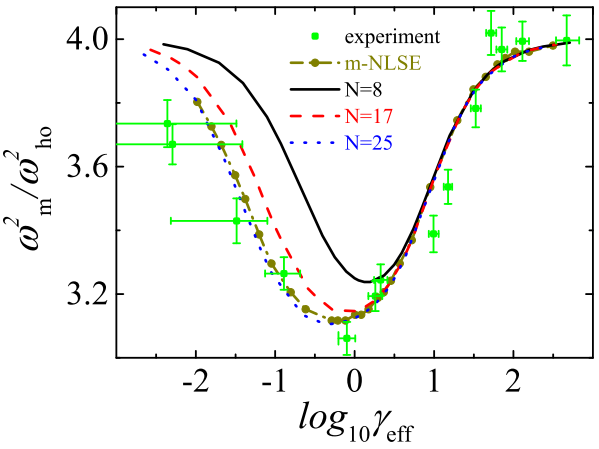


Figure 3.11: The ratio of the squared breathing mode frequency $\omega_{\rm m}^2/\omega_{\rm ho}^2$ as a function of $\log_{10}\gamma_{\rm eff}$. The plot is the same as Fig. 3.10, but is shown here as a function of the interaction parameter in a logarithmic scale, in order to emphasize the particle number dependence in the non-interacting limit.

dent: the experimental data lie systematically below the theory curves. In this limit, the particle number dependence of the breathing mode frequency is significant.

The particle number dependence is particularly clearly seen in Fig. 3.11. The decreasing of the particle number $N$ from 25 to 8 increases the ratio of the squared breathing mode frequency. Thus, taking into account the possibility of a smaller particle number (i.e., $N < 25$) in the real experiment will even enlarge the discrepancy between experiment and theory. On the other hand, this discrepancy cannot be resolved as a finite temperature effect, as in the previous subsection we have already examined that a nonzero temperature generally leads to a larger mode frequency.

### 3.3.4 Higher order collective modes

One of the advantages of our generalized Bogoliubov theory is that we can directly obtain higher order collective mode frequencies from numerical calculations. In Fig. 3.12, we present the mode frequency of the 3-rd (lower panel) and 4-th modes (upper panel) for all interaction regimes at $T = 0$, as a function of the effective interaction parameter $\log_{10}\gamma_{\rm eff}$. Similarly, the frequencies of higher modes exhibit the same reentrant behaviour as the breathing mode frequency.

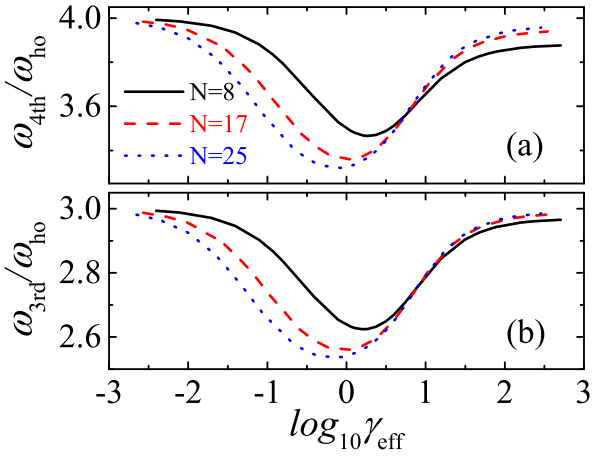


Figure 3.12: The frequency of higher order compressional modes, $\omega_{3\mathrm{rd}}/\omega_{\mathrm{ho}}$ (a) and $\omega_{4\mathrm{th}}/\omega_{\mathrm{ho}}$ (b), as a function of $\log_{10}\gamma_{\mathrm{eff}}$, at different particle numbers: $N = 8$ (black solid line), $N = 17$ (red dashed line) and $N = 25$ (blue dotted line).

Three analytic results can be used to understand the reentrant behaviour. In the non-interacting limit, the mode frequency of the $n$-th mode is simply $n\omega_{\mathrm{ho}}$. In the mean-field regime with sufficiently large number of particles, the collective mode frequency can be analytically determined from a hydrodynamic theory, which predicts $\omega_n = \sqrt{n(n+1)/2}\omega_{\mathrm{ho}}$ [172, 188]. Therefore, we have $\omega_3 \sim 2.45\omega_{\mathrm{ho}}$ and $\omega_4 \sim 3.16\omega_{\mathrm{ho}}$ if $N \to \infty$. With increasing number of particles, the minimum mode frequencies shown in Fig. 3.12 seem to approach these limiting values. Finally, in the Tonks-Girardeau limit, the mode frequency of the $n$-th mode again approach $n\omega_{\mathrm{ho}}$, due to the effective fermionization of the system [191].

It is interesting to note that for high-lying collective modes, the effect of a finite particle number also becomes significant in the Tonks-Girardeau regime as well as in the mean-field regime. This is particularly evident for the 4-th mode, as shown in the upper panel of Fig. 3.12.

## 3.4 Application to one-dimensional spin-polarized Fermi gases

The beautiful exactly-solvable models in one dimensional (1D) systems provide us a better understanding of fascinating low-dimensional quantum many-body systems in nature [192]. Recently, remarkable experimental progresses in ultracold atoms make it possible to realize the quasi-1D geometry in laboratory [12, 167, 168, 193–197], and therefore pave the way to test a number of exact theoretical predictions and to confirm the predicted intriguing many-body phenomena [165, 166]. A well-known example is a 1D Bose gas with strongly repulsive interparticle interactions, where bosons can not penetrate each other and therefore their many-body wavefunction resembles that of free spinless fermions and vanishes whenever two bosons coincide at the same position [63]. This so-called Tonks-Girardeau (TG) gas has attracted enormous attention over the past few decades, both experimentally and theoretically [12, 64, 165, 166, 168, 173, 194, 198, 199]. To date, evidences of a TG gas have been clearly identified in a number of experimental observables, including the density profile, momentum distribution, and collective oscillations [12, 168, 194] (see also Sec. 3.3). A highly-excited super-TG Bose gas, which was predicted to occur by rapidly switching the sign of the interaction strength [200, 201], has also been experimentally confirmed [12].

In this subsection, we theoretically investigate an ultracold spin-polarized atomic Fermi gas with resonant odd-channel ($p$-wave) interactions trapped in 1D harmonic traps. The experimental observation of another fascinating many-body phenomenon, a super fermionic Tonks-Girardeau (super-fTG) gas, is discussed. It was predicted to emerge in a spin-polarized Fermi gas with resonant odd-channel or $p$-wave interactions [13]. In sharp contrast to the Tonks-Girardeau (TG) or super-TG Bose gas, where the strongly correlated state is driven by a large scattering length, the super-fTG gas is caused by a non-negligible *effective range* of the interparticle interactions [13], which is rare in cold-atom experiments. To explore the realistic parameter space for observing the super-fTG gas at finite temperature, we exactly solve the Yang-Yang thermodynamic equations for the thermodynamics of the 1D $p$-wave Fermi gas based on the Bethe ansatz solution [202]. By taking into account

the external harmonic potential with a trapping frequency $\omega_{\rm ho}$ via the local density approximation (LDA) [203], we calculate the finite-temperature density distribution of the Fermi cloud and discuss the fermion-boson duality [204]. By further using the two-fluid hydrodynamic theory [173, 205, 206], we determine the sound velocity and the breathing mode frequency of the low-lying collective oscillations. Clear signatures of the appearance of a super-fTG gas in these two observables have been predicted [13, 65].

### 3.4.1 Theoretical Framework: 1D $p$-wave atomic Fermi gases

We start by briefly reviewing the two-particle scattering property in a spin-polarized Fermi gas. Due to the Pauli exclusion principle, only odd-channel scatterings are possible, and at the low-energy limit, the $p$-wave scattering in three-dimensions (3D) is the strongest [4, 207]. Unlike the $s$-wave case, the $p$-wave scattering becomes energy-dependent, and an effective range of the interaction potential has to be included in order to regularize the contact interactions. The 3D $p$-wave scattering is then described by a phase shift $\delta_p(k)$:

$$k^3 \cot \delta_p(k) = -1/w_1 - \alpha_1 k^2 + \mathcal{O}(k^4), \tag{3.92}$$

where $k$ is the relative momentum of two colliding atoms, and $w_1$ and $\alpha_1$ are the scattering volume and effective range, respectively [4, 207]. For $^6$Li ($^{40}$K) atoms, where the $p$-wave resonance occurs near $B_0 = 215.0$ (198.8) G, the effective range $\alpha_1$ is about 0.088 (0.021), in unit of inverse of Bohr radius ($a_0^{-1}$) [208–211]. In the quasi-1D geometry considered here, where the transverse motion is completely suppressed by the strong transverse confinement potential using a two-dimensional optical lattice [12, 167, 194, 195], it is known that the 1D scattering amplitude in the odd channel (denoted as $p$-wave as well for convenience) takes the form [212, 213],

$$f_p^{\rm odd}(k) = \frac{-ik}{1/l_p + \xi_p k^2 + ik}, \tag{3.93}$$

where $l_p \approx 3a_\perp \left[a_\perp^3/w_1 - 3\sqrt{2}\zeta(-1/2)\right]^{-1}$ and $\xi_p = \alpha_1 a_\perp^2/3 > 0$ are the 1D scattering length and effective range, respectively [13, 212, 213]. A confinement induced

resonance appears when the 3D scattering length $w_1^{1/3}$ is comparable to the transverse length $a_\perp = \sqrt{\hbar/(m\omega_\perp)}$, where $m$ is the atomic mass and $\omega_\perp$ is the trapping frequency of the transverse confinement [212–215].

### Bethe ansatz solution

Ignoring the 1D effective range $\xi_p$, a 1D spin-polarized Fermi gas of $N$ atoms is exactly solvable, owing to the fermion-boson duality [204, 216], which maps the system into a 1D interacting Bose gas. The latter at $T = 0$ was exactly solved by Lieb and Liniger in 1963 by using the celebrated Bethe ansatz solution [179, 180]. The finite-temperature thermodynamics of a 1D Bose gas was also solved a few years later by Yang and Yang, using an approach that is now commonly referred to as the Yang-Yang thermodynamic equations [217]. In the presence of a non-negligible effective range $\xi_p \neq 0$, a similar Bethe ansatz for all the many-body wave-functions $\Psi$ can be constructed, by imposing a Bethe-Peierls boundary condition,

$$\lim_{x\to 0^+}\left(\frac{1}{l_p} + \partial_x - \xi_p\partial_x^2\right)\Psi(x = |x_i - x_j|\,; X) = 0 \tag{3.94}$$

whenever two particles at $x_i$ and $x_j$ approach each other [13], which leads to a set of coupled equations,

$$e^{ikL} = \prod_q \frac{\xi_p\,(k-q)^2 - 1/|l_p| + i\,(k-q)}{\xi_p\,(k-q)^2 - 1/|l_p| - i\,(k-q)}. \tag{3.95}$$

Here, the quasi-momenta $k$ and $q$ take $N$ discrete values, and $L$ is the length of the system under a periodic boundary condition. We consider only the attractive case $l_p < 0$, since otherwise the energy does not have a proper thermodynamic limit [13]. At $T = 0$, the ground state of the system has been solved by Imambekov *et al.*, by seeking the lowest energy state of Eq. (3.95) [13].

### Yang-Yang thermodynamic equations

At finite temperature, the Yang-Yang thermodynamic equations of a polarized Fermi gas with a finite $\xi_p$ can also be similarly derived [202]. In the thermodynamic limit ($N \to \infty$ and $L \to \infty$), they take the exactly same form as that of bosons [13, 202],

except a new kernel function,

$$\mathcal{K}(k,q)=\frac{2|l_p|\left[1+|l_p|\xi_p\left(k-q\right)^2\right]}{\left[1-|l_p|\xi_p\left(k-q\right)^2\right]^2+l_p^2\left(k-q\right)^2}. \tag{3.96}$$

To be more explicit, the Yang-Yang thermodynamic equations are given by ($k_B=1$) [217],

$$\begin{aligned}\epsilon\left(k\right)&=\frac{\hbar^2k^2}{2m}-\mu-\frac{T}{2\pi}\int_{-\infty}^{\infty}\mathcal{K}\left(k,q\right)\ln\left[1+e^{-\frac{\epsilon(q)}{T}}\right]dq\\ 2\pi\rho\left(k\right)&\left[1+e^{\frac{\epsilon(k)}{T}}\right]=1+\int_{-\infty}^{\infty}\mathcal{K}\left(k,q\right)\rho\left(q\right)dq,\end{aligned} \tag{3.97}$$

where $\epsilon\left(k\right)$ may be interpreted as the quasi-particle excitation energy relative to the chemical potential $\mu$, and $\rho(k)$ is the quasi-momentum distribution function normalized according to $n=N/L=\int\rho(k)dk$. Once the Yang-Yang equations are solved, all the thermodynamic variables, for example, the total energy and pressure of the system can be calculated straightforwardly, by using

$$E=\frac{\hbar^2L}{(2m)}\int k^2\rho(k)dk \tag{3.98}$$

and

$$P=\frac{T}{2\pi}\int\ln[1+\exp(-\epsilon(k)/T)]dk, \tag{3.99}$$

respectively [217].

To take into account the slowly-varying harmonic trapping potential in the longitudinal $x$-direction $V_T(x)=m\omega_{\rm ho}^2x^2/2$, which is necessary to keep atoms from escaping [167, 193], we apply the LDA approximation [203]. This amounts to setting

$$\mu[n(x)]=\mu_0-V_T(x), \tag{3.100}$$

where $n(x)$ is the local density that is to be inversely solved once we know the relation $\mu(n)$ from the Yang-Yang equations and $\mu_0$ is a global chemical potential to be determined by using $\int n(x)dx=N$ [203]. In our numerical calculations, two dimensionless interaction parameters related to the 1D scattering length $|l_p|$ and effective range $\xi_p$ are needed. Therefore, we define respectively

$$\gamma_1\equiv\frac{1}{n_{\rm F}|l_p|}\text{ and }\gamma_2\equiv\frac{1}{n_{\rm F}\xi_p}, \tag{3.101}$$

using the peak density of a zero-temperature ideal Fermi gas at the same trap, $n_{\mathrm{F}} = \sqrt{2N}/(\pi a_{\mathrm{ho}})$, where $a_{\mathrm{ho}} = \sqrt{\hbar/(m\omega_{\mathrm{ho}})}$ is the characteristic length along the $x$-axis. To be specific, we consider a polarized Fermi gas of $N = 100$ $^6$Li atoms under the quasi-1D confinement with $\omega_\perp = 2\pi \times 200$ kHz and $\omega_{\mathrm{ho}} = 2\pi \times 200$ Hz, leading to a 1D effective range $\xi_p = 1.58 a_{\mathrm{ho}}$ and $\gamma_2 \simeq 0.14$.

**Two-fluid hydrodynamics**

We are particularly interested in the low-lying collective oscillations of the Fermi cloud, which are well described by a two-fluid hydrodynamic theory. At finite temperature, it takes the following form [173, 205, 206],

$$m\left(\omega^2 - \omega_{\mathrm{ho}}^2\right) n u\left(x\right) + \frac{\partial}{\partial x}\left[n\left(\frac{\partial P}{\partial n}\right)_{\bar{s}} \frac{\partial u\left(x\right)}{\partial x}\right] = 0, \tag{3.102}$$

where $u(x)$ is a displacement field characterizing the oscillation at frequency $\omega$, and the derivative of the local pressure $P$ with respect to the density $n$ should be taken at the constant local entropy per particle $\bar{s} = s/n$. In free space, the displacement field $u(x)$ takes a plane-wave solution with the dispersion $\omega = cq$, with a sound velocity

$$c = \sqrt{(\partial P/\partial n)_{\bar{s}}/m}. \tag{3.103}$$

In the presence of the confining harmonic traps, the low-lying collective modes can be solved by using a polynomial ansatz and to a good approximation, the breathing mode frequency $\omega_b$ is given by [173],

$$\omega_b^2 = \omega_{\mathrm{ho}}^2 + \frac{\int_{-\infty}^{\infty}\left[\left(\partial P/\partial n\right)_{\bar{s}}/m\right] n\left(x\right) dx}{\int_{-\infty}^{\infty} x^2 n\left(x\right) dx}, \tag{3.104}$$

which can be regarded as a finite-temperature generalization of the well-known sum-rule approach [10, 21].

### 3.4.2 Characterization of the exotic super-fTG regime

Our main result is summarized in Fig. 3.13, where we report the dependence of the breathing mode frequency on the 1D scattering length (the horizontal axis) and effective range (the vertical axis) of the $p$-wave interaction, at a temperature $0.1T_F$

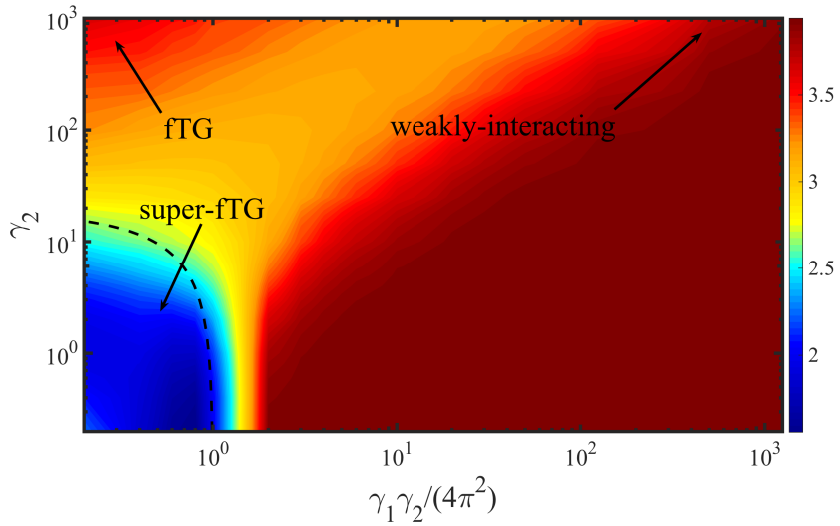


Figure 3.13: Contour plot of the squared breathing mode frequency $(\omega_b/\omega_{\rm ho})^2$ as functions of the dimensionless interaction parameters $\gamma_2$ and $\gamma_1\gamma_2/(4\pi^2)$ (see the text for their definitions) in the logarithmic scale. The black dashed line is the zero-temperature analytic result given in Eq. (3.105) [13], indicating the transition into the super-fTG regime, either from the weakly interacting limit or the strongly interacting fTG limit. We have taken a typical temperature $T = 0.1T_{\rm F}$.

that is typically available in cold-atom experiments. Three distinct regimes could be clearly identified: a weakly or strongly interacting Fermi gas with a mode frequency $\omega_b \simeq 2\omega_{\rm ho}$ and a super-fTG characterized by a much smaller mode frequency at large effective ranges (i.e., $\gamma_2 \to 0$). At large enough $\gamma_2$ (i.e. negligible effective range), the squared frequency $(\omega_b/\omega_{\rm ho})^2$ of the system shows a reentrant behaviour, valuing about 4 in the weakly-interacting limit, changing to 3 at the intermediate regime and finally returning back to 4 in the fTG limit, as a result of the duality to a 1D Bose gas. In contrast, at sufficiently small $\gamma_2$ (i.e. sizable effective range), with increasing $|l_p|$ or decreasing $\gamma_1$, the frequency ratio loses the reentrant behaviour and drops sharply to a much lower value at a critical interaction parameter, thereby signifying the phase transition to the super-fTG phase. At low temperature, the critical interaction parameter may be estimated from the ground-state energy [13],

$$\left[\frac{\gamma_1\gamma_2}{4\pi^2}\right]_{\rm super-fTG} \simeq 1 + \frac{\zeta\left(-1/2\right)a_{\rm ho}}{4\pi\sqrt{N}a_\perp}\gamma_2, \tag{3.105}$$

This estimation - illustrated by a black dashed line in the figure - agrees qualitatively well with our results and encloses the blue super-fTG area with small breathing mode frequencies. While the underlying quasiparticles in both weakly and strongly interacting regimes can be well interpreted in terms of fermions or bosons [218, 219], the behaviour of the compressible super-fTG state is more subtle to figure out. Therefore, the experimental observation of a super-fTG gas should provide a new opportunity to understand the challenging quantum many-body physics. For a $^6$Li polarized Fermi gas near the $p$-wave Feshbach resonance at $B_0 = 215.0$ G, where $\gamma_2 \simeq 0.14$, we find that $(\gamma_1)_{\text{super-fTG}} \simeq 275$ or $(a_\perp^3/w_1)_{\text{super-fTG}} \simeq -118$. This corresponds to a detuning from the resonance at about 0.05 G.

### 3.4.3 Sound speed in free space

In Fig. 3.14, we present the density dependence of the local sound velocity at some selected interaction parameters and at a typical experimental temperature (upper panel, $T = 0.1T_F$) as well as at a high temperature (lower panel, $T = T_F$). We note that, while the 1D effective range is directly measured in units of the harmonic oscillator length $a_{\text{ho}}$, the 1D scattering length is indirectly characterized using the 3D scattering volume $-w_1/a_\perp^3$ for the convenience to make contact with experiments, where the magnetic field dependence of $w_1(B)$ is known [208–211].

In the case of a negligible effective range (i.e., Figs. 3.14(a) and 3.14(d)), the sound velocity in units of the Fermi velocity, $c/v_l(n)$, decreases monotonically with increasing local density $n$. The sharp decrease at low density can be understood from the fermion-boson duality [204]. At sufficient small density $n \ll n_{\text{F}}$, the Fermi cloud lies in the fTG regime of 1D strongly interacting fermions and is equivalent to a weakly interacting Bose gas [204], in which the sound velocity $c \sim n^{1/2}$ [10, 21]. As a result, we find that $c/v_l(n) \sim (|l_p|n)^{-1/2}$, which quantitatively accounts for the observed rapid decrease. Instead, at large density ($n \gg n_{\text{F}}$), the sound velocity saturates to a value that strongly depends on the scattering volume.

The density dependence of the sound velocity changes qualitatively, when the effective range comes into play (see Figs. 3.14(b) and 3.14(c)). At low temperature, in addition to the rapid decrease at low density, a plateau develops at the moderate density $n \sim n_{\text{F}}$, whose structure sensitively relies on the scattering volume $w_1$. By

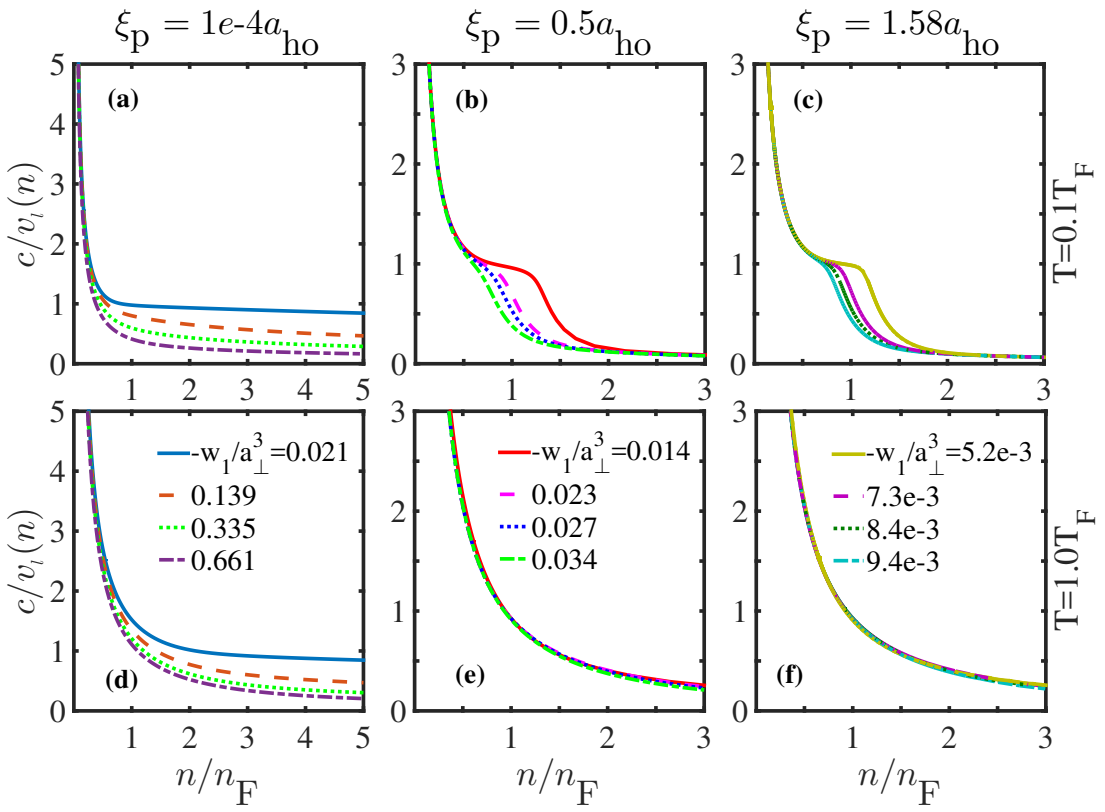


Figure 3.14: Local sound velocity $c/v_l(n)$ as a function of the local density $n/n_F$ for three sets of effective ranges $\xi_p = 10^{-4}a_{ho}$ [(a), (d)], $0.5a_{ho}$ [(b), (e)], and $1.58a_{ho}$ [(c), (f)] at low temperature $T = 0.1T_F$ (upper panel) and high temperature $T = T_F$ (lower panel). In each subplot, the four curves at different interaction parameters $-w_1/a_\perp^3$ correspond to the four highlighted points in the curves of the squared breathing mode frequency, as shown in the insets of Fig. 3.15. Here, $v_l(n) = \pi\hbar n/m$ is the local Fermi velocity and $T_F = N\hbar\omega_{ho}$ is the Fermi temperature.

further increasing density, there is another rapid decrease. The sound velocity finally approach an asymptotically value that seems less sensitive to the scattering volume. At non-negligible effective ranges, a plateau emerges in $c/v_l(n)$ which might be the non-trivial behaviour in the exotic super-fTG phase. Although the plateau is washed out at sufficiently large temperature, as shown in Fig. 3.14(e) and 3.14(f), it could be measured experimentally by creating a density dip at the trap center and then observing its propagation, following the routine established for a unitary Fermi gas

[220].

### 3.4.4 Density profile at nonzero temperature

Fig. 3.15 reports the finite-temperature density distributions at different effective ranges, and at certain values of the interaction parameter $-w_1/a_\perp^3$ as illustrated by differently colored curves. The results at a negligible effective range in Fig. 3.15(a) may again be understood from the fermion-boson duality [204]. At a weak interaction parameter (i.e., the blue line), the profile is simply an ideal Fermi gas distribution. When the interaction becomes more attractive, as described by the Cheon-Shigehara (CS) model [204], the Fermi cloud is dual to an interacting Bose

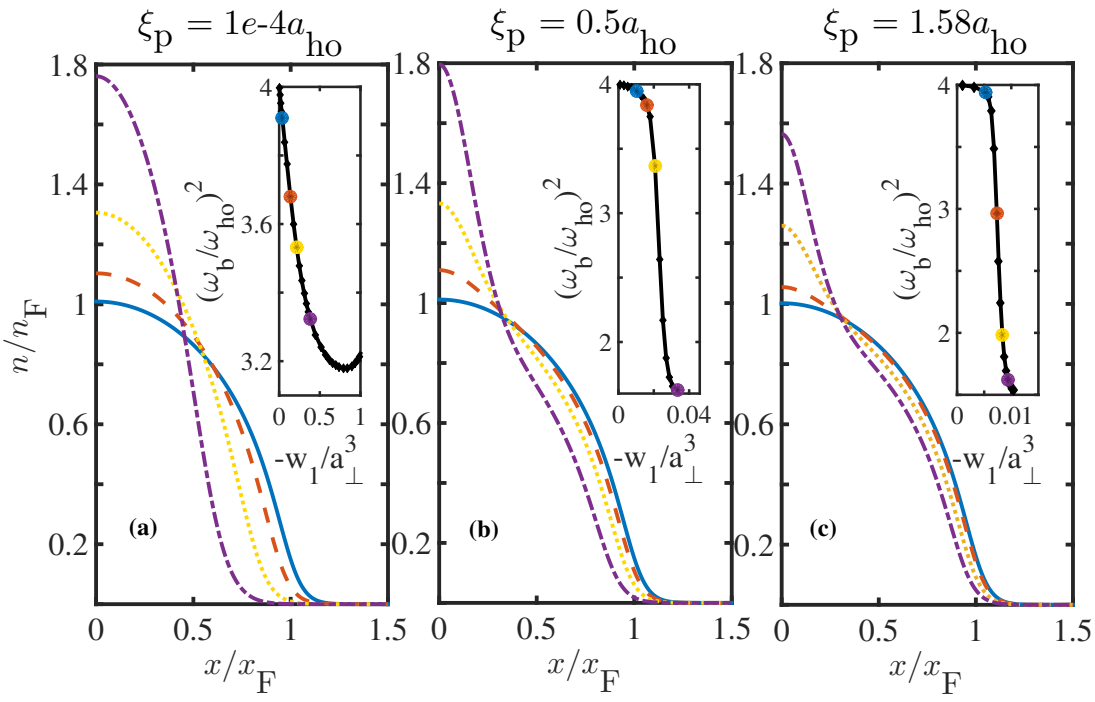


Figure 3.15: Density profiles at different effective ranges: (a) $\xi_p = 10^{-4}a_{ho}$, (b) $0.5a_{ho}$, and (c) $1.58a_{ho}$, at $T = 0.1T_F$. The inset shows the squared breathing mode frequency as a function of the interaction parameter $-w_1/a_\perp^3$. In each subplot, the interaction parameters of colored curves can be read from the highlighted points with the same color. They are also explicitly indicated in Fig 3.14. Here, $x_F = \sqrt{2N}a_{ho}$ is the radius of an ideal trapped Fermi gas at zero temperature.

gas with an appropriate repulsion strength $\propto |l_p|^{-1} \propto |w_1|^{-1}$. Thus, the profile becomes narrower and the peak density is higher, behaving exactly the same as a 1D Bose gas [203].

In the presence of sizable effective ranges, as shown in Figs. 3.15(b) and 3.15(c) for $\xi_p = 0.5a_{\rm ho}$ ($\gamma_2 \simeq 0.44$) and $\xi_p = 1.58a_{\rm ho}$ ($\gamma_2 \simeq 0.14$), the shape of the density profile is greatly altered, even by a small increase in the interaction parameter $-w_1/a_\perp^3$. The peak density increases significantly, probably due to the enhanced attraction by the finite effective-range. Furthermore, the profile at large effective range clearly shows a bimodal distribution. The dramatic change in the density distribution comes along with a sharp decrease in the breathing mode frequency, as reported in the two insets, which we shall now discuss in greater detail. We note that, at zero temperature, similar changes have been observed by Imambekov and co-workers [13].

### 3.4.5 Breathing mode at nonzero temperature

With the sound velocity $c(x)$ and density distribution $n(x)$ at hand, we calculate straightforwardly the finite-temperature breathing mode frequency using the generalized sum-rule approximation Eq. (3.104). The measurement of collective excitations proved to be a powerful and convenient way to characterize possible new quantum states of matter arising from the intriguing effects of interatomic interactions [10, 221]. In an interacting 1D Bose gas, the transition from the weakly-interacting regime to the TG regime for impenetrable bosons is characterized by a nontrivial but smooth evolution of the squared breathing mode frequency, which starts at about 4 in the ideal gas limit, decreases to 3 at the mean-field Gross-Pitaevskii regime, and then increases back to 4 in the TG limit [12, 64]. At a sufficiently small effective range, we have checked the above smooth evolution of the mode frequency, as anticipated from the fermion-boson mapping [204].

Fig. 3.16 presents the breathing mode frequency at some finite effective ranges and finite temperatures. Typically, we find that the mode frequency experiences a sudden drop at a certain critical value of $-w_1/a_\perp^3$, after which the frequency slowly increases. This sudden change could be viewed as a clear signature of the appearance of the super-fTG phase. It is readily seen that this sudden-drop feature is enhanced

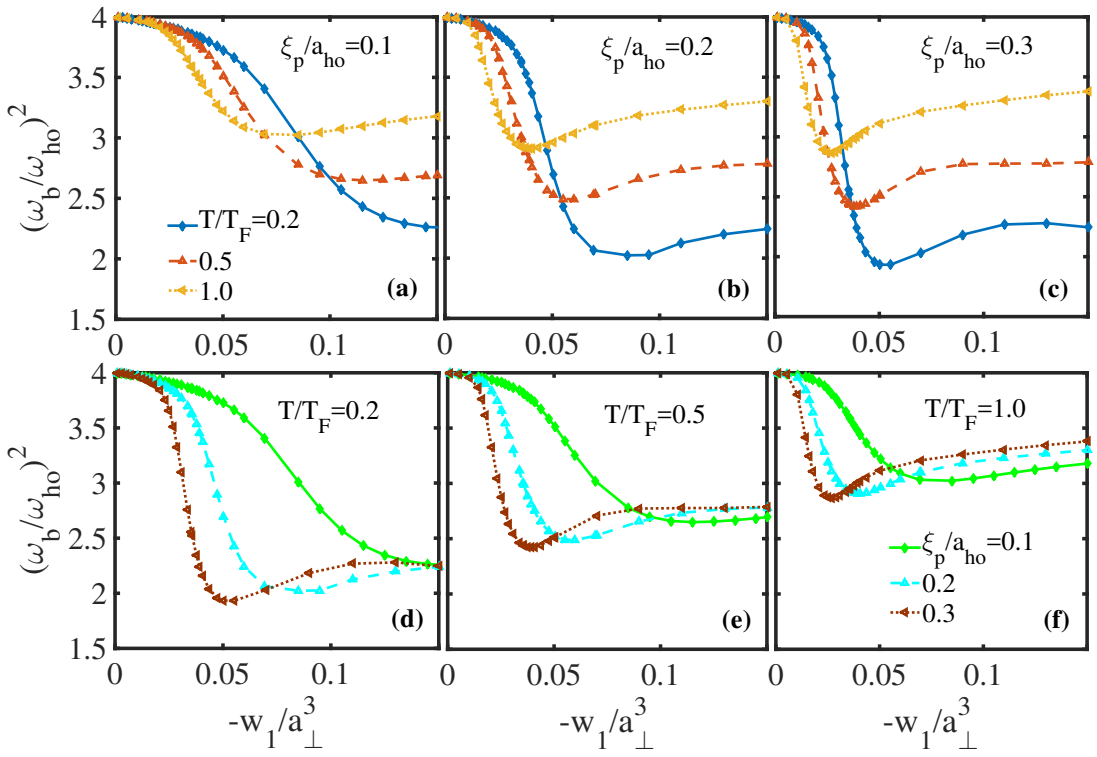


Figure 3.16: The squared breathing mode frequencies $(\omega_b/\omega_{\rm ho})^2$ as a function of the interaction parameter $-w_1/a_\perp^3$, at different effective ranges (upper panel (a)-(c)) or at different temperatures (lower panel, (d)-(e)), as indicated.

by a large effective range, which also leads to a minimum squared frequency as small as $2\omega_{\rm ho}^2$. A finite temperature tends to significantly lift the minimum frequency. However, the sudden-drop structure is merely unchanged.

We have investigated the thermodynamics and dynamics of spin-polarized fermions with a resonant $p$-wave interaction under a one-dimensional harmonic confinement at finite temperature, by solving the exact Yang-Yang thermodynamic equations and two-fluid hydrodynamic equation. We have shown that there are distinct features in the density distribution and collective mode frequency for identifying an exotic effective-range-induced super fermionic Tonks-Girardeau state. These features are not sensitive to the presence of a finite temperature. As a result, our predictions are readily testable with ultracold $^6$Li or $^{40}$K atoms near a $p$-wave Feshbach resonance at an experimental achievable temperature $T \simeq 0.1T_F$.

# Chapter 4

# The plane-wave and zero-momentum phases at nonzero temperature

In this chapter, we theoretically study a three-dimensional weakly interacting Bose gas with a one-dimensional Raman-induced spin-orbit coupling introduced in Sec. 2 at *finite* temperature, by employing a generalized Hartree-Fock-Bogoliubov theory with Popov approximation in Sec. 3.2.3. After a short introduction and motivation in Sec. 4.1, we first study the ground-state properties considering the quantum fluctuations at zero temperature in Sec. 4.2. We then determine a complete finite-temperature phase diagram in Sec. 4.3 of three exotic condensation phases (i.e., the stripe, plane-wave and zero-momentum phases), against both quantum and thermal fluctuations. In Secs. 4.4 and 4.5, the Bogoliubov excitation spectrum in the plane-wave and the zero-momentum phases are under intensive and careful studies, while the corresponding phonon mode and sound velocity are thoughtfully analyzed together with Landau critical velocity characterizing the superfluidity of the system. We report the behaviour of other physical observables, such as the magnetization of the gas in Sec. 4.6. Part of this chapter has been summarized in the publication [103].

## 4.1 Introduction and motivation

In this thesis, we are interested in a Bose gas with the specific Raman-type SOC, see Sec. 2 for details. At zero temperature, there are typically three exotic phases in such a Bose gas by tuning the Rabi frequency of the two Raman beams (see Fig. 4.2 at $T = 0$): the stripe (ST) phase, the plane-wave (PW) phase and the zero-momentum (ZM) phase [7, 93]. The zero-temperature phase diagram and relevant thermodynamic properties were explored in detail in last few years [7, 93, 95, 98, 100, 101], by using the Gross-Pitaevskii (GP) equation and the Bogoliubov theory. Only a handful of theoretical investigations have addressed the finite-temperature effects so far [97, 222], which are however unavoidable in realistic experiments [14, 105]. Theoretically, Ozawa and Baym discussed the stability of condensates against quantum and thermal fluctuations [97]. Experimentally, by measuring the magnetization of the condensate of $^{87}$Rb atoms, Ji *et al.* determined a qualitative finite-temperature phase diagram of the ST-PW transition [105]. A follow-up theoretical study by Yu perturbatively calculated the ST-PW boundary at finite temperature in terms of small Rabi frequency, and obtained a good agreement [222]. Unfortunately, this perturbation approach fails at relatively high temperature, and also is not applicable for a large difference in intra- and inter-species interaction strengths, which leads to a large critical Rabi frequency [95, 106]. Furthermore, the phase transition from the PW phase to the ZM phase in the presence of quantum and thermal fluctuations has not been explored both theoretically and experimentally. Therefore, we aim to present a solid calculation of a SOC Bose gas at finite temperature, by developing a self-consistent Hartree-Fock-Bogoliubov theory within Popov approximation. In this way, we address the quantum and thermal effects on different condensation phases.

Following our previous derivations in Sec. 3.2.3, for simplicity, we start with a plane-wave *ansatz* (see Eq. (2.28) in Sec. 2.3.1)

$$\phi(\mathbf{r}) = \sqrt{n_c} \begin{pmatrix} \cos\theta \\ -\sin\theta \end{pmatrix} e^{iP_x x}, \tag{4.1}$$

for the condensate wave function $\phi(\mathbf{r})$ in Eq. (3.53) with two variational parameters: a positive momentum $P_x\hat{e}_x$ and $\theta$ in a range $[0, \pi/4]$. $n_c = N_c/V$ is the uniform

density of the condensate which becomes $n_c = \bar{n}$ at zero temperature except for a negligible fraction of depletion induced by the quantum fluctuations.

In the homogeneous case, the Bogoliubov amplitudes $u(\mathbf{r})$, $v(\mathbf{r})$ in Eq. (3.53) can be properly written as

$$u_{j\sigma}(\mathbf{r}) = u^{(\tau)}_{\mathbf{q}\sigma}\frac{e^{i\mathbf{q}\mathbf{r}}}{\sqrt{V}}, \text{ and } v_{j\sigma}(\mathbf{r}) = v^{(\tau)}_{\mathbf{q}\sigma}\frac{e^{i\mathbf{q}\mathbf{r}}}{\sqrt{V}}, \tag{4.2}$$

and the coupled equations in Sec. 3.2.3 remain the same except that the canonical momentum operator $\hat{\mathbf{p}}$ becomes $\hat{\mathbf{p}} \pm \mathbf{q}$ for $U$ and $V^*$ respectively in Eq. (3.56). Once the generalized GP and Bogoliubov equations are self-consistently solved at finite temperature for a given set of variational parameters $(\theta, P_x)$, we obtain the excitation energy $\varepsilon_{\mathbf{q}\tau}$ for the quasimomentum $\mathbf{q}$ with the branch index $\tau = \pm$. Thus we calculate straightforwardly the free energy of the system, $\mathcal{F}(\theta, P_x)/V = \mu\bar{n} + \Omega_G/V$, where the grand thermodynamic potential per volume $V$ is given by [21, 151]

$$\frac{\Omega_G}{V} = (E_0 - \mu)n_c + \frac{k_{\mathrm{B}}T}{V}\sum_{\mathbf{q},\tau=\pm}\ln\left(1 - e^{-\beta\varepsilon_{\mathbf{q}\tau}}\right) \tag{4.3}$$

with the ground-state energy per particle of the condensate at zero temperature

$$E_0 = \frac{P_x^2 + k_{\mathrm{r}}^2 - 2P_x k_{\mathrm{r}}\cos 2\theta}{2m} + \frac{gn_c - \Omega\sin 2\theta}{2} - \frac{(g - g_{\uparrow\downarrow})n_c\sin^2 2\theta}{4}. \tag{4.4}$$

The two variational parameters $\theta$ and $P_x$ are then determined by minimizing the free energy $\mathcal{F}$,

$$\left(\frac{\partial\mathcal{F}}{\partial\theta}\right)_N = 0, \quad \left(\frac{\partial\mathcal{F}}{\partial P_x}\right)_N = 0. \tag{4.5}$$

For $^{87}$Rb atoms in recent experiment [14] with the interaction energies $g\bar{n} = 0.38E_{\mathrm{r}}$ and $g_{\uparrow\downarrow}/g = 100.99/101.20$ at typical center density of the trapping potential $n(\mathbf{r} = 0) = 0.46k_{\mathrm{r}}^3$, this minimization leads to two critical Rabi frequencies, $\Omega_{c1} \simeq 0.2E_{\mathrm{r}}$ and $\Omega_{c2} \simeq 4.0E_{\mathrm{r}}$, which locate the first-order ST-PW and second-order PW-ZM transitions at zero temperature, respectively [7, 14, 105]. The phase space for the stripe phase is therefore very narrow [105]. To amplify the interaction effects on the phase diagram, unless specifically stated, we use a total density $\bar{n} = 1.0k_{\mathrm{r}}^3$, the interaction energies $g\bar{n} = 0.8E_{\mathrm{r}}$ and $g_{\uparrow\downarrow}\bar{n} = 0.5E_{\mathrm{r}}$. The relatively large difference in the intra- and inter-species interaction strengths gives rise to a more experimentally

accessible critical Rabi frequency $\Omega_{c1} \simeq 2.4E_{\rm r}$ at $T = 0$. We note that, in the latest experiment on SOC Bose gases, where the two spin components are realized by two low-lying bands in a superlattice, the interaction energy $g_{\uparrow\downarrow}\bar{n}$ can be tuned at will by controlling the overlap in wave functions of the two bands, leading to a large phase space for the stripe phase with $\Omega_{c1} \simeq 1.5E_{\rm r}$ [106].

In the following sections, we will present several fundamental observables of such a Bose gas against the quantum and thermal fluctuations, such as ground-state properties, finite-temperature phase diagram, excitation spectrum, sound velocity, critical velocity and so on.

## 4.2 Condensation momentum

At zero temperature, three exotic condensation phases, i.e., the stripe (ST), plane-wave (PW), and zero-momentum (ZM) phases, sequentially locate in regimes $(0,\ \Omega_{c1})$, $[\Omega_{c1},\ \Omega_{c2}]$ and $(\Omega_{c2},\ +\infty)$ over the range of the Rabi frequency $\Omega$ of the Raman laser beams, see Sec. 2.3. The momentum of the condensate in the last two phases is given as $P_x^{(\rm PW)}/k_{\rm r} = \sqrt{1-\Omega^2/\Omega_{c2}^2}$ and $P_x^{(\rm ZM)}/k_{\rm r} = 0$ from Eq. (2.29) respectively, monotonically decreasing towards zero after exceeding $\Omega_{c2}$. The behaviour of the momentum is denoted by the solid black curve in Fig. 4.1.

However, when including the quantum fluctuations using the HFBP method, there is a qualitative change on the momentum of the condensate in the zero-temperature limit ($T = 10^{-4}T_0$ in the calculations, denoted by the blue curve with circles). At relatively small Rabi frequency, the momentum $P_x$ recovers the one without quantum fluctuations. As the Rabi frequency continues to increase, these two momentum start to slightly deviate from each other and the deviation is significantly enhanced near the PW-ZM transition. Meanwhile, the corresponding critical Rabi frequency $\Omega_{c2}$ of the PW-ZM transition has a small shift towards a larger value. All these qualitative changes are closely related to the quantum fluctuations and its behaviour near the critical transition will be discussed together with the quantum depletion in Sec. 5.5.

Furthermore, once we take into account the thermal fluctuations at nonzero temperatures, more dramatic changes happen on the momentum of the condensation

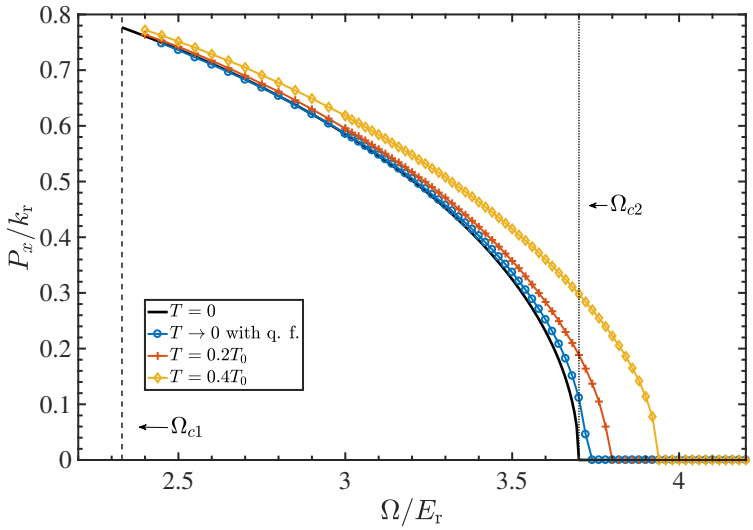


Figure 4.1: Condensation momentum $P_x$ as a function of Raman coupling strength $\Omega$ at various values of temperatures, $T = 0$ (solid black), $T \to 0$ with quantum fluctuation (blue curve with circles), $T = 0.2T_0$ (red curve with crosses) and $T = 0.4T_0$ (yellow curve with diamonds). Here, $\Omega_{c1} \simeq 2.33E_r$ and $\Omega_{c2} \simeq 3.7E_r$ indicate the first-order ST-PW and second-order PW-ZM transitions at $T = 0$ respectively.

phase and the critical Rabi frequency $\Omega_{c2}$. In Fig. 4.1, we present the calculations of the condensation momentum $P_x$ at two different temperatures, $T = 0.2T_0$ (i.e., red curve with crosses) and $T = 0.4T_0$ (i.e., yellow curve with diamonds). Together with the quantum fluctuations, nonzero temperatures lift the condensation momentum even at relatively small Rabi frequency, and the difference of the condensation momentum becomes remarkable near the critical Rabi frequency when the temperature increases. Besides, it's easy to find that thermal fluctuations significantly move the critical PW-ZM transition towards to relatively larger Rabi frequency, which will be discussed explicitly in the following section.

## 4.3 Finite-temperature phase diagram

In Fig. 4.2, we delineate a finite-temperature phase diagram on Raman Rabi frequency (the horizontal axis) and nonzero temperature (the vertical axis). Four distinct regimes could be clearly identified: the ST phase (red), the PW phase

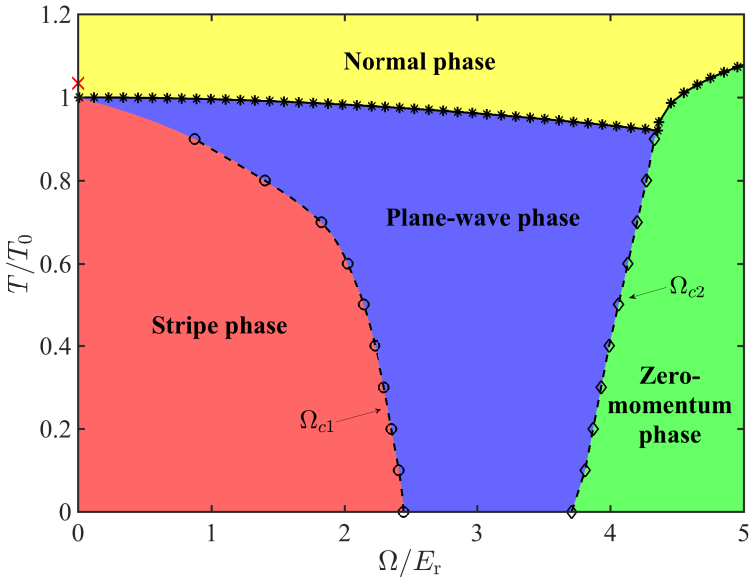


Figure 4.2: Phase diagram of a two-component Bose gas with Raman-induced spin-orbit coupling in the plane of temperature $T$ and Raman coupling strength $\Omega$. The empty circles show a *low* bound for the first-order ST-PW transition, determined from the vanishing roton gap, while the empty diamonds give the second-order PW-ZW transition. The temperature is measured in units of the critical Bose-Einstein condensate temperature of an ideal spinless Bose gas with density $\bar{n}/2$, i.e., $T_0 = 2\pi\hbar^2[(\bar{n}/2)/\zeta(3/2)]^{2/3}/(mk_B)$. We take the total density of our SOC Bose gas, $\bar{n} = 1.0k_r^3$, the intra-species interaction energy, $g\bar{n} = 0.8E_r$, and the inter-species interaction energy $g_{\uparrow\downarrow}\bar{n} = 0.5E_r$. Here, $k_r$ and $E_r = \hbar^2k_r^2/(2m)$ are Raman wave vector and the recoil energy, respectively.

(blue), the ZM phase (green) and normal phase (yellow). From the phase diagram, it is evident that the phase space of the PW phase is greatly enlarged by increasing temperature or thermal fluctuations before reaching the superfluid-to-normal phase transition. The stripe phase is not energetically favorable at relatively large temperature. As mentioned earlier, the stripe phase is driven by the difference in the intra- and inter-species interaction energies, i.e., $gn_c$ and $g_{\uparrow\downarrow}n_c$. This difference decreases with increasing temperature, since the density of the condensate decreases. Hence, the stripe phase shrinks. Our HFBP finding is consistent with the previous experimental determination of the ST-PW boundary with $^{87}$Rb atoms at nonzero

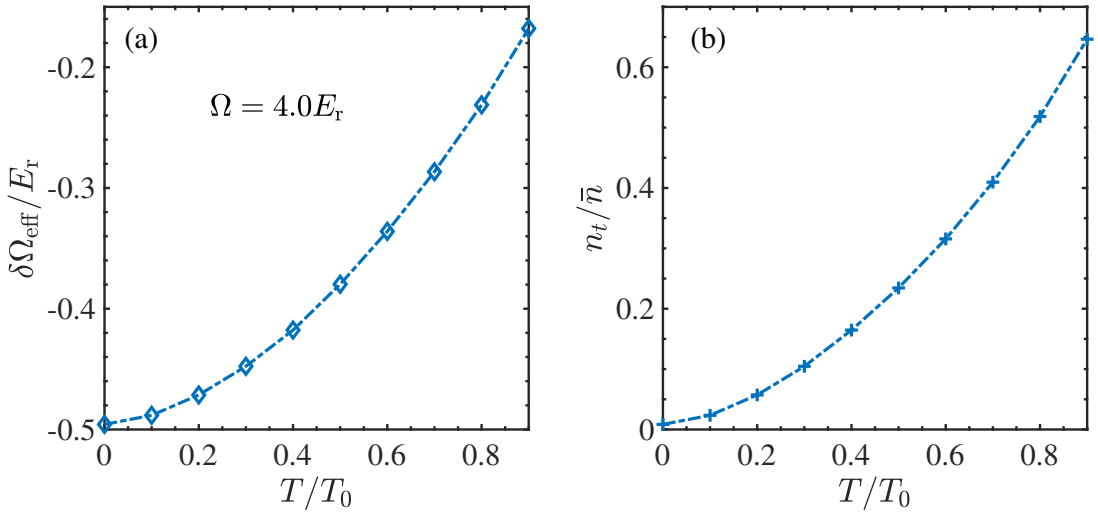


Figure 4.3: The effective Rabi frequency $\delta\Omega_{\text{eff}}$ (a) and thermal fraction $n_t/\bar{n}$ as a function of temperature $T$. Here we take $\Omega = 4.0E_{\text{r}}$. The parameters are the same as in Fig. 4.2.

temperature [105], and it also provides a useful *microscopic* confirmation of the perturbative theory by Yu [222]. In contrast, the significant shrinkage of the ZM phase at finite temperature-observed as well with parameters for $^{87}$Rb atoms-is entirely not expected (see, for example, the naive phase diagram sketched in Ref. [105]). Our results clearly reveal that the PW-ZM boundary is significantly shifted towards relatively larger Rabi frequency by nonzero temperature, which is also found in the sound velocity, exhibiting a minimum at the PW-ZM transition (see Sec. 4.5). Recall that the PW-ZM transition is largely due to the change of the single-particle dispersion with increasing Rabi frequency [7, 95]. From the mean-field point of view, therefore, the notable shift of the PW-ZM boundary suggests a strong temperature dependence of the *effective* Rabi frequency $\delta\Omega_{\text{eff}} \equiv 2g_{\uparrow\downarrow}\phi_\uparrow\phi_\downarrow = -g_{\uparrow\downarrow}n_c\sin(2\theta)$, which is resulted from the inter-species interaction in Eqs. (3.57). Indeed, as shown in Fig. 4.3, such a sensitive temperature dependence of $\delta\Omega_{\text{eff}}$ and thermal faction $n_t/\bar{n}$ is confirmed at a typical Rabi frequency $\Omega = 4.0E_{\text{r}}$.

At high temperature, the SOC Bose gas becomes normal. Unfortunately, sufficiently close to the superfluid-normal phase transition, our HFBP theory becomes less accurate [157]. To determine the transition temperature, we follow the previ-

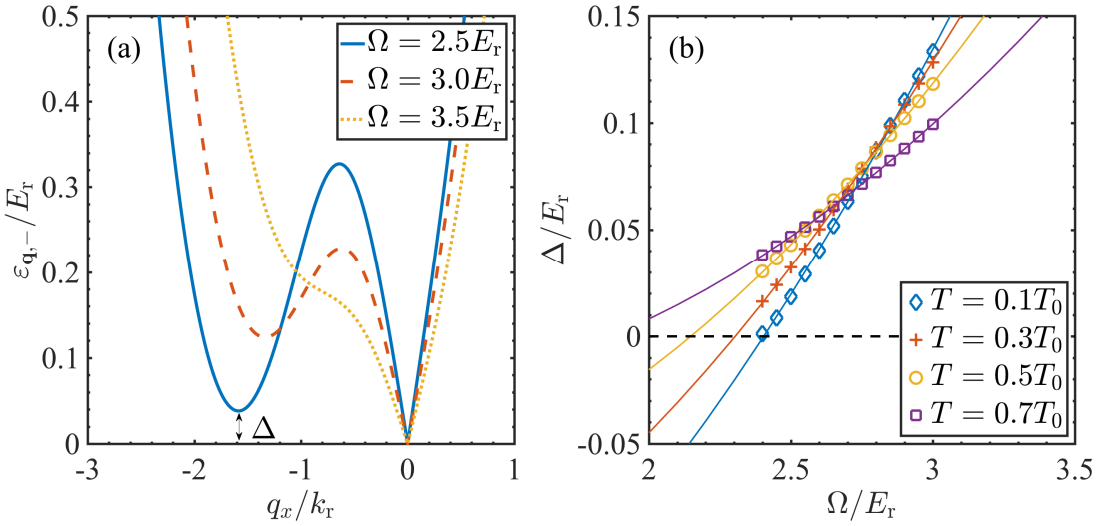


Figure 4.4: (a) The Bogoliubov excitation spectra $\varepsilon_{\mathbf{q},\tau=-}$ at temperature $T = 0.4T_0$ and at various Rabi frequencies $\Omega$, $2.5E_r$, $3.0E_r$ and $3.5E_r$. Here, we set $q_y = q_z = 0$. The roton gap at $\Omega = 2.5E_r$ is explicitly indicated. (b) The roton gap $\Delta$ as a function of Rabi frequency $\Omega$ at different temperatures, fitted with second-order polynomials (solid curves). The parameters are the same as in Fig. 4.2.

ous work by Zheng *et al.* and adopt the Hartree-Fock approximation [101], see the details in Appendix B. The resulting critical temperature $T_c$ is shown at the top of Fig. 4.2 by a solid curve with asterisks. At small Rabi frequency, the predicted $T_c$ differs slightly from the classical Monte Carlo simulation [161, 162] (red cross), which confirmed a linear shift of $T_c$ in the $s$-wave scattering length $\Delta T_c/T_0 \approx 1.3\bar{n}^{1/3}a$ given in Eq. (3.30). At large Rabi frequency (i.e., $\Omega > 4.0E_r$), it is interesting that the Hartree-Fock transition temperature matches reasonably well with the PW-ZM boundary.

## 4.4 Bogoliubov excitation spectrum

We discuss the Bogoliubov excitation spectrum in this subsection, with which we determine the ST-PW and PW-ZM phase transitions with the finite-temperature effects. An intriguing feature of the PW phase is the emergence of the roton-maxon structure in the lowest-lying Bogoliubov excitation spectrum[98, 99, 101], as re-

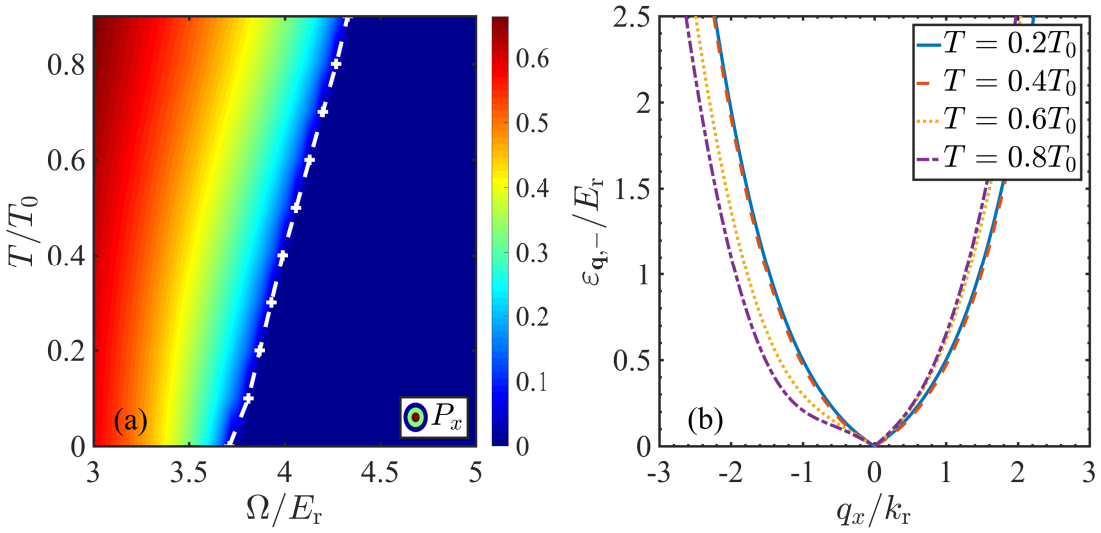


Figure 4.5: (a) The contour plot of the condensate momentum $P_x$, in units of $k_r$,as functions of $T$ and $\Omega$. The boundary $P_x = 0$ between PW and ZM phases is highlighted by the white dashed curve. (b) The Bogoliubov excitation spectra $\varepsilon_{\mathbf{q},\tau=-}$ at various temperatures $T$, with $q_y = q_z = 0$. Here we take $\Omega = 4.0E_r$. The parameters are the same as in Fig. 4.2.

ported in Fig. 4.4(a) at a nonzero temperature $T = 0.4T_0$, where $T_0$ is the critical BEC temperature of an ideal Bose gas defined in Eq. (1.10) with a density $\bar{n}/2$ in the absence of SOC. This structure becomes much more pronounced with decreasing Rabi frequency $\Omega$ and can be quantitatively characterized by a roton gap $\Delta$, as indicated in Fig. 4.4(a) with $\Omega$ from $3.5E_r$, to $3.0E_r$ and to $2.5E_r$. Toward the first-order ST-PW transition, the roton gap is gradually softened and approaches zero *slightly* after the transition [98, 223]. Therefore, as shown in Fig. 4.4(b), we may determine a *low bound* of the critical Rabi frequency $\Omega_{c1}$ from the $\Omega$ dependence of the roton gap for various values of temperature $T$. As the accuracy of our numerical calculations becomes worse at small roton gap, we typically fit the data by using a second-order polynomial [14] and then calculate $\Omega_{c1}$ from the fitting curve. By repeating this procedure at different temperatures, we obtain the temperature dependence of the low bound of the ST-PW boundary, as shown in Fig. 4.2 by the empty circles. We note that a rigorous determination of $\Omega_{c1}$ requires the solution of the HFBP equations for the stripe phase and the comparison of the thermodynamic

potentials of the stripe and plane-wave phases, which is much more involved and is to be considered in the next chapter in Sec. 5.4.

On the other hand, we can straightforwardly determine the second-order PW-ZM transition by identifying the critical Rabi frequency $\Omega_{c2}$, at which the condensate momentum $P_x$ approaches zero. This is illustrated in the contour plot Fig. 4.5(a) of $P_x$ on the $T$-$\Omega$ plane, where the transition is highlighted by the white dashed line (see also the empty diamonds in Fig. 4.2). Furthermore, in Fig. 4.5(b), we check the temperature dependence of the lowest-lying Bogoliubov excitation spectrum at $\Omega = 4.0E_{\mathrm{r}}$. By increasing temperature from $0.2T_0$ to $0.4T_0$, to $0.6T_0$, and then to $0.8T_0$, the spectrum changes from a symmetric shape (with respect to $q_x = 0$) to an asymmetric one. An asymmetric phonon dispersion near $q_x = 0$ is another characteristic feature of the PW phase. It leads to different sound velocities when a density fluctuation propagates along or opposite to the positive $x$ axis, which we shall discuss in the following subsection.

## 4.5 Sound velocity and critical velocity

In this subsection, we discuss the behaviour of the sound velocity and Landau critical velocity in the plane-wave and zero-momentum phases. In the Bogoliubov theory of a weakly interacting Bose gas, in long-wavelength limit ($\mathbf{q} \to 0$), the excitation spectrum exhibits a linear dependence on the quasimomentum $\mathbf{q}$ (i.e. phonon mode $\varepsilon_{\mathrm{exi}}(\mathbf{q}) = c\mathbf{q}$), where the slope coefficient is the corresponding sound velocity $c$ [21, 27]. In the PW phase the anisotropic phonon dispersion at small $q_x$ and the resulting two sound velocities $c_+ > c_-$ along the $x$-direction and the opposite direction respectively [95, 98, 101], which have been measured experimentally to characterize the PW-ZM transition [14]. Note that, turning into the ZM phase the two velocities would merge into one, i.e., $c_+ = c_- \equiv c$ [95, 98, 101], see Fig. 4.4 (a) and 4.5 (b).

In Fig. 4.6(a), we report the behaviour of sound velocities across the PW-ZM transition as a function of Rabi frequency at various temperatures. At zero temperature, all the previous studies predicted a vanishing velocity right at the transition point $\Omega_{c2}$. Physically, since the sound velocity may be well approximated by

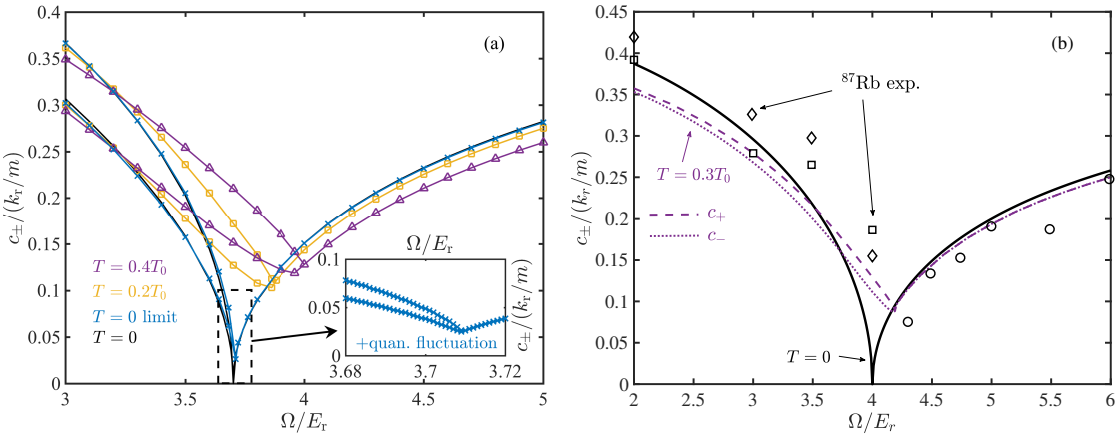


Figure 4.6: (a) Sound velocities $c_+$ and $c_-$ as a function of Rabi frequency $\Omega$ at $T = 0$ (black lines: without quantum fluctuations; blue lines with crosses: with quantum fluctuations), $T = 0.2T_0$ (yellow lines with squares), and $T = 0.4T_0$ (purple lines with triangles). The sound velocities at $T = 0$ near the transition is highlighted in the inset. (b) The sound velocities in a $^{87}$Rb SOC gas at $T = 0$ (black lines) and $T = 0.3T_0$ (purple dotted lines). The symbols are the experimental data [14]. To simulate the experiment, we take a total density $\bar{n} = 0.46k_r^3$, interaction energy strengths $g\bar{n} = 0.38E_r$ and $g_{\uparrow\downarrow}/g = 100.99/101.20$.

$c_{\text{eff}} = \sqrt{g\bar{n}/m_{\text{eff}}}$, the vanishing sound velocity is a consequence of the flatness of the single-particle spectrum at the transition and hence a divergent effective mass $m_{\text{eff}} \to \infty$ [98, 101]. This interesting feature is exactly produced by our numerical calculation if we do not account for the feedback of quantum fluctuations to the total density (see the black solid curve). However, once we take into account quantum fluctuations, there is a qualitative change. Although the sound velocities still exhibit a minimum at the transition, the minimum becomes nonzero. This unexpected gap in sound velocity opened by the enhanced quantum depletion at $\Omega_{c2}$ is typically about $0.03k_r/m$ indicated in the blue curves with crosses (see also the inset). A nonzero temperature brings even more dramatic changes. As temperature increases to $T = 0.2T_0$ (the yellow curves with squares) and to $T = 0.4T_0$ (the purple curves with triangles), we find that the minimum point of sound velocity is progressively shifted toward larger Rabi frequency, along with the shifted phase boundary $\Omega_{c2}$. At the same time, the opening gap at the minimum is significantly enlarged by thermal

fluctuations.

To connect with the recent measurement for $^{87}$Rb atoms, we perform a calculation by taking the peak density of the trapped cloud $\bar{n} = n(\mathbf{r} = 0) = 0.46k_{\mathrm{r}}^3$, which leads to $g\bar{n} = 0.38E_{\mathrm{r}}$ and $g_{\uparrow\downarrow}\bar{n} = 0.998 \times 0.38E_{\mathrm{r}}$ [14]. As shown in Fig. 4.6(b), our result at a realistic experimental temperature $T = 0.3T_0$ (purple dotted curves) agrees reasonably well with the measured sound velocities (open symbols). The experimental data show a nonzero minimum or gap at $\Omega_{c2} \simeq 4.3E_{\mathrm{r}}$ [14]. The previous theoretical studies at zero temperature instead predict a vanishing sound velocity at $\Omega_{c2} \simeq 4.0E_{\mathrm{r}}$ (see the black solid curves) and therefore fail to explain the observed shift of the minimum, $\Delta\Omega_{c2} \sim 0.3E_{\mathrm{r}}$, and the gap opening. It was suggested that the suppressed third spin state of $^{87}$Rb atoms in the experiment may be responsible for the shift and the gap opening [14]. The opening of the gap was also predicted in the case of a nonzero laser detuning $\delta \neq 0$ [224]. The good agreement between our theory and experiment indicates that actually the nonzero temperature in the experiment plays a crucial role near the PW-ZM transition and it has to be accounted for in future experimental investigations.

In the well-known Landau criterion to understand the mechanism of the superfluidity [25, 26], a critical velocity is defined as [21, 22, 225], $v_c \equiv \min\left[\varepsilon_{\mathrm{exi}}(\mathbf{q})/\mathbf{q}\right]$, related to the elementary excitation spectrum $\varepsilon_{\mathrm{exi}}(\mathbf{q})$ at quasimomentum $\mathbf{q}$. In the conventional Bose gases with weak couplings, the elementary excitation spectrum is isotropic and the Landau critical velocity $v_c$ equals the sound velocity $c$.

However, a Bose gas with the Raman-induced SOC has remarkably different excitation spectrum along the SOC direction and in the perpendicular plane, which gives rise to anisotropic critical velocity (see also Ref. [226]). In the PW phase, the excitation spectrum becomes asymmetric along $x$ axis due to the exotic single-particle dispersion relation, and it exhibits a roton-maxon structure in the negative quasimomentum regime in our case as the Rabi frequency decreases toward the ST-PW transition. In Fig. 4.7, we present the critical velocities (dashed curves with crosses) along with the sound velocities (solid curves) in the $x$ and $-x$ directions at different temperatures. In the ZM phase, the symmetric spectrum leads to two identical velocities. However below a certain Rabi frequency in the PW phase, the roton starts to emerge and significantly softens the minimum of the ratio of excitation energy over quasimomentum (i.e. the critical velocity). The important

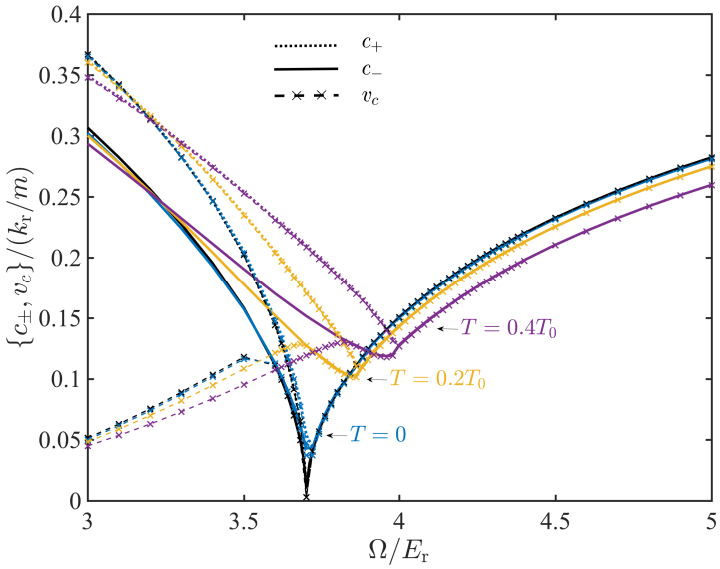


Figure 4.7: Sound velocities (solid lines) and Landau critical velocity (dashed lines with crosses) as a function of Rabi frequency $\Omega$. The parameters are the same as in Fig. 4.6 (a).

roton structure makes the critical velocity deviating from the sound velocity in the $-x$ direction. The corresponding critical velocity continues to decrease toward zero as the Rabi frequency decreases or the roton energy gap reduces, see also Sec. 4.4. This implies that it is easy to create the excitations, which will destroy the superfluidity of the system. The intriguing behaviour of the critical velocity is in sharp contrast to the conventional Bose gases without SOC. A similar behaviour also exists in the anisotropic atomic system with a dipole-dipole interaction, where the elementary excitation spectrum also exhibits an exotic roton structure [226–228].

## 4.6 Other observables

Another interesting physical property of such a spinor Bose gas with SOC is the magnetization of the gas, which is a useful observable that can be measured explicitly in the experiments [7, 105]. It is defined as

$$M_i = \frac{n_{i\uparrow} - n_{i\downarrow}}{n_{i\uparrow} + n_{i\downarrow}}, \tag{4.6}$$

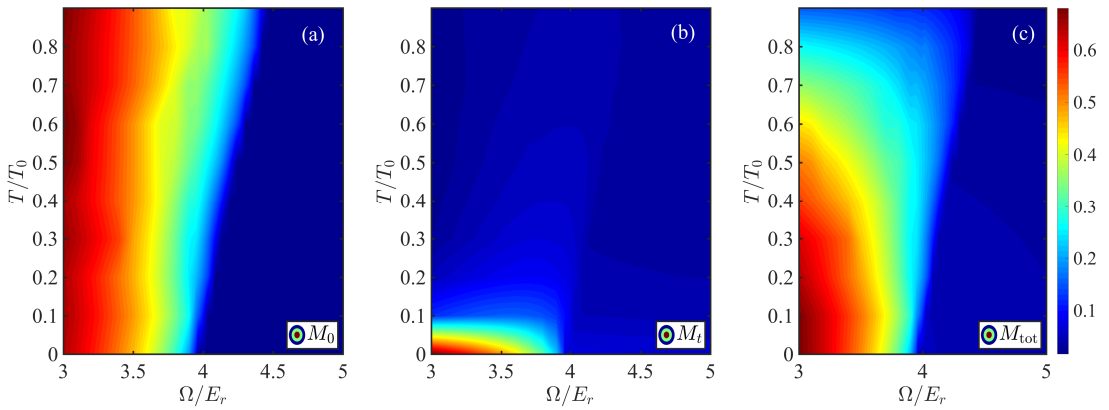


Figure 4.8: The contour plot of the magnetization for the condensate (a), non-condensate (b) and total density (c) respectively, as functions of $T$ and $\Omega$. Here, we set $g\bar{n} = 0.32E_{\rm r}$ and $g_{\uparrow\downarrow} = 0.86g$ with the total density $\bar{n} = 1.0k_{\rm r}^3$. Correspondingly two critical Rabi frequencies become $\Omega_{c1} \approx 1.50E_{\rm r}$ and $\Omega_{c2} \approx 3.96E_{\rm r}$.

where the index label $i =$ "0", "t" and "tot" denotes the one of the condensate $M_0$, of thermal gas $M_{\rm t}$ and of total atoms $M_{\rm tot}$, respectively. At zero temperature, the condensate density equals the total density when excluding the negligible quantum depletion. The analytic expression of the corresponding magnetization is [95], $M_0 = \cos 2\theta = \sqrt{1-\Omega^2/\Omega_{c2}^2}$ for $\Omega_{c1} < \Omega < \Omega_{c2}$ in the PW phase, and $M_0 = 0$ for $\Omega \leq \Omega_{c2}$ in the ZM phase (see Eq. (2.30)). To evaluate the relevant magnetization, we set $g\bar{n} = 0.32E_{\rm r}$ and $g_{\uparrow\downarrow} = 0.86g$ with the total density $\bar{n} = 1.0k_{\rm r}^3$. Correspondingly two critical Rabi frequencies become $\Omega_{c1} \approx 1.50E_{\rm r}$ and $\Omega_{c2} \approx 3.96E_{\rm r}$.

In Fig. 4.8, we depict sequentially the contour plot of the magnetization for the condensate, non-condensate and total atoms of the Bose gas. At zero temperature, as the Rabi frequency increases, the magnetization of the condensate $M_0$ in the figure will reduce monotonically in the PW phase, and becomes zero at the critical position and further in the ZM phase phase, as anticipated from the analytic prediction. At a nonzero temperature, $M_0$ and/or the magnetization of the total atoms $M_{\rm tot}$ reach zero at the PW-ZM transition position $\Omega_{c2}$ and the critical position shifts to a larger $\Omega$ as the temperature increases (see also the PW-ZM phase boundary in Sec. 4.3). These magnetizations are measurable in the experiment [105], which can be used to determine the finite-temperature phase diagram in the PW and ZM phases in future experimental investigations.

The thermal magnetization $M_{\mathrm{t}}$ is shown in the middle figure as functions of nonzero temperature and Rabi frequency. At sufficiently high temperature near the BEC temperature $T_0$ of an ideal gas, the large blue region over the total Rabi frequency range implies the non-magnetic character of the non-condensate atoms. The result shows a good agreement with the measurement in recent experiment[105]. Furthermore, it's interesting to turn to the low-temperature regime, where $M_{\mathrm{t}}$ is remarkably distinct in the PW and ZM phases. The reason is that, below the critical Rabi frequency $\Omega_{c2}$, the single-particle dispersion shows double degenerate minima. In the PW phase, the condensation locates at the positive momentum $P_x$, and $M_{\mathrm{t}}$ is positive which comes dominantly from the phonon mode in the excitation spectrum. As the Rabi frequency continues to decrease towards the ST-PW transition position $\Omega_{c1}$ or the temperature continues to increase, the roton-maxon structure emerges at $q_x = -2P_x$ in the excitation spectrum and becomes more and more pronounced (see Fig. 4.4). The roton starts to make a non-negligible negative contribution, which competes with the positive one from the phonon mode, giving rise to a smoothly reducing $M_{\mathrm{t}}$ as $\Omega$ decreases or $T$ increases.

# Chapter 5

# The supersolid stripe phase at zero temperature

In this chapter, by emphasizing the exotic stripe phase at *zero* temperature, the same three-dimensional weakly interacting Bose gas with Raman-type spin-orbit coupling are investigated via the generalized Hartree-Fock-Bogoliubov theory with Popov approximation developed in Sec. 3.2.3. We provide a short introduction and motivation first, along with a brief theoretical framework in Sec. 5.1. In Secs. 5.2 and 5.3, we present the density profile, the momentum of the condensate, the exotic Bogoliubov excitation spectrum and the corresponding sound velocities in the stripe phase. We then predict an improved critical ST-PW transition by taking high-order harmonics in the ansatz in Secs. 5.4. The quantum depletion is calculated as a function of Rabi frequency across three phases in Sec. 5.5 (Fig. 5.7). In Sec. 5.6, the analytic expression of the superfluid density is derived for all the three phases using a first-order ansatz for the ground-state wavefunction. Particularly in the stripe phase, the analytic prediction is compared with the more accurate numerical result after considering a high-order ansatz (see Fig. 5.8). Part of this chapter are summarized in the publication [145].

## 5.1 Introduction and motivation

We have introduced the three-dimensional weakly interacting Bose gases with one-dimensional Raman-type spin-orbit coupling in Secs. 2 and 4. The system exhibits sequentially three exotic condensation phases at zero temperature, i.e., the stripe (ST), plane-wave (PW), and zero-momentum (ZM) phases as the Rabi frequency of the Raman laser beams gradually increases [7, 96, 98, 101]. Previous investigations mainly focus on the last two phases. Several properties have been addressed, including the ground-state phase diagram [95, 101], quantum and thermal fluctuations [100, 103, 229, 230], collective excitations [146, 231], superfluidity and critical velocities [226, 232, 233]. However, only a handful of works involved the stripe phase, which attracts greater attention after being observed in recent experiments with ultra-cold atomic gases [106, 234].

Theoretically, the existence of a stripe phase in a spin-orbit coupled Bose gas was first predicted in Refs. [91, 93, 95] with a first-order stripe ansatz for the ground-state wavefunction. Later, by employing an improved high-order ansatz and calculating the static structure factor, Y. Li and her collaborators characterized the spin and density responses of the stripe phase, and found two gapless modes in the elementary excitation spectrum [144]. This calculation clearly indicates the importance of high-order harmonics in the trial ansatz, for the purpose of *quantitatively* characterizing the stripe phase. Unfortunately, apart from the elementary excitation spectrum, none of the other physical properties of the stripe phase has so far been investigated with taking into account high-order harmonics. Experimentally, in a SOC Bose gas of $^{87}$Rb atoms, the phase space for the stripe phase is small. G. I. Martone *et al.* tried to enhance the stripe contrast to make it visible and stable under realistic experimental conditions, by theoretically considering the loading of atoms into a two-dimensional bilayer configuration [164]. Most recently, J.-R. Li and coworkers achieved effective SOC in optical superlattices, and observed for the first time the exotic stripe phase with supersolid properties using Bragg spectroscopy [106, 235]. This experimental breakthrough provides a great opportunity to test and verify the theoretical predictions on the stripe phase.

In this chapter, motivated by previous theoretical studies and recent experiments, we explore the fascinating stripe phase and aim to make quantitative predictions

on several fundamental properties of this phase using the high-order stripe ansatz. Within the Bogoliubov approximation, we first consider the dependence of the density distribution and the excitation spectrum on the tunable Rabi frequency. By introducing high-order harmonics and comparing the free energy in different trial ansatz, we then obtain an improved critical Rabi frequency for the transition between the stripe and plane-wave phases. The depletion of the condensate induced by quantum fluctuations is numerically calculated, with which we can characterize straightforwardly the first-order ST-PW transition and the second-order PW-ZM transition. Finally, by employing a phase-twist method, we discuss the superfluidity of a SOC Bose gas via calculating the superfluid density in all three phases.

The details of the employed HFBP method are described in Sec. 3.2.3 in the presence of Raman-type SOC. By starting with a trial ansatz for the ground-state wave function $\phi(\mathbf{r})$ and then solving the GP and Bogoliubov equations, Eqs. (3.54) and (3.56), one obtains straightforwardly the ground state $\phi(\mathbf{r})$ and the elementary excitation spectrum $\varepsilon_j$, as a function of Rabi frequency $\Omega$. At zero temperature, the total energy of the system can be written in terms of wavefunctions $\phi(\mathbf{r})$ as [95]

$$\begin{aligned} E = \int d^3\mathbf{r} \Bigg[ & \left(\phi_\uparrow^\dagger(\mathbf{r}), \phi_\downarrow^\dagger(\mathbf{r})\right) \mathcal{H}^{\mathrm{SOC}} \begin{pmatrix} \phi_\uparrow(\mathbf{r}) \\ \phi_\downarrow(\mathbf{r}) \end{pmatrix} \\ & + \frac{1}{2} g \left( |\phi_\uparrow(\mathbf{r})|^4 + |\phi_\downarrow(\mathbf{r})|^4 \right) + g_{\uparrow\downarrow} |\phi_\uparrow(\mathbf{r})|^2 |\phi_\downarrow(\mathbf{r})|^2 \Bigg] . \end{aligned} \tag{5.1}$$

with the single-particle Hamiltonian $\mathcal{H}^{\mathrm{SOC}}$ given in Eq. (3.52). We set the density of the condensate to be the total density, $n_c = \bar{n}$. We note that, even at zero temperature, the condensate is still depleted by a small fraction of the total density, due to quantum fluctuations. This is the so-called quantum depletion defined in Eq. (3.17),

$$n_{\mathrm{qd}} = \sum_{j,\sigma=\uparrow,\downarrow} |v_{j\sigma}|^2, \tag{5.2}$$

involving typically about one per-cent of the total density, i.e., $n_{\mathrm{qd}} \sim 0.01n$. Here, the index $j$ indicates the quasiparticle energy level and $\sigma =\uparrow$ or $\downarrow$ is the spin component label. The quantum depletion will be explored thoroughly in Sec. 5.5. Quantum fluctuations also lead to the well-known Lee-Huang-Yang (LHY) correction to the total energy, beyond the mean-field approximation. In our calculations, for the self-

consistency of the theory, we do not include the LHY correction to the energy, which is at the order of the square root of the gas parameter $(\bar{n}a^3)^{1/2}$ [101]. Otherwise, the energy correction at the same order due to the anomalous densities may have to be taken into account on an equal footing, which is clearly beyond the scope of our work.

## The plane-wave ansatz

The magnetic plane-wave phase and the non-magnetic zero-momentum phase have been extensively investigated in previous works [15, 98, 101, 103], by using a *plane-wave ansatz* given in Eq. (3.53) with a momentum $P_x$

$$\phi(\mathbf{r}) = \sqrt{\bar{n}} \begin{pmatrix} \cos\theta \\ -\sin\theta \end{pmatrix} e^{iP_x x}. \tag{5.3}$$

Here, $\bar{n} = N/V$ is the uniform average density and the variational angle $\theta$ in the range $[0, \pi/4]$ describes the spin components of the condensate. In free space, the quasiparticle amplitudes $u_{j\sigma}(\mathbf{r})$, $v_{j\sigma}(\mathbf{r})$ with index $j = (\mathbf{q}, \tau)$ for spin component $\sigma$ can be written as $u_{j\sigma}(\mathbf{r}) = u^{\tau}_{\mathbf{q}\sigma} e^{i\mathbf{q}\mathbf{r}}/\sqrt{V}$ and $v_{j\sigma}(\mathbf{r}) = v^{\tau}_{\mathbf{q}\sigma} e^{i\mathbf{q}\mathbf{r}}/\sqrt{V}$, where the normalization condition for each branch of two physical solutions ($\tau = \pm$) is given by,

$$\sum_{\mathbf{q}\sigma} (|u^{\tau}_{\mathbf{q}\sigma}|^2 - |v^{\tau}_{\mathbf{q}\sigma}|^2) = 1. \tag{5.4}$$

In this case, the ground-state energy per particle in Eq. (5.1) becomes [95, 103] (see also Eq. (4.4))

$$\frac{E^{(\mathrm{PW})}}{N} = \frac{P_x^2 + k_{\mathrm{r}}^2 - 2P_x k_{\mathrm{r}} \cos 2\theta}{2m} - \frac{1}{2}\Omega \sin 2\theta + \frac{2g\bar{n} - (g - g_{\uparrow\downarrow})\bar{n} \sin^2 2\theta}{4}. \tag{5.5}$$

The minimization of the energy gives rise to two solutions: the plane-wave phase where the condensates occur at the momentum $P_x = \pm k_{\mathrm{r}} \sqrt{1 - \Omega^2/(4E_{\mathrm{r}} - (g - g_{\uparrow\downarrow})\bar{n})^2}$ for $\Omega \leq 4E_{\mathrm{r}} - (g - g_{\uparrow\downarrow})\bar{n}$ and the zero-momentum phase with zero momentum $P_x = 0$ for $\Omega > 4E_{\mathrm{r}} - (g - g_{\uparrow\downarrow})\bar{n}$ [95, 103], see also Sec. 2. In the lowest-lying excitation spectrum, a typical feature of the plane-wave phase is the emergence of the roton-maxon structure. The zero-momentum phase exhibits only the linear phonon mode [98, 101, 103].

### The stripe ansatz

Instead of the well-studied plane-wave phase and zero-momentum phase, we are concentrating on the exotic stripe phase in this work, which was recently observed in ultra-cold atomic systems [106, 234]. To understand the key properties of the stripe phase, a *first-order* stripe ansatz is often adopted [95, 105, 164, 222],

$$\phi(\mathbf{r}) = \sqrt{\frac{\bar{n}}{2}}\left[\begin{pmatrix}\sin\theta\\ -\cos\theta\end{pmatrix}e^{-iP_x x} + \begin{pmatrix}\cos\theta\\ -\sin\theta\end{pmatrix}e^{iP_x x}\right]. \tag{5.6}$$

This ansatz is an equal superposition of two plane-wave with momentum $\pm P_x$, in contrast to the single-plane-wave ansatz given in Eq. (5.3).

By substituting this trial wave function, Eq. (5.6), into the model Hamiltonian and minimizing the ground-state energy per particle, which takes the form [95],

$$\frac{E^{(1\mathrm{st})}}{N} = \frac{P_x^2 + k_\mathrm{r}^2 - 2P_x k_\mathrm{r}\cos 2\theta}{2m} - \frac{1}{2}\Omega\sin 2\theta + \frac{(g+g_{\uparrow\downarrow})\bar{n}}{4}(1+\frac{1}{2}\sin^2 2\theta), \tag{5.7}$$

one can straightforwardly determine the critical Rabi frequency $\Omega$ of three exotic phases in the appropriate interaction regimes (i.e., $G_2 > 0$ [1]), which are respectively given by [95], $\Omega_{c1} = 4\left[(2E_\mathrm{r}+G_1)(E_\mathrm{r}-G_2)G_2/(G_1+2G_2)\right]^{1/2}$ for the ST-PW phase transition in Eq. (2.25), and $\Omega_{c2} = 4E_\mathrm{r} - 4G_2$ for the PW-ZM phase transition in Eq. (2.26). Here, the two interaction parameters are $G_1 = (g+g_{\uparrow\downarrow})\bar{n}/4$ and $G_2 = (g-g_{\uparrow\downarrow})\bar{n}/4$. It is worth mentioning that, in the last chapter [103], we have determined the ST-PW transition at zero temperature using the criterion of a vanishing roton energy gap (see Sec. 4.4). The determined critical Rabi frequency is exactly the same as $\Omega_{c1}$, if we neglect quantum fluctuations.

The critical Rabi frequency in Eq. (2.25) for the ST-PW boundary is accurate at the sufficiently weak interaction strengths (i.e., $G_1/E_\mathrm{r}, G_2/E_\mathrm{r} \to 0$). However, when the interactions become stronger, a high-order stripe ansatz with high-order harmonics (i.e., the plane waves with wave vectors $\pm 3P_x$, $\pm 5P_x$, etc.) may have to be considered [144]. In this work, we take the following stripe ansatz that includes

[1] The condition is necessary for the existence of the exotic stripe phase, where the more strict one is $E_\mathrm{r} > 2G_2 + 2G_2^2/G_1$ in Ref. [95].

high-order terms [144]

$$\phi(\mathbf{r}) = \sqrt{\frac{\bar{n}}{2}} \sum_{\gamma=\pm} \sum_{\alpha=1}^{N_{\rm L}} \begin{pmatrix} \phi_{\uparrow}^{(\gamma\alpha)} \\ \phi_{\downarrow}^{(\gamma\alpha)} \end{pmatrix} e^{i\gamma(2\alpha-1)P_x x}, \tag{5.8}$$

which possesses a symmetry, $\phi_{\uparrow}^{(\alpha)} = -[\phi_{\downarrow}^{(-\alpha)}]^*$, and is periodically-repeating in real space. Here, $\alpha$ is the index of the stripe order and is smaller or equal to a cut-off integer $N_{\rm L}$. After solving the wave function $\phi(\mathbf{r})$, the ground-state energy $E^{(N_{\rm L})}$ can be numerically calculated using Eq. (5.1). At $N_{\rm L} = 1$, the energy $E^{(N_{\rm L}=1)}$ recovers the analytic expression for the first-order stripe ansatz, $E^{(\rm 1st)}$ in Eq. (5.7).

To investigate the low-energy excitations, the Bogoliubov quasiparticle amplitudes $u$, $v$ for the index $j = (\mathbf{q}, \tau)$ and spin $\sigma$ can be simply expanded in a Bloch form as [144]

$$u_{j\sigma}(\mathbf{r}) = e^{i\mathbf{qr}} \sum_{\gamma=\pm} \sum_{\beta=1}^{N_{\rm M}} u_{\sigma}^{(\gamma\beta,\tau)} e^{i\gamma(2\beta-1)P_x x}, \tag{5.9a}$$

$$v_{j\sigma}(\mathbf{r}) = e^{i\mathbf{qr}} \sum_{\gamma=\pm} \sum_{\beta=1}^{N_{\rm M}} v_{\sigma}^{(\gamma\beta,\tau)} e^{i\gamma(2\beta-1)P_x x}, \tag{5.9b}$$

where $\mathbf{q}$ is the quasi-momentum and $\beta$ is the expansion order index and is smaller or equal to the cut-off integer $N_{\rm M}$. We substitute Eqs. (5.9) into the Bogoliubov equations Eqs. (3.56), to determine the expansion coefficients $u_{\sigma}^{(\gamma\beta,\tau)}$ and $v_{\sigma}^{(\gamma\beta,\tau)}$.

In the recent experiments [7, 14, 105], $^{87}$Rb atoms are used. The typical interaction energy is $gn = 0.38E_{\rm r}$ with the peak density $n = 0.46k_{\rm r}^3$ in harmonic traps, and the ratio between the inter-species interaction and intra-species interaction is very close to unity, i.e., $g_{\uparrow\downarrow}/g = 100.99/101.20$ [14]. With these parameters, the two critical Rabi frequencies are respectively given by, $\Omega_{c1} = 0.2E_{\rm r}$ and $\Omega_{c2} = 4.0E_{\rm r}$ (see Eqs. (2.25) and (2.26)), characterizing the first-order ST-PW and second-order PW-ZM phase transitions at zero temperature. The stripe phase is energetically favored at only a small region $\Omega \leq 0.2E_{\rm r}$ of the Rabi frequency. The contrast in the stripe density is not large enough to be resolved in the laboratories [7, 105, 164]. In our calculations, we will consider a relatively large ratio of inter- intra-species interaction strengths (i.e., large $G_1$ and $G_2$), in order to enlarge the window for the stripe phase in the phase diagram.

It's worth noting that, in our numerical calculations, we take the cut-offs $N_{\mathrm{L}} = N_{\mathrm{M}} \geq 14$, to ensure that our results are cut-off independent (see Appendix D for the check on the cut-off dependence).

## 5.2 Ground-state property and condensate momentum

In this subsection, we study the density profile and corresponding condensate momentum in the stripe phase. At zero temperature, we assume the typical interaction energies $G_1 = 0.5E_{\mathrm{r}}$ and $G_2 = 0.1E_{\mathrm{r}}$ with the average density $\bar{n} = 1.0k_{\mathrm{r}}^3$. It gives rise to the critical Rabi frequencies, $\Omega_{c1} = 2.27E_{\mathrm{r}}$ and $\Omega_{c2} = 3.60E_{\mathrm{r}}$ in Eqs. (2.25) and (2.26), with the first-order stripe ansatz.

In Fig. 5.1, by setting two different Rabi frequencies $\Omega = 0.1E_{\mathrm{r}}$ and $1.0E_{\mathrm{r}}$, we present the respective density distributions in different colors. In contrast to the plane-wave and zero-momentum phases, the density of the condensate is modulated by the SOC strength in the stripe regime with a spatially periodic order. The total density contrast of the stripe can be estimated using the first-order stripe ansatz

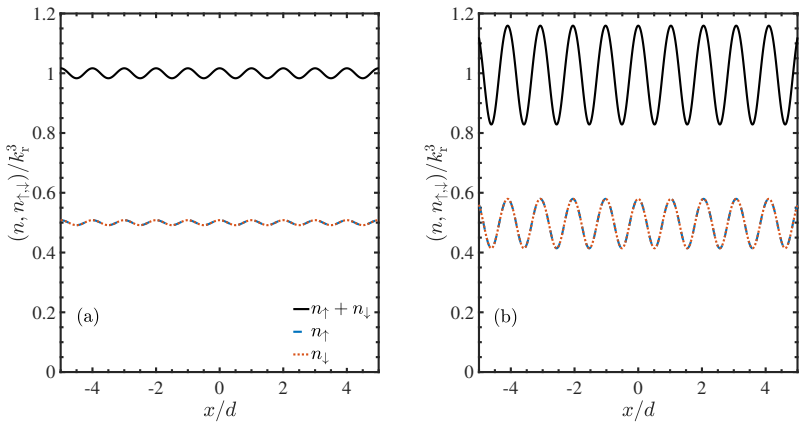


Figure 5.1: The high-order stripe density profile $n$ for spin-up atoms, spin-down atoms, and total atoms along the SOC direction at two Rabi frequencies $\Omega = 0.1E_{\mathrm{r}}$ (a) and $\Omega = 1.0E_{\mathrm{r}}$ (b). Here, we take $G_1 = 0.5E_{\mathrm{r}}$ and $G_2 = 0.1E_{\mathrm{r}}$. $d = \pi/P_x$ is the spatial periodicity of stripes. The two dashed lines in (c) show the phonon dispersion of a conventional two-component Bose gas in the limit of $\Omega = 0$.

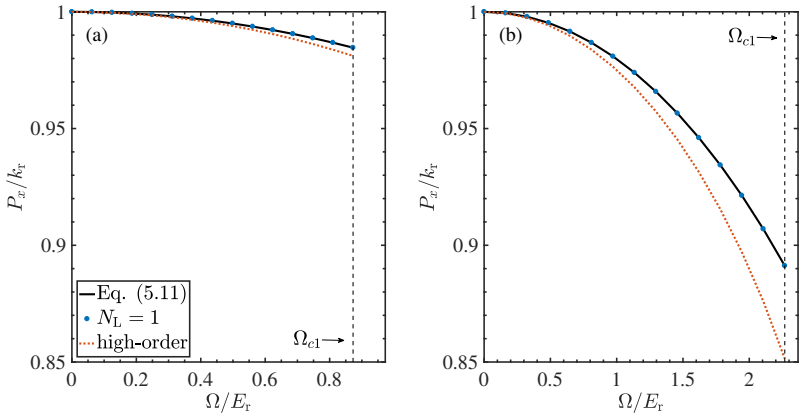


Figure 5.2: The momentum $P_x/k_r$ of the condensate as a function of the Rabi frequency $\Omega$, from Eq. (5.11) (solid black curves), and high-order calculations with $N_L = 1$ (blue circles), $N_L = 16$ (dashed red curves). Here, we take $G_1 = 0.5E_r$, $G_2 = 0.01E_r$ (a) and $G_2 = 0.1E_r$ (b). The dashed lines show the corresponding critical Rabi frequency of the ST-PW transition $\Omega_{c1}$ in Eq. (2.25).

and is given by [95, 164]

$$\mathcal{C} \equiv \frac{n_{\max} - n_{\min}}{n_{\max} + n_{\min}} = \frac{\Omega}{2(2E_r + G_1)}. \tag{5.10}$$

At $\Omega = 0.1E_r$ and $1.0E_r$, the modulation amplitude $\mathcal{C}$ is about 0.02 and 0.2 of the total average density $\bar{n}$, respectively. These estimations agree well with the high-order density profiles illustrated in Fig. 5.1(a) and 5.1(b).

In Fig. 5.2, we calculate the momentum $P_x$ of the condensate in the stripe phase as a function of the Rabi frequency $\Omega$ at two sets of interaction strengths, $G_1 = 0.5E_r$, $G_2 = 0.01E_r$ and $0.1E_r$. Starting from a first-order stripe ansatz in Eq. (5.6), the analytic expression for the condensate momentum $P_x$ of the stripe phase is given from Eq. (2.34) as

$$P_x^{(\mathrm{ST})} = k_r \sqrt{1 - \frac{\Omega^2}{(4E_r + 2G_1)^2}}, \tag{5.11}$$

denoted by the solid black curves. Meanwhile, the condensate momentum can be calculated numerically by minimizing the mean-field energy of the high-order stripe ansatz in Eq. (5.8). When $N_L = 1$, the momentum in blue circles recovers exactly the analytic one from the first-order stripe ansatz. After including high-order terms,

i.e., $N_{\mathrm{L}}$ sufficiently large, the condensate momentum $P_x$ starts to be different with the first-order result at the relatively large Rabi frequency. The difference becomes significant near the ST-PW transition $\Omega_{c1}$ when the interaction strength $G_2$ becomes relatively large. This behaviour implies the non-negligible role of high-order harmonics in the relatively large space of $G_2$. The important role of high-order harmonics can be also seen in Sec. 5.4.

## 5.3 Bogoliubov excitation spectrum and sound velocity

In this subsection, we study the low-energy Bogoliubov excitation spectrum in the stripe phase, and explore the anisotropic behaviour of sound velocity over a range of Rabi frequency.

The previous investigations in Sec. 4.4 have shown that the lowest-lying excitation spectrum in the plane-wave phase exhibits an intriguing roton-maxon structure, due to the degenerate double-minimum in the single-particle dispersion [98, 101, 103, 236]. As the Rabi frequency decreases towards the ST-PW transition, the roton structure becomes much more clear and the roton energy gap is gradually approach-

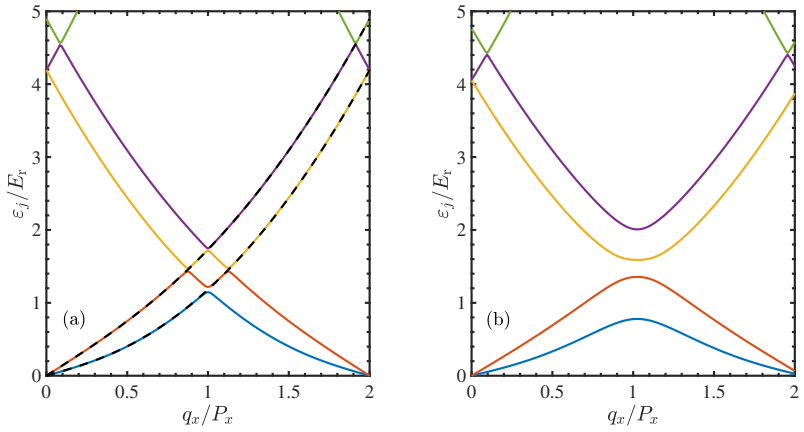


Figure 5.3: The Bogoliubov excitation spectrum $\varepsilon_j$ for the lowest five branches in the SOC direction. Here, $G_1 = 0.5E_{\mathrm{r}}$ and $G_2 = 0.1E_{\mathrm{r}}$ at the respective Rabi frequency $\Omega = 0.1E_{\mathrm{r}}$ (a) and $1.0E_{\mathrm{r}}$ (b).

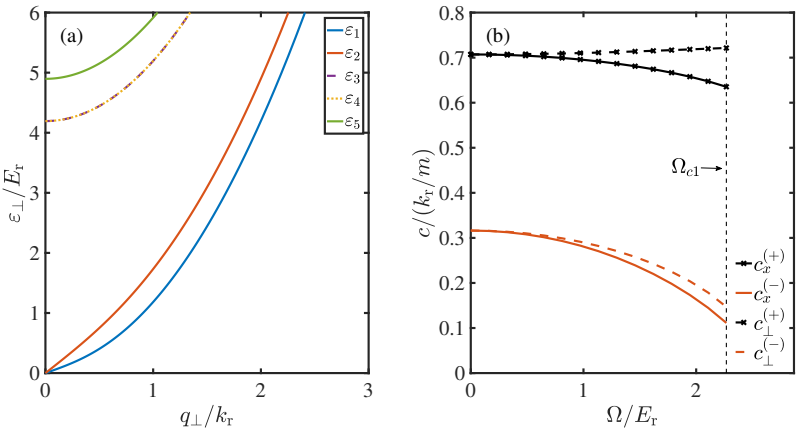


Figure 5.4: (a) The lowest five excitation spectra $\varepsilon_\perp$ in $yz$ plane ($q_\perp = \sqrt{q_y^2 + q_z^2}$) at $\Omega = 0.1E_\mathrm{r}$. (b) Sound velocity of the lowest (red) and second-lowest (black) excitation branches in $x$ direction (solid) and in $yz$ plane (dashed), as a function of $\Omega$. The dashed vertical line indicates the critical Rabi frequency $\Omega_{c1}$ for the ST-PW transition. The interaction parameters are the same as in Fig. 5.3.

ing zero, indicating a critical ST-PW Rabi frequency [103]. However, in the stripe phase, the density modulation spontaneously breaks the spatial translational symmetry, giving rise to infinite gapped branches as a function of the quasi-momentum $q_x \in [0, 2P_x]$. The lowest two branches are gapless [144], as indicated by two linear phonon modes, i.e., the red and blue curves in Fig. 5.3(a) and 5.3(b). As we decrease the Rabi frequency towards the limit $\Omega \to 0$, the gap between different excitation branches vanishes and one recovers the Bogoliubov excitation spectrum [163]

$$\omega_\pm(\mathbf{k}) = \sqrt{\frac{\hbar^2\mathbf{k}^2}{2m}\left[\frac{\hbar^2\mathbf{k}^2}{2m} + (g \pm g_{\uparrow\downarrow})\bar{n}\right]}, \tag{5.12}$$

anticipated for a conventional two-component Bose gas [see the two dashed black curves in Fig. 5.3(a)]. Furthermore, the Bogoliubov excitation spectrum in the perpendicular direction (i.e., $yz$ plane) is shown in Fig. 5.4(a). In the absence of SOC, the spectrum $\varepsilon_\perp$ exhibits two gapless branches, the same as in the conventional two-component Bose gas.

In Fig. 5.4(b), we compare the sound velocities of two gapless modes in the $x$ and $yz$ directions, i.e., $c_x^{(\pm)}$ and $c_\perp^{(\pm)}$, respectively. As the Rabi frequency increases towards the transition $\Omega_{c1}$ to the plane-wave phase, $c_x^{(\pm)}$ (solid curves) start to

be lower than $c_{\perp}^{(\pm)}$ (dashed curves) for both branches and the difference becomes big at relatively large $\Omega$, revealing the remarkable density modulation of stripes along the direction of SOC. It's worth noting that, in the limit $\Omega \to 0$, the sound velocities in two directions merge to one, and the sound velocities of two branches reproduce the analytic expression $\sqrt{(g \pm g_{\uparrow\downarrow})\bar{n}/2m}$ from the Bogoliubov theory with $c^{(+)} \approx 0.7071 k_{\rm r}/m$ and $c^{(-)} \approx 0.3162 k_{\rm r}/m$, respectively. The similar results are first reported in Ref. [144].

## 5.4 Critical Rabi frequency for the ST-PW phase transition

Generally the two critical Rabi frequencies for the ST-PW and PW-ZM phase transitions, i.e., $\Omega_{c1}$ and $\Omega_{c2}$, are determined by comparing the total energy $E^{(\rm 1st)}$ of the first-order stripe and $E^{(\rm PW)}$ of the plane-wave ansatz, (see Eqs. (5.7) and (5.5) or Sec. 2.3). By taking into account high-order harmonics in Eq. (5.8), the stripe phase may become energetically more favorable and as a consequence the first-order ST-PW transition position may shift to a relatively larger Rabi frequency $\Omega_{c1}^{(\rm new)}$. This is indeed confirmed in Fig. 5.5. At the same interaction parameters, the ground-state energy of the stripe phase becomes lower with the inclusion of high-order harmonics, i.e. $E^{(N_{\rm L})} \leq E^{(\rm 1st)}$. The window for the stripe phase is therefore enlarged, with a larger critical Rabi frequency $\Omega_{c1}^{(\rm new)} = 2.47 E_{\rm r} > \Omega_{c1} = 2.27 E_{\rm r}$ for the first order ST-PW transition.

In Fig. 5.6(a), we show the dependence of the relative shift of the ST-PW transition, $\delta\Omega_1 \equiv \Omega_{c1}^{(\rm new)} - \Omega_{c1}$, on the interaction parameters $G_1$ (the vertical axis) and $G_2$ (the horizontal axis). Fig. 5.6(b) reports the shift as a function of $G_2$ at $G_1 = 0.5 E_{\rm r}$.

In general, at sufficiently small $G_2$ (i.e., $\ll 0.01 E_{\rm r}$), the stripe phase locates at a very small range of the Rabi frequency, where the density is slightly modulated with negligible contrast. We find that the difference $\delta\Omega_1$, as shown in deep blue color in Fig. 5.6(b), is close to zero. This implies a negligible contribution of high-order harmonics, and the state of the system can be well described by the dominant first-order stripe trial wave function. When the interaction energy $G_2$ becomes relatively larger, the density modulation becomes significant and the difference $\delta\Omega_1$

is sizable, as shown by the yellow and red regions in Fig. 5.6(a). Meanwhile, as $G_1$ increases, $\delta\Omega_1$ becomes much more pronounced. The significant shift of the ST-PW phase transition position determines an improved Rabi frequency of the critical ST-PW transition, i.e., $\Omega_{c1}^{(\mathrm{new})}$. It indicates the crucial role played by the high-order harmonics in Eq. (5.8). Our results suggest that they have to be accounted for in future theoretical investigations, particularly at relatively large values of interaction parameters.

## 5.5 Quantum depletion at zero temperature

In the last subsection we determine an improved critical Rabi frequency $\Omega_{c1}^{(\mathrm{new})}$ for the ST-PW phase transition at zero temperature. In this subsection, we will calculate the quantum depletion of the total density in different ground-state phases. Within the Bogoliubov theory, it is straightforward to obtain the quantum depletion using Eq. (5.2). For a single-component Bose gas, the quantum depletion was recently measured in the laboratory [237]. In Fig. 5.7, we present the $\Omega$-dependence of the quantum depletion at zero temperature across all three phases, at $G_1 = 0.5E_\mathrm{r}$ and

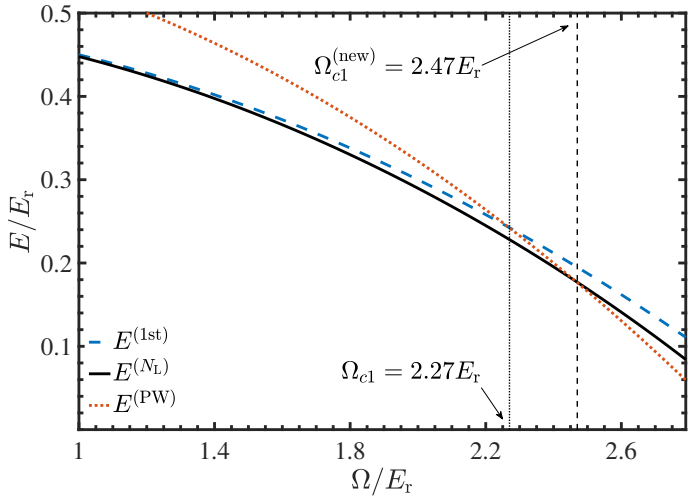


Figure 5.5: The ground-state energy as a function of the Rabi frequency in the first-order (dashed-blue), high-order (solid-black) stripe ansatz and the plane-wave ansatz (dotted-red). The interaction parameters are the same as in Fig. 5.1.

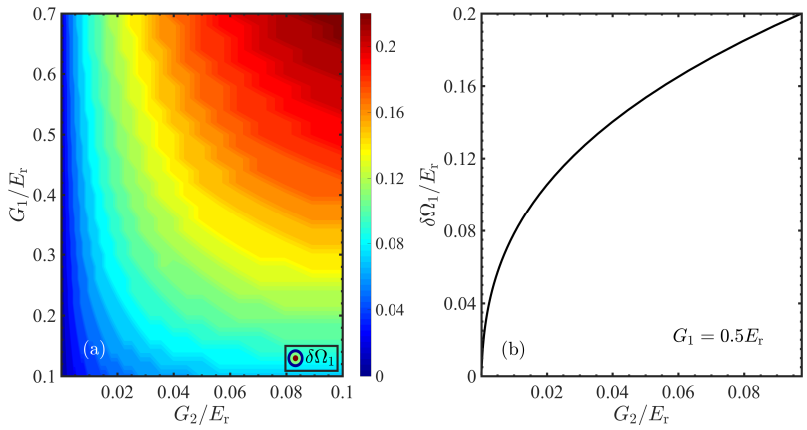


Figure 5.6: (a) Contour plot of the shift $\delta\Omega_1 = \Omega_{c1}^{(\mathrm{new})} - \Omega_{c1}$ for the ST-PW transition as functions of the interaction energy strengths $G_1$ and $G_2$. (b) The dependence of $\delta\Omega_1$ on $G_2$ at $G_1 = 0.5E_\mathrm{r}$.

at three different values of $G_2$ (i.e., $0.01E_\mathrm{r}$, $0.04E_\mathrm{r}$ and $0.07E_\mathrm{r}$).

The quantum depletion in the plane-wave and zero-momentum phases has been studied in Ref. [15]. We show their behaviour in great detail in Fig. 5.7(a)-(c) (i.e., the dashed-blue curves). It is a non-monotonic function of the Rabi frequency. In the plane-wave phase, the contribution to quantum depletion comes from both phonons and rotons in the lowest-lying excitation spectrum [14]. As one increases $\Omega$, the roton energy gap becomes larger and the phonon mode dominates the contribution. This leads to a maximum in the depletion at the PW-ZM transition $\Omega_{c2}$ (i.e., dotted-black vertical curve) [101]. As $\Omega$ continues to increase in the zero-momentum phase, the depletion decreases, since the roton contribution to the depletion disappears and the only contribution is from the phonon mode in the elementary excitation spectrum.

The behaviour of depletion in the stripe regime (i.e., the dotted-red curves) has not been studied before. It increases slowly and monotonically, as $\Omega$ increases up to the ST-PW transition $\Omega_{c1}^{(\mathrm{new})}$. This can be understood from the smooth softening of the two phonon modes, as illustrated in Fig. 5.3(a) and 5.3(b). It is worth noting that the depletion at $\Omega_{c1}^{(\mathrm{new})}$ experiences a jump due to the first-order character of the transition [95, 98, 103]. The size of the discontinuity becomes significant as we increase $G_2$.

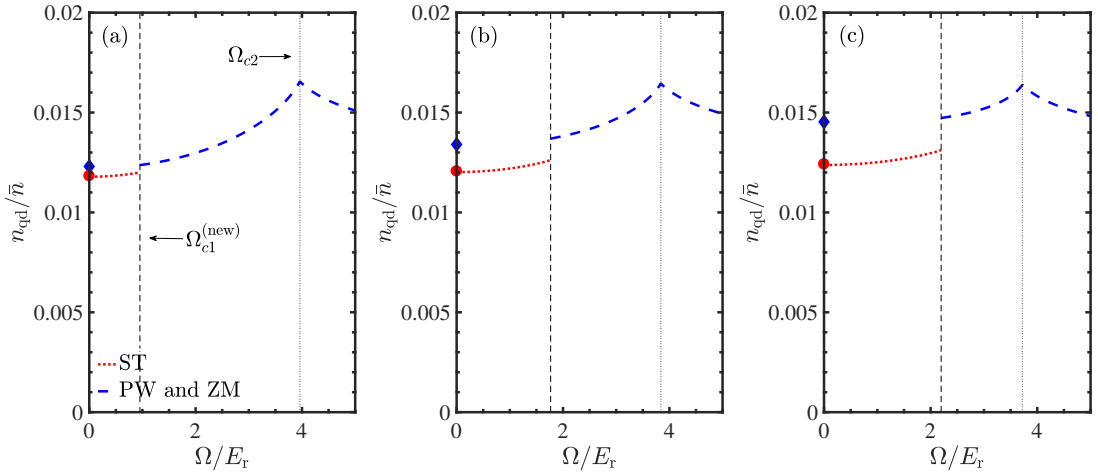


Figure 5.7: Quantum depletion $n_{\mathrm{qd}}/\bar{n}$ as a function of the Rabi frequency $\Omega$ in the ST phase (red dotted line) and in the PW and ZM phases (blue dashed line). The blue diamonds show the depletion of a uniform single-component weakly-interacting Bose gas with the same interaction parameters, while the red circles give the depletion of a two-component Bose gas. The vertical dashed and dotted curves indicate the critical $\Omega_{c1}^{(\mathrm{new})}$ and $\Omega_{c2}$, respectively. Here, we take the interaction energies $G_1 = 0.5E_{\mathrm{r}}$ and $G_2 = 0.01E_{\mathrm{r}}$ (a), $0.04E_{\mathrm{r}}$ (b) and $0.07E_{\mathrm{r}}$ (c).

The behaviour of the quantum depletion can be further understood with two analytic results. In the absence of SOC, the quantum depletion of a conventional homogeneous single-component Bose gas is of the order of $\sqrt{\bar{n}a^3}$ and can be analytically written as [21, 22]

$$\frac{n_{\mathrm{qd}}^{(1c)}}{\bar{n}} = \frac{8}{3\sqrt{\pi}}(\bar{n}a^3)^{1/2}. \tag{5.13}$$

This result can be extended to the two-component case with equal spin density as

$$\frac{n_{\mathrm{qd}}^{(2c)}}{\bar{n}} = \frac{8}{3\sqrt{\pi}}\left[(\bar{n}a_+^3)^{1/2} + (\bar{n}a_-^3)^{1/2}\right], \tag{5.14}$$

where the scattering length $a_\pm = (a \pm a_{\uparrow\downarrow})/2$ and $a \equiv a_{\uparrow\uparrow} = a_{\downarrow\downarrow}$. In Fig. 5.7, we have checked that, by starting with the plane-wave ansatz in Eq. (5.3), towards the limit $\Omega \to 0$, the depletion coincides with the single-component $n_{\mathrm{qd}}^{(1c)}$ (see blue diamonds), as the plane-wave phase tends to be fully spin-polarized, see also Fig. 4.8(a).

Similarly, the depletion predicted using the stripe ansatz in Eq. (5.8) (i.e., equal combination of two spins) recovers the two-component $n_{\rm qd}^{(2c)}$ (see red circles) in the limit $\Omega \to 0$.

## 5.6 Superfluid density fraction at zero temperature

In this section, we turn to discuss the superfluidity of the system in the presence of SOC, which can be characterized by the superfluid density. We will first derive the analytic expression of the superfluid density for all three phases with a first-order stripe ansatz and plane-wave ansatz, by applying the phase-twist method introduced in Appendix C. After including high-order harmonics in Eq. (5.8), a more accurate superfluid density in the stripe phase is calculated numerically and compared the analytic prediction.

In the presence of SOC in $x$ axis, the superfluid density can be written by a tensor form [15]

$$\hat{n}_{\rm s} = n_{\rm s}^{(x)} \hat{\mathbf{e}}_x \hat{\mathbf{e}}_x + n_{\rm s}^{(\perp)} (\hat{\mathbf{e}}_y \hat{\mathbf{e}}_y + \hat{\mathbf{e}}_z \hat{\mathbf{e}}_z), \tag{5.15}$$

where the tensor elements at $i \neq j$ vanish due to the reflection symmetry of the Hamiltonian, and $n_{\rm s}^{(i=x,\perp)}$ indicates the superfluid component along $x$-direction or in the perpendicular direction, respectively. At zero temperature, without losing the generality, we start with the first-order ansatz in Eq. (5.6), and the corresponding energy per particle $\epsilon(\theta, P_x) \equiv E/N$ is a function of two variational parameters $(\theta, P_x)$ (see also Ref. [95]). By fixing the total particle number $N$ and imposing a phase-twist $Q_i$ at the equilibrium $(\theta_0, P_0 \to \theta(Q_i), P_0(Q_i))$ [2], after some straightforward derivations on Eq. (C.3), the fraction of superfluid component can be explicitly expressed by [238]

$$\frac{n_{\rm s}^{(i=x,\perp)}}{\bar{n}} = \frac{m}{N} \left[ \frac{\partial^2 \mathcal{F}}{\partial Q_i^2} - \left( \frac{\partial^2 \mathcal{F}}{\partial \theta \partial Q_i} \right)^2 \Big/ \left( \frac{\partial^2 \mathcal{F}}{\partial \theta^2} \right) \right]_{Q_i \to 0}. \tag{5.16}$$

[2] In this work, the phase-twist is along the direction of SOC, i.e., $x$-direction, or in the perpendicular $yz$-plane

This expression is also applicable for the plane-wave and zero-momentum phases. To be specific, by substituting Eq. (5.7) of the ground-state energy for the stripe phase and Eq. (5.5) for the plane-wave and zero-momentum phases into Eq. (5.16), we obtain the analytic fraction of the superfluid component in the respective regimes as

$$\left(\frac{n_{\rm s}^{(x)}}{\bar{n}}\right)_{\rm ST} = 1 - \frac{2E_{\rm r}}{(2E_{\rm r}+G_1)(4E_{\rm r}+2G_1)^2/\Omega^2 - G_1}, \tag{5.17}$$

$$\left(\frac{n_{\rm s}^{(x)}}{\bar{n}}\right)_{\rm PW} = 1 - \frac{E_{\rm r}}{(E_{\rm r}-G_2)\Omega_{c2}^2/\Omega^2 + G_2}, \tag{5.18}$$

$$\left(\frac{n_{\rm s}^{(x)}}{\bar{n}}\right)_{\rm ZM} = 1 - \frac{4E_{\rm r}}{\Omega + 4G_2}, \tag{5.19}$$

in the direction of SOC, i.e., $x$ axis, and

$$\left(\frac{n_{\rm s}^{(\perp)}}{\bar{n}}\right)_{\rm ST} = \left(\frac{n_{\rm s}^{(\perp)}}{\bar{n}}\right)_{\rm PW} = \left(\frac{n_{\rm s}^{(\perp)}}{\bar{n}}\right)_{\rm ZM} = 1, \tag{5.20}$$

in the perpendicular plane. The expression in Eq. (5.17) should be understood as an approximate result for the superfluid fraction in the stripe phase along SOC direction. It can be improved by taking high-order harmonics in the stripe ansatz. The next two expressions, Eq. (5.18) and Eq. (5.19), were first obtained in Ref. [15]. It's worth noting that, the variational parameters $(\theta, P_x)$ are independent of the perpendicular twist $Q_\perp$ in Eq. (5.16), giving rise to the unaffected superfluid fraction $n_{\rm s}^{(\perp)}/\bar{n} = 1$ in the perpendicular direction, the same as in a usual Bose gas [15]. The explicit derivations can be seen in Appendix C.

In Fig. 5.8, we report the behaviour of the superfluid density $n_{\rm s}^{(x)}$ along the SOC-direction as a function of Rabi frequency in all the three ground-state phases. It is apparent from the figure that the superfluid density in the plane-wave and zero-momentum regimes (i.e., the dashed-blue curves), calculated by using Eqs. (5.18) and (5.19), exhibits an intriguing behaviour. It goes down monotonically in the plane-wave phase, touches zero at the PW-ZM transition $\Omega_{c2}$, and then bounces back in the zero-momentum phase. This behaviour exactly recovers the result in Ref. [15], where the normal density of the system was calculated using the transverse

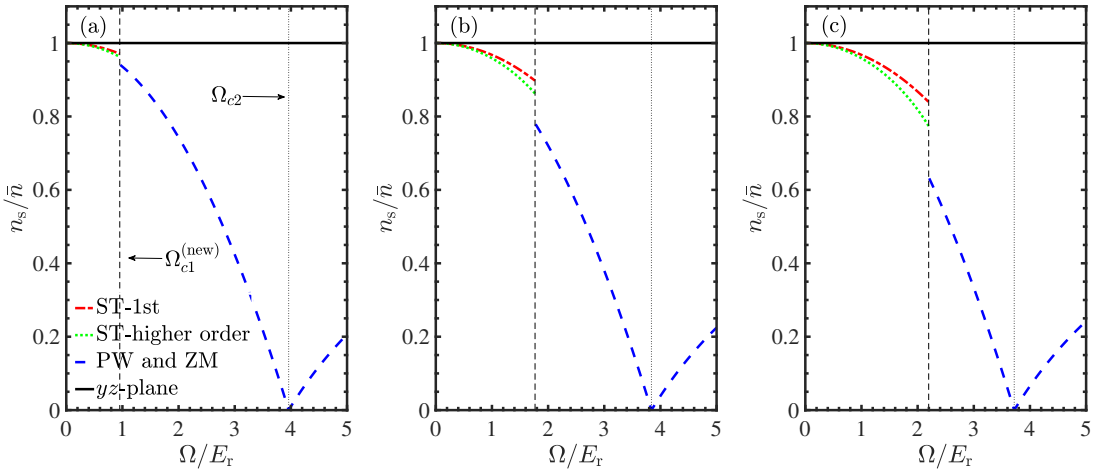


Figure 5.8: Superfluid fraction $n_\mathrm{s}^{(x)}/\bar{n}$ as a function of the Rabi frequency $\Omega$ in the ST phase (red dashed line - 1st order ansatz; green dotted line - high order ansatz), the PW and ZM phases (blue dashed line). The solid-black lines are the component $n_\mathrm{s}^{(\perp)}/\bar{n}$ in the perpendicular plane. The two vertical lines indicate the critical Rabi frequency of phase transition. The interaction parameters are the same as in Fig. 5.7.

current response function at zero temperature and the nonzero normal density was explained using a sum-rule together with a gapped branch in the elementary excitation spectrum [15]. Analogous to the remarkable absence of superfluid component at $\Omega_{c2}$, there are several physical observables exhibiting exotic behaviours due to the significant effect of SOC, such as the divergent spin polarizability [96, 104] and effective mass [101], the vanishing behaviour of the sound velocity [14, 103].

On the contrary, in the stripe phase the superfluid density can be evaluated using the first-order stripe ansatz. The resulting analytic prediction (see Eq. (5.17)) is shown by the red dotted-dashed curves in Fig. 5.8. Using the same phase-twist method with instead the high-order stripe ansatz in Eq. (5.8), we obtain the dotted-green curves in the figure. The difference between the two results (i.e., first-order vs high-order) increases with increasing $\Omega$. The difference also becomes significant if we use a large interaction parameter $G_2$ (see also in Fig. 5.6). The suppression of the superfluid density at nonzero $\Omega$ may be understood from the softening of the lowest two phonon modes in the low-energy excitation spectrum (see Fig. 5.3(a) and 5.3(b)). The critical velocity decreases as the phonon modes become soft. This means that

physically it is more favorable to create excitations to destroy the superfluidity of the system [21]. As anticipated, the superfluid density also exhibits a discontinuity at $\Omega_{c1}^{(\mathrm{new})}$, because of the first-order ST-PW transition.

It is worth noting that in the perpendicular plane, there is no density modulation due to the absence of the spin-orbit coupling. As a result, the superfluid fraction $n_{\mathrm{s}}^{(\perp)}/\bar{n}$ is 100% (see the solid-black curves), the same as in a conventional spinless Bose gas.

# Chapter 6

# Conclusions and Perspectives

In Chap. 1 and Chap. 2, we have introduced the backgrounds and recent developments in quantum gases, in particular the synthetic spin-orbit coupling simulated using neutral atoms in dilute ultracold systems. In Chaps. 3, 4 and 5, we have provided a systematical study of a weakly interacting Bose gas in the presence of a Raman-type spin-orbit coupling, by generalizing the Hartree-Fock-Bogoliubov-Popov (HFBP) theory.

The main achievements contained in the thesis are summarized below:

In chapter 3, we have made detailed investigations of the HFBP theory in the interacting one-dimensional (1D) Bose and Fermi gases. We have first studied collective modes of a 1D harmonically trapped Bose gas, by developing two numerical approaches: (a) a generalized Bogoliubov theory at zero temperature following the idea of the density-functional approach, where we have taken the local chemical potential calculated from the Lieb-Liniger model as the exchange energy; (b) a developed HFBP theory at finite temperature, where the thermal density is included to make the theory self-consistent. By using these two approaches and by emphasizing the effects of finite particle number and nonzero temperature, we have presented a systematical investigation of the breathing mode frequency in all interaction regimes and have explained the reentrant behaviour of the squared mode frequency, which varies from 4 in the non-interacting limit, to 3 in the mean-field regime and then back to 4 again in the Tonks-Girardeau limit. The frequency of higher order collective modes exhibits a similar reentrant behaviour.

We have compared our result with the recent experimental measurement [12] and a previous theoretical prediction [11]. While our result agrees well with the previous theoretical prediction, we have found that both theories cannot explain the measured mode frequency in the non-interacting limit. The discrepancy between experiment and theory becomes even larger when we take a small number of particles or a non-zero temperature. Therefore, we believe more theoretical investigations should be committed in the future in order to fully solve the discrepancy. Those works could focus on the issues such as the inter-tube tunneling and the confinement-induced three-body interparticle interaction.

On the other hand, we have studied the role of a non-negligible effective range in the interacting 1D Bose gas, by mapping to a 1D spin-polarized Fermi gas via Bose-Fermi duality. We have investigated the thermodynamics and dynamics of spin-polarized fermions with a resonant $p$-wave interaction under a 1D harmonic confinement at finite temperature, by solving the exact Yang-Yang thermodynamic equations and two-fluid hydrodynamic equation. We have shown that there are distinct features in the density distribution, sound velocity and collective mode frequency for identifying an exotic effective-range-induced super fermionic Tonks-Girardeau state. These features are not sensitive to the presence of a finite temperature. As a result, our predictions are readily testable with ultracold $^6$Li or $^{40}$K atoms near a $p$-wave Feshbach resonance at an experimental achievable temperature $T \simeq 0.1T_F$.

In chapter 4, we have discussed the effects of quantum and thermal fluctuations in a weakly interacting spin-orbit coupled Bose gas in three dimensions. We have determined a finite-temperature phase diagram for three generic phases, where quantum and thermal fluctuations play a significant role in enlarging the phase space for the plane-wave phase. These fluctuations also change the momentum in the condensation phase to a relatively larger value, particularly near the transition from the plane-wave phase to the zero-momentum phase. We have also studied the lowest elementary excitation spectrum, and it shows an exotic roton-maxon structure in the plane-wave phase.

We have explored the behaviour of sound velocity against the fluctuations, which is qualitatively changed near the transition, with a shifted velocity minimum and a finite gap. For $^{87}$Rb atoms, our prediction on sound velocity at finite temperature

agrees qualitative well with the recent experimental measurement, and therefore provides a reasonable explanation for the puzzling observation of gap opening [14]. We have also calculated the Landau critical velocity, which exhibits a difference with the sound velocity in the plane-wave phase, due to the intriguing roton-maxon structure in the elementary excitation spectrum. Besides, we also discuss the behaviour of other physical observables such as the magnetization of the condensate or of thermal atoms.

In chapter 5, we have thoroughly investigated the stripe phase of a Raman-type spin-orbit-coupled Bose gas at zero temperature, by employing an improved stripe ansatz including high-order harmonics. We find that the stripe density of the condensate is significantly modulated by the strength of spin-orbit coupling, and the inclusion of high-order harmonics reduces the momentum value of the finite-momentum condensate. Meanwhile, the low-lying elementary excitation spectra exhibit intriguing structure with two gapless Goldstone modes. The modes will be gradually softened with two reduced sound velocities as the Rabi frequency increases. We have shown that, the critical transition from the stripe to the plane-wave phases is shifted to a relatively larger Rabi frequency compared to the prediction by previous work [95] using a first-order stripe ansatz.

We have also calculated the quantum depletion and superfluid density over a large range of Rabi frequency in different phases. The depletion exhibits an intriguing behaviour with a discontinuous jump at the transition between the stripe and plane-wave phases, and a maximum at the transition between the plane-wave and zero-momentum phases. The analytic approximate expression of the superfluid density has been derived via a phase-twist approach using a first-order trial wave function, and has been compared with the more accurate numerical calculations in the stripe phase using the improved ansatz with high-order harmonics. In the plane-wave and zero-momentum phases, it is significantly suppressed along the spin-orbit-coupling direction and vanishes at the transition, consistent with a recent work [15], while in the stripe phase, it smoothly decreases with increasing Rabi frequency. The difference between the first-order and high-order results depends on the interaction energy strengths.

Further questions remain to be investigated to thoroughly understand this spin-orbit coupled Bose gas. For instance, one may explore the finite-temperature effects

on other physical observables such as anisotropic superfluid density and the moment of inertia [239]. It is also interesting to investigate the relevant dynamic properties, such as the damping behaviour due to interactions between quasiparticles, or the dynamic structure factor which can be measured in the experiment. Moreover, with respect to the coupling of linear momentum and atomic spin discussed in this thesis, there is a so-called spin-orbital-angular-momentum coupling, which couples the spin to another degrees of freedom–the orbital angular momentum. This new type of spin-orbit coupling gives rise to several intriguing phenomena [240–244], and will attract plenty of interests especially after its recent realization in the laboratory [245, 246].

# Appendix A

# Some details of the derivations in the thesis

## A.1 Derivations in the variational formalism

In this section, we present the details of the variational formalism in Sec. 2.3 starting with the trail wavefunction ansatz in Eq. (2.17) with four variational parameters ($C_1$, $C_2$, $k_{x0}$, $\theta$).

The normalization condition is written as

$$\sum_{i=\uparrow,\downarrow} \int d^3r |\Phi_i(\mathbf{r})|^2 = N \tag{A.1}$$

with the total particle number $N$, and we substitute the wavefunction of the condensate, which gives rise to

$$\begin{aligned}
N = & \int d^3r \Big[ \sqrt{\bar{n}}(C_1^* \cos\theta e^{-ik_{x0}x} + C_2^* \sin\theta e^{ik_{x0}x}) \sqrt{\bar{n}}(C_1 \cos\theta e^{ik_{x0}x} + C_2 \sin\theta e^{-ik_{x0}x}) \\
& + \sqrt{\bar{n}}(-C_1^* \sin\theta e^{-ik_{x0}x} - C_2^* \cos\theta e^{ik_{x0}x}) \sqrt{\bar{n}}(-C_1 \sin\theta e^{ik_{x0}x} - C_2 \cos\theta e^{-ik_{x0}x}) \Big] \\
= & \int d^3r \Big[ \bar{n}(|C_1|^2 \cos^2\theta + |C_2|^2 \sin^2\theta + C_1^* C_2 \sin\theta\cos\theta e^{-i2k_{x0}x} + C_2^* C_1 \sin\theta\cos\theta e^{i2k_{x0}x}) \\
& + \bar{n}(|C_1|^2 \sin^2\theta + |C_2|^2 \cos^2\theta + C_1^* C_2 \sin\theta\cos\theta e^{-i2k_{x0}x} + C_2^* C_1 \sin\theta\cos\theta e^{i2k_{x0}x}) \Big] \\
= & \int d^3r \bar{n} \left[ |C_1|^2 + |C_2|^2 + \sin(2\theta)(C_1^* C_2 e^{-i2k_{x0}x} + C_2^* C_1 e^{i2k_{x0}x}) \right],
\end{aligned} \tag{A.2}$$

where $\bar{n} = N/V$ is the average particle density. If we define $C_1 = |C_1|e^{i\phi_1}$, $C_2 = |C_2|e^{i\phi_2}$ and $\phi = \phi_1 - \phi_2$, the last term of the sine function in the above integral equation becomes

$$\begin{aligned}\text{terms} =& \sin(2\theta)(C_1^* C_2 e^{-i2k_{x0}x} + C_2^* C_1 e^{i2k_{x0}x}) \\ =& \sin(2\theta)|C_1 C_2|(e^{-i(2k_{x0}x+\phi)} + e^{i(2k_{x0}x+\phi)}) \\ =& 2|C_1 C_2| \sin(2\theta)\cos(2k_{x0}x + \phi).\end{aligned} \tag{A.3}$$

Thus in the calculations one may take the interval in $x$ axis integer times of the spatial period $d \equiv \pi/k_{x0}$ and eliminate the above term in the integral of the normalization condition, which leads to

$$|C_1|^2 + |C_2|^2 = 1. \tag{A.4}$$

The single-particle energy in Eq. (2.19) can be calculated as (set $\hbar = 1$)

$$\begin{aligned}E_0 =& \int d^3r \Phi(\mathbf{r})^\dagger \left[\frac{(\mathbf{k} - k_\mathrm{r}\hat{\mathbf{e}}_x\sigma_z)^2}{2m} + \frac{\Omega}{2}\sigma_x\right]\Phi(\mathbf{r}) \\ =& \int d^3r \bar{n} \cdot \frac{k_{x0}^2 + k_\perp^2 + k_\mathrm{r}^2}{2m} \cdot (|C_1|^2 + |C_2|^2) \\ & - \int d^3r \frac{\bar{n}}{2m}\left[\cos(2\theta)(|C_1|^2 + |C_2|^2)\right] \cdot 2k_{x0}k_\mathrm{r} + \int d^3r \frac{\Omega}{2}\bar{n}\sin(2\theta)(|C_1|^2 + |C_2|^2) \\ =& N \cdot \left[\frac{k_{x0}^2 + k_\perp^2 + k_\mathrm{r}^2}{2m} - \frac{k_{x0}}{m}k_\mathrm{r}\cos(2\theta) - \frac{\Omega}{2}\sin(2\theta)\right].\end{aligned} \tag{A.5}$$

It's worth noting that, the parameter $k_{x0}$ only appears in the single-particle energy. Hence, one can minimize straightforwardly with respect to $k_{x0}$

$$\frac{\partial E_0}{\partial k_{x0}} = k_{x0} - k_\mathrm{r}\cos(2\theta) = 0, \tag{A.6}$$

giving rise to

$$k_{x0} = k_\mathrm{r}\cos(2\theta). \tag{A.7}$$

Thus, by substituting $k_{x0}$ we can rewrite the single-particle energy as

$$\begin{aligned}E_0 =& N \cdot \left[\frac{k_\perp^2 + k_\mathrm{r}^2 + k_\mathrm{r}^2\cos^2(2\theta)}{2m} - \frac{k_\mathrm{r}^2\cos^2(2\theta)}{m} - \frac{\Omega}{2}\sin(2\theta)\right] \\ =& N \cdot \left[\frac{k_\perp^2 + k_\mathrm{r}^2\sin^2(2\theta)}{2m} - \frac{\Omega}{2}\sin(2\theta)\right].\end{aligned} \tag{A.8}$$

On the other hand, the interaction energy in Eq. (2.13) is given by

$$\begin{aligned}
E_{\text{int}} =& \frac{1}{2}\int d^3r\,\left[g(|\Phi_\uparrow(\mathbf{r})|^4+|\Phi_\downarrow(\mathbf{r})|^4)+2g_{\uparrow\downarrow}|\Phi_\uparrow(\mathbf{r})|^2|\Phi_\downarrow(\mathbf{r})|^2\right]\\
=& G_1\cdot\int d^3r\bar{n}\cdot\left[(|C_1|^2+|C_2|^2)^2+2|C_1|^2|C_2|^2(1-\cos^2(2\theta))\right]\\
&+G_2\cdot\int d^3r\bar{n}\cdot\left[(|C_1|^2+|C_2|^2)^2-4|C_1|^2|C_2|^2\right]\cdot\cos^2(2\theta)\\
=& N\cdot\{G_1\cdot\left[1+2|C_1|^2|C_2|^2\left(1-\cos^2(2\theta)\right)\right]+G_2\cos^2(2\theta)\cdot\left[1-4|C_1|^2|C_2|^2\right]\},
\end{aligned} \tag{A.9}$$

with two interaction energies $G_1=(g+g_{\uparrow\downarrow})\bar{n}/4$ and $G_2=(g-g_{\uparrow\downarrow})\bar{n}/4$.

The total energy per particle can be written as $\epsilon=(E_0+E_{\text{int}})/N$. It's apparent that, the energy now depends on only two parameters, $\theta\in[0,\pi/4]$ and $\beta\equiv|C_1|^2|C_2|^2\in[0,1/4]$ introduced in Ref. [95]. Thus the mean-field energy per particle reads

$$\begin{aligned}
\epsilon(\theta,\beta)=&\frac{k_\perp^2+k_{\text{r}}^2\sin^2(2\theta)}{2m}-\frac{\Omega}{2}\sin(2\theta)\\
&+G_1(1+2\beta)+[G_2-2\beta(G_1+2G_2)]\cos^2(2\theta).
\end{aligned} \tag{A.10}$$

It's convenient to minimize $\epsilon(\theta,\beta)$ with respect to $\theta$ as

$$\begin{aligned}
\frac{\partial\epsilon}{\partial\theta}=&\frac{k_{\text{r}}^2\cdot 2\sin(2\theta)\cdot 2\cos(2\theta)}{2m}-\frac{\Omega}{2}\cdot 2\cos\theta\\
&-[G_2-2\beta(G_1+2G_2)]\cdot 2\cos(2\theta)\cdot 2\sin(2\theta)\\
=&\cos(2\theta)\cdot\left[\frac{2k_{\text{r}}^2}{m}\sin(2\theta)-\Omega-4\left[G_2-2\beta(G_1+2G_2)\right]\sin(2\theta)\right]=0.
\end{aligned} \tag{A.11}$$

The above implies two conditions:

- The first is $\frac{2k_{\text{r}}^2}{m}\sin(2\theta)-\Omega-4\left[G_2-2\beta(G_1+2G_2)\right]\sin(2\theta)=0$. This leads to a solution

$$\sin(2\theta)=\frac{\Omega}{\frac{2k_{\text{r}}^2}{m}-4\left[G_2-2\beta(G_1+2G_2)\right]}, \tag{A.12}$$

  which restricts the Rabi frequency $\Omega$ to be $\Omega\leq\Omega_c$ with

$$\Omega_c=4E_{\text{r}}-4\left[G_2-2\beta(G_1+2G_2)\right]. \tag{A.13}$$

- For $\Omega > \Omega_c$, the minimum occurs at $\cos(2\theta) = 0$. It indicates that the momentum of the condensate $k_{x0}$ is zero.

After substituting the solutions, the energy becomes dependent only on $\beta$. We first consider the simpler case $\Omega > \Omega_c$, where the minimization of the energy $\partial_\beta \epsilon(\beta)$ is a positive number $2G_1$, indicating the minimum at $\beta = 0$ and corresponding to the zero-momentum (ZM) phase. On the other hand for the other solution, the energy is concave down function with a negative value of the second-order derivative. This means that the minimum locates at the boundaries of $\beta$, i.e., $\beta = 0$ or $\beta = 1/4$, which correspond to the so-called plane-wave (PW) and stripe (ST) phases, respectively. By comparing two energy terms with two wavefunctions of the condensate

$$\epsilon^{(\mathrm{ST})}(\theta, \beta = \frac{1}{4}, \Omega_{c1}) = \epsilon^{(\mathrm{PW})}(\theta, \beta = 0, \Omega_{c1}), \tag{A.14}$$

the critical Rabi frequency $\Omega_{c1}$ of the ST-PW transition are obtained as

$$\Omega_{c1} = 2\left[(2E_\mathrm{r} + G_1)(2E_\mathrm{r} - 2G_2)\frac{2G_2}{G_1 + 2G_2}\right]^{1/2}. \tag{A.15}$$

The critical Rabi frequency $\Omega_{c2}$ of the PW-ZM phase transition is then obtained from Eq. (A.13) by

$$\Omega_{c2} = 4E_\mathrm{r} - 4G_2. \tag{A.16}$$

# Appendix B

# SOC BEC transition temperature at the Hartree-Fock level

In this appendix, following the formalism in Ref. [101] at the Hartree-Fock (HF) level, we aim to calculate the BEC transition temperature $T_c$ as a function of the Rabi frequency $\Omega$, in the presence of spin-orbit coupling with a density $n$.

**Non-interacting system** The critical temperature for BEC of ideal Bose gases in the box with a density $n$, which is of form

$$T_0 = 2\pi\hbar^2[n/\zeta(3/2)]^{2/3}/(mk_B), \tag{B.1}$$

see also Eq. (1.10).The condensation transition temperature of a uniform system is then determined by

$$n = \int_{-\infty}^{\infty} d\varepsilon \frac{D(\varepsilon)}{e^{(\varepsilon-\mu)/T_0} - 1}. \tag{B.2}$$

Here, $D(\varepsilon)$ is the density of state and $\mu$ takes the bottom of single-particle spectrum by $\mu = \epsilon_{min}$.

In the presence of Raman coupling strength $\Omega$ and detuning $\delta$, the single-particle spectrum takes a form of (set $\hbar = 1$)

$$\epsilon_{\mathbf{p},\pm} = \frac{\mathbf{p}^2}{2m} + \frac{k_{\mathrm{r}}^2}{2m} \pm \sqrt{(\frac{p_x k_{\mathrm{r}}}{m} - \frac{\delta}{2})^2 + (\frac{\Omega}{2})^2}. \tag{B.3}$$

By defining $\Omega = aE_{\rm r}$ and setting $\delta = 0$, we have the chemical potential in Eq. (B.2) as

$$\mu = \epsilon_{min} = \begin{cases} -\frac{a^2}{16}E_{\rm r}; & \text{with} \quad p_{x_0} = \pm k_{\rm r}\sqrt{1-(\frac{\Omega}{4E_{\rm r}})^2} \quad \text{at} \quad 0 \le \Omega \le 4E_{\rm r} \\ (1-\frac{a}{2})E_{\rm r}. & \text{with} \quad p_{x_0} = 0 \quad \text{at} \quad \Omega > 4E_{\rm r} \end{cases} \tag{B.4}$$

**Weak interaction** If we take into account the weak interactions, it's well known that the contact interaction does not affect the transition temperature $T_c$ at the mean-field level. However, in the presence of spin-orbit coupling, the interactions start to provide a non-trivial effect even at mean-field level.

In Hartree-Fock theory, the average density for spin component $\sigma$ can be constructed as

$$n_\sigma = \frac{1}{V}\sum_{\mathbf{p}} \langle \hat{\Phi}^\dagger_{\mathbf{p},\sigma}\hat{\Phi}_{\mathbf{p},\sigma}\rangle, \tag{B.5}$$

and another parameter related to the spin-flip term induced by SOC is written as

$$\xi = \frac{1}{V}\sum_{\mathbf{p}} \langle \hat{\Phi}^\dagger_{\mathbf{p},\uparrow}\hat{\Phi}_{\mathbf{p},\downarrow}\rangle. \tag{B.6}$$

Taking into account the interaction term

$$\int dr^3 \frac{1}{2}\left(g_{\uparrow\uparrow}\hat{\Phi}^\dagger_\uparrow\hat{\Phi}^\dagger_\uparrow\hat{\Phi}_\uparrow\hat{\Phi}_\uparrow + g_{\downarrow\downarrow}\hat{\Phi}^\dagger_\downarrow\hat{\Phi}^\dagger_\downarrow\hat{\Phi}_\downarrow\hat{\Phi}_\downarrow + 2g_{\uparrow\downarrow}\hat{\Phi}^\dagger_\uparrow\hat{\Phi}^\dagger_\downarrow\hat{\Phi}_\downarrow\hat{\Phi}_\uparrow\right), \tag{B.7}$$

and consider the HF approximation, we have

$$\frac{1}{2}g\hat{\Phi}^\dagger\hat{\Phi}^\dagger\hat{\Phi}\hat{\Phi} = g\left[\langle\hat{\Phi}^\dagger\hat{\Phi}\rangle\hat{\Phi}^\dagger\hat{\Phi} + \hat{\Phi}^\dagger\hat{\Phi}\langle\hat{\Phi}^\dagger\hat{\Phi}\rangle - \langle\hat{\Phi}^\dagger\hat{\Phi}\rangle\langle\hat{\Phi}^\dagger\hat{\Phi}\rangle\right] = g\left[2n\hat{\Phi}^\dagger\hat{\Phi} - n^2\right] \tag{B.8}$$

and

$$\begin{aligned} g_{\uparrow\downarrow}\hat{\Phi}^\dagger_\uparrow\hat{\Phi}^\dagger_\downarrow\hat{\Phi}_\downarrow\hat{\Phi}_\uparrow =& g_{\uparrow\downarrow}\Big[\langle\hat{\Phi}^\dagger_\uparrow\hat{\Phi}_\uparrow\rangle\hat{\Phi}^\dagger_\downarrow\hat{\Phi}_\downarrow + \hat{\Phi}^\dagger_\uparrow\hat{\Phi}_\uparrow\langle\hat{\Phi}^\dagger_\downarrow\hat{\Phi}_\downarrow\rangle - \langle\hat{\Phi}^\dagger_\uparrow\hat{\Phi}_\uparrow\rangle\langle\hat{\Phi}^\dagger_\downarrow\hat{\Phi}_\downarrow\rangle + \langle\hat{\Phi}^\dagger_\uparrow\hat{\Phi}_\downarrow\rangle\hat{\Phi}^\dagger_\downarrow\hat{\Phi}_\uparrow \\ &+ \hat{\Phi}^\dagger_\uparrow\hat{\Phi}_\downarrow\langle\hat{\Phi}^\dagger_\downarrow\hat{\Phi}_\uparrow\rangle - \langle\hat{\Phi}^\dagger_\downarrow\hat{\Phi}_\uparrow\rangle\langle\hat{\Phi}^\dagger_\uparrow\hat{\Phi}_\downarrow\rangle\Big] \\ =& g_{\uparrow\downarrow}\left[n_\uparrow\hat{\Phi}^\dagger_\downarrow\hat{\Phi}_\downarrow + n_\downarrow\hat{\Phi}^\dagger_\uparrow\hat{\Phi}_\uparrow - n_\uparrow n_\downarrow + \xi\hat{\Phi}^\dagger_\downarrow\hat{\Phi}_\uparrow + \xi\hat{\Phi}^\dagger_\downarrow\hat{\Phi}_\uparrow - \xi^2\right]. \end{aligned} \tag{B.9}$$

Hence the mean-field interaction $\hat{H}_{int} = \frac{1}{2}\sum_{\sigma,\sigma'} g_{\sigma\sigma'}\hat{\Phi}^\dagger_\sigma\hat{\Phi}^\dagger_{\sigma'}\hat{\Phi}_\sigma\hat{\Phi}_{\sigma'}$ becomes

$$\begin{aligned}\hat{H}_{int} =& g\left[2n_\uparrow\hat{\Phi}^\dagger_\uparrow\hat{\Phi}_\uparrow - n^2_\uparrow + 2n_\downarrow\hat{\Phi}^\dagger_\downarrow\hat{\Phi}_\downarrow - n^2_\downarrow\right] \\ &+ g_{\uparrow\downarrow}\left[n_\uparrow\hat{\Phi}^\dagger_\downarrow\hat{\Phi}_\downarrow + n_\downarrow\hat{\Phi}^\dagger_\uparrow\hat{\Phi}_\uparrow - n_\uparrow n_\downarrow + \xi\hat{\Phi}^\dagger_\downarrow\hat{\Phi}_\uparrow + \xi\hat{\Phi}^\dagger_\downarrow\hat{\Phi}_\uparrow - \xi^2\right] \\ =&(2gn_\uparrow + g_{\uparrow\downarrow}n_\downarrow)\hat{\Phi}^\dagger_\uparrow\hat{\Phi}_\uparrow + (2gn_\downarrow + g_{\uparrow\downarrow}n_\uparrow)\hat{\Phi}^\dagger_\downarrow\hat{\Phi}_\downarrow \\ &+ g_{\uparrow\downarrow}\xi(\hat{\Phi}^\dagger_\downarrow\hat{\Phi}_\uparrow + \hat{\Phi}^\dagger_\downarrow\hat{\Phi}_\uparrow) - gn^2_\uparrow - gn^2_\downarrow - g_{\uparrow\downarrow}n_\uparrow n_\downarrow - g_{\uparrow\downarrow}\xi^2.\end{aligned} \tag{B.10}$$

Now the mean-field Hamiltonian can be rewritten as

$$\begin{aligned}\mathrm{H}_{HF} =&\mathrm{H}_0 + \sum_{\mathbf{p}}[(2gn_\uparrow + g_{\uparrow\downarrow}n_\downarrow)\hat{\Phi}^\dagger_\uparrow\hat{\Phi}_\uparrow + (2gn_\downarrow + g_{\uparrow\downarrow}n_\uparrow)\hat{\Phi}^\dagger_\downarrow\hat{\Phi}_\downarrow + g_{\uparrow\downarrow}\xi(\hat{\Phi}^\dagger_\uparrow\hat{\Phi}_\downarrow + \hat{\Phi}^\dagger_\downarrow\hat{\Phi}_\uparrow)] \\ &+ \text{constant},\end{aligned} \tag{B.11}$$

with single-particle Hamiltonian $\mathrm{H}_0$ in Eq. 2.8. The normal state above $T_c$ is unpolarized with $n_\uparrow = n_\downarrow = n/2$, and the HF Hamiltonian has the same structure with $\mathrm{H}_0$ except for a effective Raman coupling strength $\Omega_{\text{eff}} = \Omega + 2g_{\uparrow\downarrow}\xi$.

Similarly with non-interacting calculations, in the presence of the effective Raman coupling strength $\Omega_{\text{eff}}$ and detuning $\delta$, the dispersion spectrum takes a form of

$$\epsilon_{\mathbf{p},\pm} = \frac{\mathbf{p}^2}{2m} + \frac{k^2_{\mathrm{r}}}{2m} + (gn + \frac{1}{2}g_{\uparrow\downarrow}n) \pm \sqrt{(\frac{p_x k_{\mathrm{r}}}{m} - \frac{\delta}{2})^2 + (\frac{\Omega_{\text{eff}}}{2})^2}. \tag{B.12}$$

By defining $\Omega_{\text{eff}} = aE_{\mathrm{r}}$ and setting $\delta = 0$, we have the chemical potential in Eq. (B.2) as

$$\mu = \epsilon_{min} = \begin{cases} -\frac{a^2}{16}E_{\mathrm{r}} + (gn + \frac{1}{2}g_{\uparrow\downarrow}n); & p_{x_0} = \pm k_{\mathrm{r}}\sqrt{1 - (\frac{\Omega_{\text{eff}}}{4E_{\mathrm{r}}})^2} \quad \text{at} \quad 0 \le \Omega_{\text{eff}} \le 4E_{\mathrm{r}} \\ (1 - \frac{a}{2})E_{\mathrm{r}} + (gn + \frac{1}{2}g_{\uparrow\downarrow}n). & p_{x_0} = 0 \quad \text{at} \quad \Omega_{\text{eff}} > 4E_{\mathrm{r}} \end{cases} \tag{B.13}$$

When the temperature $T$ rises, the chemical potential lowers and once $T$ reaches $T_c$, the total density $n$ get the value of our initially-setted value $n_{in}$.

$$n = \iiint \frac{\mathrm{d}^3 p}{(2\pi)^3}\left[\frac{1}{e^{(\varepsilon_{\mathbf{p},+} - \mu)/T_c} - 1} + \frac{1}{e^{(\varepsilon_{\mathbf{p},-} - \mu)/T_c} - 1}\right]. \tag{B.14}$$

By calculating Eqs. (B.13) and (B.14), we obtain the relation of critical temperature $T_c$ as a function of effective Raman coupling stregth $\Omega_{\text{eff}}$, and after calculating

spin-flip term [101]

$$\xi = \frac{1}{V}\sum_{\mathbf{p}} \sin\theta_{\mathbf{p}} \cos\theta_{\mathbf{p}} (n_{\mathbf{p},+} - n_{\mathbf{p},-}), \tag{B.15}$$

with $\theta_{\mathbf{p}} = \arcsin\left[\frac{1}{2}\left(1 - \frac{p_x k_\mathrm{r} - \delta/2}{\sqrt{(p_x k_\mathrm{r} - \delta/2)^2 + \Omega_{\mathrm{eff}}^2/4}}\right)\right]^{1/2}$ and $n_{\mathbf{p},\pm}$ are the Bose distribution functions with the dispersions $\epsilon_{\mathbf{p},\pm}$ in Eq. (B.12). And then the transition temperature of a interacting gas with density $n$ as a function of real Raman coupling stregth $\Omega = \Omega_{\mathrm{eff}} - 2g_{\uparrow\downarrow}\xi$ in the semi-classical approximation can be obtained, as shown in Fig. B.1.

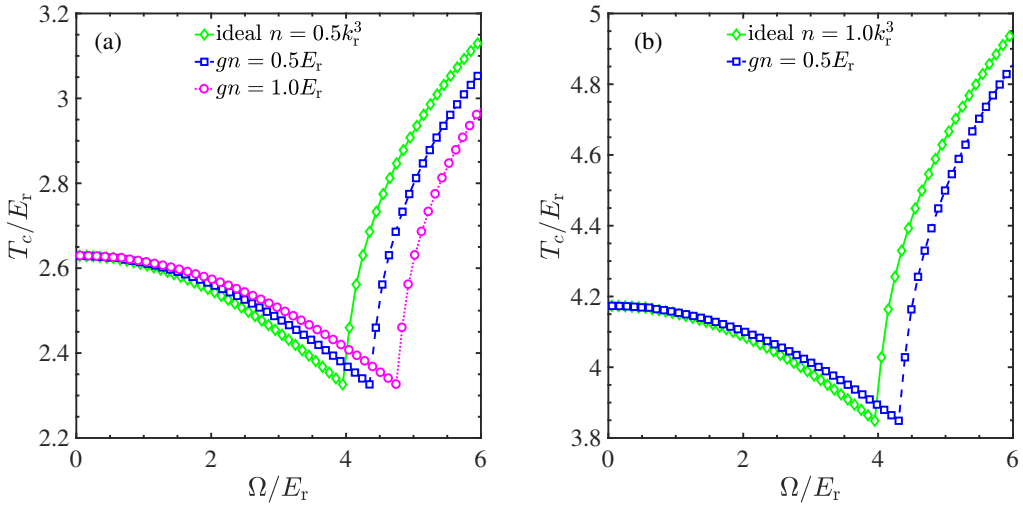


Figure B.1: BEC temperature $T_c/E_\mathrm{r}$ as a function of the Rabi frequency $\Omega/E_\mathrm{r}$ at two sets of density $n = 0.5k_\mathrm{r}^3$ (a) and $n = 1.0k_\mathrm{r}^3$ (b).

# Appendix C

# The phase-twist method in a SOC Bose gas

In Ref. [247], M. E. Fisher *et al.* have constructed a microscopic description of superfluid density $n_s$ related to the response of free energy with respect to a phase twist.

Microscopically, by imposing a phase-twist $\mathbf{Q}$, i.e., a supercurrent, on the order parameter

$$\phi(\mathbf{r}) \to e^{i\mathbf{Q}\cdot\mathbf{r}}\phi(\mathbf{r}), \tag{C.1}$$

the superfluid will flow with a velocity $\mathbf{v}_\mathrm{s} = \hbar\mathbf{Q}/m$. In the limit $\mathbf{Q} \to 0$, the variation of free energy $\Delta\mathcal{F}(\mathbf{Q}) \equiv \mathcal{F}(\mathbf{Q}) - \mathcal{F}(0)$ is approximately given by the extra kinetic energy of the imposed supercurrent,

$$\Delta\mathcal{F}(\mathbf{Q}) \approx \frac{\mathbf{Q}^2}{2}\lim_{\mathbf{Q}\to 0}\frac{d^2\mathcal{F}(\mathbf{Q})}{d\mathbf{Q}^2} \equiv \frac{1}{2}n_s m\mathbf{v}_\mathrm{s}^2 V. \tag{C.2}$$

Therefore, the ratio of the superfluid density $n_s$ over the total density $n = N/V$ can be expressed by [238, 247, 248]

$$\frac{n_\mathrm{s}}{n} \equiv \frac{m}{\hbar^2 N}\lim_{\mathbf{Q}\to 0}\frac{d^2\mathcal{F}(\mathbf{Q})}{d\mathbf{Q}^2}. \tag{C.3}$$

In the presence of SOC at zero temperature, without losing the generality, we start with the first-order ansatz in Eq. (5.6), and the corresponding energy per particle $\epsilon(\theta, P_x) \equiv E/N$ is a function of two variational parameters $(\theta, P_x)$ (see also

Ref. [95]). By fixing the total particle number $N$ and imposing a phase-twist $\mathbf{Q}$ at the equilibrium $(\theta_0, P_0 \to \theta(\mathbf{Q}), P_0(\mathbf{Q}))$, after some straightforward derivations on Eq. (C.3), the superfluid fraction can be explicitly expressed by [238] (set $\hbar = 1$)

$$\frac{n_{\mathrm{s}}}{n} = \frac{m}{N}\left[\frac{\partial^2 \mathcal{F}}{\partial \mathbf{Q}^2} - \left(\frac{\partial^2 \mathcal{F}}{\partial\theta\partial\mathbf{Q}}\right)^2 \Big/ \left(\frac{\partial^2 \mathcal{F}}{\partial\theta^2}\right)\right]_{\mathbf{Q}\to 0}. \tag{C.4}$$

## Stripe ansatz

Analytically we start with a 1st-order stripe ansatz with the condensation momentum $P_x\hat{e}_x$, which takes a form of [95]

$$\phi(\mathbf{r}) = \sqrt{\frac{n}{2}}\left[\begin{pmatrix}\sin\theta\\ -\cos\theta\end{pmatrix} e^{-iP_x x} + \begin{pmatrix}\cos\theta\\ -\sin\theta\end{pmatrix} e^{iP_x x}\right]. \tag{C.5}$$

Here $\theta$ varies in the range $[0, \pi/4]$ and $n = N/V$ is the average density.

At zero temperature, by substituting the stripe ansatz $\phi(\mathbf{r})$ back to the Hamiltonian and calculate the total energy $E$, we obtain the corresponding energy per volume $\epsilon(\theta, P_x) \equiv E/V$ as

$$\begin{aligned}\epsilon &= 2\phi_{1\uparrow}^2\frac{(-\mathbf{P} - k_{\mathrm{r}}\hat{e}_x)^2}{2m} + 2\phi_{1\downarrow}^2\frac{(\mathbf{P} - k_{\mathrm{r}}\hat{e}_x)^2}{2m} + 2\Omega\phi_{1\uparrow}\phi_{1\downarrow} + \frac{g + g_{\uparrow\downarrow}}{n}\left[(\phi_{1\uparrow}^2 + \phi_{1\downarrow}^2)^2 + 2\phi_{1\uparrow}^2\phi_{1\downarrow}^2\right]\\ &= n\left[\frac{P_x^2 + P_\perp^2 + k_{\mathrm{r}}^2}{2m} - \frac{P_x k_{\mathrm{r}}}{m}\cos 2\theta - \frac{\Omega}{2}\sin 2\theta + G_1(1 + \frac{1}{2}\sin^2 2\theta)\right],\end{aligned} \tag{C.6a}$$

with the interaction parameter $G_1 \equiv (g + g_{\uparrow\downarrow})n/4$. It's worth noting that here we consider a sufficiently large box, and along $x$-axis we take the integer times of the spatial period of density oscillation as $x \in [-n, n]\cdot\pi/P_x$ so that $\epsilon$ is independent of spatial coordinates.

Then the first-order derivatives of the energy with respect to the variables are given as

$$\frac{\partial\epsilon}{\partial P_x} = n\frac{P_x - k_{\mathrm{r}}\cos 2\theta}{m}, \tag{C.7a}$$

$$\frac{\partial\epsilon}{\partial\theta} = n\left[\frac{2P_x k_{\mathrm{r}}\sin 2\theta}{m} - \Omega\cos 2\theta + G_1\sin 4\theta\right], \tag{C.7b}$$

which lead to the corresponding second-order derivatives as

$$\frac{\partial^2\epsilon}{\partial P_x^2} = \frac{n}{m}, \tag{C.8a}$$

$$\frac{\partial^2\epsilon}{\partial\theta^2} = n\left[\frac{4P_x k_\mathrm{r}\cos 2\theta}{m} + 2\Omega\sin 2\theta + 4G_1\cos 4\theta\right], \tag{C.8b}$$

$$\frac{\partial^2\epsilon}{\partial P_x\partial\theta} = n\frac{2k_\mathrm{r}\sin 2\theta}{m}. \tag{C.8c}$$

Now we can write the superfluid density in Eq. (C.4) as

$$n_s = m\left[\frac{\partial^2(\epsilon V)}{\partial Q_x^2} - \left(\frac{\partial^2(\epsilon V)}{\partial\theta\partial Q_x}\right)^2 \Big/ \left(\frac{\partial^2(\epsilon V)}{\partial\theta^2}\right)\right]_{P_0,\theta_0}, \tag{C.9}$$

leading to

$$n_s/n = m\left[\frac{1}{m} - \left(\frac{2k_\mathrm{r}\sin 2\theta}{m}\right)^2 \Big/ \left(\frac{4P_x k_\mathrm{r}\cos 2\theta}{m} + 2\Omega\sin 2\theta + 4G_1\cos 4\theta\right)\right]_{P_0,\theta_0}. \tag{C.10}$$

In the stripe phase (i.e. $\Omega \le \Omega_{c1}$), the condensation exhibits a double minimum with momentum $P_0 = \pm k_\mathrm{r}\cos 2\theta_0$ with $\cos 2\theta_0 = \sqrt{1-\Omega^2/\Omega_0^2}$ with $\Omega_0 \equiv 4E_\mathrm{r} + 2G_1$. We substitute them back to Eq. (C.10) and obtain

$$\begin{aligned} n_s/n &= m\left[\frac{1}{m} - \frac{1}{m}\cdot\frac{4k_\mathrm{r}^2/m\cdot\Omega^2/\Omega_0^2}{4k_\mathrm{r}^2/m\cdot(1-\Omega^2/\Omega_0^2) + 2\Omega^2/\Omega_0 + 4G_1(1-2\Omega^2/\Omega_0^2)}\right], \\ &= 1 - \frac{2E_\mathrm{r}}{(2E_\mathrm{r}+G_1)(4E_\mathrm{r}+2G_1)^2/\Omega^2 - G_1}. \end{aligned} \tag{C.11}$$

## Plane-wave ansatz

Recall the plane-wave ansatz of the condensate, which lies at a positive momentum $P_x\hat{e}_x$, taking a form of [98, 101]

$$\phi(\mathbf{r}) = \sqrt{n}\begin{pmatrix}\cos\theta \\ -\sin\theta\end{pmatrix}e^{iP_x x}, \tag{C.12}$$

with $\theta$ varying in the range $[0, \pi/4]$ and a uniform density $n = N/V$.

At zero temperature, by substituting the plane-wave ansatz $\phi(\mathbf{r})$ back to the total energy $E$, we obtain the corresponding energy per particle $\epsilon(\theta, P_x) \equiv E/N$ as

$$\epsilon = \frac{P_x^2 + k_{\rm r}^2}{2m} - \frac{P_x k_{\rm r}}{m}\cos 2\theta - \frac{\Omega}{2}\sin 2\theta + \frac{1}{2}gn - G_2 \sin^2 2\theta, \tag{C.13}$$

with the interaction parameter $G_2 \equiv (g - g_{\uparrow\downarrow})n/4$.

Similarly the first-order derivatives of the energy are given as

$$\frac{\partial \epsilon}{\partial P_x} = \frac{P_x - k_{\rm r}\cos 2\theta}{m}, \tag{C.14a}$$

$$\frac{\partial \epsilon}{\partial \theta} = \frac{2P_x k_{\rm r}\sin 2\theta}{m} - \Omega\cos 2\theta - 4G_2 \sin 2\theta \cos 2\theta, \tag{C.14b}$$

which lead to the second-order derivatives as

$$\frac{\partial^2 \epsilon}{\partial P_x^2} = \frac{1}{m}, \tag{C.15a}$$

$$\frac{\partial^2 \epsilon}{\partial \theta^2} = \frac{4P_x k_{\rm r}\cos 2\theta}{m} + 2\Omega \sin 2\theta - 8G_2 \cos 4\theta, \tag{C.15b}$$

$$\frac{\partial^2 \epsilon}{\partial P_x \partial \theta} = \frac{2k_{\rm r}\sin 2\theta}{m}. \tag{C.15c}$$

And then the superfluid density reads

$$n_s = \frac{m}{V}\left[\frac{\partial^2(\epsilon N)}{\partial Q_x^2} - \left(\frac{\partial^2(\epsilon N)}{\partial\theta \partial Q_x}\right)^2 \Big/ \left(\frac{\partial^2(\epsilon N)}{\partial\theta^2}\right)\right]_{P_0,\theta_0}, \tag{C.16}$$

leading to

$$n_s/n = m\left[\frac{1}{m} - \left(\frac{2k_{\rm r}\sin 2\theta}{m}\right)^2 \Big/ \left(\frac{4P_x k_{\rm r}\cos 2\theta}{m} + 2\Omega\sin 2\theta - 8G_2\cos 4\theta\right)\right]_{P_0,\theta_0}. \tag{C.17}$$

In the PW phase (i.e. $\Omega_{c1} < \Omega \leq \Omega_{c2}$), the condensation takes a nonzero momentum at $P_0 = \pm k_{\rm r}\sqrt{1 - \Omega^2/\Omega_{c2}^2}$ with $P_0 = k_{\rm r}\cos 2\theta_0$ and $\Omega_{c2} = 4E_{\rm r} - 4G_2$ [95, 101]. We substitute them back to Eq. (C.17), and obtain

$$\begin{aligned} n_s/n &= m\left[\frac{1}{m} - \frac{1}{m}\cdot\frac{2k_{\rm r}^2/m}{\Omega_{c2} + (2k_{\rm r}^2/m - 4G_2)\Omega_{c2}^2/\Omega^2 - 2k_{\rm r}^2/m + 8G_2}\right], \\ &= 1 - \frac{E_{\rm r}}{(E_{\rm r} - G_2)\Omega_{c2}^2/\Omega^2 + G_2}. \end{aligned} \tag{C.18}$$

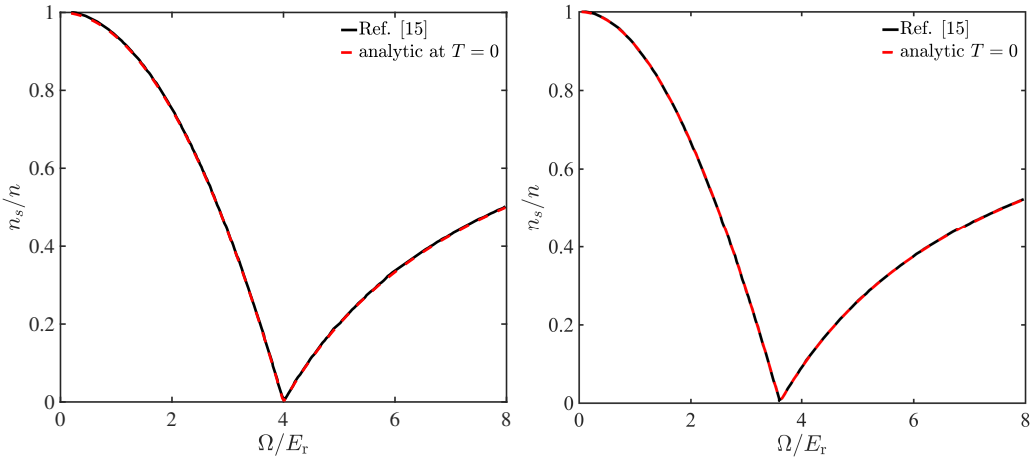


Figure C.1: Superfluid fraction as a function of the Rabi frequency $\Omega$, compared with Ref. [15]. Here $G_2/E_r$ is given by $2.4 \times 10^{-4}$ and 0.1, respectively.

In the ZM phase (i.e. $\Omega > \Omega_{c2}$), we have zero momentum $P_0$ and $\sin 2\theta_0 = 1$ in the ZM condensation phase. Eq. (C.17) becomes then

$$\begin{aligned} n_s/n &= m\left[\frac{1}{m} - \frac{1}{m}\cdot\frac{2k_r^2/m}{\Omega + 4G_2}\right], \\ &= 1 - \frac{4E_r}{\Omega + 4G_2}. \end{aligned} \tag{C.19}$$

In the descriptions above, we have derived the analytic expression for three generic ground-state phases, by using a first-order stripe ansatz and a plane-wave ansatz. In Fig. C.1, we show that our analytic result in the PW and ZM phases at zero temperature, which recovers the one in previous work [15]. In particular, at the PW-ZM transition $\Omega = \Omega_{c2}$, our previous studies show that there will be finite condensate fraction $n_c/n \approx 1$ at zero temperature, with a negligible quantum depletion less than 1%. However, it's worth noting that there will be no superfluid density $n_s/n = 0$ at $\Omega_{c2}$, and the total atoms are normal component as shown in Fig. C.1.

# Appendix D

# The choice of the cut-offs $N_{\mathrm{L}}$ and $N_{\mathrm{M}}$

In this Appendix, we check the convergence of our numerical calculations with respect to the cut-offs $N_{\mathrm{L}}$ and $N_{\mathrm{M}}$, by calculating the quantum depletion. In principle, $N_{\mathrm{L}}$ and $N_{\mathrm{M}}$ should be infinitely large to include all high-order terms. However, in practice we have to use finite cutoffs to ensure the computational efficiency. In Fig. D.1, we show the depletion (blue crosses) at different sets of cutoffs $N_{\mathrm{L}}$ and $N_{\mathrm{M}}$ in the zero Rabi frequency limit $\Omega \to 0$. In this limit, the quantum depletion is analytically known (see the dashed line), as the system reduces to a uniform two-component Bose gas without spin-orbit coupling. At $N_{\mathrm{L}} = N_{\mathrm{M}} = 14$, we find that the relative deviation of the calculated depletion is less than 1%. Therefore, we use $N_{\mathrm{L}} \geq 14$ and $N_{\mathrm{M}} \geq 14$ in our numerical calculations.

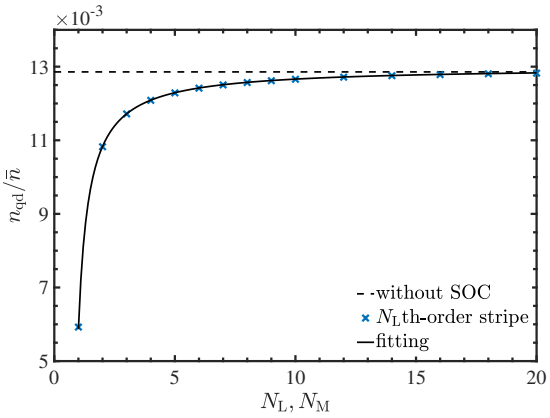


Figure D.1: Quantum depletion in the limit of $\Omega \to 0$, as a function of $N_{\mathrm{L}} = N_{\mathrm{M}}$. The anticipated result of a two-component Bose gas is shown by a dashed line. The interaction parameters are the same as in Fig. 5.1.

# Bibliography


[1] *JILA BEC & Ultracold Atoms, Picture of Bose-Einstein Condensation.* Available at http://jila.colorado.edu/bec/index.html.

[2] *Atomic Quantum Gases at MIT, Picture Gallery of Bose-Einstein Condensation.* Available at http://www.rle.mit.edu/cua_pub/ketterle_group/Nice_pics.htm.

[3] L.J. LeBlanc, *Laser cooling and trapping: Additional trapping and manipulation tools.* Available at https://www.ualberta.ca/~ljleblan/Bkgd6.html.

[4] C. Chin, R. Grimm, P. Julienne, E. Tiesinga, Feshbach resonances in ultracold gases. Rev. Mod. Phys. **82**, 1225 (2010).

[5] M. Randeria, Ultracold Fermi gases: Pre-pairing for condensation. Nature Physics **6**, 561 (2010).

[6] Y.-J. Lin, R.L. Compton, A.R. Perry, W.D. Phillips, J.V. Porto, I.B. Spielman, Bose-Einstein Condensate in a Uniform Light-Induced Vector Potential. Phys. Rev. Lett. **102**, 130401 (2009).

[7] Y.-J. Lin, K. Jiménez-García, I.B. Spielman, Spin–orbit-coupled Bose–Einstein condensates. Nature **471**, 83 (2011).

[8] Y. Li, G.I. Martone, S. Stringari, SPIN-ORBIT-COUPLED BOSE-EINSTEIN CONDENSATES, pp. 201. Chap. CHAPTER 5

[9] W. Ketterle, N.J. van Druten, Bose-Einstein condensation of a finite number of particles trapped in one or three dimensions. Phys. Rev. A **54**, 656 (1996).

[10] F. Dalfovo, S. Giorgini, L.P. Pitaevskii, S. Stringari, Theory of Bose-Einstein condensation in trapped gases. Rev. Mod. Phys. **71**, 463 (1999).

[11] S. Choi, V. Dunjko, Z.D. Zhang, M. Olshanii, Monopole Excitations of a Harmonically Trapped One-Dimensional Bose Gas from the Ideal Gas to the Tonks-Girardeau Regime. Phys. Rev. Lett. **115**, 115302 (2015).

[12] E. Haller, M. Gustavsson, M.J. Mark, J.G. Danzl, R. Hart, G. Pupillo, H.-C. Nägerl, Realization of an Excited, Strongly Correlated Quantum Gas Phase. Science **325**, 1224 (2009).

[13] A. Imambekov, A.A. Lukyanov, L.I. Glazman, V. Gritsev, Exact Solution for 1D Spin-Polarized Fermions with Resonant Interactions. Phys. Rev. Lett. **104**, 040402 (2010).

[14] S.-C. Ji, L. Zhang, X.-T. Xu, Z. Wu, Y. Deng, S. Chen, J.-W. Pan, Softening of Roton and Phonon Modes in a Bose-Einstein Condensate with Spin-Orbit Coupling. Phys. Rev. Lett. **114**, 105301 (2015).

[15] Y.-C. Zhang, Z.-Q. Yu, T.K. Ng, S. Zhang, L. Pitaevskii, S. Stringari, Superfluid density of a spin-orbit-coupled Bose gas. Phys. Rev. A **94**, 033635 (2016).

[16] W. Ketterle, D.S. Durfee, D. Stamper-Kurn, Making, probing and understanding Bose-Einstein condensates. (1999).

[17] P. Kapitza, Viscosity of liquid helium below the $\lambda$-point. Nature **141**, 74 (1938).

[18] J. Allen, A. Misener, Flow of liquid helium II. Nature **141**, 75 (1938).

[19] S.N. Bose, Plancks Gesetz und Lichtquantenhypothese. Zeitschrift fr Physik **26**, 178 (1924).

[20] A. Einstein, Quantentheorie des einatomigen idealen Gases. Sitzungsberichte der Preussischen Akademie der Wissenschaften **1:3** (1925).

[21] L.P. Pítajevskíj, S. Stringari, *Bose-Einstein Condensation.* Comparative Pathobiology - Studies in the Postmodern Theory of Education (Oxford University Press, Oxford, 2003). ISBN 9780198507192

[22] C.J. Pethick, H. Smith, *Bose-Einstein Condensation in Dilute Gases* (Cambridge University Press, 2002). ISBN 9780521665803

[23] F. London, The $\lambda$-phenomenon of liquid helium and the Bose-Einstein degeneracy. Nature **141**, 643 (1938).

[24] L. Tisza, Transport phenomena in helium II. Nature **141**, 913 (1938).

[25] L. Landau, Theory of the Superfluidity of Helium II. Phys. Rev. **60**, 356 (1941).

[26] L. Landau, Two-fluid model of liquid helium II. J. Phys. USSR **5**, 71 (1941).

[27] N. Bogoliubov, On the theory of superfluidity. J. Phys **11**, 23 (1947).

[28] L.D. Landau, E.M. Lifshitz, Statisticheskai Fizika. (1951).

[29] O. Penrose, CXXXVI. On the quantum mechanics of helium II. The London, Edinburgh, and Dublin Philosophical Magazine and Journal of Science **42**, 1373 (1951).

[30] O. Penrose, L. Onsager, Bose-Einstein Condensation and Liquid Helium. Phys. Rev. **104**, 576 (1956).

[31] H.E. Hall, W. Vinen, The rotation of liquid helium II I. Experiments on the propagation of second sound in uniformly rotating helium II. Proc. R. Soc. Lond. A **238**, 204 (1956).

[32] L. Onsager, The effects of shape on the interaction of colloidal particles. Annals of the New York Academy of Sciences **51**, 627 (1949).

[33] R.P. Feynman, Chapter II Application of quantum mechanics to liquid helium, in *Progress in low temperature physics*, vol. 1 vol. 1 (Elsevier, 1955)., pp. 17

[34] S. Chu, Nobel Lecture: The manipulation of neutral particles. Rev. Mod. Phys. **70**, 685 (1998).

[35] C.N. Cohen-Tannoudji, Nobel Lecture: Manipulating atoms with photons. Rev. Mod. Phys. **70**, 707 (1998).

[36] W.D. Phillips, Nobel Lecture: Laser cooling and trapping of neutral atoms. Rev. Mod. Phys. **70**, 721 (1998).

[37] M.H. Anderson, J.R. Ensher, M.R. Matthews, C.E. Wieman, E.A. Cornell, Observation of Bose-Einstein Condensation in a Dilute Atomic Vapor. Science **269**, 198 (1995).

[38] K.B. Davis, M.-O. Mewes, M.R. Andrews, N.J. van Druten, D.S. Durfee, D.M. Kurn, W. Ketterle, Bose-Einstein Condensation in a Gas of Sodium Atoms. Phys. Rev. Lett. **75**, 3969 (1995).

[39] C.C. Bradley, C.A. Sackett, J.J. Tollett, R.G. Hulet, Evidence of Bose-Einstein Condensation in an Atomic Gas with Attractive Interactions. Phys. Rev. Lett. **75**, 1687 (1995).

[40] S. Giorgini, L.P. Pitaevskii, S. Stringari, Theory of ultracold atomic Fermi gases. Rev. Mod. Phys. **80**, 1215 (2008).

[41] I. Bloch, J. Dalibard, W. Zwerger, Many-body physics with ultracold gases. Rev. Mod. Phys. **80**, 885 (2008).

[42] A.J. Leggett, Bose-Einstein condensation in the alkali gases: Some fundamental concepts. Rev. Mod. Phys. **73**, 307 (2001).

[43] M.H. Anderson, J.R. Ensher, M.R. Matthews, C.E. Wieman, E.A. Cornell, Observation of Bose-Einstein condensation in a dilute atomic vapor. science **269**, 198 (1995).

[44] C.C. Bradley, C.A. Sackett, R.G. Hulet, Bose-Einstein Condensation of Lithium: Observation of Limited Condensate Number. Phys. Rev. Lett. **78**, 985 (1997).

[45] D.G. Fried, T.C. Killian, L. Willmann, D. Landhuis, S.C. Moss, D. Kleppner, T.J. Greytak, Bose-Einstein Condensation of Atomic Hydrogen. Phys. Rev. Lett. **81**, 3811 (1998).

[46] B. DeMarco, D.S. Jin, Onset of Fermi Degeneracy in a Trapped Atomic Gas. Science **285**, 1703 (1999).

[47] K. O'hara, S. Hemmer, M. Gehm, S. Granade, J. Thomas, Observation of a strongly interacting degenerate Fermi gas of atoms. Science **298**, 2179 (2002).

[48] C.A. Regal, M. Greiner, D.S. Jin, Observation of Resonance Condensation of Fermionic Atom Pairs. Phys. Rev. Lett. **92**, 040403 (2004).

[49] G. Roati, F. Riboli, G. Modugno, M. Inguscio, Fermi-Bose Quantum Degenerate $^{40}$K$-^{87}$Rb Mixture with Attractive Interaction. Phys. Rev. Lett. **89**, 150403 (2002).

[50] A.G. Truscott, K.E. Strecker, W.I. McAlexander, G.B. Partridge, R.G. Hulet, Observation of Fermi Pressure in a Gas of Trapped Atoms. Science **291**, 2570 (2001).

[51] F. Schreck, L. Khaykovich, K.L. Corwin, G. Ferrari, T. Bourdel, J. Cubizolles, C. Salomon, Quasipure Bose-Einstein Condensate Immersed in a Fermi Sea. Phys. Rev. Lett. **87**, 080403 (2001).

[52] S.R. Granade, M.E. Gehm, K.M. O'Hara, J.E. Thomas, All-Optical Production of a Degenerate Fermi Gas. Phys. Rev. Lett. **88**, 120405 (2002).

[53] Z. Hadzibabic, C.A. Stan, K. Dieckmann, S. Gupta, M.W. Zwierlein, A. Görlitz, W. Ketterle, Two-Species Mixture of Quantum Degenerate Bose and Fermi Gases. Phys. Rev. Lett. **88**, 160401 (2002).

[54] S. Jochim, M. Bartenstein, A. Altmeyer, G. Hendl, S. Riedl, C. Chin, J. Hecker Denschlag, R. Grimm, Bose-Einstein Condensation of Molecules. Science **302**, 2101 (2003).

[55] M. Greiner, C.A. Regal, D.S. Jin, Emergence of a molecular Bose–Einstein condensate from a Fermi gas. Nature **426**, 537 (2003).

[56] M.W. Zwierlein, C.A. Stan, C.H. Schunck, S.M.F. Raupach, S. Gupta, Z. Hadzibabic, W. Ketterle, Observation of Bose-Einstein Condensation of Molecules. Phys. Rev. Lett. **91**, 250401 (2003).

[57] L. Pitaevskii, S. Stringari, *Bose-Einstein Condensation and Superfluidity*. International Series of Monographs on Physics, vol. 164 (Oxford University Press, Oxford, 2016). ISBN 9780191076688

[58] E. Tiesinga, B.J. Verhaar, H.T.C. Stoof, Threshold and resonance phenomena in ultracold ground-state collisions. Phys. Rev. A **47**, 4114 (1993).

[59] D. Jaksch, C. Bruder, J.I. Cirac, C.W. Gardiner, P. Zoller, Cold Bosonic Atoms in Optical Lattices. Phys. Rev. Lett. **81**, 3108 (1998).

[60] O. Morsch, M. Oberthaler, Dynamics of Bose-Einstein condensates in optical lattices. Rev. Mod. Phys. **78**, 179 (2006).

[61] M.R. Andrews, C.G. Townsend, H.-J. Miesner, D.S. Durfee, D.M. Kurn, W. Ketterle, Observation of Interference Between Two Bose Condensates. Science **275**, 637 (1997).

[62] E.W. Streed, A. Jechow, B.G. Norton, D. Kielpinski, Absorption imaging of a single atom. Nature communications **3**, 933 (2012).

[63] M. Girardeau, Relationship between Systems of Impenetrable Bosons and Fermions in One Dimension. Journal of Mathematical Physics **1**, 516 (1960).

[64] X.-L. Chen, Y. Li, H. Hu, Collective modes of a harmonically trapped one-dimensional Bose gas: The effects of finite particle number and nonzero temperature. Phys. Rev. A **91**, 063631 (2015).

[65] X.-L. Chen, X.-J. Liu, H. Hu, Probing an effective-range-induced super fermionic Tonks-Girardeau gas with ultracold atoms in one-dimensional harmonic traps. Phys. Rev. A **94**, 033630 (2016).

[66] W. Zwerger, *The BCS-BEC Crossover and the Unitary Fermi Gas*. Lecture Notes in Physics, vol. 836 (Springer Berlin Heidelberg, 2011). ISBN 9783642219771

[67] P. Makotyn, C.E. Klauss, D.L. Goldberger, E.A. Cornell, D.S. Jin, Universal dynamics of a degenerate unitary Bose gas. Nature Physics **10**, 116 (2014).

[68] Q. Chen, J. Stajic, S. Tan, K. Levin, BCS–BEC crossover: From high temperature superconductors to ultracold superfluids. Physics Reports **412**, 1 (2005).

[69] T.-L. Ho, Universal Thermodynamics of Degenerate Quantum Gases in the Unitarity Limit. Phys. Rev. Lett. **92**, 090402 (2004).

[70] T. Köhler, K. Góral, P.S. Julienne, Production of cold molecules via magnetically tunable Feshbach resonances. Rev. Mod. Phys. **78**, 1311 (2006).

[71] V. Efimov, Energy levels arising from resonant two-body forces in a three-body system. Physics Letters B **33**, 563 (1970).

[72] F. Ferlaino, R. Grimm, Trend: Forty years of Efimov physics: How a bizarre prediction turned into a hot topic. Physics **3**, 9 (2010).

[73] T. Kraemer, M. Mark, P. Waldburger, J. Danzl, C. Chin, B. Engeser, A. Lange, K. Pilch, A. Jaakkola, H.-C. Nägerl, et al., Evidence for Efimov quantum states in an ultracold gas of caesium atoms. Nature **440**, 315 (2006).

[74] C. Chin, M. Bartenstein, A. Altmeyer, S. Riedl, S. Jochim, J.H. Denschlag, R. Grimm, Observation of the pairing gap in a strongly interacting Fermi gas. Science **305**, 1128 (2004).

[75] J. Gaebler, J. Stewart, T. Drake, D. Jin, A. Perali, P. Pieri, G. Strinati, Observation of pseudogap behaviour in a strongly interacting Fermi gas. Nature Physics **6**, 569 (2010).

[76] J. Dalibard, F. Gerbier, G. Juzeliūnas, P. Öhberg, *Colloquium*: Artificial gauge potentials for neutral atoms. Rev. Mod. Phys. **83**, 1523 (2011).

[77] N. Goldman, G. Juzeliūnas, P. Öhberg, I.B. Spielman, Light-induced gauge fields for ultracold atoms. Reports on Progress in Physics **77**, 126401 (2014).

[78] A.L. Fetter, Rotating trapped Bose-Einstein condensates. Rev. Mod. Phys. **81**, 647 (2009).

[79] K.W. Madison, F. Chevy, W. Wohlleben, J. Dalibard, Vortex Formation in a Stirred Bose-Einstein Condensate. Phys. Rev. Lett. **84**, 806 (2000).

[80] J. Abo-Shaeer, C. Raman, J. Vogels, W. Ketterle, Observation of vortex lattices in Bose-Einstein condensates. Science **292**, 476 (2001).

[81] D. Jaksch, P. Zoller, Creation of effective magnetic fields in optical lattices: the Hofstadter butterfly for cold neutral atoms. New Journal of Physics **5**, 56 (2003).

[82] G. Juzeliūnas, P. Öhberg, Slow Light in Degenerate Fermi Gases. Phys. Rev. Lett. **93**, 033602 (2004).

[83] X.-J. Liu, X. Liu, L.C. Kwek, C.H. Oh, Optically Induced Spin-Hall Effect in Atoms. Phys. Rev. Lett. **98**, 026602 (2007).

[84] S.-L. Zhu, H. Fu, C.-J. Wu, S.-C. Zhang, L.-M. Duan, Spin Hall Effects for Cold Atoms in a Light-Induced Gauge Potential. Phys. Rev. Lett. **97**, 240401 (2006).

[85] K. Osterloh, M. Baig, L. Santos, P. Zoller, M. Lewenstein, Cold Atoms in Non-Abelian Gauge Potentials: From the Hofstadter "Moth" to Lattice Gauge Theory. Phys. Rev. Lett. **95**, 010403 (2005).

[86] J. Ruseckas, G. Juzeliūnas, P. Öhberg, M. Fleischhauer, Non-Abelian Gauge Potentials for Ultracold Atoms with Degenerate Dark States. Phys. Rev. Lett. **95**, 010404 (2005).

[87] X.-J. Liu, M.F. Borunda, X. Liu, J. Sinova, Effect of Induced Spin-Orbit Coupling for Atoms via Laser Fields. Phys. Rev. Lett. **102**, 046402 (2009).

[88] I.B. Spielman, Raman processes and effective gauge potentials. Phys. Rev. A **79**, 063613 (2009).

[89] Y.-J. Lin, R.L. Compton, K. Jiménez-García, J.V. Porto, I.B. Spielman, Synthetic magnetic fields for ultracold neutral atoms. Nature **462**, 628 (2009).

[90] Y.-J. Lin, R.L. Compton, K. Jiménez-García, W.D. Phillips, J.V. Porto, I.B. Spielman, A synthetic electric force acting on neutral atoms. Nature Physics **7**, 531 (2011).

[91] C. Wang, C. Gao, C.-M. Jian, H. Zhai, Spin-Orbit Coupled Spinor Bose-Einstein Condensates. Phys. Rev. Lett. **105**, 160403 (2010).

[92] C.-J. Wu, M.-S. Ian, X.-F. Zhou, Unconventional BoseEinstein Condensations from Spin-Orbit Coupling. Chinese Physics Letters **28**, 097102 (2011).

[93] T.-L. Ho, S. Zhang, Bose-Einstein Condensates with Spin-Orbit Interaction. Phys. Rev. Lett. **107**, 150403 (2011).

[94] H. Hu, B. Ramachandhran, H. Pu, X.-J. Liu, Spin-Orbit Coupled Weakly Interacting Bose-Einstein Condensates in Harmonic Traps. Phys. Rev. Lett. **108**, 010402 (2012).

[95] Y. Li, L.P. Pitaevskii, S. Stringari, Quantum Tricriticality and Phase Transitions in Spin-Orbit Coupled Bose-Einstein Condensates. Phys. Rev. Lett. **108**, 225301 (2012).

[96] Y. Li, G.I. Martone, S. Stringari, Sum rules, dipole oscillation and spin polarizability of a spin-orbit coupled quantum gas. EPL (Europhysics Letters) **99**, 56008 (2012).

[97] T. Ozawa, G. Baym, Ground-state phases of ultracold bosons with Rashba-Dresselhaus spin-orbit coupling. Phys. Rev. A **85**, 013612 (2012).

[98] G.I. Martone, Y. Li, L.P. Pitaevskii, S. Stringari, Anisotropic dynamics of a spin-orbit-coupled Bose-Einstein condensate. Phys. Rev. A **86**, 063621 (2012).

[99] W. Zheng, Z. Li, Collective modes of a spin-orbit-coupled Bose-Einstein condensate: A hydrodynamic approach. Phys. Rev. A **85**, 053607 (2012).

[100] T. Ozawa, G. Baym, Stability of Ultracold Atomic Bose Condensates with Rashba Spin-Orbit Coupling against Quantum and Thermal Fluctuations. Phys. Rev. Lett. **109**, 025301 (2012).

[101] W. Zheng, Z.-Q. Yu, X. Cui, H. Zhai, Properties of Bose gases with the Raman-induced spin–orbit coupling. Journal of Physics B: Atomic, Molecular and Optical Physics **46**, 134007 (2013).

[102] Z.-Q. Yu, Ground-state phase diagram and critical temperature of two-component Bose gases with Rashba spin-orbit coupling. Phys. Rev. A **87**, 051606 (2013).

[103] X.-L. Chen, X.-J. Liu, H. Hu, Quantum and thermal fluctuations in a Raman spin-orbit-coupled Bose gas. Phys. Rev. A **96**, 013625 (2017).

[104] J.-Y. Zhang, S.-C. Ji, Z. Chen, L. Zhang, Z.-D. Du, B. Yan, G.-S. Pan, B. Zhao, Y.-J. Deng, H. Zhai, S. Chen, J.-W. Pan, Collective Dipole Oscillations of a Spin-Orbit Coupled Bose-Einstein Condensate. Phys. Rev. Lett. **109**, 115301 (2012).

[105] S.-C. Ji, J.-Y. Zhang, L. Zhang, Z.-D. Du, W. Zheng, Y.-J. Deng, H. Zhai, S. Chen, J.-W. Pan, Experimental determination of the finite-temperature phase diagram of a spin-orbit coupled Bose gas. Nature Physics **10**, 314 (2014).

[106] J.-R. Li, J. Lee, W. Huang, S. Burchesky, B. Shteynas, F.Ç. Top, A.O. Jamison, W. Ketterle, A stripe phase with supersolid properties in spin–orbit-coupled Bose–Einstein condensates. Nature **543**, 91 (2017).

[107] P. Wang, Z.-Q. Yu, Z. Fu, J. Miao, L. Huang, S. Chai, H. Zhai, J. Zhang, Spin-Orbit Coupled Degenerate Fermi Gases. Phys. Rev. Lett. **109**, 095301 (2012).

[108] L.W. Cheuk, A.T. Sommer, Z. Hadzibabic, T. Yefsah, W.S. Bakr, M.W. Zwierlein, Spin-Injection Spectroscopy of a Spin-Orbit Coupled Fermi Gas. Phys. Rev. Lett. **109**, 095302 (2012).

[109] Z. Fu, L. Huang, Z. Meng, P. Wang, L. Zhang, S. Zhang, H. Zhai, P. Zhang, J. Zhang, Production of Feshbach molecules induced by spin–orbit coupling in Fermi gases. Nature Physics **10**, 110 (2014).

[110] C. Qu, C. Hamner, M. Gong, C. Zhang, P. Engels, Observation of Zitterbewegung in a spin-orbit-coupled Bose-Einstein condensate. Phys. Rev. A **88**, 021604 (2013).

[111] A.J. Olson, S.-J. Wang, R.J. Niffenegger, C.-H. Li, C.H. Greene, Y.P. Chen, Tunable Landau-Zener transitions in a spin-orbit-coupled Bose-Einstein condensate. Phys. Rev. A **90**, 013616 (2014).

[112] M.L. Wall, A.P. Koller, S. Li, X. Zhang, N.R. Cooper, J. Ye, A.M. Rey, Synthetic Spin-Orbit Coupling in an Optical Lattice Clock. Phys. Rev. Lett. **116**, 035301 (2016).

[113] B. Song, C. He, S. Zhang, E. Hajiyev, W. Huang, X.-J. Liu, G.-B. Jo, Spin-orbit-coupled two-electron Fermi gases of ytterbium atoms. Phys. Rev. A **94**, 061604 (2016).

[114] N.Q. Burdick, Y. Tang, B.L. Lev, Long-Lived Spin-Orbit-Coupled Degenerate Dipolar Fermi Gas. Phys. Rev. X **6**, 031022 (2016).

[115] C. Zhang, Spin-orbit coupling and perpendicular Zeeman field for fermionic cold atoms: Observation of the intrinsic anomalous Hall effect. Phys. Rev. A **82**, 021607 (2010).

[116] D.L. Campbell, G. Juzeliūnas, I.B. Spielman, Realistic Rashba and Dresselhaus spin-orbit coupling for neutral atoms. Phys. Rev. A **84**, 025602 (2011).

[117] B.M. Anderson, G. Juzeliūnas, V.M. Galitski, I.B. Spielman, Synthetic 3D Spin-Orbit Coupling. Phys. Rev. Lett. **108**, 235301 (2012).

[118] Z.-F. Xu, L. You, M. Ueda, Atomic spin-orbit coupling synthesized with magnetic-field-gradient pulses. Phys. Rev. A **87**, 063634 (2013).

[119] X.-J. Liu, K.T. Law, T.K. Ng, Realization of 2D Spin-Orbit Interaction and Exotic Topological Orders in Cold Atoms. Phys. Rev. Lett. **112**, 086401 (2014).

[120] B.-Z. Wang, Y.-H. Lu, W. Sun, S. Chen, Y. Deng, X.-J. Liu, Dirac-, Rashba-, and Weyl-type spin-orbit couplings: Toward experimental realization in ultracold atoms. Phys. Rev. A **97**, 011605 (2018).

[121] L. Huang, Z. Meng, P. Wang, P. Peng, S.-L. Zhang, L. Chen, D. Li, Q. Zhou, J. Zhang, Experimental realization of two-dimensional synthetic spin–orbit coupling in ultracold Fermi gases. Nature Physics **12**, 540 (2016).

[122] Z. Wu, L. Zhang, W. Sun, X.-T. Xu, B.-Z. Wang, S.-C. Ji, Y. Deng, S. Chen, X.-J. Liu, J.-W. Pan, Realization of two-dimensional spin-orbit coupling for Bose-Einstein condensates. Science **354**, 83 (2016).

[123] W. Sun, B.-Z. Wang, X.-T. Xu, C.-R. Yi, L. Zhang, Z. Wu, Y. Deng, X.-J. Liu, S. Chen, J.-W. Pan, Highly Controllable and Robust 2D Spin-Orbit Coupling for Quantum Gases. Phys. Rev. Lett. **121**, 150401 (2018).

[124] M. Lewenstein, A. Sanpera, V. Ahufinger, B. Damski, A. Sen, U. Sen, Ultracold atomic gases in optical lattices: mimicking condensed matter physics and beyond. Advances in Physics **56**, 243 (2007).

[125] M.Z. Hasan, C.L. Kane, Colloquium: Topological insulators. Rev. Mod. Phys. **82**, 3045 (2010).

[126] X.-L. Qi, S.-C. Zhang, Topological insulators and superconductors. Rev. Mod. Phys. **83**, 1057 (2011).

[127] M. Lewenstein, A. Sanpera, V. Ahufinger, *Ultracold Atoms in Optical Lattices: Simulating Quantum Many-body Systems*. EBSCO ebook academic collection (Oxford University Press, Oxford, 2012). ISBN 9780199573127

[128] V. Galitski, I.B. Spielman, Spin-orbit coupling in quantum gases. Nature **494**, 49 (2013).

[129] H. Zhai, Degenerate quantum gases with spinorbit coupling: a review. Reports on Progress in Physics **78**, 026001 (2015).

[130] M. Beeler, R. Williams, K. Jimenez-Garcia, L. LeBlanc, A. Perry, I. Spielman, The spin Hall effect in a quantum gas. Nature **498**, 201 (2013).

[131] K. von Klitzing, The quantized Hall effect. Rev. Mod. Phys. **58**, 519 (1986).

[132] Y. Hatsugai, Chern number and edge states in the integer quantum Hall effect. Phys. Rev. Lett. **71**, 3697 (1993).

[133] H.L. Stormer, D.C. Tsui, A.C. Gossard, The fractional quantum Hall effect. Rev. Mod. Phys. **71**, 298 (1999).

[134] H. Weng, R. Yu, X. Hu, X. Dai, Z. Fang, Quantum anomalous Hall effect and related topological electronic states. Advances in Physics **64**, 227 (2015).

[135] J. Wang, B. Lian, S.-C. Zhang, Quantum anomalous Hall effect in magnetic topological insulators. Physica Scripta **2015**, 014003 (2015).

[136] F. Wilczek, Majorana returns. Nature Physics **5**, 614 (2009).

[137] M. Sato, Y. Takahashi, S. Fujimoto, Non-Abelian Topological Order in $s$-Wave Superfluids of Ultracold Fermionic Atoms. Phys. Rev. Lett. **103**, 020401 (2009).

[138] L. Jiang, T. Kitagawa, J. Alicea, A.R. Akhmerov, D. Pekker, G. Refael, J.I. Cirac, E. Demler, M.D. Lukin, P. Zoller, Majorana Fermions in Equilibrium and in Driven Cold-Atom Quantum Wires. Phys. Rev. Lett. **106**, 220402 (2011).

[139] X.-J. Liu, L. Jiang, H. Pu, H. Hu, Probing Majorana fermions in spin-orbit-coupled atomic Fermi gases. Phys. Rev. A **85**, 021603 (2012).

[140] X.-J. Liu, H. Hu, Topological superfluid in one-dimensional spin-orbit-coupled atomic Fermi gases. Phys. Rev. A **85**, 033622 (2012).

[141] X.-J. Liu, H. Hu, Topological Fulde-Ferrell superfluid in spin-orbit-coupled atomic Fermi gases. Phys. Rev. A **88**, 023622 (2013).

[142] E.J. Mueller, Viewpoint: Strong Staggered Flux Lattices for Cold Atoms. Physics **4**, 107 (2011).

[143] M. Schirber, Focus: Cold Atoms Reveal Their Crystalline Nature. Physics **28**, 12 (2011).

[144] Y. Li, G.I. Martone, L.P. Pitaevskii, S. Stringari, Superstripes and the Excitation Spectrum of a Spin-Orbit-Coupled Bose-Einstein Condensate. Phys. Rev. Lett. **110**, 235302 (2013).

[145] X.-L. Chen, J. Wang, Y. Li, X.-J. Liu, H. Hu, Quantum depletion and superfluid density of a supersolid in Raman spin-orbit-coupled Bose gases. Phys. Rev. A **98**, 013614 (2018).

[146] L. Chen, H. Pu, Z.-Q. Yu, Y. Zhang, Collective excitation of a trapped Bose-Einstein condensate with spin-orbit coupling. Phys. Rev. A **95**, 033616 (2017).

[147] Q.-Z. Zhu, B. Wu, Superfluidity of BoseEinstein condensates in ultracold atomic gases. Chinese Physics B **24**, 050507 (2015).

[148] H. Shi, Finite temperature excitations in a dilute Bose-condensed gas, Ph.D. thesis, University of Toronto, 1997.

[149] H. Shi, A. Griffin, Finite-temperature excitations in a dilute Bose-condensed gas. Physics Reports **304**, 1 (1998).

[150] T. Gao, J.-S. Pan, D. Zhang, L. Kong, R. Li, X. Shen, X. Chen, S.-G. Peng, M. Zhan, W.V. Liu, K. Jiang, State control of phonon collision in a spherical Bose-Einstein condensate. (2018).

[151] A.L. Fetter, J.D. Walecka, *Quantum Theory of Many-particle Systems*. Dover Books on Physics (Dover Publications, 2003). Chap. 8. ISBN 9780486428277

[152] E. Feenberg, *Theory of Quantum Fluids*. Pure and applied physics, vol. 31 (Elsevier Science, 2012). Chap. 10. ISBN 9780323157933

[153] A.L. Fetter, Nonuniform states of an imperfect bose gas. Annals of Physics **70**, 67 (1972).

[154] M. Edwards, R. Dodd, C.W. Clark, K. Burnett, Zero-temperature, mean-field theory of atomic Bose-Einstein condensates. National Institute of Standards and Technology, Journal of Research **101**, 553 (1996).

[155] M. Edwards, P.A. Ruprecht, K. Burnett, R.J. Dodd, C.W. Clark, Collective Excitations of Atomic Bose-Einstein Condensates. Phys. Rev. Lett. **77**, 1671 (1996).

[156] R.J. Dodd, M. Edwards, C.W. Clark, K. Burnett, Collective excitations of Bose-Einstein-condensed gases at finite temperatures. Phys. Rev. A **57**, 32 (1998).

[157] A. Griffin, Conserving and gapless approximations for an inhomogeneous Bose gas at finite temperatures. Phys. Rev. B **53**, 9341 (1996).

[158] V.N. Popov, V.N. Popov, *Functional Integrals and Collective Excitations*. Cambridge Monographs on Mathematical Physics (Cambridge University Press, 1991). ISBN 9780521407878

[159] H. Buljan, M. Segev, A. Vardi, Incoherent Matter-Wave Solitons and Pairing Instability in an Attractively Interacting Bose-Einstein Condensate. Phys. Rev. Lett. **95**, 180401 (2005).

[160] J.O. Andersen, Theory of the weakly interacting Bose gas. Rev. Mod. Phys. **76**, 599 (2004).

[161] P. Arnold, G. Moore, BEC Transition Temperature of a Dilute Homogeneous Imperfect Bose Gas. Phys. Rev. Lett. **87**, 120401 (2001).

[162] V.A. Kashurnikov, N.V. Prokof'ev, B.V. Svistunov, Critical Temperature Shift in Weakly Interacting Bose Gas. Phys. Rev. Lett. **87**, 120402 (2001).

[163] M. Abad, A. Recati, A study of coherently coupled two-component Bose-Einstein condensates. The European Physical Journal D **67**, 1 (2013).

[164] G.I. Martone, Y. Li, S. Stringari, Approach for making visible and stable stripes in a spin-orbit-coupled Bose-Einstein superfluid. Phys. Rev. A **90**, 041604 (2014).

[165] M.A. Cazalilla, R. Citro, T. Giamarchi, E. Orignac, M. Rigol, One dimensional bosons: From condensed matter systems to ultracold gases. Rev. Mod. Phys. **83**, 1405 (2011).

[166] X.-W. Guan, M.T. Batchelor, C. Lee, Fermi gases in one dimension: From Bethe ansatz to experiments. Rev. Mod. Phys. **85**, 1633 (2013).

[167] H. Moritz, T. Stöferle, M. Köhl, T. Esslinger, Exciting Collective Oscillations in a Trapped 1D Gas. Phys. Rev. Lett. **91**, 250402 (2003).

[168] B. Paredes, A. Widera, V. Murg, O. Mandel, S. Fölling, I. Cirac, G.V. Shlyapnikov, T.W. Hänsch, I. Bloch, Tonks–Girardeau gas of ultracold atoms in an optical lattice. Nature **429**, 277 (2004).

[169] J. Esteve, J.-B. Trebbia, T. Schumm, A. Aspect, C.I. Westbrook, I. Bouchoule, Observations of Density Fluctuations in an Elongated Bose Gas: Ideal Gas and Quasicondensate Regimes. Phys. Rev. Lett. **96**, 130403 (2006).

[170] B. Fang, G. Carleo, A. Johnson, I. Bouchoule, Quench-Induced Breathing Mode of One-Dimensional Bose Gases. Phys. Rev. Lett. **113**, 035301 (2014).

[171] M. Cheneau, P. Barmettler, D. Poletti, M. Endres, P. Schauß, T. Fukuhara, C. Gross, I. Bloch, C. Kollath, S. Kuhr, Light-cone-like spreading of correlations in a quantum many-body system. Nature **481**, 484 (2012).

[172] C. Menotti, S. Stringari, Collective oscillations of a one-dimensional trapped Bose-Einstein gas. Phys. Rev. A **66**, 043610 (2002).

[173] H. Hu, G. Xianlong, X.-J. Liu, Collective modes of a one-dimensional trapped atomic Bose gas at finite temperatures. Phys. Rev. A **90**, 013622 (2014).

[174] A.I. Gudyma, G.E. Astrakharchik, M.B. Zvonarev, Reentrant behavior of the breathing-mode-oscillation frequency in a one-dimensional Bose gas. Phys. Rev. A **92**, 021601 (2015).

[175] M.J. Davis, P.B. Blakie, A.H. van Amerongen, N.J. van Druten, K.V. Kheruntsyan, Yang-Yang thermometry and momentum distribution of a trapped one-dimensional Bose gas. Phys. Rev. A **85**, 031604 (2012).

[176] K.V. Kheruntsyan, D.M. Gangardt, P.D. Drummond, G.V. Shlyapnikov, Pair Correlations in a Finite-Temperature 1D Bose Gas. Phys. Rev. Lett. **91**, 040403 (2003).

[177] K.V. Kheruntsyan, D.M. Gangardt, P.D. Drummond, G.V. Shlyapnikov, Finite-temperature correlations and density profiles of an inhomogeneous interacting one-dimensional Bose gas. Phys. Rev. A **71**, 053615 (2005).

[178] T. Kinoshita, T. Wenger, D.S. Weiss, Local Pair Correlations in One-Dimensional Bose Gases. Phys. Rev. Lett. **95**, 190406 (2005).

[179] E.H. Lieb, W. Liniger, Exact Analysis of an Interacting Bose Gas. I. The General Solution and the Ground State. Phys. Rev. **130**, 1605 (1963).

[180] E.H. Lieb, Exact Analysis of an Interacting Bose Gas. II. The Excitation Spectrum. Phys. Rev. **130**, 1616 (1963).

[181] E.H. Lieb, W. Liniger, Exact Analysis of an Interacting Bose Gas. I. The General Solution and the Ground State. Phys. Rev. **130**, 1605 (1963).

[182] E.H. Lieb, Exact Analysis of an Interacting Bose Gas. II. The Excitation Spectrum. Phys. Rev. **130**, 1616 (1963).

[183] M. Olshanii, Atomic Scattering in the Presence of an External Confinement and a Gas of Impenetrable Bosons. Phys. Rev. Lett. **81**, 938 (1998).

[184] H. Bethe, Zur Theorie der Metalle. Zeitschrift fr Physik **71**, 205 (1931).

[185] E.B. Kolomeisky, T.J. Newman, J.P. Straley, X. Qi, Low-Dimensional Bose Liquids: Beyond the Gross-Pitaevskii Approximation. Phys. Rev. Lett. **85**, 1146 (2000).

[186] V. Dunjko, V. Lorent, M. Olshanii, Bosons in Cigar-Shaped Traps: Thomas-Fermi Regime, Tonks-Girardeau Regime, and In Between. Phys. Rev. Lett. **86**, 5413 (2001).

[187] A.I. Gudyma, G.E. Astrakharchik, M.B. Zvonarev, Reentrant behavior of the breathing-mode-oscillation frequency in a one-dimensional Bose gas. Phys. Rev. A **92**, 021601 (2015).

[188] J.N. Fuchs, X. Leyronas, R. Combescot, Hydrodynamic modes of a one-dimensional trapped Bose gas. Phys. Rev. A **68**, 043610 (2003).

[189] Z.D. Zhang, G.E. Astrakharchik, D.C. Aveline, S. Choi, H. Perrin, T.H. Bergeman, M. Olshanii, Breakdown of scale invariance in the vicinity of the Tonks-Girardeau limit. Phys. Rev. A **89**, 063616 (2014).

[190] D.S. Jin, M.R. Matthews, J.R. Ensher, C.E. Wieman, E.A. Cornell, Temperature-Dependent Damping and Frequency Shifts in Collective Excitations of a Dilute Bose-Einstein Condensate. Phys. Rev. Lett. **78**, 764 (1997).

[191] A. Minguzzi, P. Vignolo, M.L. Chiofalo, M.P. Tosi, Hydrodynamic excitations in a spin-polarized Fermi gas under harmonic confinement in one dimension. Phys. Rev. A **64**, 033605 (2001).

[192] B. Sutherland, *Beautiful Models: 70 Years of Exactly Solved Quantum Many-body Problems* (World Scientific, 2004). ISBN 9789812388971

[193] S. Richard, F. Gerbier, J.H. Thywissen, M. Hugbart, P. Bouyer, A. Aspect, Momentum Spectroscopy of 1D Phase Fluctuations in Bose-Einstein Condensates. Phys. Rev. Lett. **91**, 010405 (2003).

[194] T. Kinoshita, T. Wenger, D.S. Weiss, Observation of a one-dimensional Tonks-Girardeau gas. Science **305**, 1125 (2004).

[195] H. Moritz, T. Stöferle, K. Günter, M. Köhl, T. Esslinger, Confinement Induced Molecules in a 1D Fermi Gas. Phys. Rev. Lett. **94**, 210401 (2005).

[196] K. Günter, T. Stöferle, H. Moritz, M. Köhl, T. Esslinger, $p$-Wave Interactions in Low-Dimensional Fermionic Gases. Phys. Rev. Lett. **95**, 230401 (2005).

[197] B. Fang, G. Carleo, A. Johnson, I. Bouchoule, Quench-Induced Breathing Mode of One-Dimensional Bose Gases. Phys. Rev. Lett. **113**, 035301 (2014).

[198] K.V. Kheruntsyan, D.M. Gangardt, P.D. Drummond, G.V. Shlyapnikov, Pair Correlations in a Finite-Temperature 1D Bose Gas. Phys. Rev. Lett. **91**, 040403 (2003).

[199] A. Minguzzi, D.M. Gangardt, Exact Coherent States of a Harmonically Confined Tonks-Girardeau Gas. Phys. Rev. Lett. **94**, 240404 (2005).

[200] G.E. Astrakharchik, J. Boronat, J. Casulleras, S. Giorgini, Beyond the Tonks-Girardeau Gas: Strongly Correlated Regime in Quasi-One-Dimensional Bose Gases. Phys. Rev. Lett. **95**, 190407 (2005).

[201] M. Batchelor, M. Bortz, X.-W. Guan, N. Oelkers, Evidence for the super Tonks–Girardeau gas. Journal of Statistical Mechanics: Theory and Experiment **2005**, 10001 (2005).

[202] X.-W. Guan, *Private Communications*, 2016

[203] V. Dunjko, V. Lorent, M. Olshanii, Bosons in Cigar-Shaped Traps: Thomas-Fermi Regime, Tonks-Girardeau Regime, and In Between. Phys. Rev. Lett. **86**, 5413 (2001).

[204] T. Cheon, T. Shigehara, Fermion-Boson Duality of One-Dimensional Quantum Particles with Generalized Contact Interactions. Phys. Rev. Lett. **82**, 2536 (1999).

[205] E. Taylor, H. Hu, X.-J. Liu, A. Griffin, Variational theory of two-fluid hydrodynamic modes at unitarity. Phys. Rev. A **77**, 033608 (2008).

[206] E. Taylor, H. Hu, X.-J. Liu, L.P. Pitaevskii, A. Griffin, S. Stringari, First and second sound in a strongly interacting Fermi gas. Phys. Rev. A **80**, 053601 (2009).

[207] L.D. Landau, E.M. Lifshitz, *Quantum Mechanics: Non-Relativistic Theory*. Teoreticheskaia fizika (Elsevier Science, 2013). ISBN 9781483149127

[208] J. Zhang, E.G.M. van Kempen, T. Bourdel, L. Khaykovich, J. Cubizolles, F. Chevy, M. Teichmann, L. Tarruell, S.J.J.M.F. Kokkelmans, C. Salomon, $P$-wave Feshbach resonances of ultracold $^6$Li. Phys. Rev. A **70**, 030702 (2004).

[209] C. Ticknor, C.A. Regal, D.S. Jin, J.L. Bohn, Multiplet structure of Feshbach resonances in nonzero partial waves. Phys. Rev. A **69**, 042712 (2004).

[210] C.H. Schunck, M.W. Zwierlein, C.A. Stan, S.M.F. Raupach, W. Ketterle, A. Simoni, E. Tiesinga, C.J. Williams, P.S. Julienne, Feshbach resonances in fermionic $^6$Li. Phys. Rev. A **71**, 045601 (2005).

[211] J. Fuchs, C. Ticknor, P. Dyke, G. Veeravalli, E. Kuhnle, W. Rowlands, P. Hannaford, C.J. Vale, Binding energies of $^6$Li $p$-wave Feshbach molecules. Phys. Rev. A **77**, 053616 (2008).

[212] B.E. Granger, D. Blume, Tuning the Interactions of Spin-Polarized Fermions Using Quasi-One-Dimensional Confinement. Phys. Rev. Lett. **92**, 133202 (2004).

[213] L. Pricoupenko, Resonant Scattering of Ultracold Atoms in Low Dimensions. Phys. Rev. Lett. **100**, 170404 (2008).

[214] M. Olshanii, Atomic Scattering in the Presence of an External Confinement and a Gas of Impenetrable Bosons. Phys. Rev. Lett. **81**, 938 (1998).

[215] S.-G. Peng, S. Tan, K. Jiang, Manipulation of $p$-Wave Scattering of Cold Atoms in Low Dimensions Using the Magnetic Field Vector. Phys. Rev. Lett. **112**, 250401 (2014).

[216] T. Cheon, T. Shigehara, Realizing discontinuous wave functions with renormalized short-range potentials. Physics Letters A **243**, 111 (1998).

[217] C.N. Yang, C.P. Yang, Thermodynamics of a OneDimensional System of Bosons with Repulsive DeltaFunction Interaction. Journal of Mathematical Physics **10**, 1115 (1969).

[218] M.A. Cazalilla, R. Citro, T. Giamarchi, E. Orignac, M. Rigol, One dimensional bosons: From condensed matter systems to ultracold gases. Rev. Mod. Phys. **83**, 1405 (2011).

[219] X.-W. Guan, M.T. Batchelor, C. Lee, Fermi gases in one dimension: From Bethe ansatz to experiments. Rev. Mod. Phys. **85**, 1633 (2013).

[220] J. Joseph, B. Clancy, L. Luo, J. Kinast, A. Turlapov, J.E. Thomas, Measurement of Sound Velocity in a Fermi Gas near a Feshbach Resonance. Phys. Rev. Lett. **98**, 170401 (2007).

[221] H. Hu, A. Minguzzi, X.-J. Liu, M.P. Tosi, Collective Modes and Ballistic Expansion of a Fermi Gas in the BCS-BEC Crossover. Phys. Rev. Lett. **93**, 190403 (2004).

[222] Z.-Q. Yu, Equation of state and phase transition in spin-orbit-coupled Bose gases at finite temperature: A perturbation approach. Phys. Rev. A **90**, 053608 (2014).

[223] R. Liao, O. Fialko, J. Brand, U. Zülicke, Multicriticality, metastability, and the roton feature in Bose-Einstein condensates with three-dimensional spin-orbit coupling. Phys. Rev. A **92**, 043633 (2015).

[224] T. Congy, A.M. Kamchatnov, N. Pavloff, Nonlinear waves in coherently coupled Bose-Einstein condensates. Phys. Rev. A **93**, 043613 (2016).

[225] L.D. Landau, E.M. Lifšic, *Statistical Physics: Part 1.* Course of theoretical physics vol. 2 (Pergamon Press, New York, 1980). ISBN 9780080230399

[226] Z.-Q. Yu, Landau criterion for an anisotropic Bose-Einstein condensate. Phys. Rev. A **95**, 033618 (2017).

[227] L. Santos, G.V. Shlyapnikov, M. Lewenstein, Roton-Maxon Spectrum and Stability of Trapped Dipolar Bose-Einstein Condensates. Phys. Rev. Lett. **90**, 250403 (2003).

[228] R.M. Wilson, C. Ticknor, J.L. Bohn, E. Timmermans, Roton immiscibility in a two-component dipolar Bose gas. Phys. Rev. A **86**, 033606 (2012).

[229] X. Cui, Q. Zhou, Enhancement of condensate depletion due to spin-orbit coupling. Phys. Rev. A **87**, 031604 (2013).

[230] R. Liao, Z.-G. Huang, X.-M. Lin, O. Fialko, Spin-orbit-coupled Bose gases at finite temperatures. Phys. Rev. A **89**, 063614 (2014).

[231] M.A. Khamehchi, Y. Zhang, C. Hamner, T. Busch, P. Engels, Measurement of collective excitations in a spin-orbit-coupled Bose-Einstein condensate. Phys. Rev. A **90**, 063624 (2014).

[232] Q. Zhu, C. Zhang, B. Wu, Exotic superfluidity in spin-orbit coupled Bose-Einstein condensates. EPL (Europhysics Letters) **100**, 50003 (2012).

[233] K. Zhou, Z. Zhang, Opposite Effect of Spin-Orbit Coupling on Condensation and Superfluidity. Phys. Rev. Lett. **108**, 025301 (2012).

[234] J. Léonard, A. Morales, P. Zupancic, T. Esslinger, T. Donner, Supersolid formation in a quantum gas breaking a continuous translational symmetry. Nature **543**, 87 (2017).

[235] J. Li, W. Huang, B. Shteynas, S. Burchesky, F.Ç. Top, E. Su, J. Lee, A.O. Jamison, W. Ketterle, Spin-Orbit Coupling and Spin Textures in Optical Superlattices. Phys. Rev. Lett. **117**, 185301 (2016).

[236] F. Mivehvar, D.L. Feder, Enhanced stripe phases in spin-orbit-coupled Bose-Einstein condensates in ring cavities. Phys. Rev. A **92**, 023611 (2015).

[237] R. Lopes, C. Eigen, N. Navon, D. Clément, R.P. Smith, Z. Hadzibabic, Quantum Depletion of a Homogeneous Bose-Einstein Condensate. Phys. Rev. Lett. **119**, 190404 (2017).

[238] L. He, H. Hu, X.-J. Liu, Realizing Fulde-Ferrell Superfluids via a Dark-State Control of Feshbach Resonances. Phys. Rev. Lett. **120**, 045302 (2018).

[239] S. Stringari, Diffused Vorticity and Moment of Inertia of a Spin-Orbit Coupled Bose-Einstein Condensate. Phys. Rev. Lett. **118**, 145302 (2017).

[240] Y.-X. Hu, C. Miniatura, B. Grémaud, Half-skyrmion and vortex-antivortex pairs in spinor condensates. Phys. Rev. A **92**, 033615 (2015).

[241] M. DeMarco, H. Pu, Angular spin-orbit coupling in cold atoms. Phys. Rev. A **91**, 033630 (2015).

[242] C. Qu, K. Sun, C. Zhang, Quantum phases of Bose-Einstein condensates with synthetic spin–orbital-angular-momentum coupling. Phys. Rev. A **91**, 053630 (2015).

[243] K. Sun, C. Qu, C. Zhang, Spin–orbital-angular-momentum coupling in Bose-Einstein condensates. Phys. Rev. A **91**, 063627 (2015).

[244] L. Chen, H. Pu, Y. Zhang, Spin-orbit angular momentum coupling in a spin-1 Bose-Einstein condensate. Phys. Rev. A **93**, 013629 (2016).

[245] H.-R. Chen, K.-Y. Lin, P.-K. Chen, N.-C. Chiu, J.-B. Wang, C.-A. Chen, P.-P. Huang, S.-K. Yip, Y. Kawaguchi, Y.-J. Lin, Spin–Orbital-Angular-Momentum Coupled Bose-Einstein Condensates. Phys. Rev. Lett. **121**, 113204 (2018).

[246] D. Zhang, T. Gao, P. Zou, L. Kong, R. Li, X. Shen, X.-L. Chen, S.-G. Peng, M. Zhan, H. Pu, K. Jiang, Observation of quantum phase transition in spin-orbital-angular-momentum coupled Bose-Einstein condensate. (2018).

[247] M.E. Fisher, M.N. Barber, D. Jasnow, Helicity Modulus, Superfluidity, and Scaling in Isotropic Systems. Phys. Rev. A **8**, 1111 (1973).

[248] E. Taylor, A. Griffin, N. Fukushima, Y. Ohashi, Pairing fluctuations and the superfluid density through the BCS-BEC crossover. Phys. Rev. A **74**, 063626 (2006).

# List of Publications

The major contents of this thesis have already appeared in some of the following journal papers or preprints co-authored during my PhD study:

1. **Xiao-Long Chen**, Yun Li, and Hui Hu,
   *Collective modes of a harmonically trapped one-dimensional Bose gas: The effects of finite particle number and nonzero temperature*,
   Phys. Rev. A **91**, 063631 (2015).

2. **Xiao-Long Chen**, Xia-Ji Liu, and Hui Hu,
   *Probing an effective-range-induced super fermionic Tonks-Girardeau gas with ultracold atoms in one-dimensional harmonic traps*,
   Phys. Rev. A **94**, 033630 (2016).

3. **Xiao-Long Chen**, Xia-Ji Liu, and Hui Hu,
   *Quantum and thermal fluctuations in a Raman spin-orbit-coupled Bose gas*,
   Phys. Rev. A **96**, 013625 (2017).

4. **Xiao-Long Chen**, Jia Wang, Yun Li, Xia-Ji Liu, and Hui Hu,
   *Quantum depletion and superfluid density of a supersolid in Raman spin-orbit coupled Bose gases*,
   Phys. Rev. A **98**, 013614 (2018).

5. Tianyou Gao, Jian-Song Pan, Dongfang Zhang, Lingran Kong, Ruizong Li, Xing Shen, **Xiao-Long Chen**, Shi-Guo Peng, Mingsheng Zhan, W. Vincent Liu and Kaijun Jiang,
   *State control of phonon collision in a spherical Bose-Einstein condensate*,
   arXiv:1805.04727 (2018).

6. Dongfang Zhang, Tianyou Gao, Peng Zou, Lingran Kong, Ruizong Li, Xing Shen, **Xiao-Long Chen**, Shi-Guo Peng, Mingsheng Zhan, Han Pu, and Kaijun Jiang,

*Observation of quantum phase transition in spin-orbital-angular-momentum coupled Bose-Einstein condensate*,
arXiv:1806.06263 (2018).